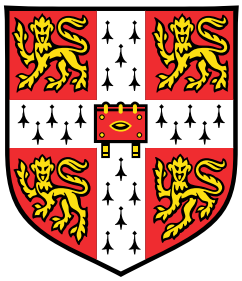

University of Cambridge

Dynamic Acoustic Control of Semiconductor Quantum Dot-Based Devices for Quantum Light Generation

Bruno Villa Piñeros

Department of Physics
Girton College

This dissertation is submitted for the degree of Doctor of Philosophy

November 2019

DISSERTATION

Dynamic Acoustic Control of Semiconductor Quantum Dot-Based Devices for Quantum Light Generation

Bruno Villa Piñeros

Department of Physics
Cavendish Laboratory
University of Cambridge
Cambridge, United Kingdom

November 2019

Dynamic Acoustic Control of Semiconductor Quantum Dot-Based Devices for Quantum Light Generation

Bruno Villa Piñeros

Supervisors: Dr. Andrew J. Shields
Prof. Chris J. B. Ford

Toshiba Research Europe Ltd.
Cambridge Research Laboratory
208 Cambridge Science Park
Cambridge CB4 0GZ, United Kingdom
Telephone +44 1223 436909

Semiconductor Physics Group
University of Cambridge
JJ Thomson Ave,
Cambridge CB3 0HE, United Kingdom
Telephone +44 1223 337200

This project has received funding from the European Union's Horizon 2020 research and innovation programme under the Marie Skłodowska-Curie grant agreement No 642688.

Declaration

I hereby declare that except where specific reference is made to the work of others, the contents of this dissertation are original. This dissertation is the result of my own work and contains nothing which is the outcome of work done in collaboration with others, except as specified in the text and Acknowledgements. This dissertation does not exceed 60,000 words including including summary/abstract, tables, footnotes and appendices, and has fewer than 150 figures.

It is not substantially the same as any that I have submitted, or, is being concurrently submitted for a degree or diploma or other qualification at the University of Cambridge or any other University or similar institution except as declared in the Preface and specified in the text. I further state that no substantial part of my dissertation has already been submitted, or, is being concurrently submitted for any such degree, diploma or other qualification at the University of Cambridge or any other University or similar institution except as declared in the Preface and specified in the text.

Bruno Villa Piñeros
November 2019

Acknowledgements

Looking back at the decision to join the SAWtrain network to pursue a Ph.D., it is a decision I would always make again. The past years have brought many friendships and unique experiences and opportunities. I am very grateful to all of the PIs involved in the creation and running of the network. I am also indebted to Prof. Chris Ford and Dr. Andrew Shields for the opportunity to become a part of their teams and for the time they dedicate to valuable discussions despite their busy schedules. Scientific research is a complex task requiring deep knowledge across various fields, such that a single person could not succeed alone. It is good then that I have had the fortune to work alongside extremely talented and helpful people. I would like to thank all of the those I've had the pleasure to work with at Toshiba Research Europe, the Cavendish Laboratory, the University of Augsburg and the SAWtrain network. In particular I would like to express my deepest gratitude to Anthony, Dave, and Mark for their guidance and advice. They have the rare ability to combine professionalism with approachability and seem to always have a simple solution at hand. I'm also thankful to Martin Ward for his insight and discussions, to Melanie and Joanna for their invaluable help in the cleanroom, and to Jon and Tom for the impeccable e-beam jobs.

Naturally, I'm also very grateful to my fellow PhD students and friends at Toshiba, who have made this time an incredible experience both in and outside of the workplace. I have learned so much from you guys and can not imagine a better group of people to have shared all the lunches, squash games, board games, holiday trips, pub trips and more with. Last but not least in the list of people I'm indebted and grateful to are my family and my friends, both the old and the new, on whom I know I can always rely as they can rely on me. Thank you.

Abstract

This thesis presents work on a series of devices for the generation of photonic quantum states based on self-assembled InAs quantum dots, which are among the most technologically mature candidates for practical quantum photonic applications due to their high internal quantum efficiency, narrow linewidth, tunability and straightforward integration with photonic and electric components. The primary results presented concern sources of multi-photon entangled states and single-photon sources with high repetition rate, both of which are crucial components for emerging photonic quantum technologies. First, we propose a scheme for the sequential generation of entangled photon chains by resonant scattering of a laser field on a single charged particle in a cavity-enhanced quantum dot. The charge has an associated spin that can determine the time bin of a photon, allowing for information encoding in this degree of freedom. We demonstrate coherent operations on this spin and realize a proof-of-principle experiment of the proposed scheme by showing that the time bin of a single-photon is dependent on the measured state of the trapped spin.

The second main avenue of work investigates the effects of a surface acoustic wave, a mechanical displacement wave confined to the surface of a substrate, on the optical properties of quantum dots. In particular, we exploit the dynamic acoustically-induced tuning of the emission energy to modulate the Purcell effect in a pillar microcavity. Under resonant optical excitation we demonstrate the conversion of the continuous wave laser into a pulsed single-photon stream inheriting the acoustic frequency of 1 GHz as the repetition rate. High resolution spectroscopy reveals the presence of narrow sidebands in the emission spectrum, whose relative intensity can be controlled by the acoustic power and laser detuning. Furthermore, we develop a platform for analogous in-plane experiments by transferring GaAs membranes hosting quantum dots onto $LiNbO_3$ substrates and patterning them into whispering gallery mode optical resonators. In addition to Purcell enhancement and acoustic tuning of the emission, the devices exhibit strong localized mechanical resonances. Finally, we perform initial experiments on the effects of a surface acoustic wave on the spin of a charge trapped in a quantum dot. We integrate acoustic transducers with charge-tunable diodes, where the charge state of the dot can be precisely controlled by an applied bias voltage, and demonstrate the frustration of optical spin pumping by the acoustic wave.

List of Publications

- **Villa B.**, Bennett A. J., Ellis D. J. P. , Lee J. P., Skiba-Szymanska J., Mitchell T. A., Griffiths J. P., Farrer I., Ritchie D. A., Ford C.J.B., Shields A. J. – Surface Acoustic Wave Modulation of a Coherently Driven Quantum Dot in a Pillar Microcavity. Applied Physics Letters 111, 011103 – 2017
- Lee J.P., **Villa B.**, Bennett A. J., Stevenson R. M., Ellis D. J. P., Farrer I., Ritchie D. A., Shields A. J. – A Quantum Dot as a Source of Time-Bin Entangled Multi-Photon States. Quantum Science and Technology 4, 025011 – 2019
- Lee J.P., Wells L.M., **Villa B.**, Kalliakos S., Stevenson R.M., Ellis D.J.P., Farrer I., Ritchie D. A., Bennett, A. J., Shields A. J. – Controllable Photonic Time-Bin Qubits from a Quantum Dot. Phys. Rev. X. 8, 021078 – 2018
- Wells L.M., Kalliakos S., **Villa B.**, Ellis D.J.P., Stevenson R.M., Bennett A.J., Farrer I., Ritchie D.A., Shields A.J. – Photon Phase Shift at the Few-Photon Level and Optical Switching by a Quantum Dot in a Microcavity. Phys. Rev. Applied 11, 061001 – 2019

List of Conferences

- Presentation at Solid State Devices and Materials (SSDM), Sep 11 2018, Tokyo, Japan
- Presentation at DPG spring meeting, Mar 11-16 2018, Berlin, Germany
- Presentation at Rank Price Funds symposium on “Solid State Nano-Photonics for Quantum Science & Technology”, September 25-28 2017, Grasmere, UK
- Presentation at SAWtrain Summer School “Physics and applications of GHz vibrations in semiconductors”, July 11-21 2017, Cargèse, France
- Poster presentation at SPICE Workshop on Quantum Acoustics, May 17-20 2016, Mainz, Germany

Table of contents

Nomenclature

Acronyms / Abbreviations

2DEG	Two-dimensional electron gas
H_2O_2	Hydrogen peroxide
H_2SO_4	Sulphuric acid
$LiNbO_3$	Lithium niobate
Si_3N_4	Silicon nitride
µPL	Micro-photoluminescence spectroscopy
ADC	Analog-to-digital converter
AlAs	Aluminium arsenide
AlGaAs	Aluminium gallium arsenide
AlN	Aliminium nitride
APD	Avalanche photodiode
BHF	Buffered hydrofluoric acid
BS	Beam splitter
CB	Conduction band
CNOT	Controlled NOT
cw	Continuous wave
DBR	Distributed Bragg reflector

EL	Electroluminescence
ELO	Epitaxial lift-off
FEM	Finite element method
FSR	Free spectral range
FSS	Fine structure splitting
GaAs	Gallium arsenide
GHZ	Greenberger-Horne-Zeilinger
HBT	Hanbury-Brown and Twiss
HOM	Hong-Ou-Mandel
ICP	Inductively coupled plasma
IDT	Interdigitated transducer
IL	Insertion loss
InAs	Indium arsenide
KLM	Knill Laflamme Milburn
LED	Light-emitting diode
LOQC	Linear optical quantum computing
MBE	Molecular-beam epitaxy
NA	Numerical aperture
PCB	Printed circuit board
PECVD	Plasma enhanced chemical vapour deposition
PL	Photoluminescence
PML	Perfectly matched layer
PMMA	Poly(methyl) methacrylate
PR	Photoresist

QD	Quantum dot
QED	Quantum electrodynamics
QIP	Quantum information processing
QKD	Quantum key distribution
QPIC	Quantum photonic integrated circuit
RF	Resonance fluorescence
rf	Radio-frequency
RIE	Reactive ion etching
RRS	Resonant Rayleigh scattering
SAW	Surface acoustic wave
SK	Stranski-Krastanov
SLD	Superluminescent diode
SOI	Silicon on insulator
SPCM	Single-photon counting module
SPS	Single-photon source
TAC	Time-to-amplitude converter
TE	Transverse electric
TLS	Two-level system
TM	Transverse magnetic
VB	Valence band
WGM	Whispering-gallery-mode
WL	Wetting layer
ZnO	Zinc oxide

Introduction & Motivation

Nowadays, quantum technologies are common and embedded in our society. A prime example is atomic clocks, which dictate global time with incredible precision and provide the platform on which the world trading and global positioning systems work. Advances in our understanding of quantum mechanics have led to other widespread inventions such as light-emitting diodes (LEDs) and magnetic-resonance imaging. However, quantum technologies have the potential to further revolutionize multiple industries. The main areas of intense development efforts are quantum sensing, secure quantum communications, and quantum computing.

Quantum sensing and metrology encompass any advance that overcomes classical measurement limits. For example, stimulated-emission depletion (STED) microscopy[1] is a technique that overcomes the diffraction limit and has contributed enormously to advances in biology and medicine through accurate imaging of live tissue. Similar breakthroughs have been achieved in the measurement of other physical quantities.

Quantum communication refers to the transfer of quantum information between distant parties[2]. As such, it is a very broad field, whose ultimate goal is to arrive at a "quantum internet" in close analogy with classical communications[3]. However, the analogues only go so far and remarkable hurdles need to be overcome. One of them is the no-cloning theorem, which states that a general quantum state cannot be copied, thus precluding the amplification of quantum information for its transmission over global distances. This has spawned diverse ideas on how to implement a quantum repeater that can boost the signal between two distant endpoints[4]. Although we are still far from a global quantum network, there are equally useful milestones on the way there. One particularly active field is quantum key distribution (QKD), where a quantum channel is used to securely transfer encryption keys for classical communication between parties. The security of these keys can be proven because any interception on the quantum channel is detected by the legitimate parties. When these parties detect an interception, they can repeat the procedure until they successfully share encryption keys that have not been compromised. This hybrid approach therefore provides provably secure communication. Protocols for the implementation of QKD have evolved since the original proposal by Bennett and Brassard[5] and the concept has reached the maturity to become commercially available for short distances.

Finally, the fields of quantum computing and quantum information processing (QIP) comprise the research efforts towards a physical implementation of quantum systems that can perform computations[6]. The idea was put forward in the 1980s by Feynman[7]. Since then, the theoretical framework has been extended and algorithms for such a machine have been devised. Two of them are particularly exciting because of their direct application to real-world problems. The first is Shor's algorithm, which achieves an exponential speedup in prime number factorization over the best classical algorithms[8]. The second is Grover's search algorithm[9], which provides a polynomial speedup that could make an immense difference searching through

today's vast databases. Another major motivation is the fact that a computable quantum system would be able to simulate the behaviour of quantum systems, such as complex enzymes. This would represent a tool unlike any other thus far in fields like drug discovery and materials science.

The appeal of these technologies has led to an astounding diversity in the physical systems being considered for their realization. Among these, photons stand out for their practicality and compatibility with most systems. A photon itself can represent a qubit, the quantum computing analogue of a classical bit, by any property such as its polarisation. Photons are attractive candidates for QIP and ubiquitous in quantum communication because they have negligible interaction between themselves and can thus propagate over long distances (kms) in optical fibre while preserving quantum information. It is this property, however, that also makes the implementation of two-photon logic gates – required for the implementation of algorithms – challenging. We highlight two photonic approaches to QIP. The first is the traditional model, where computation steps are performed on "stationary" qubits, which are in turn linked by "flying" qubits (photons)[3, 10]. In the second approach, known as linear optical quantum computing[11], all information is carried and processed by photonic qubits.

The work presented in this thesis concerns devices capable of generating specific quantum light states and therefore of potential use for future quantum computation and communication hardware. The work focuses on semiconductor quantum dots, which are among the most promising and advanced candidates for quantum applications for a variety of reasons. First, they can trap charge carriers with an associated spin that efficiently couples to photons and has a sufficiently long lifetime to perform operations on it[12–14]. Second, they are a near-ideal source of single-photons with high internal quantum efficiency[15] and narrow linewidths[16]. Third, their emission can be tuned to a specific wavelength range by careful growth. Finally, they have the potential to be scalable with mature growth techniques, while the solid-state nature of the platform lends itself to on-chip integration, as well as careful engineering of the photonic and phononic environment. We take advantage of this fact to study single quantum dots coupled to optical microcavities and under the influence of mechanical waves propagating along the surface of the samples.

Thesis Outline

Chapters 1 and 2 provide an overview of the research field and present the employed research methods needed to recreate or elaborate on the present work.

Chapter 3 presents a single-photon source based on the dynamical tuning of the Purcell effect of a quantum dot in a micropillar cavity by a surface acoustic wave. This expands on the results published in Ref.[17].

Chapter 4 is conceptually similar to Ch.3 but explores a new hybrid platform for on-chip integration using GaAs ring microcavities on $LiNbO_3$. We demonstrate the fabrication of such devices and present their initial characterisation, including Purcell enhancement of the quantum dots contained in the GaAs.

Chapter 5 summarizes measurements on a device with simultaneous electrical, optical and acoustical control over a quantum dot. We show selective population of the dot with a hole and demonstrate its spin initialisation via optical spin pumping. We then show that a surface acoustic wave can reverse this spin initialisation.

Chapter 6 puts forward a scheme to generate multi-photon entangled states in time-bin encoding from a quantum dot. Such states constitute a key resource for LOQC. We present experimental evidence of the feasibility of this scheme using a quantum dot. The contents of this chapter are an extension of Ref.[18].

The main results and avenues for further work are summarised in the final chapter.

Chapter 1

Background & State of the Art

1.1 Quantum Information Processing

As briefly mentioned in the previous chapter, the basic building block in quantum computing is the qubit, in analogy to the classical binary bit. A qubit can be any two-level system with states $|0\rangle$ and $|1\rangle$, which is described by a wavefunction

$$|\psi\rangle = \alpha\,|0\rangle + \beta\,|1\rangle\,, \tag{1.1}$$

with complex coefficients α and β normalized such that $|\alpha|^2 + |\beta|^2 = 1$. This can also be expressed as

$$|\psi(\theta,\phi)\rangle = \cos\frac{\theta}{2}\,|0\rangle + e^{i\phi}\sin\frac{\theta}{2}\,|1\rangle\,, \tag{1.2}$$

which represents an arbitrary superposition of the basis states $|0\rangle$ and $|1\rangle$. All possible states are determined by two angles ϕ and θ and can thus be mapped onto a unit sphere known as the Bloch sphere. A state on the Bloch sphere is described by a wavevector from the origin to the surface. Any computational operation requires control over this qubit wavevector with quantum logic gates. After initialisation into a known state such as $|0\rangle$, a single-qubit rotation can drive the qubit onto any of its possible states. In order to scale this to multiple qubits, at least one multi-qubit gate that links the states of two qubits is required. An example is the quantum controlled NOT (CNOT) gate. For two qubits

$$|\psi\rangle = \alpha\,|0\rangle + \beta\,|1\rangle \tag{1.3}$$

and

$$|\phi\rangle = \gamma\,|0\rangle + \delta\,|1\rangle \tag{1.4}$$

the joint system is described by the tensor product

$$\begin{aligned} |\psi\rangle \otimes |\phi\rangle &= (\alpha\,|0_a\rangle + \beta\,|1_a\rangle) \otimes (\gamma\,|0_b\rangle + \delta\,|1_b\rangle) \\ &= \alpha\gamma\,|00\rangle + \alpha\delta\,|01\rangle + \beta\gamma\,|10\rangle + \beta\delta\,|11\rangle = \begin{pmatrix} \alpha\gamma \\ \alpha\delta \\ \beta\gamma \\ \beta\delta \end{pmatrix}. \end{aligned} \tag{1.5}$$

The CNOT gate acts on the second qubit conditional on the state of the first one. It is defined as

$$U_{\text{CNOT}} = \begin{pmatrix} 1 & 0 & 0 & 0 \\ 0 & 1 & 0 & 0 \\ 0 & 0 & 0 & 1 \\ 0 & 0 & 1 & 0 \end{pmatrix}. \tag{1.6}$$

Single-qubit rotations together with the quantum CNOT gate form a set of universal gates, meaning that any other gate needed for the execution of an algorithm can be made out of combinations from this set of gates[19]. It follows that finding a scalable physical implementation of these gates alone is in principle enough to build a quantum computer.

This task has proven challenging because of a fundamental contradiction: a system that is well isolated from the environment and thus retains fragile quantum information is inherently difficult to address to perform operations such as qubit rotations. Conversely, if the system can be easily manipulated, its desired state will easily be lost through unwanted interactions with the environment. This is known as decoherence. The goal is to find a system with a coherence time long enough to perform the deterministic operations that make up a quantum algorithm and read out the result before the information is lost. In addition, the physical implementation of two-qubit gates between arbitrary qubits presents a challenge of equal magnitude on its own.

A wide range of potential physical platforms have been identified. Two well-addressable states can be separated from almost any single system, resulting in a rich variety of experiments. Examples include atoms and ions confined in magneto-optical traps, charge and flux qubits in superconducting circuits, nuclear magnetic resonance, spin qubits in solid-state hosts and in particular spin or charge qubits in quantum dots. Trapped atoms have been pioneering in the field but have been challenging to scale up due to the massive experimental overhead. Implementations of two-qubit gates have been reported in various of the more technologically mature systems but scaling further remains an elusive goal[20–23]. It is widely believed that solid-state based implementations are the most promising for overcoming the scaling issue.

1.1.1 Entangled States

Of particular interest for many applications are a special set of states known as entangled states. In general, a state $|\psi\rangle$ is said to be entangled if there is no set of single qubit states $|a_0\rangle, \ldots, |a_n\rangle$ such that $|a_0\rangle \otimes |a_1\rangle \ldots \otimes |a_n\rangle = |\psi\rangle$[19]. For two qubits, there are four distinct maximally

entangled states known as Bell states. They are

$$\begin{array}{ll} \dfrac{|00\rangle + |11\rangle}{\sqrt{2}} & \dfrac{|10\rangle + |01\rangle}{\sqrt{2}} \\ \dfrac{|00\rangle - |11\rangle}{\sqrt{2}} & \dfrac{|01\rangle - |10\rangle}{\sqrt{2}}. \end{array} \tag{1.7}$$

The striking property of these states is that the measurement of one qubit immediately determines the state of the other. It is this feature that is exploited for quantum teleportation[24] and makes entangled states indispensable for a variety of applications, such as quantum repeaters[25].

Entanglement is routinely used in laboratories. For example, it can be generated from non-linear crystals by spontaneous parametric downconversion[26, 27] or from quantum dots by the biexciton-exciton radiative cascade[28]. However, these entanglement generation schemes are limited to two-photon entangled states. A source of multi-qubit entangled states is an invaluable resource for photonic quantum technologies and is an intense area of research.

1.1.2 Linear Optical Quantum Computation

In contrast to the common approach of separating the computation from the relaying of quantum information, there have been efforts to create an all-photonic optical quantum computer. Knill, Laflamme and Milburn showed that it is possible to perform conditional operations on two photons in a scalable fashion[11]. Their scheme, known as KLM scheme, proposes the use of the Hong-Ou-Mandel effect, described in Sec.1.2.7, to introduce probabilistic photon-photon interactions. This sidesteps the central challenge of all-optical computation, which is the weak photon-photon interaction that makes photons robust against decoherence but at the same time precludes straightforward implementation of conditional operations[29, 30]. The introduction of the KLM scheme opened new research avenues but although scalable in principle, its probabilistic nature leads to an experimental overhead too great to be feasibly implemented[31]. There have been many proposals to mitigate the overhead issue and bring LOQC with the KLM scheme within the realms of possibility[32–35]. Many of them are based on cluster state quantum computation, which is introduced in the next section.

1.1.3 Cluster-State Quantum Computation

Cluster- or graph-state quantum computing was introduced by Raussendorf and Briegel in 2001[36]. It presents an alternative to the conventional circuit-based model of quantum computation, where qubits are represented as rails and quantum gates act on them. In cluster

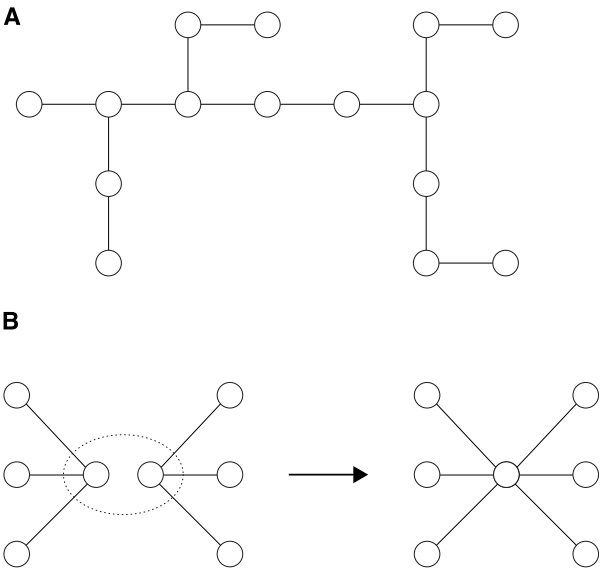

Fig. 1.1: A. A representation of a general cluster or graph state. **B.** Fusion of two graph states.

state quantum computing the quantum information is held in a graph of entangled qubits, as shown in Fig.1.1A. In this graph representation, each node amounts to a qubit and the edges denote entanglement. A computation is then carried out by performing measurements on specific qubits, which removes them from the total state and determines the basis for subsequent measurements. Both single and two-qubit measurements can be implemented locally within the graph. A review of cluster state computing protocols can be found in Ref.[37]. Importantly, the validity of the scheme has been confirmed experimentally[38].

A feature of cluster state computing is that two cluster states can be "fused" together to increase the size of the state, as schematically presented in Fig.1.1B. Browne and Rudolph introduced two types of probabilistic fusion mechanisms based on Hong-Ou-Mandel interference[32]. These can join two cluster states with n_1 and n_2 photons to create a state with $n_1 + n_2 - 1$ or $n_1 + n_2 - 2$ photons. A failure of the operation is equivalent to a measurement of the target photon in each state so each state is decreased by one photon. Cluster-state computing therefore still requires highly efficient photon sources and detectors to be implemented, as the success probability needs to be above a threshold for the state to grow through fusion operations.

Recent advances in integrated photonic circuits[39–42] and photon detection efficiencies[43, 44] have boosted the appeal of LOQC to the point that it has been suggested that a source of three-photon entangled states suitable for fusion would bring the all-photonic quantum computer within reach[45]. The importance of such a source of entangled states has sparked many ideas on how to generate them[46–49]. Chapter 6 discusses the proposal put forward by Lindner and Rudolph in Ref.[49] and proposes improvements, as well as demonstrating experimental steps towards its execution.

1.2 Semiconductor Quantum Dots

Generally speaking, a quantum dot (QD) is a structure with the capability to confine charged particles within a reduced volume, such that quantization of the energy levels arises. They have been realized in a variety of ways. For example, they can be synthesized in layered nanospheres, defined electrostatically, or be grown on a wafer by careful deposition of material, among others. For the purpose of this thesis, we focus on semiconductor quantum dots formed by embedding a small-bandgap semiconductor in a high-bandgap matrix. This can be thought of as a quantum well in all spatial dimensions. Figure 1.2 shows an example of the type of dots discussed here, which consist of epitaxially grown InAs "islands" in a GaAs matrix. The substrate is covered in a thin InAs film byproduct of the growth process, known as the wetting layer (WL). Details on the fabrication are described in Ch.2. Each dot has a roughly Gaussian profile and elliptical top view, with the major and minor axes aligned to the crystallographic axes. The lateral size is generally 10 - 20 nm, and the height 4 - 8 nm[50]. With these dimensions, a charged particle in this system can be treated like the traditional particle in a box problem – there is quantum confinement. The confinement creates a set of discrete energy states for this particle in analogy to atomic physics, which is why QDs are often referred to as "artificial atoms".

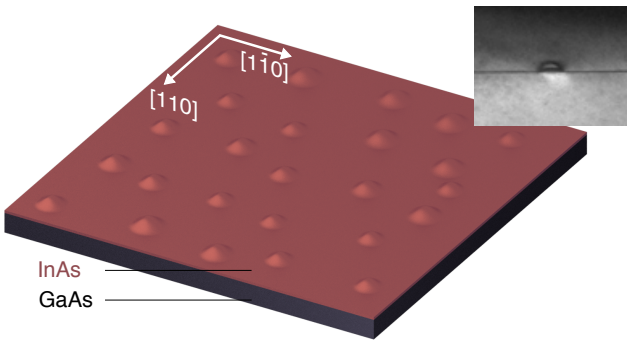

Fig. 1.2: Schematic of InAs quantum dots on GaAs. Lens-shaped dots are formed at random locations with slight elongation along the [1 1 0] crystallographic axis. The inset shows a transmission electron microscope image of a single dot (courtesy of Dr. Joanna Skiba-Szymanska).

This type of QDs is highly relevant for quantum applications and has benefited from mature processing techniques. Thorough treatments of the theory and details of such systems can be found in Refs.[51–53]. Here we review the basic concepts and highlight recently reported achievements.

1.2.1 Electronic Properties

The two types of charge carriers considered here are electrons and holes. The latter are not real particles per se but rather the result of charge imbalance after an electron is promoted from the valence to the conduction band. Conveniently, they can be described as a particle with positive elementary charge.

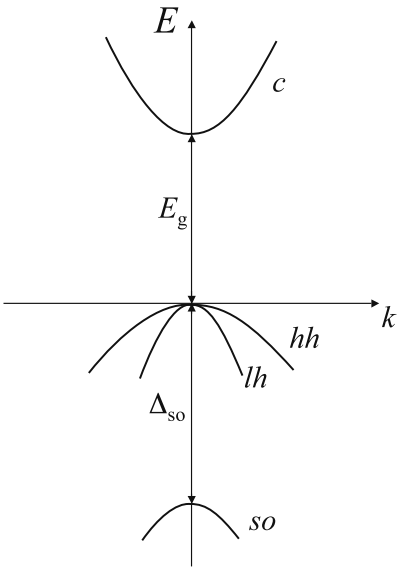

Fig. 1.3: Parabolic approximation of the bandstructure around $k = 0$ for a stress-free zincblende crystal. The bands are labelled (c) for the conduction band, lh and hh for the light and heavy-hole bands and so for the split-off band. E_g is the band gap, which is the only energy taken into account in the spatial representation of a semiconductor. Adapted from Ref.[53].

The influence of the periodic crystal lattice on charged particles is embedded in the dispersion relation $E(k)$ and can be described by an effective mass m^* such that the kinetic energy is

$$E(k) = \frac{\hbar^2 k^2}{2m^*}. \tag{1.8}$$

Around $k = 0$ the effective mass is constant and therefore the conduction and valence bands can be approximated by a parabola, as shown in Fig.1.3. The valence band comprises three sub-bands: the light and heavy-hole bands and the split-off band. The latter is split off by hundreds of meV[53] and is not relevant for the optical processes of interest here. The angular momentum of charged particles is quantified along z and they are described by states $\left|j, m_j\right\rangle$ with total angular momentum j and projection m_j. Electrons in the conduction band and holes in the valence sub-bands are then described by

$$\begin{aligned} &\text{Conduction band} && |1/2, \pm 1/2\rangle \\ &\text{Heavy-hole band} && |3/2, \pm 3/2\rangle \\ &\text{Light-hole band} && |3/2, \pm 1/2\rangle \\ &\text{Split-off band} && |1/2, \pm 1/2\rangle\,. \end{aligned} \tag{1.9}$$

It is this difference in angular momentum projection between heavy and light-holes that changes their effective mass and therefore the curvature of the band. The energy splitting between the two bands at $k = 0$ is determined by strain. The QDs studied here have built-in strain so the bands are typically offset by tens of meV and only the heavy-hole band is relevant to optical

experiments[52, 54]. However, it is possible for a dot to exhibit heavy–light-hole mixing, enabling optical transitions to the light-hole states. In general, the resulting state can be described as

$$\left|j', m_{j'}\right\rangle = \frac{|3/2, \pm 3/2\rangle + \beta\,|3/2, \mp 1/2\rangle}{\sqrt{1+\beta^2}}. \tag{1.10}$$

Previous experiments in our lab have determined $\beta = 0.02\text{ - }0.2$ with most dots in the lower part of this range, suggesting that the simplified treatment of heavy-holes exclusively is mostly valid[55].

We now discuss the quantization effects that arise when the particles are confined within a volume smaller than their de Broglie wavelength, which is around 10 nm for electrons and holes. The simplest model is that of a cube of side length a_0. The corresponding cubic potential of infinite barrier height leads to the well-known energies

$$E_{n_x,n_y,n_z} = \frac{\hbar^2}{2ma_0^2}\pi^2\left(n_x^2 + n_y^2 + n_z^2\right), \tag{1.11}$$

where m is the mass of the particle. This very rough model shows the clear quantization. It can be refined by considering more accurate geometries and finite potential barriers. The QDs studied here typically have very low aspect ratios, leading to a much stronger confinement in z than in-plane and the Hamiltonian of trapped charge carriers can be separated into a vertical and an in-plane component[52]. Consequently, the energy level separation in z is much greater than that in-plane and all relevant states are in the ground state of the z quantization. Therefore, it suffices to describe the quantization in-plane. An isotropic dot can be described by a harmonic potential. This is known as the Fock-Darwin Hamiltonian[56]

$$H_{\text{Fock–Darwin}} = \frac{1}{2m^*}\left(\boldsymbol{p} - e\boldsymbol{A}(\boldsymbol{r})\right)^2 + \frac{1}{2}m^*\omega_0^2\left(x^2 + y^2\right), \tag{1.12}$$

where $\boldsymbol{p}$ is the momentum, e is the elementary charge, $\boldsymbol{A}$ is the magnetic vector potential and $\hbar\omega_0$ is the harmonic oscillator energy. In the absence of a magnetic field $\boldsymbol{A} = \boldsymbol{0}$ and the energy levels are given by

$$E_{xy,s} = \hbar\omega(2r + |l| + 1) = \hbar\omega(s+1) \tag{1.13}$$

with

$$s = 2r + |l| + 1. \tag{1.14}$$

Here the two quantum numbers are the radial $r = 0, 1, 2, \ldots$ and azimuthal $l = 0, \pm 1, \pm 2, \ldots$ numbers. Continuing the analogy with atomic physics, the resulting set of energies is grouped in shells labelled s, p, d, and so on for $s = 0, 1, 2$, etc. Each shell has a $2(s+1)$-fold degeneracy

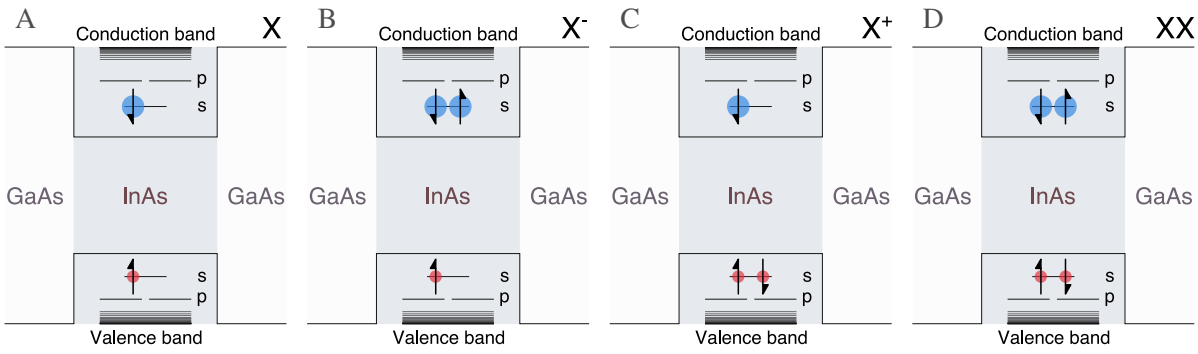

Fig. 1.4: Schematic occupations of the ground state of a QD. Electrons (holes) are represented by blue (red) dots with a corresponding spin. Four possible configurations are presented: exciton (**A**), negatively charged exciton (**B**), positively charged exciton (**C**) and biexciton (**D**).

from the azimuthal quantum number and the spin degree of freedom. There can therefore be 2 electrons (holes) in the s-shell and 4 in the p-shell.

1.2.2 Excitonic Complexes

Figure 1.4 presents the possible configurations for the occupation of the s shell of the conduction and heavy-hole bands. An electron-hole pair trapped inside the QD is bound through the Coulomb interaction and is referred to as an exciton, denoted as X. The addition of a second electron or hole leads to a charged exciton also known as trion and labelled X^- or X^+, respectively. Lastly, two excitons in the same dot are collectively called a biexciton XX. Due to the Pauli exclusion principle, no further charges can be added to the same bands and the p shell starts to be populated for complexes with higher numbers of particles.

Figure 1.4 only shows one particular arrangement of the charges' spins. For an exciton, there are four possible spin configurations. The total angular momentum projection for the electron and hole is $M_j = m_{j1} + m_{j2}$. Therefore $M = \pm 2$ for parallel spin $M = \pm 1$ for antiparallel spin configurations. The former precludes electric dipole transitions and is thus known as a *dark* exciton. In contrast, the latter is known as a *bright* exciton because the electron and hole can recombine under emission of a photon. Indeed, this is a strong transition with photon energies 900 - 1200 nm for the dots studied here[57]. A consequence is that dark excitons are long-lived but more challenging to excite and detect. The two bright excitons are degenerate for symmetric dots. However, for asymmetric dots the exchange interaction between unpaired electrons and holes leads to an energy splitting known as the fine-structure splitting (FSS), schematically drawn in Fig.1.5. The FSS depends on the dot morphology but is generally in the the 1 - 100 µeV range.

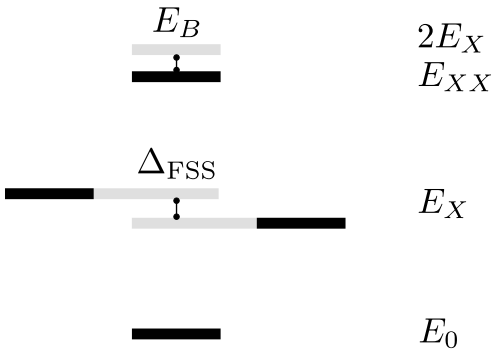

Fig. 1.5: Energy diagram showing the fine-structure splitting of excitons and the binding energy of biexcitons. Note the binding energy can be both positive and negative.

Trions on the other hand are either an electron or a hole interacting with a spin singlet ($S = 0$) and therefore have a vanishing exchange interaction[58]. Most of the work presented here is performed on this type of exciton complex, because the state after radiative recombination is a single spin particle suitable as a qubit for quantum information processing.

For the sake of completeness, we note that the Coulomb interaction between charged particles yields a finite binding energy such that $E_{XX} \neq 2E_X$. In addition, the weak interaction between an exciton and additional charges is responsible for the emission from all complexes lying in the same spectral range[52]. As will be described later, the emission spectra of single QDs can be used to distinguish the presence of different exciton complexes.

1.2.3 Spins in Magnetic Fields

The addition of a magnetic field modifies the quantization energies on a scale of 1 meV and has profound consequences for the excitonic complexes. Here we focus on charged excitons. The interaction of holes and electrons with a magnetic field $\boldsymbol{B}$ is governed by the Zeeman Hamiltonian[59]

$$H_{\mathrm{Zeeman}} = \sum_{i=x,y,z} \mu_{\mathrm{B}} \left(g_{e,i} m_{je,i} - \frac{g_{h,i}}{3} m_{jh,i} \right) B_i, \tag{1.15}$$

where μ_{B} is the Bohr magneton, $\boldsymbol{m}_{je}$ and $\boldsymbol{m}_{jh}$ are the electron and hole spin projections and $\boldsymbol{g}_e$ and $\boldsymbol{g}_h$ the electron and hole g-factors. This lifts the degeneracy of the spin states, inducing an energy shift*

$$\Delta E = g \mu_{\mathrm{B}} B = (g_{\mathrm{e}} + g_{\mathrm{h}}) \mu_{\mathrm{B}} B. \tag{1.16}$$

Figure 1.6 shows the modified energy levels of the system using the more intuitive notation

$$\begin{aligned} |\blacktriangle\rangle &= |1/2, 1/2\rangle \qquad |\vartriangle\rangle = |3/2, 3/2\rangle \\ |\blacktriangledown\rangle &= |1/2, -1/2\rangle \qquad |\triangledown\rangle = |3/2, -3/2\rangle \end{aligned} \tag{1.17}$$

*The magnetic field also induces a diamagnetic energy shift $\Delta E = \gamma_2 B^2$ that is safely neglected here[60].

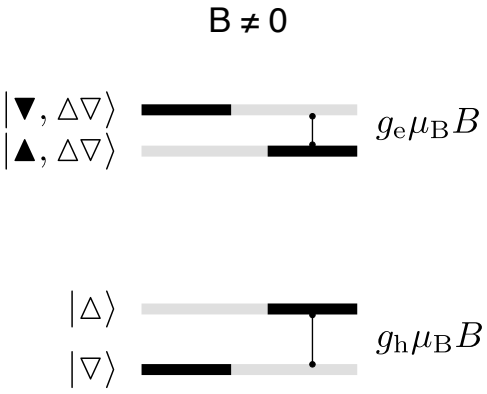

Fig. 1.6: Zeeman energy splitting on a positively charged exciton.

to describe single electrons and holes. The magnetic field effectively turns a single charge in the QD together with the trion into a double Λ* system. With sufficient separation of the energy levels they can become individually addressable and a single Λ system can be isolated. This provides an ideal platform for quantum optics experiments.

The g-factor and therefore the Zeeman splitting are dependent on the orientation of the magnetic field. The two main configurations are known as Faraday and Voigt geometries. In the former, the field is parallel to the growth and quantization axis. In the latter, the field falls perpendicular to that, parallel to the QD plane. In contrast to Faraday configuration, a Voigt magnetic field breaks the in-plane symmetry of the dot and the new eigenstates are linear combinations of the z eigenstates[57, 61]

$$\begin{aligned} |\blacktriangle, \triangle\triangledown\rangle_x &= |\blacktriangle\rangle_z \otimes (|\triangle\triangledown\rangle_z - |\triangledown\triangle\rangle_z) \\ |\blacktriangledown, \triangle\triangledown\rangle_x &= |\blacktriangledown\rangle_z \otimes (|\triangle\triangledown\rangle_z - |\triangledown\triangle\rangle_z), \end{aligned} \tag{1.18}$$

omitting the normalization factors. This determines the optical transition rules between trion and single charge states. These are summarized in Fig.1.7 for a single hole, but are analogous for a single electron. The first thing to note is that the polarization of the emitted photons is different in both cases. The second point is that while in the Voigt geometry all transitions are allowed, in the Faraday geometry the diagonal transitions are ideally forbidden. The selection rules are imperfect due to finite light-hole contributions so the excitonic states can decay via these transitions, but at a much reduced rate compared to the vertical transitions[14, 57].

This has important implications for applications. For example, initializing the spin to a known ground state is one of the most fundamental tasks for a usable algorithm. This can be done here by optical spin pumping[62]. To initialize the spin in $|\triangledown\rangle$, one can drive the vertical transition of $|\triangle\rangle$ with a coherent laser. Once excited the system can relax back into $|\triangle\rangle$, in

*Two ground-state levels and one excited level are known as a Λ system due to the resemblance to the Greek letter.

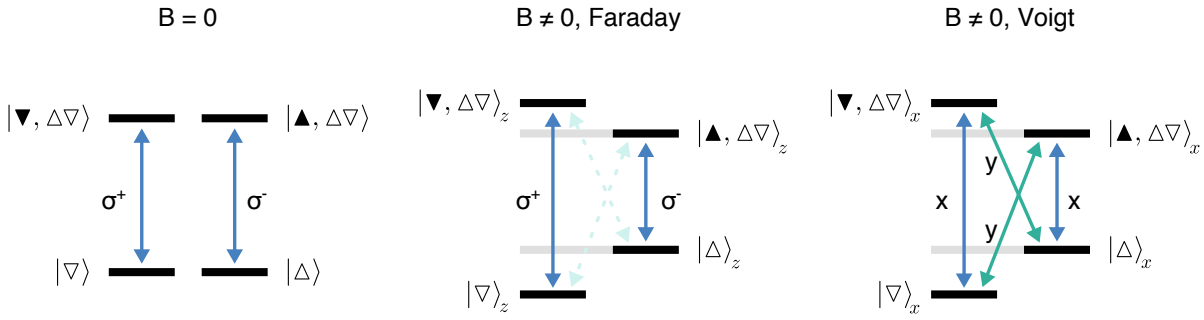

Fig. 1.7: Optical tansitions between trion states in a magnetic field. **A.** No magnetic field. The states are degenerate. **B.** Faraday field. Only vertical transitions with circular polarisation are allowed. **C.** Voigt geometry. Both vertical and diagonal transitions are allowed. They have orthogonal linear polarisations.

which case it is re-excited by the optical "pump", or it can relax into $|\nabla\rangle$, the desired outcome. Leaving the pump laser on, the system will eventually be shelved in the $|\nabla\rangle$ state with high probability. The key difference is that the process is three orders of magnitude faster in the Voigt geometry when compared to the Faraday geometry. A single spin can be initialized in ~1 ns vs. ~1 µs, respectively[63].

1.2.4 Excitation Methods

The main mechanisms to populate a QD with charge carriers are electrical and optical injection. The former requires that the QD is embedded in a diode structure, where carriers can be introduced from doped regions acting as reservoirs. In the optical case carriers are introduced directly by exciting electrons to the conduction band through the absorption of a photon. Both methods are briefly outlined here.

Photoluminescence

Electrons can be directly excited from the valence to the conduction band by irradiation with photons of energy larger than the bandgap. The subsequently emitted light following carrier recombination is known as photoluminescence (PL). The details of the steps between excitation and radiative recombination are dependent on the energy of the excitation light. Figure 1.8 summarizes the three main processes unleashed in the QD:

Above-band excitation If the photon energy is greater than the bandgap of the GaAs matrix or WL, electrons are promoted from the valence band into the conduction band, where they can diffuse until reaching the QD. At that stage, a series of non-radiative decay processes lowers their energy until they eventually occupy a radiative state and recombine

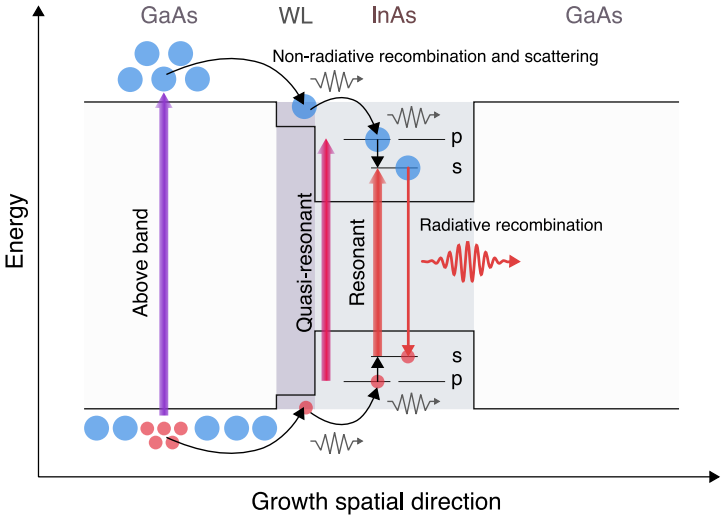

Fig. 1.8: Optical excitation regimes for a QD. Off-resonant, above band excitation: electrons are excited into the valence band and have to go through non-radiative relaxation processes before combining with a hole to generate light. Quasi-resonant excitation: the electron is excited to a higher level within the QD. Resonant excitation: the incoming light matches the exciton energy of the QD, resonantly exciting carriers.

emitting a lower energy photon[64]. Phonon-assisted relaxation takes place in a 10 - 100 ps timescale[65]. The radiative recombination time T_1 is around 0.7 - 1 ns for an exciton in InAs/GaAs QDs. Experimentally this excitation is the simplest to achieve but by its nature does not preserve coherence. In addition, the emission time exhibits inherent jitter.

Quasi-resonant excitation When the incoming laser energy matches the energy difference between higher order states such as the *p*-shell states within the QD, the transition can be driven directly and the ability to preserve coherence is improved[54].

Resonant excitation The photon energy matches the lowest energy difference of the *s*-states in the QD. The process and the collected light are known as resonance fluorescence (RF). It is evident that under RF the timing uncertainty and dephasing processes are minimized since the non-radiative decay channels are bypassed. RF is thus the ideal form of excitation. The drawback is that it is experimentally more challenging. For one, the frequency has to be tuned precisely. More importantly, because the input and collection light have the same energy, it is critical to reliably suppress the exciting light from the detection. This can be done by polarisation filtering[66] or geometrical solutions, where the input beam is perpendicular to the collection[67]. Within RF there are two main regimes defined by the input laser power. For high laser powers it is possible to observe Rabi oscillations in the time-resolved signal from the dot[67]. The spectrum of such a system exhibits the appearance of dressed states known as the Mollow triplet[68, 69]. In contrast, if the Rabi frequency is lower than the spontaneous emission rate the RF signal inherits the coherence properties of the driving laser[65, 70]. This is known as the resonant-Rayleigh-scattering (RRS) or Heitler regime and is used extensively throughout the experiments presented in this work.

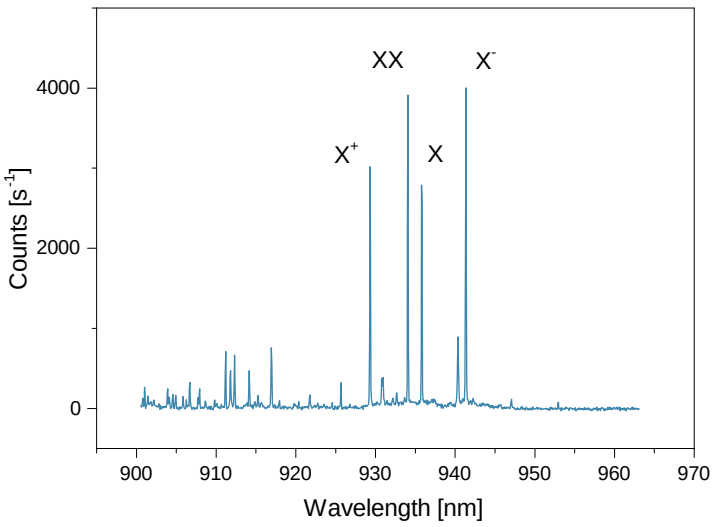

Fig. 1.9: Photoluminescence spectrum from a QD. The transitions due to the exciton, charged excitons, and biexciton are marked. Other visible lines are from higher-particle-count complexes and residual light from neighbouring dots.

Figure 1.9 shows an exemplary above-band excitation PL spectrum from a QD. The individual transition can be identified from diverse measurements. First, their relative intensities depend on the excitation power. Charged and neutral excitons show a linear dependence on the excitation power, whereas that of biexcitons is ideally quadratic[51]. Trions and neutral excitons can be differentiated by the presence of FSS in the latter, reflected in distinct emission energies for X at orthogonal polarisations. The identification of the charge state can generally be done by energy relative to the X line. The theory predicts a blueshift for X^+ and a redshift for X^- consequence of the Coulomb interaction between the respective charge and the additional exciton[71]. Experiments where the charge inside the dot can be controlled (see next section) have corroborated this[72–74].

Electroluminescence and Charge-Tunable Diodes

Growing QDs within the intrinsic region of a p-i-n junction allows the population of the QD states by an applied voltage. The process of radiative recombination following electrical injection of charge carriers is known as electroluminescence (EL). A single dot can be studied with this method, showing evidence of exciton and biexciton formation depending on the current through the device[75, 76]. However, most electrical pumping schemes share the problems of above-band excitation, as the carriers undergo non-radiative relaxation prior to recombination[65].

A particularly elegant design first introduced in Ref.[72] extends this idea to allow control of the number of charge carriers within the dot. The band diagram of such a device* is presented in Fig.1.10. The main difference from a traditional p-i-n diode is the addition of a blocking barrier that prevents current flow through the device and tunnelling of the other type of charge

*The original device features a Schottky contact to the top layer, but the diagram pictured and discussed uses an ohmic contact to a p-doped top layer.

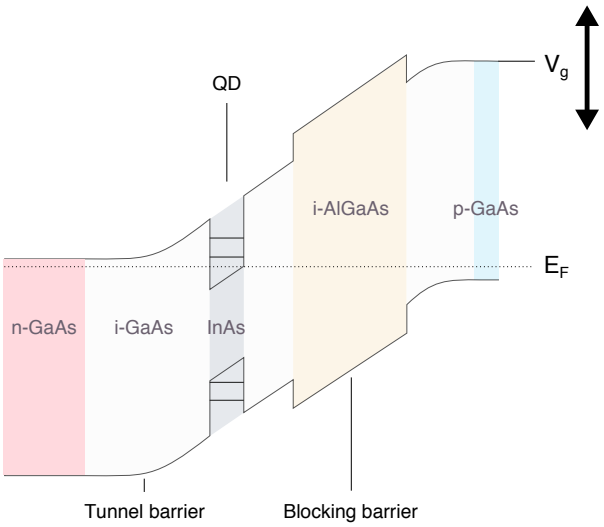

Fig. 1.10: Band diagram of a charge-tunable diode. The QD is embedded in the intrinsic region. Electrons can tunnel from the back n contact when a QD level is aligned with the Fermi energy E_F by varying the applied voltage V_g. An AlGaAs barrier avoids current flow.

carrier. Individual QD levels can be populated by controlling their distance from the Fermi level E_F via the top-gate voltage V_g. Once a charge has tunnelled into the QD, the Coulomb blockade prevents further charges from tunnelling in[73]. Hence, a predefined charge state can be studied with the addition of a laser for PL measurements. Such devices are presented and discussed further in Ch.5.

1.2.5 Tuning Mechanisms

The energy of QD transitions does not have any inherent tuning after the dot has formed with a given composition and dimensions. However, tunability is a desirable quality for the analysis in the lab and for technological applications. This can be required to bring a QD into resonance with another system, such as other QDs, a particular excitation laser, or an optical cavity for enhanced emission. There are various tuning mechanisms that can be exploited for the dots used in this thesis. These are:

Temperature tuning – Often this is the most straightforward way to tune QD emission energy. Up to tens of degrees K retains narrow excitonic emission, with the emission wavelength being redshifted for increasing temperatures.

Electric field tuning – Within a diode structure, an electric field applied across the device can be used to tune the emission energy by the quantum-confined Stark effect[53]. This allows for considerable tuning up to 25 meV[77].

Magnetic field tuning – As detailed in Sec.1.2.3, the degeneracy of the spin states is lifted once a magnetic field is applied. The transitions can be tuned over ~1 meV, which in some circumstances can be exploited as a tuning mechanism.

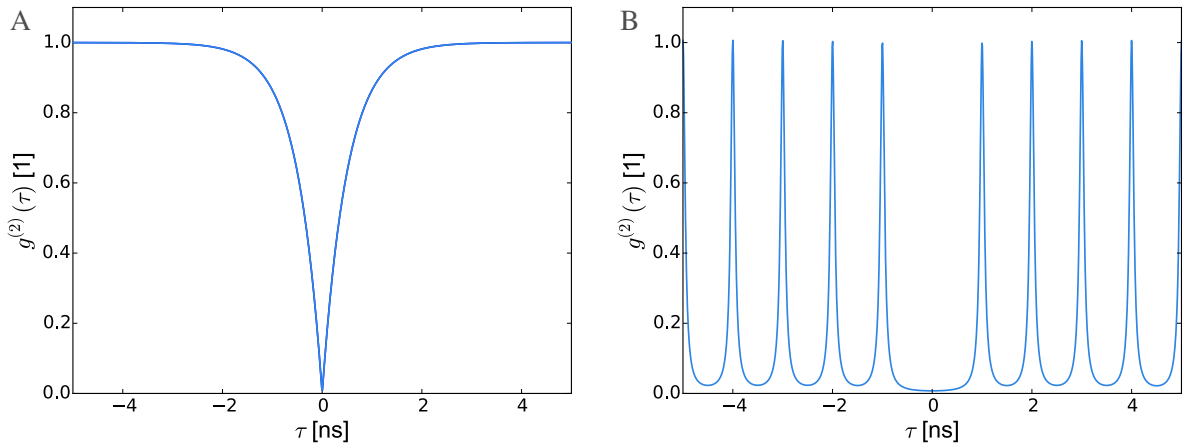

Fig. 1.11: Ideal second-order autocorrelation function of a single-photon emitter under CW (A) and pulsed (B) excitation.

Strain tuning – Additional strain also provides a tuning control over a ~1 meV range. In this work we exploit dynamical strain tuning, as described below in Sec.1.4.5.

1.2.6 Single-Photon Statistics

Non-classical light can be differentiated from classical light by its statistical correlations. The second-order correlation function, defined as[78]

$$g^{(2)}(\tau) = \frac{\langle I(t)I(t+\tau)\rangle}{\langle I(t)\rangle^2} = \frac{\langle a^\dagger(t)a^\dagger(t+\tau)a(t+\tau)a(t)\rangle}{\langle a^\dagger(t)a(t)\rangle^2}, \tag{1.19}$$

determines the degree of correlation between the intensities of light at a given time t and light from the same source at an earlier or later time $t \pm \tau$. Here, the angled brackets represent time averages, I denotes the light intensity, and $a^\dagger$ and a are the creation and annihilation operators, respectively. For delays longer than the temporal coherence length of the source no correlations are expected and $g^{(2)}(\tau)$ approaches 1. Therefore, the interesting range of the function is around zero time delay. A classical thermal light source shows fluctuations in the intensity that produces light with photons coming in packets. That means if a photon is present at time $t = 0$, the probability of having a second photon is higher around $t = 0$. This effect is known as photon bunching and is characterized by showing $g^{(2)}(0) > 1$. A very different picture is observed with coherent light. A coherent state $|\alpha\rangle$ is an eigenstate of the annihilation operator and consequently $g^{(2)}(\tau) = 1$ for all time delays.

This means that classically one never expects to have a correlation $g^{(2)}(\tau) < 1$. In contrast, quantum light is precisely characterized by this quality. Indeed, if a single-photon results from a radiation process in a quantum-mechanical system, no second photon can be produced until the

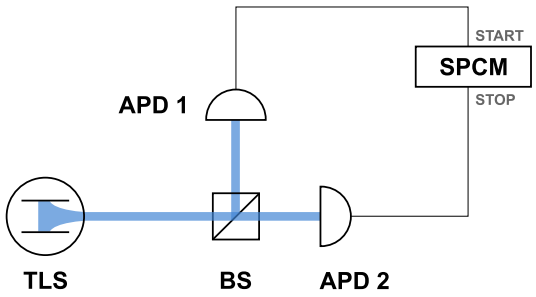

Fig. 1.12: Hanbury Brown and Twiss (HBT) setup to measure $g^{(2)}(\tau)$. APD: avalanche photodiode, TLS: two-level system, BS: 50:50 beam splitter, SPCM: single-photon counting module.

system is excited anew. The result is a dip in the second-order correlation function, referred to as anti-bunching. The theoretically expected $g^{(2)}(\tau)$ for such a single-photon source is presented in figures 1.11 (A) and (B) for continuous-wave (cw) and pulsed excitation, respectively. For a number or Fock state $|n\rangle$ at zero delay, equation (1.19) yields

$$g^{(2)}(0) = 1 - \frac{1}{n}. \tag{1.20}$$

From this follows that a measurement showing $g^{(2)}(0) < 1$ is definitive proof that the light is of quantum nature. It is often assumed that the condition $g^{(2)}(0) < 0.5$ further demonstrates the collected light originates from a single emitter. However, such a measurement could also stem from the collective emission of a single photon by an ensemble of emitters[79]. Nevertheless, the value of $g^{(2)}(0)$ quantifies the multi-photon emission probability and thus minimizing it has become one of the key goals for researchers in the field.

The second-order autocorrelation function can be directly measured by an elegant and simple experiment devised by Hanbury Brown and Twiss, which is routinely used in optical laboratories today[80]. The modern version of it is shown schematically in Fig.1.12. Light from the studied emitter is sent through two separate paths to two photodetectors, which send an electric signal to a counter card that records a histogram of coincident events as a function of time. In a real measurement the dip does not quite reach zero due to the finite response time of the detection hardware, which usually is in the order of hundreds of ps. For a QD with a lifetime of ~1 ns this response time gives a non-negligible chance to register an event at $\tau = 0$. Furthermore, even the best detectors can register a count when no photon reached them (dark counts). An in-depth treatment of quantum optics expanding on what is outlined here can be found in Refs.[78, 81, 82].

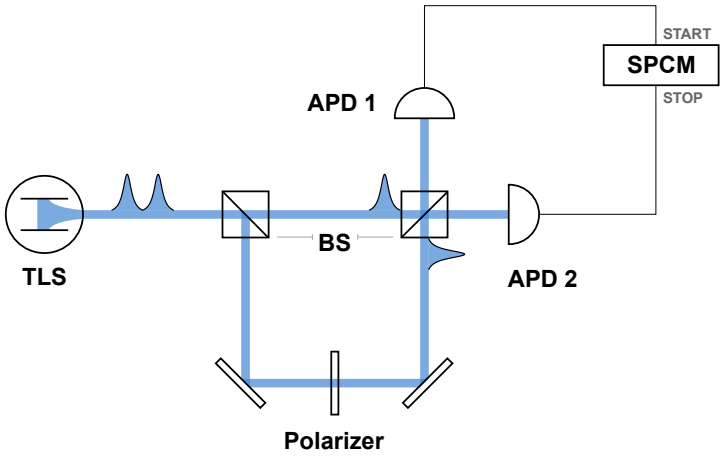

Fig. 1.13: Hong-Ou-Mandel interference measurement setup. Photons are split into two paths at the first BS. When the path length difference matches the photon separation two photons enter the second BS at the same time. If they are indistinguishable they "bunch" and exit the BS through the same port, so that only one detector registers a signal.

1.2.7 Two-Photon Interference

For many applications such as LOQC it is of utmost importance that photons emitted at different times are indistinguishable, meaning they coincide in all properties such as polarization, frequency, spatial mode, pulse shape, etc. The degree of indistinguishability is limited by the photon's coherence time T_2[83]

$$\frac{1}{T_2} = \frac{1}{2T_1} + \frac{1}{T_2^*} = \frac{1}{2}\Gamma + \Gamma^*. \tag{1.21}$$

This is the inverse of the dephasing rate and has contributions from the radiative dephasing Γ and pure dephasing Γ^*. The former is simply the light emission from exciton recombination with lifetime $T_1 = \Gamma^{-1}$. The latter describes the dephasing due to external factors, with a characteristic lifetime T_2^*. In the case of self-assembled QDs at low temperatures, the prevalent dephasing mechanisms are of electric nature due to charge noise and magnetic due to the spin bath of the matrix[84–88]. These fluctuations in the environment cause drifts over short and long timescales. Notably, the central emission wavelength can vary over time, a phenomenon known as spectral diffusion or spectral wandering. An ideal source would have no contribution from pure dephasing and thus

$$\frac{T_2}{2T_1} = 1. \tag{1.22}$$

This condition is known as the Fourier-transform limit. QDs driven resonantly have been shown to emit photons close to this limit[16].

Experimentally, the coherence time and the degree of indistinguishability can be extracted from a two-photon interference measurement. If two indistinguishable photons simultaneously enter a balanced beam splitter from separate ports, higher-order interference leads to a cancellation of the probabilities of finding one photon in each output port. The only possible

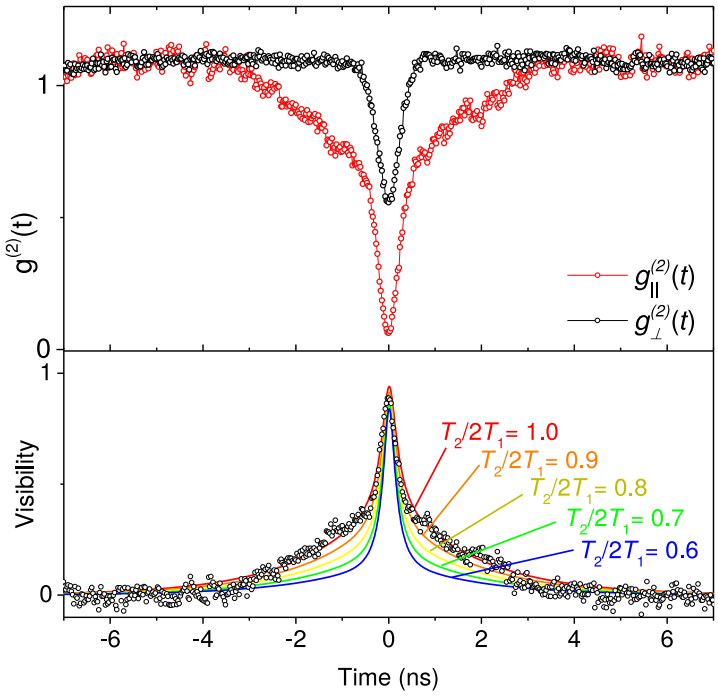

Fig. 1.14: Autocorrelations and visibility from a HOM measurement on a QD in a micropillar cavity. Adapted from Ref.[16].

outcomes are finding both photons in the transmission or in the reflection path (or a superposition of both). This was first experimentally demonstrated by Hong, Ou and Mandel with photon pairs from parametric downconversion and is known as the Hong-Ou-Mandel (HOM) effect[26]. Similar to HBT, the experimental method has not changed since then and is schematically pictured in Fig.1.13. Building a histogram of the detection events on the APDs versus time delay between pulses reveals a dip around zero delay, with a width determined by the coherence time T_2 of the photons. By measuring the histogram with and without intentional distinguishability, a two-photon interference visibility can be defined and used as a figure of merit. In the case of polarization the visibility is

$$V_{\mathrm{HOM}} = \frac{g_{\perp}^{(2)}(\tau) - g_{\parallel}^{(2)}(\tau)}{g_{\perp}^{(2)}(\tau)}, \tag{1.23}$$

with the second-order autocorrelation functions $g_{\perp}^{(2)}(\tau)$ and $g_{\parallel}^{(2)}(\tau)$ for distinguishable and indistinguishable measurements, respectively. Figure 1.14 shows experimental autocorrelations and the corresponding visibility with a maximal value of 89%[16]. Similarly high visibilities have been reported by other groups[89–94]. All of these works make use of an optical cavity to achieve these high visibilities, which helps getting closer to the Fourier-transform limit by reducing T_1 as described in the next section.

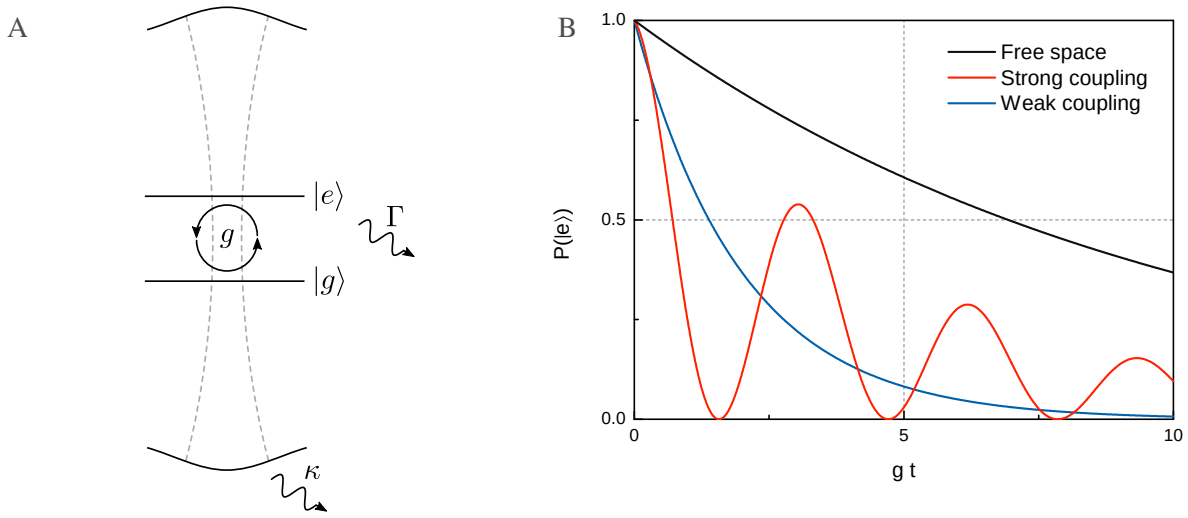

Fig. 1.15: A. Two-level system in an optical cavity. The interactions are represented by the coupling rate g, cavity dissipation rate κ and system radiative decay rate Γ. **B.** Temporal excited state decay for a system in free-space and the two cavity-QED regimes, showing enhanced decay and Rabi oscillations.

1.3 Optical Microcavities and Purcell Effect

As mentioned above, one of the advantages of solid-state approaches to quantum information processing is the ability to engineer the local surroundings of the quantum emitters. In particular, this can be exploited to enhance the collection of light emission by embedding the emitters in optical microcavities[95, 96], solid-state immersion lenses[97], and nano-antennae[98]. Here, we take a closer look at optical microcavities, as these are used for all experiments described in this work. The study of this type of coupled system has given rise to a field known as cavity quantum electrodynamics (cavity QED).

Considering a TLS defined by a ground state $|g\rangle$, an excited state $|e\rangle$ and a dipole transition between the two, the decay rate from $|e\rangle$ is determined by Fermi's Golden Rule[96]

$$\Gamma_{e-g} = \frac{2\pi}{\hbar^2} |\langle g| H_{\text{int}} |e\rangle|^2 \rho(\omega). \tag{1.24}$$

Here, $\hbar$ is the reduced Planck constant, H_{int} is the interaction Hamiltonian containing the dipole matrix elements, and $\rho(\omega)$ denotes the photonic mode density. The latter represents the number of modes available for photons at a given frequency and is determined by the photonic environment. It is because of this factor that the confinement in an optical cavity can drastically alter the dynamics of a TLS. The mode density in a cavity is determined by its supported modes or resonances. Hence, a cavity can both suppress and enhance the emission rate of the TLS, depending on whether the energy difference between $|e\rangle$ and $|g\rangle$ is resonant with the cavity. The degree of enhancement is quantified by the Purcell factor, defined as the ratio of decay

rates in the presence and absence of a cavity[99],

$$F_{\mathrm{P}} \equiv \frac{\Gamma_{\mathrm{cavity}}}{\Gamma_{\mathrm{free}}} \leq \frac{3}{4\pi^2}\left(\frac{\lambda_0}{n}\right)^3 \frac{Q}{V}, \tag{1.25}$$

where λ_0/n gives the resonant wavelength corrected by the refractive index and Q and V are the quality or Q factor and mode volume of the cavity, respectively. It is worth noting that equation (1.25) omits three factors ≤ 1 that can lower the actual Purcell factor from the ideal attainable factor, hence the inequality[100]. These missing factors account for imperfect spatial overlap of emitter and mode, spectral mismatch, and deviations in polarisation matching. The key point is that for a perfectly located and oriented emitter, the ideal Purcell factor in equation (1.25) depends solely on the cavity, with the Q/V ratio being the figure of merit.

This description holds as long as the interaction strength g between photons in the cavity and the TLS is weak compared to the dissipative losses originating from the cavity photon-loss rate κ and the incoherent decay into radiative modes Γ_{loss}. It is thus known as the weak coupling regime. If g^2 becomes larger than $\kappa \cdot \Gamma_{\mathrm{loss}}$, a photon emitted into the cavity mode can be reabsorbed, and the system effectively drives itself. This is known as the strong-coupling regime. The description of the coupled TLS-cavity system has to be extended into the Jaynes-Cummings Hamiltonian. The situation and comparison of regimes is presented in Fig.1.15.

QDs have been embedded in diverse cavities to reach both the weak[89, 101, 102] and the strong[103–105] coupling regimes. The main types of optical microcavities are Fabry-Pérot, whispering-gallery-mode and photonic-crystal cavities[106]. Each type is further divided into multiple designs, creating a wide variety of structures. In general, the most critical aspects in the choice of cavity are whether the emission is in or out of plane, how high the coupling to external optics can be, and how high a Q/V factor can be attained. This work presents experiments performed on devices featuring Fabry-Pérot and whispering-gallery-mode cavities, which are introduced in the following sections after a brief general discussion on the Q factor and mode volumes.

1.3.1 Quality Factor and Mode Volume

Regardless of cavity design, the Q factor is defined as angular frequency times the stored energy W over the dissipation rate per period:

$$Q = \omega W \left|\frac{dW}{dt}\right|^{-1} \tag{1.26}$$

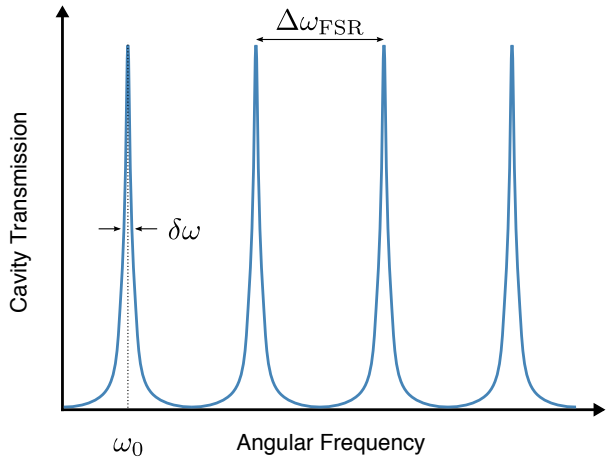

Fig. 1.16: Transmission spectrum of an optical cavity supporting multiple resonances. The linewidth and free spectral range are labelled.

Given that the stored energy decays exponentially as $W = W_0 \exp(-\kappa t)$, this is equivalent to

$$Q = \frac{\omega}{\kappa}. \tag{1.27}$$

The Q factor is then inversely proportional to the cavity photon loss rate κ and thus represents a measure of the cavity's energy storage capability. An equivalent definition for optical resonators is given by the ratio of resonance frequency to its linewidth $\delta\omega$,

$$Q = \frac{\omega_0}{\delta\omega}, \tag{1.28}$$

as marked in Fig.1.16. This follows from the uncertainty principle between resonance $\delta\omega$ and photon lifetime κ^{-1} using equation (1.27). Equation (1.28) allows for the estimation of a cavity's Q factor from a simple transmission measurement.

As the Q factor quantifies energy storage, the mode volume quantifies its confinement. A general definition compatible with any resonator geometry is given by the volume integral over the energy stored in the mode normalized by its maximal value[107]

$$V = \frac{\int \epsilon(\boldsymbol{r})|\boldsymbol{E}(\boldsymbol{r})|^2 d\boldsymbol{r}}{\max\left[\epsilon(\boldsymbol{r})|\boldsymbol{E}(\boldsymbol{r})|^2\right]}, \tag{1.29}$$

where $|\boldsymbol{E}|$ is the electric field amplitude and ϵ is the dielectric permittivity.

1.3.2 Micropillar Cavities

Micropillar cavities are a type of Fabry-Pérot cavity. They are fabricated starting from planar cavities formed by two opposing distributed Bragg reflectors (DBRs). These consist of stacks

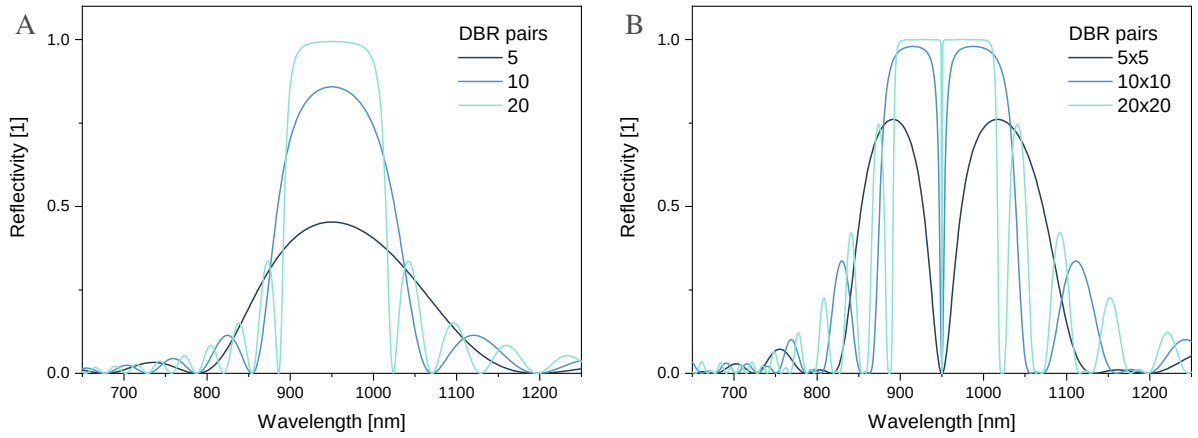

Fig. 1.17: Theoretical reflectivities for Bragg stacks centered around 950 nm calculated by the matrix formalism. (A) Single DBR mirror. (B) Two equal DBRs with a λ cavity in between.

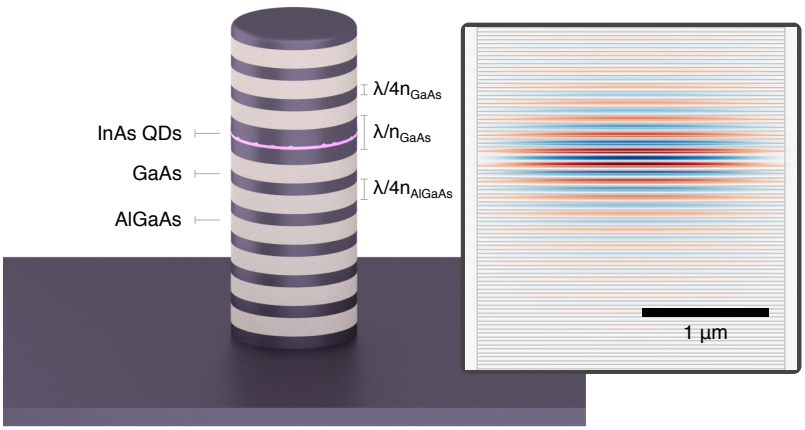

Fig. 1.18: Schematic of a pillar GaAs/AlGaAs microcavity. The number of mirror pairs is typically 10 - 30 . The inset shows a simulation of the electric field of the fundamental cavity mode of a pillar with 18 and 28 mirror pairs, represented by the color scale.

of thin films with alternating refractive index, engineered such that their thickness corresponds to a quarter of the target resonant wavelength in the material. In that case the reflections and transmissions at the interfaces add up to create a stopband, as presented in Fig.1.17 (A) for an increasing number of repeats. Leaving a space of half or a full wavelength between two DBRs opens a window in the stopband, thus creating a cavity as in Fig.1.17 (B). Increasing the number of repeats makes the reflectivity dip narrower, thus making the cavity more selective and increasing its Q factor. The pillar cavity is formed by removing material from the planar cavity to define a pillar. This reduces the mode volume, as the light is confined sideways by total internal reflection. Figure 1.18 shows a schematic of a micropillar and a simulated photonic mode within.

These cavities do not have the best Q factors nor the smallest mode volumes. The Q factor of the micropillar is reduced from that of the planar cavity and its values usually lie in the thousands to tens of thousands. Mode volumes are generally a few μm^3[108]. Nevertheless, QDs in micropillars exhibit modest Purcell enhancement with F_P ~4 - 7 [90, 109–112] and in exceptional

cases above 20[113], close to the theoretical limit. Their main advantage is a good overall collection efficiency. This is in part due to a good matching of the modes to free-space Gaussian modes, which are the main form of optical access[114]. Another reason is that the cavities can be made highly directional by having an asymmetric number of DBR repeats on the top and on the bottom. With 12 repeats on the bottom and 4 on the top, there is a 24-fold increase in light collection from the top facet[115]. Finally, they also exhibit a high β factor, which quantifies the degree of coupling between an emitter and the optical mode. This factor is related to the Purcell enhancement by[110]

$$\beta = \frac{F_P - 1}{F_P}. \tag{1.30}$$

Values in excess of 80 % have been reported for pillar microcavities[109, 111]. These features have attracted much attention and some of the best single-photon sources in terms of purity are made in these cavities[90, 112]. Collection efficiencies of 79 % have been reported[116].

Pillar microcavities support a variety of modes. Since the lateral confinement arises from total internal reflection they can be thought of as an electromagnetic waveguide. The theoretical treatment of the modes then follows the conventional optical waveguide theory and the modes are labelled according to their electric and magnetic field profiles. For pillars of cylindrical symmetry, the supported modes are generally hybrid modes with both transverse-electric (TE)

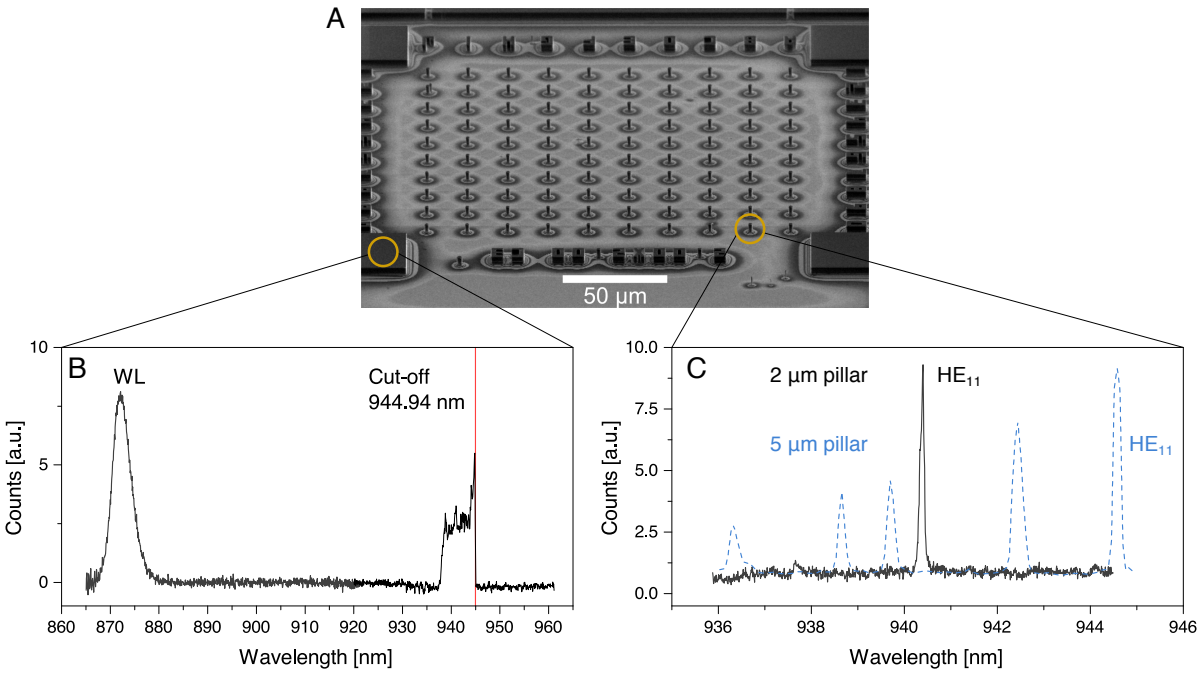

Fig. 1.19: A. SEM micrograph of micropillar array. The sample is tilted at 45°. **B.** PL spectrum on a planar cavity with 660 nm light irradiation revealing the InAs wetting layer (WL) and cavity modes. **C.** PL spectrum on a micropillar cavity showing the fundamental mode.

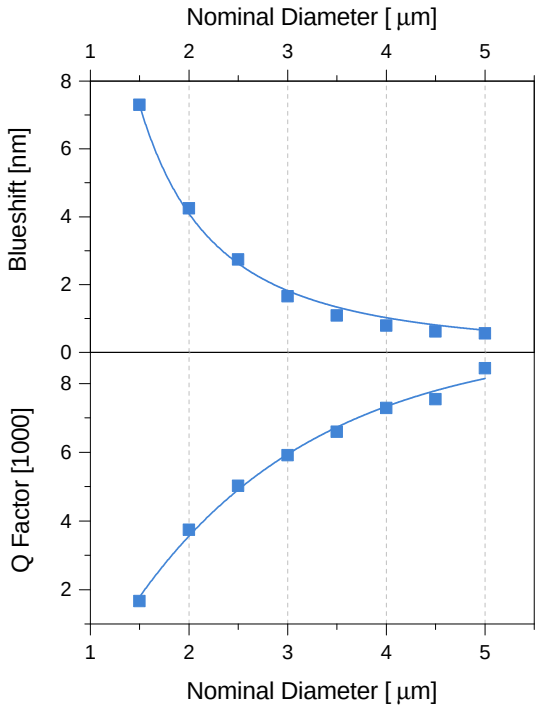

Fig. 1.20: Blueshift and Q factor as a function of pillar diameter. Each data point is averaged over three nominally identical pillars. **Top.** Blueshift of the fundamental mode versus pillar diameter d. Data points are fit with a inverse function $\propto 1/d$. **Bottom.** Q factor versus pillar diameter. The fit line corresponds to an exponential decrease towards smaller pillars.

and transverse-magnetic (TM) contributions. Modes with a dominant electric (magnetic) field contribution are labelled HE_{lm} (EH_{lm}), with $l = 0, 1, 2, \ldots$ and $m = 1, 2, 3, \ldots$ denoting the mode order and eigenvalues of the propagation constant, respectively[117].

Figure 1.19 shows spectra taken on a planar region and on a micropillar cavity. The planar spectrum shows emission from the wetting layer at 870 nm and a broad emission signature around the cavity design wavelength of 940 nm. The low-energy side of this feature presents an abrupt cut-off wavelength, which corresponds to the energy of the fundamental HE_{11} mode. Longer wavelengths are effectively reflected by the DBRs and are therefore not collected. This is also true for lower wavelengths. However, modes with a non-zero incidence angle are supported and have an effectively blueshifted wavelength. The mode can thus not be identified from this spectrum, only its position. The collection of the oblique rays is limited by the numerical aperture (NA) of the collecting lens, which is responsible for the cut-off at the lower-wavelength side.

As the planar structure is etched into pillars with smaller radii the individual modes can be resolved in the spectrum. As the $\boldsymbol{k}$ vector is confined and directed vertically the modes experience a blueshift[118, 119]. They do not cross in energy and HE_{11} is always the lowest-energy mode. Figure 1.20 shows measurements on the magnitude of the blueshift for this mode. It also shows that the Q factor is reduced compared to the planar Q factor below a critical pillar diameter. This accompanying drop in Q factor comes about from the higher contribution of losses from imperfections at the sidewalls as the mode is increasingly tightly confined[120]. It is

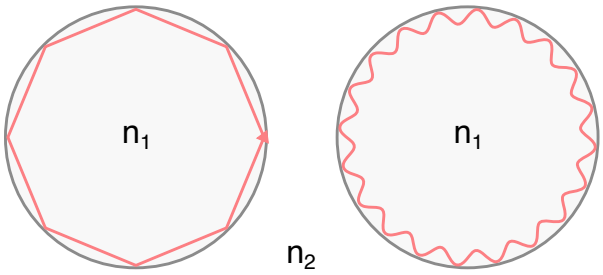

Fig. 1.21: Schematic of whispering-gallery modes in a resonator with $n_1 > n_2$. In the ray-optics picture the light is confined by total internal reflection at the boundaries. In the wave-optics picture the resonator supports modes that interfere constructively.

also worth noting that the symmetry of the pillar plays an important role, as the HE_{11} is not polarisation-degenerate in an asymmetric pillar[121].

1.3.3 Whispering Gallery Mode Cavities

In contrast to micropillars, whispering-gallery-mode (WGM) cavities confine light exclusively by total internal reflection. The curved boundary of a body such as a ring, disk, torus or sphere can confine these modes, which owe their name to their acoustic analogue in which a whisper can be heard along the walls of a gallery, as discovered by Lord Rayleigh in St. Paul's Cathedral[122]. Figure 1.21 shows a simple illustration of such a resonator. The light confinement by total internal reflection is clear from the ray-optics picture. Beyond a critical incidence angle the subsequent reflections on the boundary guide the light back onto its initial entry point. The incidence angle is necessarily shallow and thus the light is confined in close proximity to the edge. The wave picture also provides some intuitive insight into the resonance condition. Requiring an integer number of wavelengths to fit in the circumference of the ring leads to the expression

$$m\lambda = 2\pi R n_{\text{eff}}, \tag{1.31}$$

with the radial mode order m, ring radius R and effective refractive index of the mode n_{eff}.

WGM resonators are known for record high-Q values, up to 1×10^9 - 1×10^{10} in mesoscopic crystalline bodies[123, 124]. This is one of the reasons behind interest in such resonators for multiple applications, such as optical communications, lasers[125], non-linear optics[126–129], cavity QED[130, 131], sensing[132] and bio-photonics[133]. Accordingly, a wide variety of designs and material combinations have been studied. In this work we focus on on-chip ring and disk resonators. These can also show high-Q values up to ~1×10^5[134, 135]. Purcell enhancement factors of F_P ~3 - 12 have been reported in such structures[101, 136].

One of the challenges with WGM resonators is that, in contrast to micropillars, they are not efficiently excited by direct plane-wave illumination[137]. For an on-chip ring the conventional excitation scheme is evanescent coupling from a neighbouring waveguide, as illustrated in Fig.1.22. The mode inside the ring has an amplitude $A(t)$ and is coupled to the waveguide with

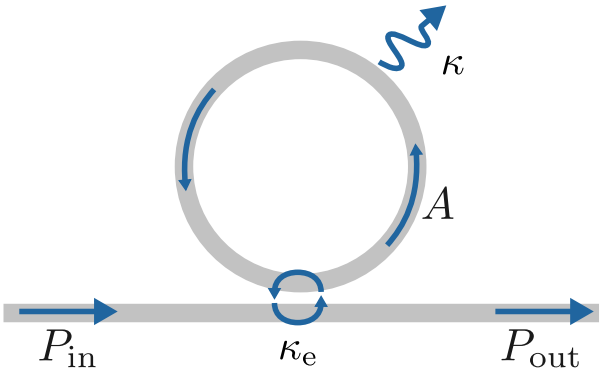

Fig. 1.22: Schematic of a ring resonator and an access waveguide. The ring and the waveguide are coupled with a rate $1/\tau_e$ and the cavity has a loss rate κ.

a rate κ_e. The waveguide not only provides access but also an additional path for the light to escape the resonator. This is reflected in the Q factor. Through Eq. (1.27) we can define a Q factor for the cavity loss rate κ and one for the coupling rate κ_e. They are referred to as the intrinsic and external Q factors Q_i and Q_e, respectively. The overall Q factor then becomes

$$\frac{1}{Q} = \frac{1}{Q_i} + \frac{1}{Q_e} \tag{1.32}$$

and is sometimes known as the "loaded" Q factor. It is evident then that κ_e is a critical parameter. In the simplified case of a single-mode waveguide coupling to the fundamental mode of the cavity, the steady-state solution of the transmission T through the waveguide is[138]

$$T = \left|\frac{P_{out}}{P_{in}}\right| = \left(\frac{\kappa^2 - \kappa_e^2}{\kappa^2 + \kappa_e^2}\right)^2 . \tag{1.33}$$

From this equation three main regimes of operation of the coupled system can be distinghished:

$\kappa > \kappa_e$
: The system is undercoupled and the light field does not fully build up.

$\kappa = \kappa_e$
: The system is critically coupled. The transmission drops to zero as all input light couples into the resonator and is dissipated there. This is usually the targeted operation.

$\kappa < \kappa_e$
: The system is overcoupled and the waveguide damps the light-field buildup.

The coupling strength is determined by the separation between waveguide and cavity and the mode profiles, which can be influenced by geometry and refractive index contrasts. This

covers the basics of WGM resonators needed here. Detailed information and derivations of the theory can be found in Refs.[137, 139, 140].

1.4 Surface Acoustic Waves

As the name suggests, SAWs are mechanical waves that propagate along the surface of a body. They have found multiple applications in electronics for decades, notably as delay lines and filters that are included in essentially all consumer electronics. Another area of use has been sensing applications, where the adhesion of specific molecules on the surface can be detected by the change in acoustic wave frequency or amplitude[141]. They are also widespread in lab-on-a-chip experiments, where they can be used to controllably transport and more importantly mix analytes on a microfluidic chip[142]. The inexhaustive list continues with non-linear integrated optical elements and RFID tags, and more recently quantum information applications that will be outlined later. This vast variety leads to an extensive literature collection on SAWs, with the usual textbooks being Refs.[143–145]. As has been done throughout this chapter, only the pertinent part of the theory and closely related applications are revisited here.

SAWs encompass different modes, which are classified according to the directions of displacement of the wavefronts. The waves used in this work are known as Rayleigh waves. They are characterized by the lattice sites undergoing an elliptical motion on a plane perpendicular to the interface, as shown in Fig.1.23. The strain field decays exponentially into the substrate within an acoustic wavelength[146]. In piezoelectric materials the strain on the crystal lattice

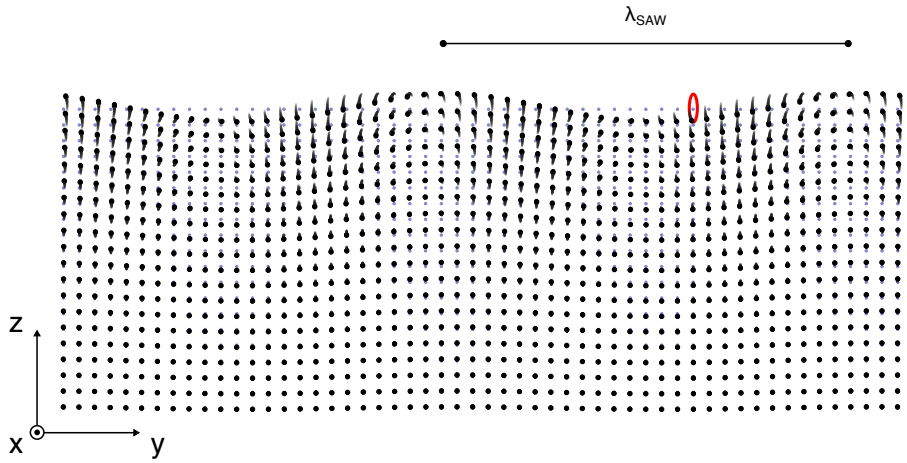

Fig. 1.23: Displacement of a solid lattice by a Rayleigh wave. Light grey dots show a uniform static lattice, while the black dots show the distorted lattice, where each lattice site follows an elliptical path as the wave propagates. There is no displacement out of plane. The maximal displacement amplitude along z is typically up to a few nanometres[146].

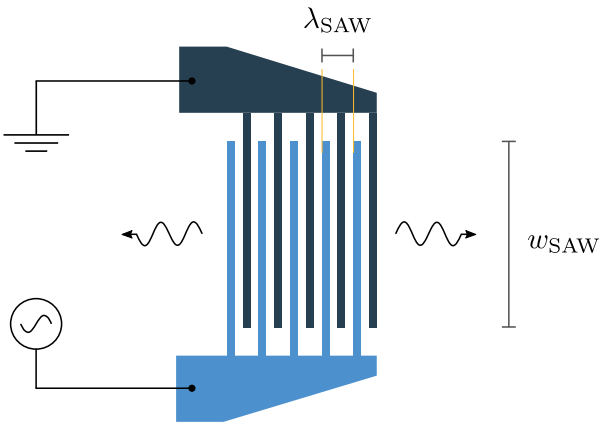

Fig. 1.24: Schematic of a single-finger IDT. The finger spacing determines the wavelength of the generated SAW. This simple design only needs a fabrication resolution of $\lambda_{SAW}/4$ and generates a SAW in both directions. The aperture w_{SAW} of the SAW beam is determined by the finger overlap.

can induce dipoles. Therefore, a SAW on a piezoelectric material consists of a strain and an electric potential wave. The piezoelectricity depends on the lattice structure and on the cut of the crystal along which the wave is propagating, making SAWs strongly anisotropic.

SAWs are also sensitive to the surface quality, as dirt and roughness inevitably introduce losses. On a clean chip SAWs can have long propagation lengths in the mm–cm range[145]. That means in most cases they can propagate along the length of the sample*. One of the reasons for their long propagation lengths is the fact that the material at an interface is less rigid, which leads to a lower sound velocity than in the bulk and thus in principle SAWs cannot lose energy by coupling to bulk waves[146].

1.4.1 Generation of SAWs on a Chip

SAWs can be generated either by short laser pulse excitation[147–149] or by the piezoelectric effect with a carefully designed transducer. We exclusively use the latter method, employing interdigitated or interdigital transducers (IDTs). These consist of two metal gates with interleaved fingers (hence the name), as presented schematically in Fig.1.24. In the simplest configuration, known as the single-finger transducer, the distance between the fingers and their width correspond to a quarter of the target acoustic wavelength λ_{SAW}, which is usually in the µm range. A SAW is generated on a material with sound velocity v when a radio frequency (rf) voltage is applied to the IDT at the resonance frequency $f_{SAW} = v\lambda_{SAW}^{-1}$. The same structure can also act as a receiver by the inverse piezoelectric effect. Thus, a pair of opposing IDTs can be used to transmit a signal through the material. This is a common structure known as a delay line.

The SAW propagating from an IDT is generally well collimated. Though there are diffraction effects that need to be considered for accurate applications, in the samples studied here the

*When a SAW reaches the edge of a chip it is reflected, which might need to be taken into account depending on the device under study.

receiver IDT or the structures under influence of the waves reside within the near field and diffraction can be neglected.

There are various designs of IDT beyond single-finger. A widespread extension on the single-finger design is the double-finger IDT, in which each finger is further split in half while keeping the same polarity. The motivation for this is to reduce reflections which arise from individual partial reflection of an incoming SAW on each finger. In the single-finger IDT, the whole structure acts as a Bragg reflector. In contrast, in the double-finger design the reflected waves interfere destructively. The downside of the design is a two-fold higher accuracy requirement for the fabrication of an IDT at the same frequency, since each individual finger is $\lambda_{\mathrm{SAW}}/8$ wide.

Chapters 4 and 5 present measurements on devices with a third type of IDT design, the split-5-2 transducer[150]. In this design a period corresponding to one acoustic wavelength comprises five fingers, two pairs of which have opposite polarity and a single finger of floating potential. This design allows for the generation of a SAW at a fundamental frequency determined by the finger spacing but also at higher harmonics, including even ones. In contrast, a single-finger IDT can only generate odd overtones.

Figure 1.25 shows the arrangement of the three types of IDT as well as an example of their expected delay line response calculated by the delta-function model[151]. In this basic model the fingers are assumed to be non-reflective and each finger acts as a point source of waves that add up to the total wave. The name comes from the fact that this is equivalent to a delta-function in space. Taking the IDT to consist of a series $x_1, x_2, ..., x_N$ of finger positions separated by a constant pitch p we can add up waves of the form $\exp(i\omega x/v)\exp(i\omega t)$ originating from each finger. To account for the polarity of the fingers we add a factor P_n defined as $(-1)^n$ for a single-finger IDT. The wave amplitude is then proportional to

$$\begin{aligned} A(\omega) &= \sum_{n=1}^{N} P_n \exp\left(i\omega\frac{x-x_n}{v}\right)\exp(i\omega t) \\ &= \sum_{n=1}^{N} P_n \exp\left(-i\omega\frac{x_n}{v}\right)\exp\left(i\omega\frac{x}{v}\right)\exp(i\omega t). \end{aligned} \tag{1.34}$$

The second to last and last factors do not vary in the sum and therefore represent a constant factor. They can thus be left out without loss of generality. Given that the finger positions are $x_n = pn$ the IDT response is given by

$$H(\omega) = E(\omega)A(\omega) = E(\omega)\sum_{n=1}^{N} P_n \exp\left(i\omega\frac{np}{v}\right). \tag{1.35}$$

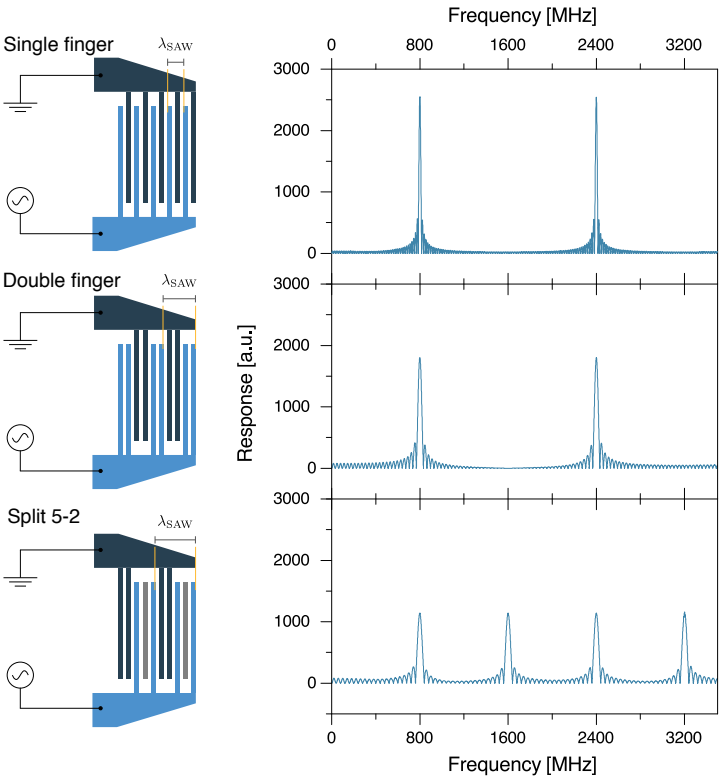

Fig. 1.25: Comparison of IDT finger arrangements for three designs and their corresponding response function following the delta-function model. The model assumes 100 fingers and their positions are chosen such that the fundamental frequency is at 800 MHz.

Here, $E(\omega)$ includes all of the neglected factors and can generally be dependent on frequency to incorporate dispersive effects[143]. The responses calculated for Fig.1.25 take $E(\omega) = 1$. It should be noted that although this simple model is useful in determinig the frequency response of an IDT, it might not always be applicable because it neglects reflections, the physical width of the fingers and the effects of the metal on the surface.

We note that the bandwith of SAW generation is inversely proportional to the number of finger pairs N_p and is limited up to tens of MHz. For some experiments it is desirable to have a broader range of excitation frequencies. Fortunately, IDTs can be chirped while maintaining the phase relationship of the response[151]. The delta-function model can provide an idea of the increased bandwidth for a given chirp rate. Recently, chirped split-5-2 IDTs have been demonstrated[152].

1.4.2 Electrical to Acoustic Conversion Efficiency

One issue with the acoustic transducers presented is that they generate a SAW in both positive and negative directions. This can complicate experiments where reflections are important and at the very least provides an unwanted loss of half the acoustic power. IDTs have been designed to produce a wave in a single direction. These are known as single-phase unidirectional transducers[153]. An alternative is the addition of a Bragg grating at the unwanted end of the

Material	Speed of sound [m/s]	K^2 [%]	Reference
128 Y-X $LiNbO_3$	3979	5.4	Ref.[143]
Y-Z $LiNbO_3$	3488	4.8	Ref.[143]
ST-X Quartz	3159	0.12	Ref.[143]
a-plane AlN	5741	0.47	Ref.[154]
(1 0 0) GaAs	2868	0.07	Ref.[149, 155]
(1 0 0) AlAs	3387	-	Ref.[156]
ZnO/GaAs	2880	0.7	Ref.[143]
AlN/Diamond	9200	-	Ref.[143]

Table 1.1: Material parameters for selected SAW-supporting materials. The last two are examples of thin film systems, which can be used to enhance piezoeletricity or to use SAWs on non-piezoelectric materials such as diamond.

IDT. This is essentially the same as an IDT but where all fingers are shorted to have the same electric potential. The incoming SAW is then reflected back towards the IDT and can add up constructively with the outgoing SAW in the desired direction.

More fundamentally, the degree of conversion efficiency between electrical and mechanical energy is given by the electromechanical coupling coefficient K^2, defined as[145]

$$K^2 = \frac{e}{c\epsilon} = 2\frac{\Delta v}{v}, \tag{1.36}$$

where e is the piezoelectric coefficient, c is the elastic constant, ϵ is the dielectric permittivity and Δv is the difference in sound velocity between a free surface and a metallized surface. Table 1.1 summarizes the sound velocity and K^2 for selected materials and thin films. The following sections briefly comment on GaAs and $LiNbO_3$, which are the materials employed in this work.

Following these considerations, it is also important to consider the impedance matching of the IDT to the exterior circuit which is usually 50 Ω. Matching helps to avoid unwanted reflections and losses which can be significant when considering that the rf power sent into a cryostat can be enough to warm up the sample. Following Ref.[157] the conductance G_a of an IDT is derived from the equivalent-circuit model:

$$G_a(\omega) \approx 1.3K^2 N_\mathrm{p}^2 \omega_0 w_\mathrm{IDT} C_\mathrm{S} \left(\frac{\sin X}{X}\right)^2, \tag{1.37}$$

with $X = N_\mathrm{p}\pi(\omega - \omega_0)\omega_0^{-1}$. In this equation C_S is the capacitance per unit length of an IDT finger pair. The number of finger pairs N_p and IDT aperture w_IDT can then be chosen to satisfy the condition $G_a = 1/50\,\Omega$ for a given K^2. This is not always easily achievable, as the condition could require an unfeasible number of finger pairs. For example, an IDT with 200 µm aperture at 1 GHz in GaAs already requires 380 finger pairs. Very large numbers of pairs are avoided

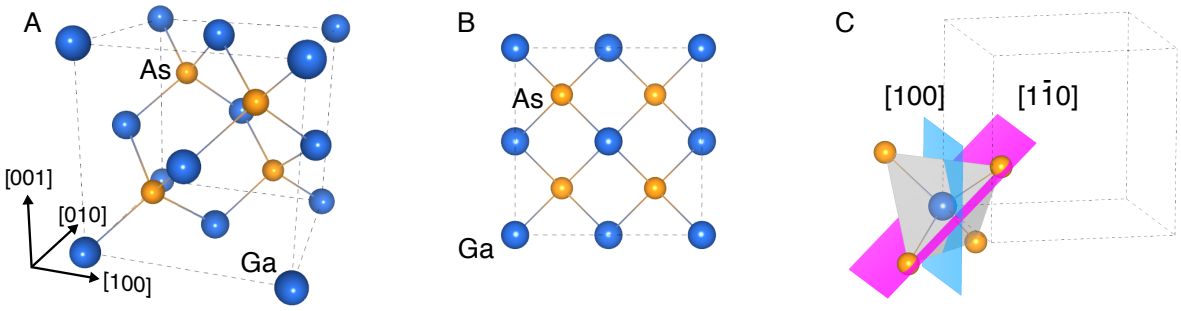

Fig. 1.26: A. Unit cell of GaAs with zincblende structure. **B.** View along main axes. **C.** A polyhedral cell showing two crystallographic planes. Compression and tension along (perpendicular to) [1 $\bar{1}$ 0] results in a dipole. This is not the case for [1 0 0].

because the fingers are not non-reflective[158]. More fingers present more scattering centres where energy can be lost to bulk modes and the problem becomes more relevant at higher frequencies, since the wave is more closely confined to the interface and therefore to the metal. In cases where the number of finger pairs required to match the IDT is exceedingly large, a matching circuit is needed.

Finally, we note that metal on the surface can affect SAW propagation in two ways: electrically and mechanically. The two effects are known as electrical and mass-loading, respectively. In the former, a metal layer shorts the electric field at the surface, thereby eliminating the potential wave field. In the latter, the mass of the metal is enough to significantly alter the sound velocity at the surface. This is the reason behind the reflectivity of fingers in an IDT.

1.4.3 SAWs on GaAs

As evidenced by Tab.1.1 GaAs is only weakly piezoelectric. In (1 0 0) GaAs wafers SAWs can be generated through the piezoelectric effect along the [1 1 0] and [1 $\bar{1}$ 0] directions. SAWs propagating along other directions such as [1 0 0] cannot be generated directly through electrical transducers[146, 159]. The reason for this becomes clear considering the crystal structure of GaAs, shown in Fig.1.26. As a SAW propagates through the material the lattice is compressed and tensioned, changing the bond lengths and angles. For a SAW propagating along [1 1 0] or [1 $\bar{1}$ 0] this deformation generates a dipole. In contrast, a SAW in [1 0 0] does not. To generate a SAW in this direction, a thin piezoelectric film, such as zinc oxide, would be necessary[159]. The same considerations apply for other piezoelectric materials and in particular with the same planes to $Al_xGa_{1-x}As$.

In Ch.3 and Ch.5 SAWs are generated on DBR structures. The layers are smaller than one acoustic wavelength so the SAW propagates in both AlAs and GaAs. Most material

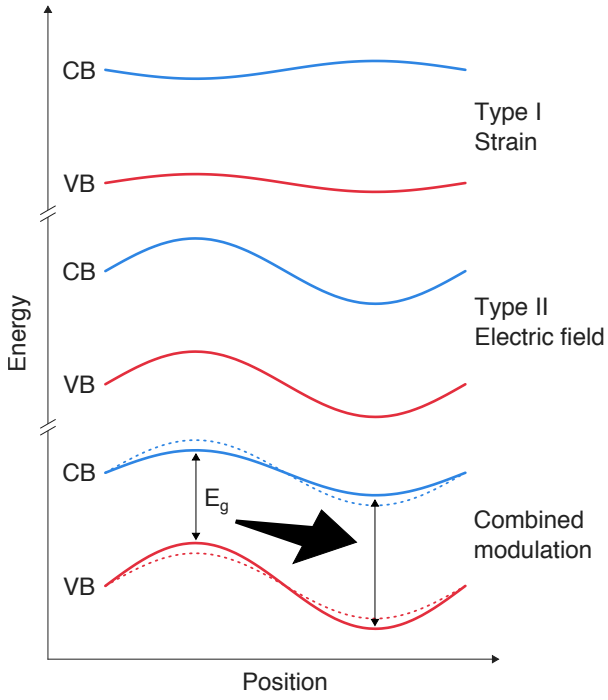

Fig. 1.27: Modulation of the bandgap due to a SAW within one acoustic wavelength. The strain field produces the type I modulation, which affects the CB and VB in opposite phase. The electric field modulates the bands in phase. The combined effect results in a modulation of the bandgap. Note this is also true in time as the wave propagates through a certain point.

parameters are very similar[146] but AlAs has a higher sound velocity than GaAs, causing strong dispersion[156, 160]. This is detrimental to the efficiency of operation, as measured between samples and confirmed by simulations. This is discussed further in Sec.2.8.

1.4.4 SAWs on $LiNbO_3$

$LiNbO_3$ is one of the most common substrates for SAW and other acoustic devices thanks to its large piezoelectricity. As for GaAs, the waves supported and their excitation depends on the crystal orientation. There are multiple crystal cuts where $LiNbO_3$ supports SAWs. For the samples used in Ch.4 we use 128° Y-cut $LiNbO_3$. This cut only supports electric generation of SAWs along one axis, X.

1.4.5 Coupling to Semiconductor Structures

Both the acoustic and electric fields associated with a SAW have an effect on the band structure of a semiconductor, resulting in a periodic modulation of the conduction band (CB) and the valence band (VB) as presented in Fig.1.27. The modulation due to the strain field is known as type I modulation and is usually on the order of 0.1 - 1 meV in GaAs[146, 150]. Notably, the compression and expansion of the lattice shifts the valence and conduction bands in opposite directions, thus increasing and reducing the bandgap. This is not the case for the modulation caused by the electric field, known as type II modulation, which in GaAs can shift the bands by

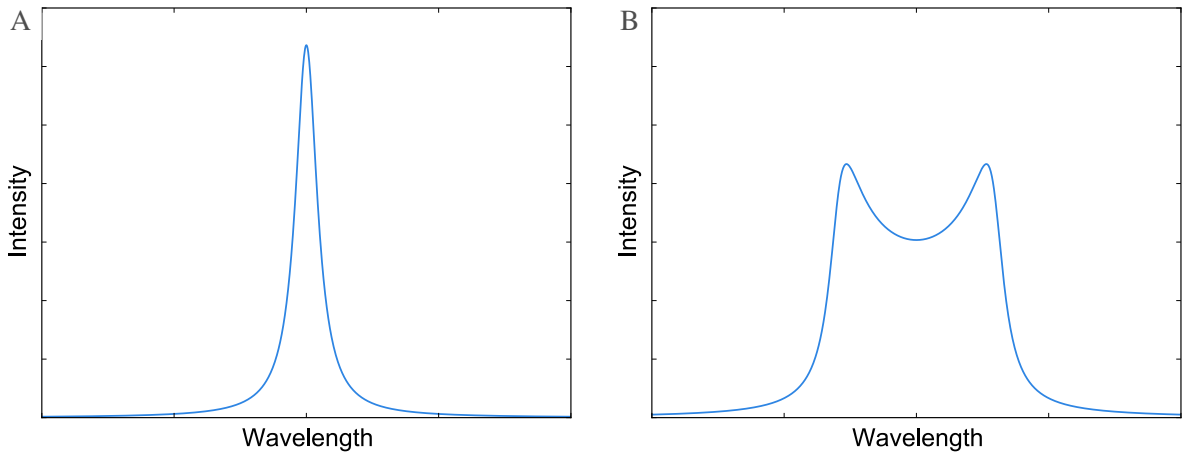

Fig. 1.28: Broadening of an emission line due to the periodic tuning by the strain field. **A.** Lorentzian lineshape. **B.** Time averaged signal of a Lorentzian with sinusoidal modulation of the center frequency.

larger values of around 50 - 150 meV[161]. The resulting dynamic modulation of the bandgap is a common theme in this work and is exploited to produce a single-photon source, as detailed in Ch.3. The spectrum of a QD transition can evidence the presence of a SAW, as schematically pictured in Fig.1.28. Without a SAW, the transition is ideally a Lorentzian line at energy E_0. Under the presence of a SAW E_0 becomes time-dependent. For a sinusoidal SAW it oscillates around its original value with an amplitude χ dependent on the acoustic power. The central emission energy is thus modified to

$$E_0(t) = E_0 + \chi \sin(\omega_{\mathrm{SAW}} t)\,. \tag{1.38}$$

Measuring the emission spectrum is equivalent to the temporal integration of the intensity. The effect of the SAW is then measurable as a broadening of the emission line. For a sinusoidal modulation the transition spends more time at the extrema of the modulation and a characteristic two-lobed curve is observed, as presented in Fig.1.28B. This intensity profile can be expressed as

$$I(E) = \int_{-\infty}^{\infty} \mathrm{d}t \frac{\delta\omega}{(E - E_0(t))^2 + \delta\omega^2} \tag{1.39}$$

$$= \int_{E_0-\chi}^{E_0+\chi} \mathrm{d}E' \frac{\mathrm{d}t}{\mathrm{d}E'} \frac{\delta\omega}{(E - E')^2 + \delta\omega^2} \tag{1.40}$$

$$= \frac{1}{\chi} \int_{E_0-\chi}^{E_0+\chi} \mathrm{d}E' \frac{1}{\sqrt{1 - \left(\frac{E'-E_0}{\chi}\right)^2}} \frac{\delta\omega}{(E - E')^2 + \delta\omega^2}, \tag{1.41}$$

where T is the SAW period and the linewidth of the Lorentzian transition is $2\delta\omega$.

1.4.6 Applications for Quantum Information

Recent years have seen a renewed interest in SAWs for experiments in the quantum regime and in compact electronics. The "slowness" of sound* is practical for on-chip circuits, as it provides time for signal relaying and feed-forward. In addition, SAWs typically operate in frequency ranges compatible with the typical energies of various physical qubit candidates[162] and the overlap of acoustic and photonic wavelengths can be controlled across technically relevant spectra[163, 164]. As such, SAWs have been exploited for multiple experiments. Some prominent examples include:

Single electron transport The band modulation can be thought of as a moving potential well, giving SAWs the ability to confine and transport carriers. Many experiments have taken advantage of this fact to separate electrons and holes in a two-dimensional electron gas (2DEG) and carry them across a chip[165, 166] Adding confinement from a one-dimensional channel, single electrons can be transported[167]. This enables control over single carriers, such as the targeted population and depopulation of an electrostatically defined quantum dot. It has been proposed that this mechanism cold be used as a platform for on-chip quantum information processing[168].

Single phonon physics An active area of research is the development of an acoustic analogue to cavity quantum electrodynamics (CQED), dubbed cavity quantum acousto-dynamics (CQAD)[169–173].

Optomechanics SAWs provide a controllable photon-phonon interface. Recently, SAWs and light have been confined in phononic waveguides with integrated optical cavities, demonstrating coherent interactions[163]. Outside the quantum regime, SAWs can be used for on-chip photon routing by modulating the refractive index. Acousto-optical modulation of optical cavities of up to 19 GHz has been reported[174, 175]. Refs.[176, 177] highlight applications of optomechanics.

Spintronics Related to the electron transport, a SAW spatially separates electrons and holes, thereby decreasing the spin relaxation rate. Therefore, SAWs are attractive for spin transport and spin manipulation[178]. Experimental demonstrations have reached spin coherence lifetimes as long as 25 ns[179].

Single-photon trigger SAWs have been proposed as a high-repetition timing mechanism for a single-photon source[161]. This idea has been experimentally demonstrated[180] and

*The sound speed is ~3000 m s^{-1} in GaAs, 5 orders of magnitude lower than $c \sim 3 \times 10^8$ m s^{-1} (in free-space).

in this work is expanded onto cavity systems. The idea of a SAW-driven single-photon source is discussed in detail in Ch.3.

Chapter 2

Experimental Methods & Sample Fabrication

This chapter gives an overview of the methods used. The first part outlines the fabrication methods used in the cleanroom. All of these are standard in micro and nanofabrication so their description is kept short given the abundance of in-depth resources such as Ref.[181]. The second part focuses on the general spectroscopic measurements carried out in the optical laboratories. More specific measurements based on these techniques are described in the appropriate chapters.

2.1 Sample Growth

The starting point for obtaining a sample is the design of the material and doping composition of layers followed by their precise growth. A variety of techniques have been developed for growth of high purity crystalline layers with atomic thickness control. They are collectively known as epitaxy. All of the wafers processed for the work presented here were grown by molecular beam epitaxy, which is briefly described below. With the exception of the sample used in Ch.4, which was grown at Walter Schottky Institut (Munich), the samples were grown at the Semiconductor Physics Group in the Cavendish Laboratory (Cambridge) by either Dr. Ian Farrer and Dr. Peter Spencer.

2.1.1 Molecular-Beam Epitaxy

Molecular-beam epitaxy (MBE) is an epitaxial technique well-suited to the growth of III-V semiconductor alloys. The process starts with a commercially available wafer, cut from an ingot of material grown by thermal crystallization (e.g. Bridgman or Czochralski growth)[182]. The wafer is placed in an ultra-high vacuum chamber (~10×10^{-10} mbar), where effusion cells loaded with the materials to be grown (e.g. Ga, As, Al, In) are targeted at the wafer. During growth the wafer is heated to ~550 - 650 °C and a beam of material is ejected from the desired effusion cells, where the flow rate is controlled thermally[52]. Upon impinging on the wafer, molecules can either stay in place, desorb, or migrate on the surface. The balance of the rates at which these processes take place has a broad parameter space that constitutes one of the main challenges of MBE. When appropriately tuned, the surface migration can homogeneously cover the wafer, forming an atomically thin layer of material known as a monolayer. Growth rates vary but are usually around 1 µm h^{-1} or about a monolayer per second[181].

All Cavendish-grown samples used in this work are grown on (1 0 0) wafers with nominally no doping. They do show evidence of carbon p-doping originating from the chamber, with an average concentration of 1×10^{13} cm^{-3}[183]. This correlates with a preference for positively charged lines in the quantum dots found in these samples.

2.1.2 Self-Assembled Quantum Dots

The dots studied in this work are grown by the Stranski-Krastanov (SK) method[184, 185]. Figure 2.1 shows the process schematically. SK growth relies on lattice mismatch between semiconductors layers. In the case of InAs and GaAs the strain is 7 %[57]. As a result, tension builds up as monolayers of InAs are grown on GaAs. At a critical number of layers the growth stops being uniform and nucleation sites start to form[186, 187]. The growth at these sites is faster and forms the QDs as material accumulates. The dot size can be controlled by the material deposition time and temperature. The result is a planar layer, known as the wetting layer (WL), and a series of randomly distributed QDs.

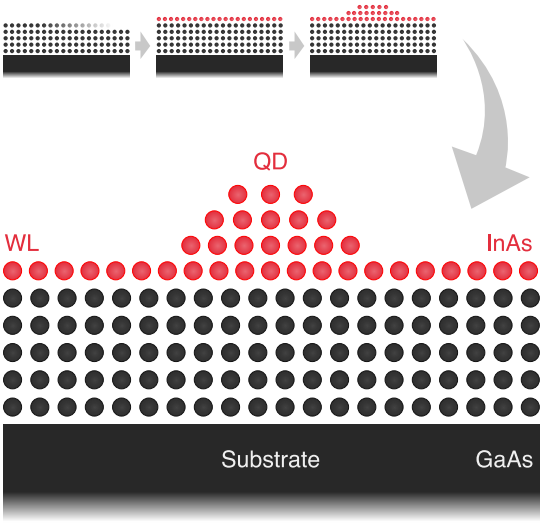

Fig. 2.1: Stranski-Krastanov growth mode of quantum dots. Epitaxial GaAs is grown on a commercial substrate. The first InAs monolayers form the WL. QDs form due to strain. After formation, dots are capped with GaAs (not shown).

The inherently random position and size (energy) distribution of SK dots poses a considerable challenge for scalable networks, where one would ideally want a predetermined grid of QD positions with identical optical properties. There have been attempts to position QDs by preferential nucleation in pre-selected sites, for example by etching small holes serving as nucleation centres and regrowing[188, 189]. However, it has been found that interrupting the growth process to allow for the positioning degrades the optical properties of the produced dots[190]. Nevertheless, progress on mitigating the detrimental effects of positioning has been recently reported[191]. An alternative constitutes measuring the sample after growth to create a map of dot positions. The map can be extracted for example from μPL, atomic force microscopy or scanning electron microscopy. Alignment markers can then be added for further processing at the accurate dot locations. However, the additional complexity and requirement of tailored maps for each sample makes this inefficient for mass scaling. With that said, it can be useful for proof-of-principle experiments where the positioning is of paramount importance – for example

for a dot inside a cavity. As for the energy degree of freedom, dots can be tuned into resonance after fabrication by any of the mechanisms outlined in Sec.1.2.5.

It should be noted that the growth process is not perfectly homogeneous. This means that the coverage of dots on the wafer exhibits a gradient. If the wafer is stationary during growth the dot density gradient is linear. On the other hand, if the wafer is rotated during QD growth, the gradient is radial. It is critical to perform an initial characterization on a newly grown wafer to have an idea of which regions are suited for a particular sample. This characterization can be done on a wafer scale or by cleaving the wafer and looking at smaller pieces from all cardinal regions.

2.2 Microfabrication of Samples

The general procedures followed for the fabrication of the samples used in this thesis are outlined here. Specific details on the individual steps are not included as some of these are considered privileged information.

2.2.1 Photo- and Electron-Beam Lithography

Photolithography is the backbone of the semiconductor industry. In this process a light sensitive polymer known as a photoresist (PR) is coated on a substrate. Subsequent illumination through a stencil metal pattern selectively exposes some parts of the resist. Depending on the type of PR, the exposed area is cross-linked, making it more robust and insoluble in a developer (negative tone PR) or the bonds are broken, making short polymer chains that are easily dissolved by a developer (positive tone PR). In this fashion the wanted pattern is transfered onto the PR. This can then be used to transfer the pattern onto the underlying substrate or to selectively deposit metal. Figure 2.2 shows a representation of the process. The process can be iterated multiple times to create complex devices.

Electron-beam lithography (e-beam) follows the same principle as photolithography but instead of using light for the exposure of the resist, a more energetic electron beam is used to "write" the structure on the resist. The main advantage is an improved resolution, which can be down to ~10 nm compared to ~1 µm resolution for standard basic photolithography. The downside is that the process is more complex and has a low throughput, as the writing is a sequential process where the beam has to scan through the pattern.

One of the complexities of e-beam is that the electrons are scattered as they go into the sample. This can trigger processes that can lead to the resist being exposed where it is not supposed to be, causing deviations from the ideal pattern. The main contributions to this are

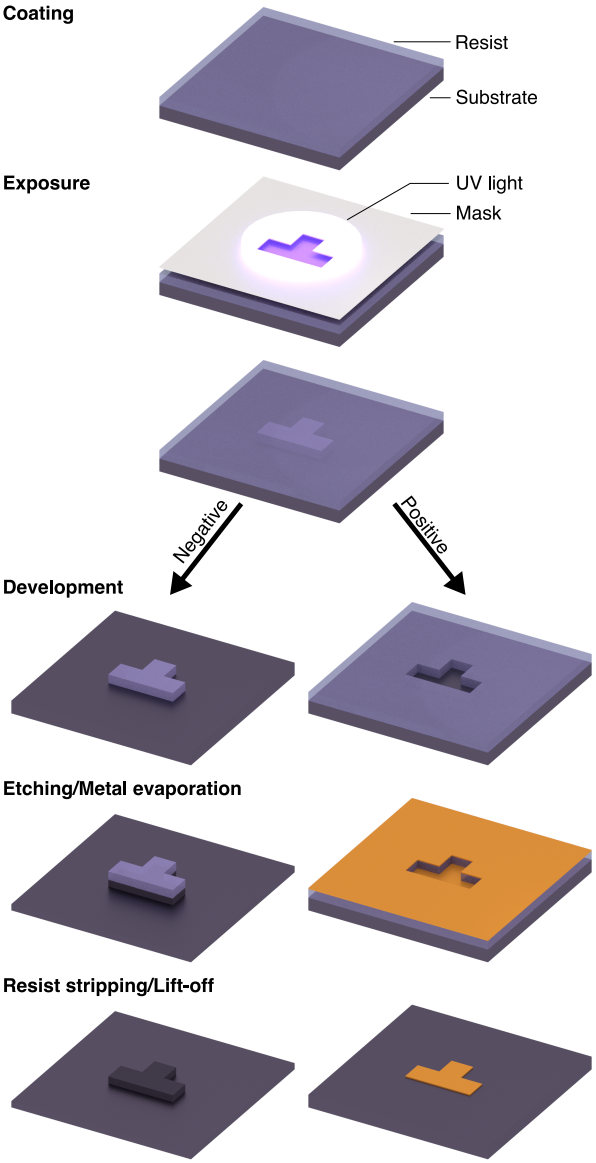

Fig. 2.2: Typical workflow for a photolithography step in sample fabrication. Photoresist is spin-coated on the sample. For negative (positive) tone resist, the exposed areas are made insoluble (soluble) in a corresponding solvent. Negative resist is used for etching of the top layers of the sample. Positive resist is mostly used for lift-off, where metal is deposited in the exposed areas.

backscattered electrons and secondary-electrons released on impact by an electron from the incoming beam. These processes are material-dependent. It is therefore necessary to simulate the electron backscattering and secondary-electron generation rate to have an idea of the electron spread when aiming for high-resolution structures. With an accurate simulation it is possible to compensate for these effects by modifying the dosage across a design. An example is shown in Fig.2.3, where the corrected dose is represented by the colour. Given that the decrease in fidelity to the original design is most prominent in parts where two exposure areas are in close proximity, this process is known as proximity correction.

Another point that is worth of a quick mention is the fact that by irradiating a sample with electrons it will charge up if it is not sufficiently conductive. This will naturally lead to a field

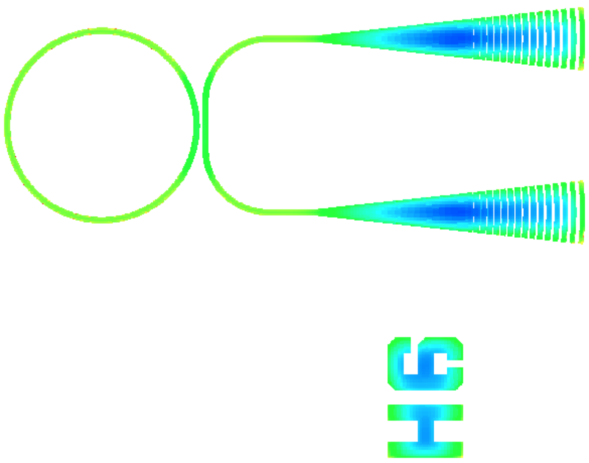

Fig. 2.3: Example of proximity correction on a ring resonator, waveguide tapers, and gratings. The original design is split into smaller areas. The dose is codified in the colour of the regions, with blue corresponding to a lower dose than green.

deflecting further incoming electrons and causing the exposure to fail. When writing on semi insulating samples a conductive layer is needed on top. This can be a conductive polymer or a thin (< 10 nm) metal film.

Virtually all samples discussed in this thesis used e-beam lithography for the definition of IDTs, as the finger dimensions needed for the targeted GHz frequencies are usually around 700 nm. This can be done without much worries on proximity correction.

2.2.2 Metal Evaporation

Once a pattern is defined on the resist on top of the substrate it is possible to deposit a thin metal film* on the chip (e.g. to define gates). The general apparatus used is presented in Fig.2.4. Subsequent immersion in a solvent will clear the remaining resist, along with the metal that was deposited on top of it. This process is known as lift-off. A critical factor in its success is the resist profile, which should ideally have an undercut thereby allowing the solvent to easily act on the resist from beneath the top metal layer and avoid metal bridging. The devices fabricated for this work mostly use bi-layer PMMA as an e-beam resist and Shipley S1800s as an optical resist. An undercut can be reliably obtained for both.

For some of the devices discussed here, the sample surface was not homogeneous enough to be evenly covered by a resist layer. In these cases a shadow mask was used in addition to the resist. The shadow mask is an external element that covers the sample to shield a particular region during evaporation. Presented in Fig.2.5 are two shadow masks used for this project. The first one is very basic: a custom clamp with a beam can be used to cover regions with ~100 µm precision. The clamp is made of Teflon™ to avoid damage to the sample by thermal expansion

*More often than not multiple layers are evaporated. Au is standard for Au wire bonds but needs Cr or Ti as an adhesion layer underneath.

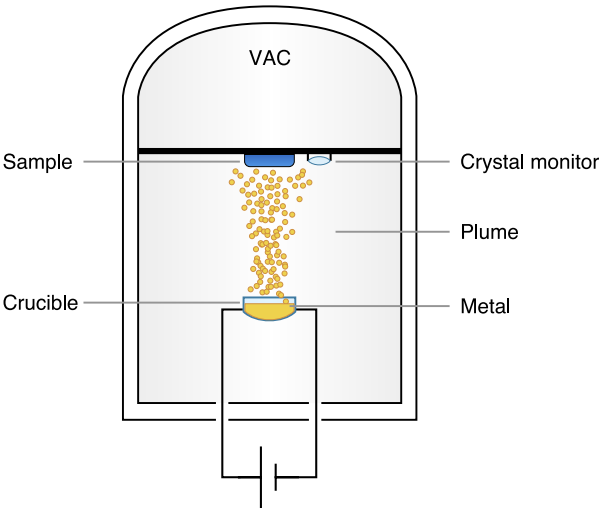

Fig. 2.4: Schematic of a metal evaporator. The sample with the pattern defined on the resist is placed in a vacuum chamber. The metals to be deposited are placed in a crucible with a higher melting point (usually tungsten). Passing a current through will melt and evaporate the metal. The thickness can be monitored with a crystal, whose oscillation frequency changes proportionally to the mass deposited. Multiple metals can be evaporated sequentially. An alternative to thermal evaporation of the metal is electron beam evaporation, where the metal is evaporated by kinetic energy transfer from an electron beam.

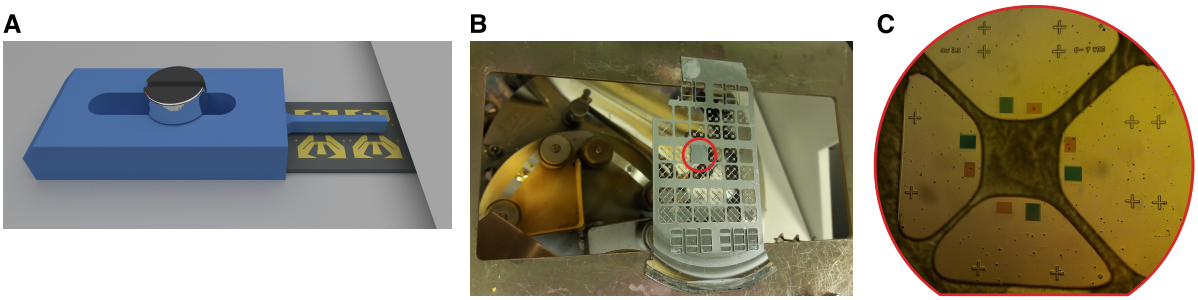

Fig. 2.5: **A.** Schematic of a simple shadow mask consisting of a clamp with a protruding beam that can cover a rough area on the sample during metal evaporation. **B.** Picture of a Si-wafer shadow mask with a sample (circled) aligned. **C.** Microscope view of the Si-wafer and the sample. The IDTs meant for metal deposition are clearly visible, while the central region is covered.

during evaporation. The second mask is more elaborate: a protective pattern is written on a Si wafer which is subsequently thinned down and etched through by Bosch etching[192]. The result is a precise and thin mask that can be aligned on the chip under a mask aligner (the sample is held in place by little blobs of resist on the corners).

Finally, in situations where the metal needs to extend over an etched trench or mesa, such as when contacting LEDs, it can be problematic to achieve coverage without interruption at the perimeter of structures. This issue can be mitigated by using a rotating sample holder held at an angle during evaporation. The angle ensures coverage of the sidewall of steep features and the rotation ensures homogeneity and coverage from all sides.

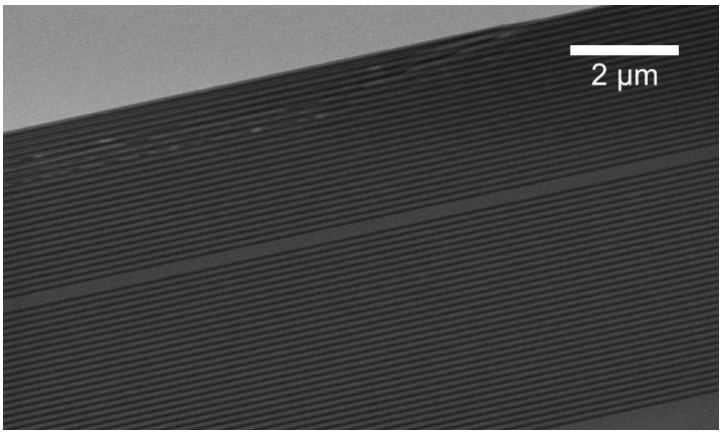

Fig. 2.6: SEM micrograph of a cleaved facet on a grown planar cavity structure. Light regions are GaAs and dark regions are AlGaAs.

2.2.3 Dry and Wet Etching

Just as a milling machine is used in traditional machining in a workshop, removing material is one of the basic approaches to fabrication of semiconductor devices. There are two main ways to do so: physical or chemical processing. Physical removal involves bombardment of the material with high-energy particles that can sputter off material when they impinge on the substrate. Chemical removal relies on interaction with reactive substances such as halogens or acids. There is also a distinction between dry and wet etching. In the former the etchant is found as an ion beam or a plasma and tends to rely more heavily on physical etching, while the latter only works by chemical etching in a liquid. The applicable processes will depend on the materials at hand.

For GaAs, multiple etching processes have been developed and the main difference between dry and wet etching is the resulting profile. Dry etching can be made directional, yielding straight edges, while wet etching is isotropic by nature. For dry etching, it is especially important to consider the type of mask used. Photoresist can be used for some processes but it will also be removed to some degree during the etching process. Its suitability will therefore depend on the target etch depth. This is quantified by the selectivity of the process, which is the ratio of etch rate of the underling material to the etch rate of the mask. An additional caveat of using resist is that it can melt and deform or even burn if the etching process reaches a high temperature. In cases where resist is not well suited it is necessary to perform an additional step to use a "hard" mask, which can be metallic or dielectric. The following sections give more details on the procedures used for this work.

2.2.4 Fabrication of Pillar Microcavities

As mentioned in Ch.1, a pillar cavity is made by growing a planar DBR cavity and subsequently etching it to define the pillars. The DBRs used in this work are made of $Al_{0.98}Ga_{0.02}As$/GaAs

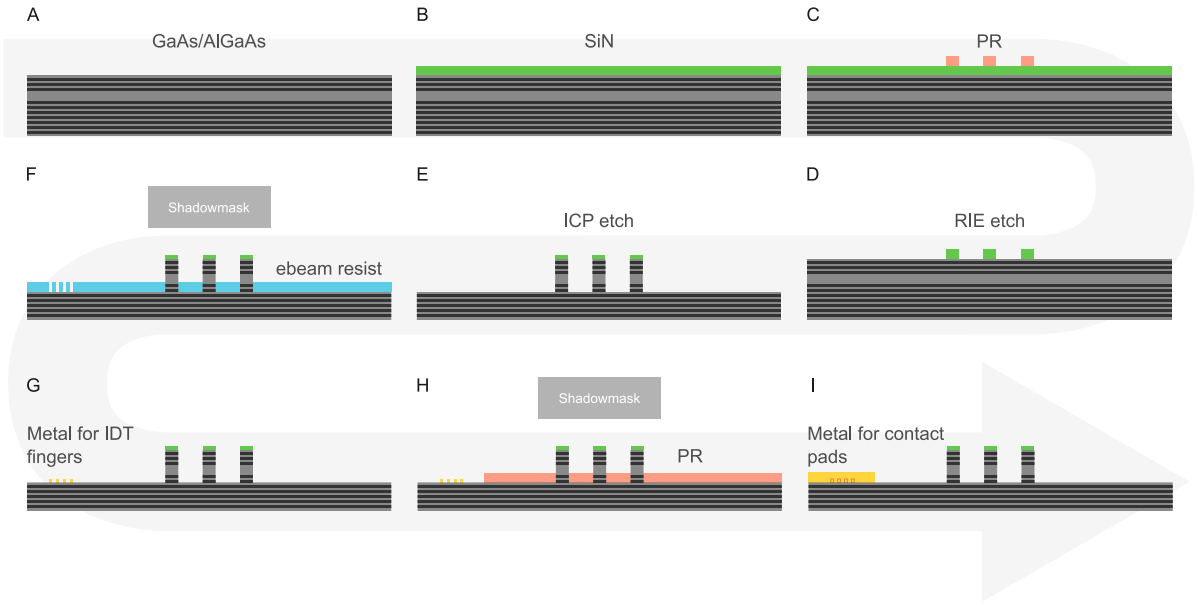

Fig. 2.7: Process flow diagram for the fabrication of pillar microcavities in the path of a SAW. **A.** Growth of cavity structure by MBE. **B.** PECVD deposition of SiN thin film to be used as a hard mask. **C.** Definition of pillars by photolithography. PR: photoresist. **D.** Transfer of the pillars onto the SiN by dry etching. **E.** Dry etching of the wafer to form the actual pillars. **F, G.** E-beam lithography to define IDT fingers. A shadow mask is used during the evaporation to protect the pillars. **H, I.** Similar process to evaporate the IDT contact pads.

stacks. This combination is widely used because the two materials have a high refractive index contrast* and closely matching lattice constants[114]. The former translates into a higher partial reflectivity per DBR period and thus reduced mirror thickness. The latter is a requirement for strain-free growth of the multiple layers required. Even so the growth of high-Q cavities requires multiple repeats and can be challenging as defects propagate with the growth. In addition, there will be a variation of deposition thickness across a wafer, such that central wavelengths can vary by as much as 10 nm.

An image of a planar cavity prior to patterning into pillars is shown in Fig.2.6. Pillar microcavities on the Ga/AlGaAs system are traditionally made by either dry-etching the material to define the pillar, or by etching only partially and defining an aperture by oxidation of an AlAs layer[193]. We exclusively use the former method, which is schematically presented in figure 2.7. These cavities require high numbers of DBR mirror pairs to attain high-Q factors, which poses challenges on their fabrication. Firstly, a mask with a high enough selectivity is needed to ensure it survives the etch process and the patterns are transferred with high fidelity. Secondly, for the definition of pillars with diameters of some µm, the etch needs to go through the various

*$n_{\mathrm{GaAs}} = 3.47$ and $n_{\mathrm{Al_{0.98}Ga_{0.02}As}} = 3.21$ at 940 nm and 5 K inferred from measurements on cavities of known thickness.

DBR layers as vertically as possible to avoid undercutting the structure. The former issue can be alleviated by using a hard mask instead of resist. We use a ~100 nm thick Si_3N_4 film deposited by plasma enhanced chemical vapour deposition (PECVD) due to its chemical compatibility and accessibility. The circles that define the pillar circumference are transferred onto this film by dry etching a resist mask (Shipley 1813 or S1813). This etch is not homogeneous and the remaining surface is not perfectly clean, which is absolutely necessary before etching the actual wafer. To solve that, a wet etching step with buffered HF (BHF) is used to clean any residue. BHF does not attack GaAs but it does attack AlGaAs and Si_3N_4 so the timing is critical to avoid damage to the desired structures. The final step is a dry etch, which uses an $Ar/SiCl_4$ inductively coupled plasma (ICP). Laser end-point detection is used to monitor the etch. This system shines a laser on the sample during the etch and records the reflected intensity. As the alternating GaAs/AlGaAs layers are etched the signal fluctuates and one can count the number of periods that have been etched, allowing for precise control of the depth regardless of variations in the process conditions. This is important to avoid finishing the process on an AlGaAs layer, which would quickly oxidise, causing damage to the sample and a rough surface unsuited to SAW propagation. The AlGaAs on the pillar sidewalls is protected by a polymer film that is formed as a byproduct of the etch, in analogy to the Bosch process[192]. Figure 2.8A shows an image of this polymer peeling off a structure after a short DI water bath.

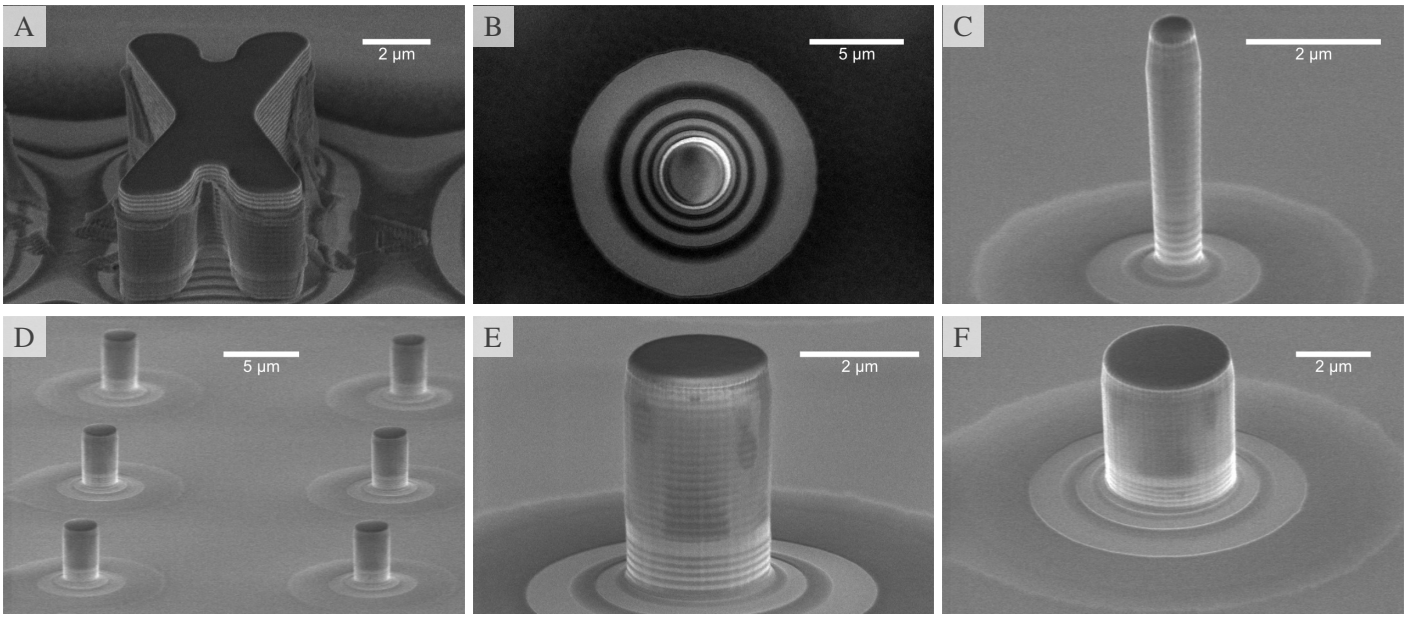

Fig. 2.8: SEM micrographs. **A.** Polymer peeling off from sidewalls of a positioning mark. **B.** Top view of a Ø 2 µm pillar. **C.** Angled view of a Ø 1 µm pillar. **D.** Angled view close-up of a pillar field. **E.** Angled view of a Ø 2 µm pillar. **F.** Angled view of a Ø 3.5 µm pillar.

The circular patterns are initially defined by optical lithography. This was found to be sufficient for pillars down to 1 µm diameter and is considerably faster than the alternative of e-beam lithography. Before transfer of the structures onto the hard mask, a hard bake is used to increase the symmetry of the resist disks by surface tension, reducing the splitting of perpendicular modes (c.f. Sec.1.3.2). Figure 2.8B shows a top view of a patterned pillar showing a highly symmetric profile.

The height of the pillars is ~3 µm depending on the number of DBR pairs and how many are etched through. This poses a challenge for the integration of acoustic transducers. The main reason is that the IDTs are defined by metal lift-off on e-beam-written Poly(methyl methacrylate) (PMMA). The thickness of PMMA can be adjusted by its dilution and molecular weight but for high-resolution it is generally well below 500 nm thick, making it impossible to have a proper lift-off on the pillars. It is possible to cover the pillars with a thicker window of resist prior to PMMA coating and exposure. However, tests with S1828 and double-coating of S1813* showed this is not optimal, as it causes damage to the pillars and is difficult to remove due to incompatibilities in the bake temperatures of the resists involved. The shadow mask introduced above is a clear preferred alternative.

2.2.5 Fabrication of Charge-Tunable LEDs

Similar to micropillars, the charge-tunable LEDs discussed in this work are processed from a planar cavity. The difference is that it is a much weaker cavity (i.e. fewer DBR pairs per mirror) and the mirrors are doped to generate the Schottky structure. The complete process is outlined in Figure 2.9. Again, S1813 is used for all photolithography steps. First step is to define a mesa where the active area of the LED will be located. Variants with ICP and wet etching were fabricated. In this case ICP etching can be performed directly with resist as a mask given the reduced etch depth of ~1 µm. Wet etching of GaAs/AlGaAs is done in $H_2SO_4 \cdot H_2O_2 \cdot H_2O$. The relative concentrations are of great importance to the profile of the etch along different crystal axes. All etches here were done with a mixing ratio of 1:8:1600 by volume, which has a "slow" etch rate of ~25 nm/min and yields a smooth profile along all axes.

The mesa is defined in two steps. The first clears the top p-doping to allow the later addition of an ohmic contact to the n-doped bottom DBR. The second etch clears the bottom doping. This is necessary to have an undoped surface on which to fabricate the IDTs. Multiple tests showed definitive shorting of IDTs when fabricated on n-doped surfaces. The ohmic contact is fabricated by AuGeNi evaporation and subsequent annealing at 430 °C. The IDT fingers

*The name gives an indication of the nominal thickness when spin coating at 3000 RPM. S1813 and S1828 should produce a 1.3 µm and 2.8 µm thick layer, respectively.

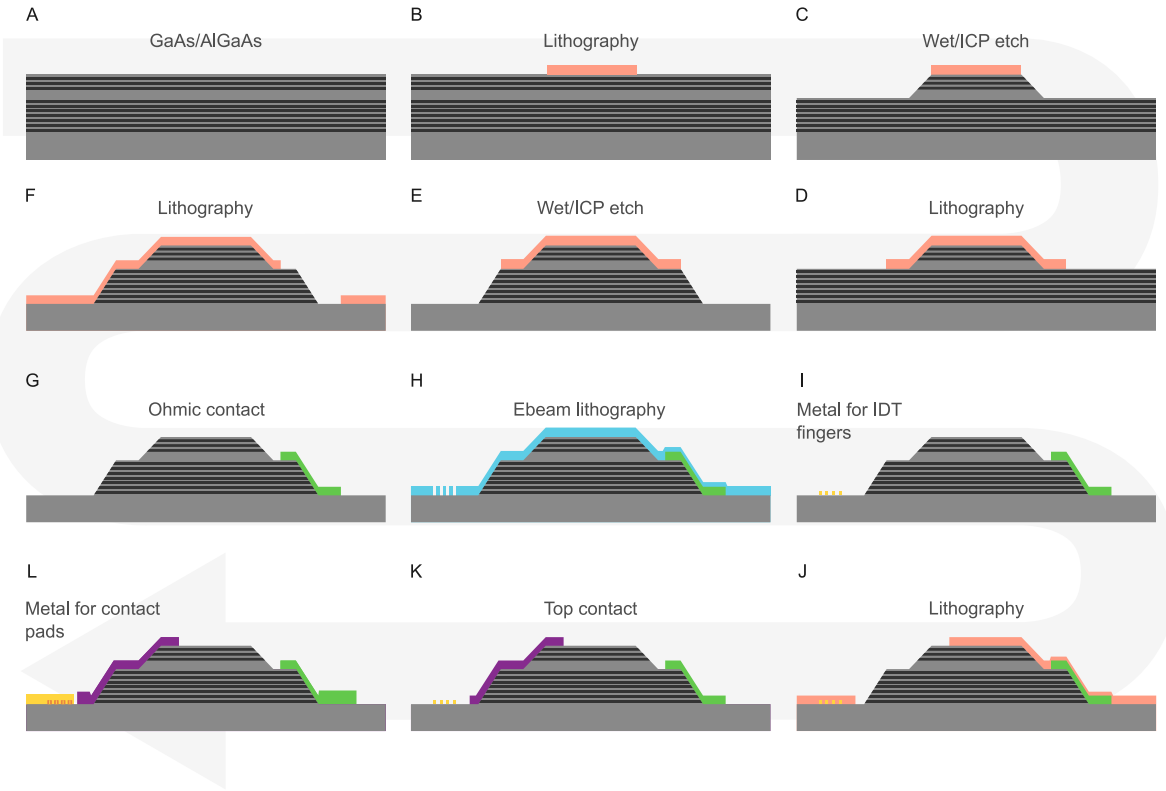

Fig. 2.9: Process flow diagram for the fabrication of LEDs with IDTs. **A.** Growth of cavity structure by MBE. **B.** Definition of mesa opening by lithography. **C.** Etching of top DBR. **D.** Definition of mesa step by lithography. **E.** Etching of bottom DBR. **F, G.** Lithography and metal evaporation and annealing for ohmic contact to bottom DBR. **H, I.** E-beam lithography and metal evaporation to define IDT fingers. **J, K.** Lithography and metal evaporation for top contact. **L.** Evaporation of thicker metal layer for contact pads.

are evaporated next, followed by the top contact. The device is then finished with the final evaporation of metal for all contact pads.

2.2.6 Fabrication of Hybrid Devices with GaAs Photonic Elements

Chapter 4 presents experiments on GaAs/$LiNbO_3$ as a platform for integrated quantum photonic applications. Initial tests were performed with simple devices to assess the feasibility of the technology. The main challenge revolves around the reliable transfer of a GaAs membrane onto the $LiNbO_3$ carrier substrate. The main established techniques for such a transfer are wafer bonding and epitaxial lift-off (ELO). We employed the latter, observing remarkably good adhesion even without the presence of a promoting metal layer, which is commonly used for this process.

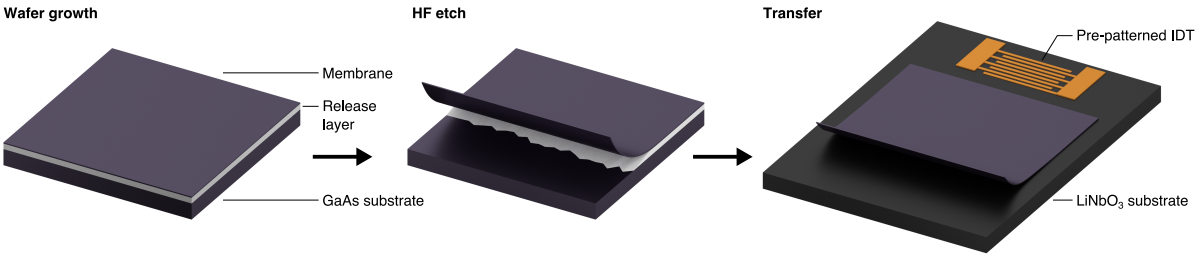

Fig. 2.10: Epitaxial lift-off schematic. The grown membrane can be underetched in HF (10 %). The transfer is performed by melting wax (M&I Materials) on top of the membrane prior to the underetch (not shown). The wax preserves the shape of the membrane after it is separated from the substrate. The membrane can then be placed between pre-patterned IDTs on a $LiNbO_3$ substrate and the wax is removed in a solvent.

The ELO process involves wafer growth to include a sacrificial AlAs layer, which can be completely etched post-growth to release the GaAs membrane grown above it, as depicted in Fig.2.10. This membrane is then transferred without flipping. That is, the growth order is preserved after transfer. In the tests performed, membranes with sizes of approximately $3 \times 3\,\mathrm{mm}^2$ were manually placed onto $LiNbO_3$ chips. Drying on a hotplate at 40 °C for > 4 h is sufficient to effectively bond the membrane to the new substrate. The membrane can then be etched by ICP into photonic elements. For this step we use a negative e-beam resist: ma-N 2403.

2.2.7 Device Packaging

A custom sample holder was designed to allow electrical access to the investigated devices within the cryostat. All but one of the samples used for this work required at least rf connections to the acoustic transducers. Figure 2.11 shows a schematic of the holder. The sample is glued with silver paint onto a printed circuit board (PCB). The board material is not standard FR4 but a ceramic with high dielectric constant for rf applications (RO4003C – Rogers Corp.). Its dimensions are such that it can be screwed tightly into the sample positioners (AttoCube). The layout of the PCB is flexible. For each rf connection a coplanar waveguide is milled and a miniature connector (U.FL – Hirose) is soldered onto it. The dimensions of the waveguide are estimated to be close to 50 Ω at 1 GHz and it is either tapered or stepped down to dimensions close to those of the pads on the sample. However, it should be noted that given the wavelength at 1 GHz is ~30 cm and the side length of the holder is 2.4 cm, the exact layout is not expected to have a great influence on reflections from impedance mismatch. Other sockets (preci-dip) are soldered onto the PCB for dc connections where needed. The PCB is coated with gold prior

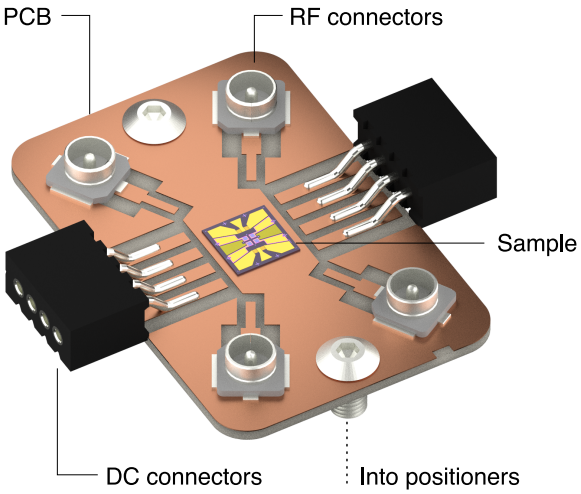

Fig. 2.11: Schematic of one of the sample holders used. Wire-bonds from the sample to the connectors are not shown. The PCB base plate is $24 \times 16\,\mathrm{mm}^2$.

to milling to allow for stable wire/ribbon bonding to the sample. The profile of the holder is restricted vertically by the working distance of the lens (2.5 mm).

2.3 Cryogenic System

All measurements on QDs are performed in a He gas cryostat able to reach temperatures down to 5 K*. This is necessary as InAs QDs do not have good optical properties at room temperature primarily due to coupling to optical phonons and escape of charge carriers due to thermal energy. The highest temperatures used for experiments in this work is ~30 K, which can be reached with a resistive heater located under the sample holder. The cryostat has optical and electrical access and the possibility of generating a magnetic field with superconducting coils up to 9 T. The system is schematically shown in Fig.2.12.

Electrical access to cryogenic spaces is a known problem given the thermal conductivity of the cables. DC access cables are thermally anchored along the thermal stages of the cryostat. For rf cables, the inner conductor is shielded and thermal anchoring is less effective. Two types of rf access arrangements were used. The first is a direct connection of U.FL cables from the sample holder to the cryostat flange. This is a 1 m long cable with 810 µm diameter†. The base temperature is not significantly increased with the addition of this cabling. The trade-off is they are lossy, with 6.52 dB m^{-1} attenuation at 3 GHz. The second solution is the use of a semi-rigid stainless steel SMA cable (R2 – Amphenol) from the flange to the sample holder (1 m), with

*Save for wafer characterisation PL measurements, which were performed on a cold-finger He flow cryostat.

†Thicker cable assemblies with the same connector are available. The next one is 1.32 mm in diameter. The thicker wire decreases losses but increases the base temperature. The main issue however is that the thicker cable is much more rigid and can impede the movement of the positioners.

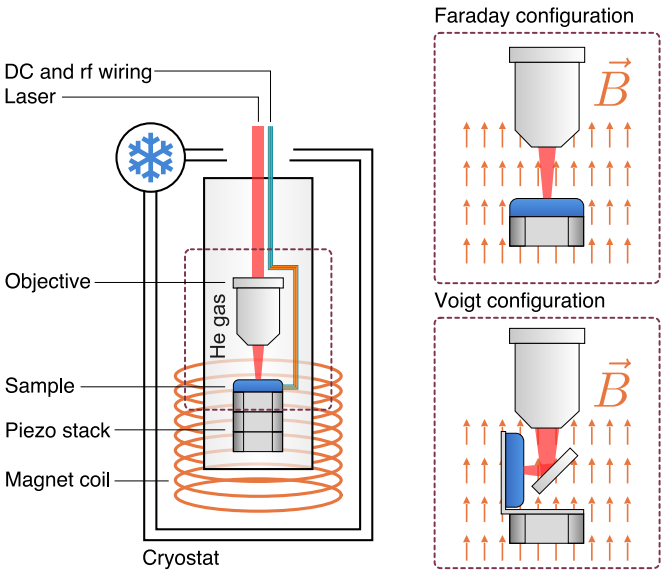

Fig. 2.12: Schematic of the cryostat. The inner chamber is filled with low pressure He gas. It is enclosed within a closed-cycle He flow chamber where the magnetic coil is housed. An external heat exchanger cools down the He, allowing for long term operation. The sample is mounted on slip-stick (AttoCube) and piezoelectric positioners. A heater (not shown) is also included in the stack. The direction of the magnetic field is fixed so to change configuration the sample position must be adjusted. Voigt configuration can be easily attained using a 90° plate and a mirror.

the final connection to the sample via a short U.FL cable. This lowers losses at the expense of a 3 K increase in base temperature.

2.4 Micro-Photoluminescence Spectroscopy

Photoluminescence (PL) is a standard measurement of the emission spectrum of a sample resulting from optical excitation. In the case of measurements on QDs it is often referred to as micro PL, or µPL, given that it is inherently spatially resolving and the focal spot is usually a few µm in diameter. PL measurements are generally straightforward, as the only requirement is to collect the light emitted from the sample and send it to a spectrometer. Figure 2.13 shows the general experimental arrangement used. The essence of the technique is to excite charge carriers by an above-band energy laser and collect the light emitted from their recombination. This exhibits the transitions within a QD, as well as the GaAs matrix and the wetting layer. In this work most µPL measurements are performed using an 850 nm laser, which can be operated in either pulsed or cw mode. The InAs wetting layer lies around 870 nm, meaning that charges are generated effectively in this region.

The resolution and efficiency of the spectrometer are determined by the grating used to diffract the light into the pixels of the CCD camera. They are naturally inversely related. The spectrometer used in this work has two gratings, with 1200 and 1800 grooves/mm. This translates to a maximal resolution of 0.016 nm.

PL measurements are used to characterize newly grown wafers, determining the density of dots and finding out where their emission lines are on the energy spectrum. Determining the dot density is particularly important when one is interested in looking at a single emitter, in

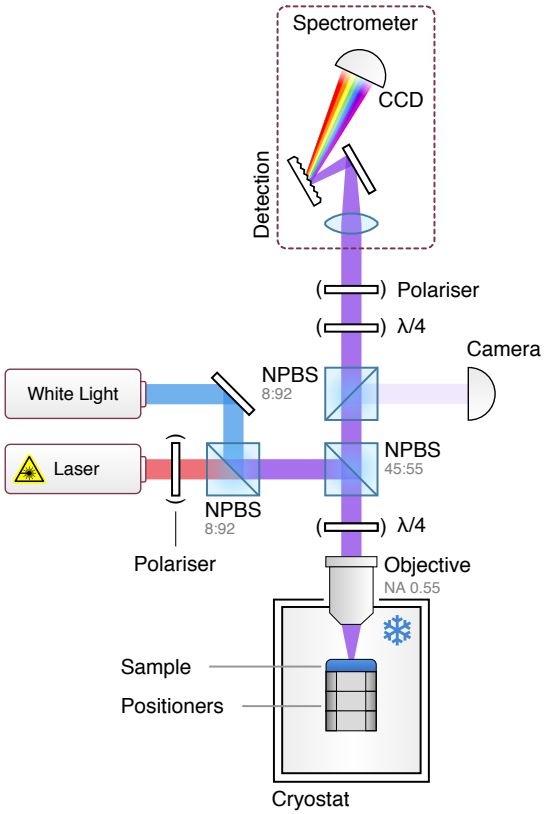

Fig. 2.13: Confocal microscope arrangement for μPL measurements. The sample can be navigated by moving the positioners on which it sits, while monitoring the image on the camera when the white light source is turned on. Polarisers and $\lambda/4$ plates are optional depending on the particular measurement being carried out. The objective before the sample is completely within the cryostat and optical access is provided by a window.

which case a low density is desired to avoid having multiple dots inside the focal spot. In some cases where the density is high enough for this to happen with high probability one can still get around the problem by patterning the material into nanostructures, thereby removing dots, or by using a metal mask with holes serving as apertures that filter the collected light to a single dot. Another useful use of the space resolving nature of μPL is to check the emission for signatures like the WL at 870 nm. This can for example determine whether a particular region of a sample has been etched past the WL.

2.5 Resonance Fluorescence

From the technical point of view resonance fluorescence is a special case of PL. As mentioned in Sec.1.2.4, the additional challenge it poses is that the light coming from the sample to be investigated coincides in energy with the excitation light and has to be filtered to a degree where it does not contribute significantly to the measurement. To reiterate, the two main ways to achieve this are either geometrically[67] or through polarisation rejection[16]. In the former case the excitation and collection light paths are separated, unlike in Fig.2.13. If the laser light is directed at the sample from the side, it can be guided along the sample by total

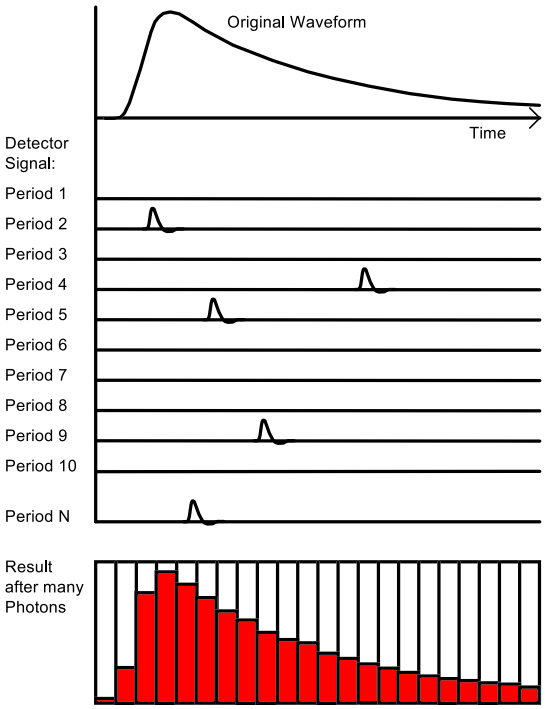

Fig. 2.14: Principle of time-correlated single-photon counting. The time axis is binned and the results from multiple repetitions are added up, yielding a histogram that matches the original curve. From Ref.[195].

internal reflection and reach the QDs. The only contribution to the collected signal will be from spurious reflections. The second approach uses the polarising optics included in Fig.2.13. The polariser at the input and collection arms are set to be orthogonal to each other. This cross-polarisation rejection can suppress the contribution of laser light by orders of magnitude. Signal to background ratios in excess of 10^4 : 1 are attainable with commercially available polarisers[194]. The flip side is that the collected light is also going through the polariser so one must be clear what transition one is looking at and set the global angle accordingly. It is worth noting that, when looking at pillar microcavities, the pair of polarisers is not enough to reach an acceptable extinction ratio. The reason is that GaAs has a finite birefringence that becomes significant when accumulated over multiple reflections inside the pillar. The laser light acquires a phase difference that rotates its polarisation. Therefore, a $\lambda/4$ waveplate is needed before the collection polariser to restore the linearity of the excitation polarisation.

2.6 Time-Resolved Spectroscopy

For studies on dynamic processes within the QD it is necessary to resolve measurements in time. The HBT and HOM setups described in Ch.1 are examples of such measurements. The basic idea behind time-resolved single-photon measurements is explained in Fig.2.14. Multiple measurements of single-photon events are discretised in time and collected to form a histogram. After several repetitions the histogram takes the shape of the investigated curve. The time-axis

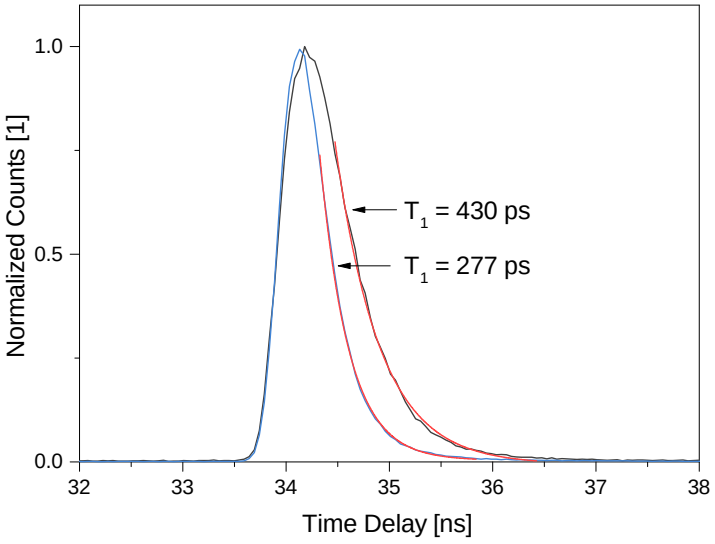

Fig. 2.15: Example of typical time-resolved measurement of the decay of a transition in a single QD. The faster decaying curve is measured on resonance with an optical cavity, exhibiting a Purcell enhancement. The slower curve is only partially resonant.

discretisation is achieved with electronic memory blocks populated by the signal after passing through a time-to-amplitude converter (TAC) and an analog-to-digital converter (ADC). The start and stop signals for the TAC have to be adjusted depending on the experiment. In an HBT measurement both start and stop signals come from photon-detection events at two APDs. For a lifetime measurement the sample is excited with a pulsed laser. In this case the sync pulse from the laser pulse controller is used as the stop signal and the firing APD as the start. This is known as the reverse start-stop operation mode. Its advantage over the more intuitive start-stop mode is that the TAC only needs to operate at the photon detection rate, rather than the laser pulse repetition rate, which is often faster than the time needed by the TAC and ADC between measurements (dead time)[196]. Figure 2.15 shows an example of decay-time measurements on a single QD. The lifetime T_1 is inferred from an exponential decay fit to the tail of the curve.

The timing resolution of the measurement is determined by the response of the electronics and the detectors. It is important to note that any measured data consists of the investigated curve convoluted with the instrument response function. The APDs used in our laboratory have a time resolution of ~250 ps and a dark-count rate < 100 Hz.

2.6.1 Photon Time-Tagging

Time resolved spectroscopy reveals the temporal properties of an event, but only as an ensemble average. There are cases where this is insufficient if one is interested in looking at correlations between specific events and their temporal vicinity. In this work this is the case in Ch.6. In such instances, it is necessary to record each single-photon detection event within the global runtime of an experiment. This is naturally more data-intensive both for recording and processing. The technique is known as photon time-tagging, as each detected photon is tagged with metadata

including the detector on which it was found, the time from the last sync pulse and the global time. Figure 2.16 illustrates the operation principle using PicoQuant's nomenclature. This assumes the experiment is running on a stable clock which provides the sync signal, such as the repetition rate of a laser as in lifetime measurements.

A natural problem is that, as in histogramming, the dead time of the photon counting module precludes continuous measurements at the high rates typically found in laser excitation sources of 80 MHz. This can be circumvented by applying a frequency divider directly at the sync input, which can be reversed at the data-analysis step[196]. In addition, the counting module can be operated in the equivalent of reverse mode in histogramming, by only storing the photon events, rather than each sync event. The sync pulses can simply be counted and the macro-time τ_{macro} is trivially retrieved due to the sync periodicity.

2.7 Acoustic Transducer Characterization

The standard way to test IDTs is to measure the scattering or S-parameters. This is a common measurement in telecommunications and can be performed trivially with a network analyser, as presented in Fig.2.17. The analyser has two ports and measures the reflection r_i and transmission t_i from each one. The former is characterized by S_{11} and S_{22}, while the latter is expressed in S_{12} and S_{21}. These S-parameters are usually given in dB, defined as

$$\begin{aligned} S_{11} &= 20\log_{10}\left(\frac{r_1}{t_1}\right) \\ S_{21} &= 20\log_{10}\left(\frac{t_2}{t_1}\right). \end{aligned} \tag{2.1}$$

In order to measure the transmission, it is necessary for the device to have an acoustic delay line. That is, two opposing transducers, so that the rf signal can be converted to a SAW, propagate along the chip, and be converted back to an electrical signal at the opposite end. In this case the relation $S_{12} = S_{21}$ holds. Figure 2.17B shows an exemplary measurement of a delay line

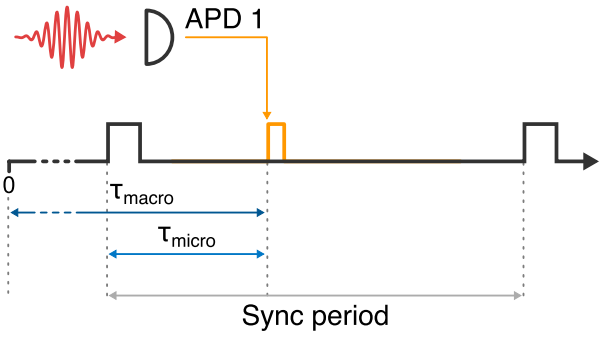

Fig. 2.16: Illustration of the principle of photon time-tagging. Each photon detection event is saved with its corresponding detector id, sync pulse number and micro-time τ_{micro}. The macro-time τ_{macro} can be recovered from the sync number and the known sync period.

on GaAs. The dip in the S_{11} measurement corresponds to the resonance frequency of the transducer, where less power is reflected into port 1 since it is converted into acoustic power. For IDTs on GaAs at room temperature, the resonance dip is typically up to ~1 dB in depth. At the same time, S_{21} follows a typical sinc profile centred around the resonance frequency[143]. The maximum value is known as the insertion loss (IL) of the device. Away from the resonance the background level amounts to the electromagnetic coupling between the IDTs, which can act as an antenna. The high-frequency ripples seen on the side lobes originate from this cross-talk.

As mentioned in Ch.1, the metal of the IDT fingers changes the speed of sound at the interface. This mass-loading effect can lead to reflections and can also considerably shift the resonance frequency. Figure 2.18 shows a comparison of single-finger IDTs on GaAs for Au and Al metallization made from a single chip cleaved only directly before metal evaporation. Al is much lighter than Au and therefore induces a smaller shift of the resonant frequency.

2.8 Finite Element Numerical Simulations

Simulations were used primarily in the design stage for the devices presented in this work. In particular, numerical simulations based on the finite-element method (FEM) were used for optics and mechanics problems. The idea behind such methods is to approximate a global

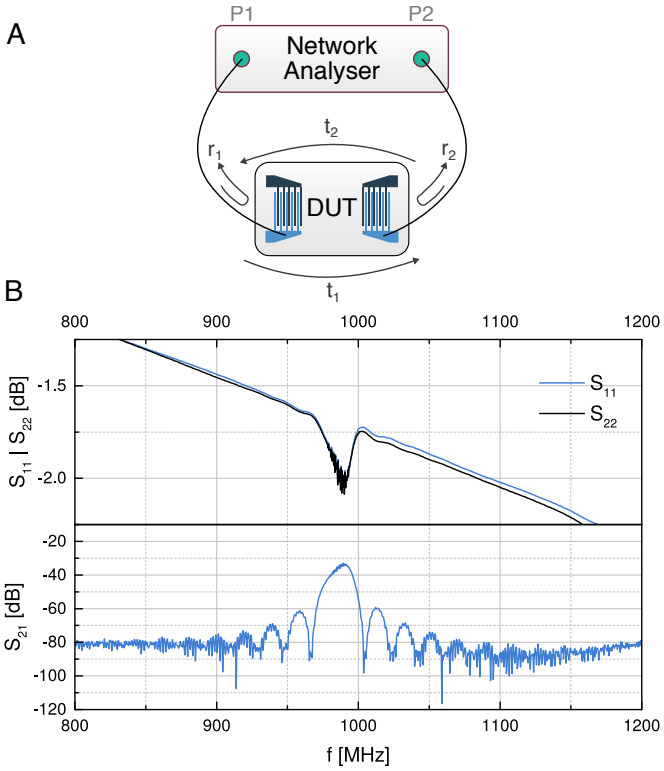

Fig. 2.17: **A.** Schematic of S-parameter measurement with a network analyser. DUT: device under test. **B.** Example measurement of S-parameters on an IDT delay line on GaAs for an 800 MHz transducer.

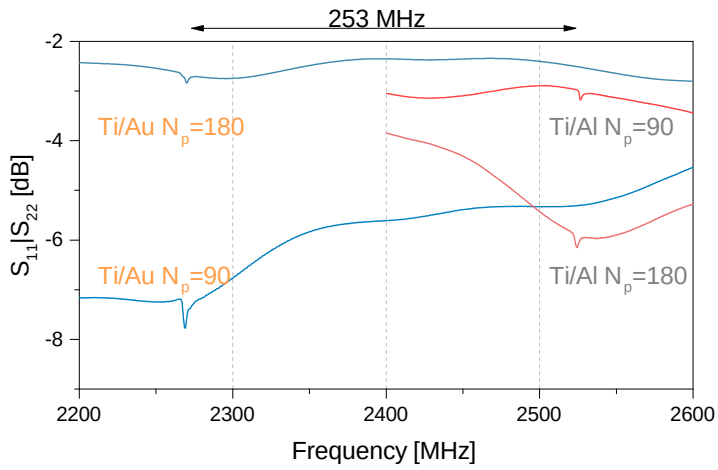

Fig. 2.18: S-parameter measurements for four distinct transducers with different numbers of finger pairs N_p and Ti/Au or Ti/Al metallisation. The resonance frequency is shifted by 250 MHz by the metallisation.

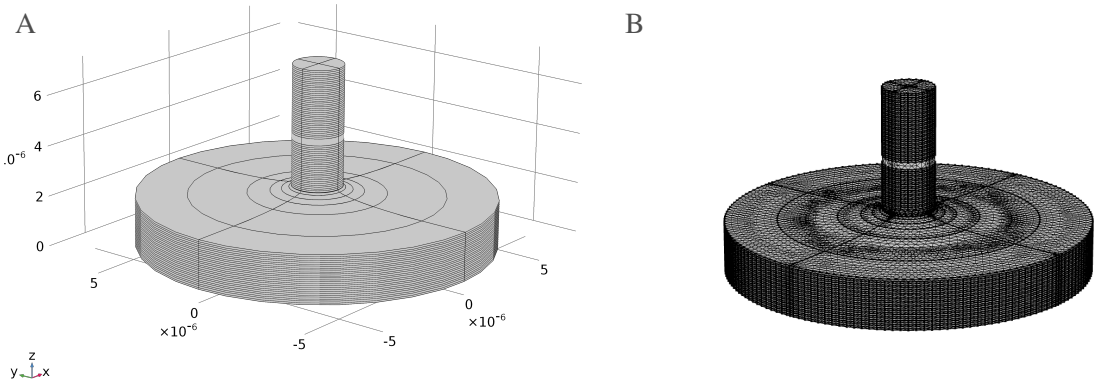

Fig. 2.19: **A.** Simulation domain for a pillar microcavity in 3D. **B.** Meshing of the domain. In reality, only one quarter of the model needs to be solved, due to the symmetry of the problem.

solution to partial differential equations (e.g. a wave equation) over a given simulation domain by discretizing the domain and combining the local solutions. In-depth treatments can be found in Refs.[197, 198]. For the work carried out here we use the commercial software COMSOL. As an example, take the micropillar cavity shown in Fig.2.19A. This represents the simulation domain, which is discretized into smaller elements with the appropriate properties, such as the refractive index in this case. This results in a mesh of the domain, as presented in Fig.2.19B. Generally speaking, the accuracy of the global solution improves with decreasing mesh element size, at the cost of computational time and memory. For optical problems it is necessary to resolve the optical wavelength studied, having at least three discrete elements per wavelength. The wave equation is solved at each node and a polynomial interpolation is used between nodes, with the requirement of continuity across adjacent element boundaries. The meshing is therefore one of the most critical steps in such simulations.

Another important configuration is the definition of boundary conditions. Boundary conditions can be used to exploit symmetry and reduce the computational cost of a model.

For example, the pillar model shown in Fig.2.19 can be solved completely by simulating only a quarter of the domain. Boundary conditions are also responsible for the accuracy of the results. For electromagnetic problems a common issue is unwanted reflections at the outer boundaries, which distort the characterization of the simulated component. These reflections can be alleviated with scattering boundary conditions. Even better performance is achieved by surrounding the complete simulation domain with a "shell" where incoming electromagnetic fields are heavily absorbed, immitating the ideal condition of the studied device being in an infinite free-space. The layers around the modeling domain are known as perfectly matched layers[199].

Chapter 3

Acoustic Modulation of a Quantum Dot in a Pillar Microcavity

This chapter focuses on individual quantum dots embedded in pillar microcavities. We show that the dynamic tuning of the trion emission energy due to a passing acoustic wave can be used as an accurate timing mechanism for single-photon generation. The main results have been published in Ref.[17] and are expanded upon here.

3.1 Introduction

Single-photon sources (SPS) are a key component in emerging quantum technologies and thus constitute an extremely active area of research[15, 50, 200, 201]. In principle any two-level system is a quantum emitter that only allows for one photon to be emitted after an excitation cycle. The first demonstration of the signature antibunching of the autocorrelation of single-photons was published from studies on sodium atoms in 1977[202]. Further confirmation followed with other systems such as other atoms[203], individual ions[204] and molecules[205], and in particular solid-state sources such as nitrogen-vacancy (NV) centers in diamond[206, 207] and epitaxially grown QDs[95, 208–210]. Although many systems are single-photon emitters by nature, their practical use has been limited mostly due to inefficiencies in the photon extraction, instabilities, or experimental complexity.

Generally speaking, for an SPS to be of interest for applications it must satisfy various criteria[211]. First, the photons must be of high purity and ideally mutually indistinguishable. Second, the source must be efficient and able to operate at high repetition rates*. Third, the operation should be on-demand. Fulfilling all of these qualities simultaneously has proven challenging and is the subject of continuous research. Presently, the available SPS are not developed enough for widespread use. For example, current QKD applications use weak laser pulses instead of true single-photon sources. Attenuated laser pulses show a Poissonian distribution that can compromise the theoretical security of the communication, but have the advantage of high count rates.

Single QDs are one of the most technologically advanced candidates for the realization of a practical SPS. A major area of study has been the engineering of microfabricated photonic structures around the dots to increase the efficiency with which photons are collected[212]. Most promising are those cavities which both enhance the emission rate, and funnel photons into a Gaussian mode that can be efficiently collected. Nanowire antennae can achieve the highest collection efficiencies[98] but display no Purcell enhancement. Conversely, photonic crystals can obtain the highest Purcell enhancements but only by suppressing the easy-to-collect vertical emission[213]. In contrast pillar microcavities can achieve state-of-the-art performance in both

*_Brightness_, which includes the system emission rate and collection efficiency at the first lens, is commonly used as a figure of merit.

metrics. Recently, there has been renewed interest in these cavities as it has been shown that, in conjunction with resonant excitation, they can act as photon sources with unprecedented efficiency, purity and indistinguishability[16, 86, 94, 112].

In addition to engineering the photonic density of states it is also possible to modify the phonon environment of a dot through phononic engineering[163] or by driving the sample with a sound wave. A SAW excited on the surface of a piezoelectric semiconductor can change the separation of the energy levels in the dot as the lattice is stretched and compressed (see Sec.1.4.5). The idea of using a SAW as a clock for timed single-photon emission was first formally proposed in Ref.[161], as outlined in Fig.3.1. Their idea exploits the ability of the electric field modulation by a surface acoustic wave to transport electrons and holes within a 2D electron gas. This provides a convenient "conveyer belt" of single electrons. Wiele *et. al.* realized that this could be used to feed carriers into a QD to give rise to regulated photon emission[161]. Since then, this idea has been experimentally demonstrated[180, 214] and adapted[215–217]. A key feature is that the photon emission inherits the SAW frequency and intrinsically high repetition rates become possible, given that SAWs can span frequencies of MHz to tens of GHz[175, 218–220]. These are difficult to realize with alternate approaches, although some electrically driven sources with repetition rates from tens of MHz to 2 GHz have been reported[221–226].

Here we show that it is possible to modulate the energy levels of a QD inside a pillar microcavity with a SAW. The principle behind the device proposed here is similar to the highlighted literature but relies on type I modulation instead of type II. Most reports on SAW-modulated quantum structures to date are limited to samples without Purcell effect[180, 227, 228]. Although there is a recent report of SAW modulated emission from a photonic crystal cavity[229], the combination of SAWs on pillar microcavities has clear advantages and are not yet investigated.

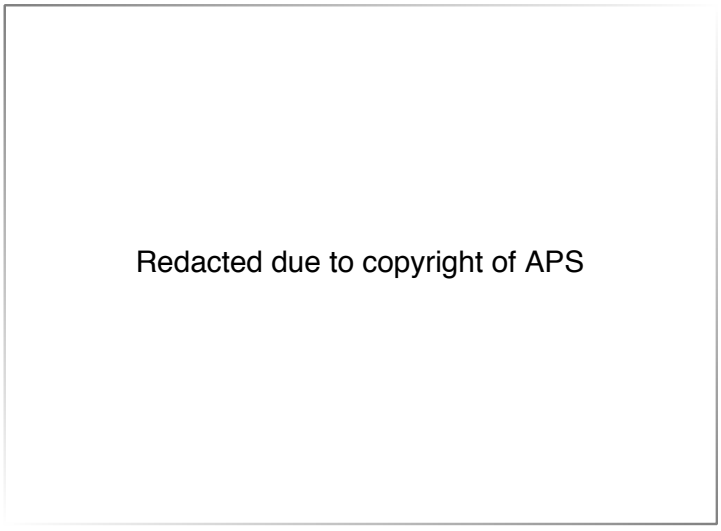

Fig. 3.1: SAW driven SPS. Carriers are excited in the quantum well by a laser and are subsequently separated and transported by the SAW potential. Upon reaching the QD they are trapped and can recombine radiatively. From Ref.[161].

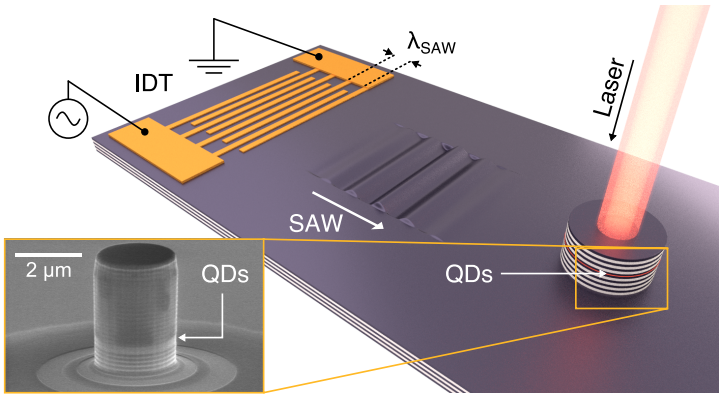

Fig. 3.2: Schematic sample design. The device consists of an interdigitated transducer (IDT) and an optical cavity in the path of the SAW. QDs in the cavity are excited optically. Inset: scanning electron micrograph of a pillar microcavity partially etched through the bottom mirror.

We perform resonant excitation of this system, to create a stream of single-photons at a rate defined by the SAW. Importantly, the cavity mode retains the ability to enhance the emission of the dot and is not modulated by the SAW.

3.2 Device Design

The sample used in these experiments is fabricated from a planar cavity consisting of 18 and 28 repeats of $\lambda/4$ thick alternating GaAs/AlGaAs layers for the top and bottom DBRs, respectively*. The dots are grown in a λ thick GaAs spacer in-between the DBRs and emit light around 880 nm. The cavity is etched into pillars of ~2.1 µm diameter with Q factors around 3000 as described in Ch.2. A single-finger Ti/Au interdigitated transducer is deposited on the etched surface to generate a SAW through the piezoelectric effect. In this simple design, each finger alternates in voltage and is $\lambda_{SAW}/4$ wide. The transducer is designed to excite a SAW in GaAs a frequency $f_{SAW} \sim 1$ GHz. The sample is schematically depicted in Fig.3.2.

An important consideration is the optimal etch depths for the phononic and photonic aspects of the device. These do not coincide and need to be balanced. Because the SAW is confined to within one acoustic wavelength normal to the surface, the planar cavity should ideally only be etched close to the QD growth plane to achieve maximal strain tuning. However, this would compromise the cavity mode confinement and lower the Q factor compared to a pillar that is etched completely through the bottom mirror. FEM simulations corroborate this intuitive picture, as illustrated in Fig.3.3. Both the Q factor and the mode confinement converge quickly towards their achievable limits with increasing etch depth past the cavity region. Thus, it is only necessary to etch the first few periods into the bottom DBR to get a cavity enhancement, while keeping the QD growth plane in range of the SAW. The measurements presented here were performed on a device etched seven periods into the DBR.

*The Cavendish wafer number is W0704.

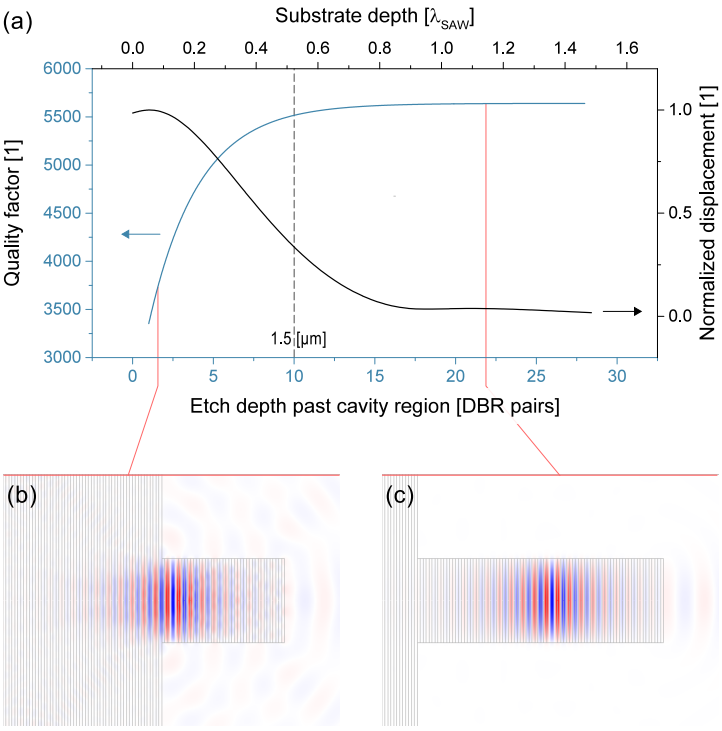

Fig. 3.3: FEM simulations. **A.** Extracted Q factors of pillar microcavities etched a fixed number of DBR pairs past the cavity region (bottom left) and substrate displacement for a 1 GHz SAW on GaAs (top right). The Q factors are calculated by FEM, whereas the displacement curve is the analytical solution for a SAW. Ten DBR periods corespond to 1.5 µm in this device. **B, C.** Out-of-plane electric field component of the cavity mode at selected etch depths (1, 22 DBR pairs, respectively).

In addition, the inherently random positioning of the QDs means the possibility of finding a dot within a cavity relies on statistics. We therefore aim to place as many pillars as possible in the path of the SAW. The IDT uses a coplanar waveguide design as presented in Fig.3.4. This is equivalent to two IDTs sharing a common signal pad, thereby doubling the area covered at the expense of acoustic energy density. The coplanar design is convenient to avoid additional rf connections to the sample, which increase the base temperature. We note that the top and bottom IDTs do not necessarily have to be identical and it is possible to test different IDT designs simultaneously, as the fingers for each one can be designed independently. Since these are fabricated by e-beam lithography their design is flexible from sample to sample*. The sample mask then consists of two acoustic paths and two pillar fields. Each field contains 256 pillars, providing enough devices to find a suitable QD with high probability. The acoustic aperture of the IDTs is 165 µm.

3.3 SAW Modulation of QD Lines

SAWs generated on a DBR are weaker compared to those on pure GaAs due to the mismatching speed of sound in the alternating layers. Comparing samples with delay lines on epitaxial GaAs

*For example, with the more sophisticated Si shadow mask discussed in Ch.2, it is possible to bring the IDTs closer to the pillars.

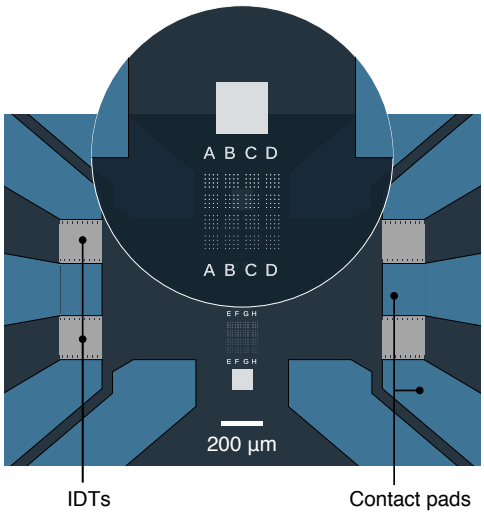

Fig. 3.4: Mask design for the first generation of SPS devices. The circled region is a magnification of the top pillar field. The square is $100 \times 100\,\mu m^2$. It also is unetched and serves for alignment purposes and location of the cavity mode.

and on a DBR with etched pillars shows a dramatic effect, as presented in Fig.3.5. The two samples have nominally the same IDTs in design and metallisation (7 nm Ti and 10 nm Au). The number of finger pairs is $N_p = 51$. For the DBR sample the SAW frequency is blue shifted due to the higher speed of sound in AlAs, which means the effective speed is also higher (c.f. Tab.1.1). FEM simulations of the unit cell of a SAW on a DBR and pure GaAs show a frequency shift of 69.3 MHz, in agreement with the observed shift of ~79 MHz in these two samples. Besides the frequency shift, the increased insertion loss is an unavoidable consequence of the DBR surface. As will be shown below, data on the SAW effect on QD modulation suggests there is little contribution from scattering on the pillars to this transmission loss. Therefore, the DBR is the main source of loss. In future this could be mitigated by using a stronger piezoelectric layer such as ZnO before IDT deposition*[230].

We now examine the modulation of QD transitions by the SAW. As outlined in Ch.1, a sinusoidal mechanical wave induces a corresponding change in central emission energy

$$E_0(t) = E_0 + \chi \sin(\omega_{SAW} t), \tag{3.1}$$

which is equivalent to a change in central wavelength

$$\lambda_0(t) = \lambda_0 + \frac{\chi \lambda_0}{\chi \sin(\omega_{SAW} t) + \lambda_0} \sin(\omega_{SAW} t) \approx \lambda_0 + \chi \sin(\omega_{SAW} t). \tag{3.2}$$

Averaged over time, this process gives rise to a two-lobe intensity profile, with the maxima at the modulation edges and a net broadening of the line shape. Figure 3.6 shows the typical double peaked features observed in the spectrum as a 1 GHz SAW traverses the pillar field.

*ZnO deposition was tested on an optically defined IDT. The conclusion is that ZnO on top of the IDT does not enhance SAW generation. As detailed in Ref.[230], depositing ZnO *before* the IDT does improve performance.

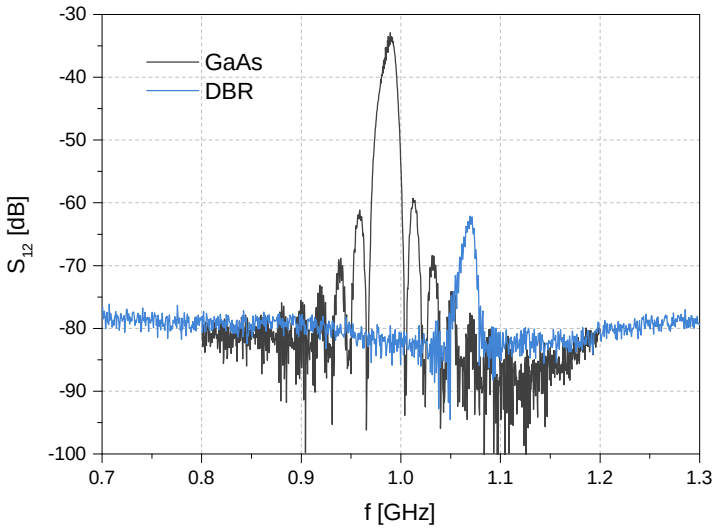

Fig. 3.5: Measured S-parameter transmission through an acoustic delay line for a sample on pure epitaxial GaAs and a sample with pillars, where the IDTs lie on the remaining bottom DBR.

The spectra show an increase in splitting with increasing acoustic power. On close inspection one can also see that the centre of the line shifts to higher wavelengths as the SAW power is increased above 20 dBm. This is due to heating of the sample. The magnitude of the heating varies with sample but is usually on the order of 4 K at 25 dBm. We note that the signal is noisy due to low intensity. The reason is that these transitions are measured outside the cavity mode to exclude any possible additional effect. Hence, they are effectively reflected by the DBRs and most of the recorded signal is likely to stem from losses at the pillar sidewalls. Each curve is fitted with the convolution of a Lorentzian (from a fit to the SAW-free spectrum) and the energy modulation, following equation (1.41). This allows the extraction of the splitting amplitude A. Figure 3.7 shows this parameter vs SAW power for various dots along the center of the pillar field in the SAW propagation direction. Intuitively we expect the regular array of pillars to damp the SAW as it propagates. For the dimensions of these devices and the acoustic wavelength this proves to be an erroneous assumption. The amplitude of the peak splitting, which is a direct measurement of the acoustic displacement at the position of the dot, does not decrease as the SAW propagates through the field. Instead we see a comparable splitting throughout the field and even higher splitting on the opposite end. On a single dot, there is no measurable difference in the SAW splitting when exciting from the left or from the right. We can therefore conclude that the effects of the SAW are approximately uniform in a pillar array and therefore their simultaneous action on a dot-pillar array could be exploited. We expect this to be heavily dependent on the acoustic wavelength, with the pillars having a more pronounced effect at higher frequencies.

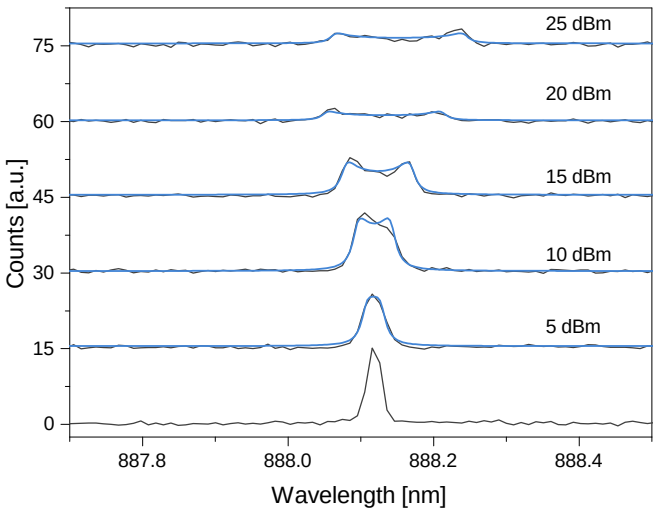

Fig. 3.6: Time-averaged modulation of a QD spectral line under cw 660 nm laser light excitation and cw SAW excitation with varying applied SAW powers. Curves are shifted for clarity. The bottom spectrum is unperturbed by a SAW.

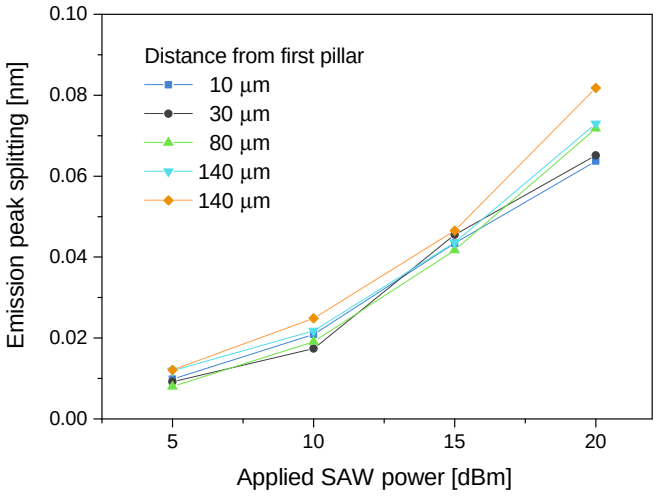

Fig. 3.7: Modulation amplitude parameter χ extracted from fits to the emission of different dots vs. applied SAW power.

3.4 Single Photon Emission from the Modulated System

We now discuss the effect of a SAW on a dot resonant with the cavity. We focus on a charged transition, which is brought close to resonance with the cavity by means of temperature tuning. At 26 K the two are overlapping but not completely resonant, as shown in Fig.3.8. The addition of a SAW to the system completes the resonance tuning through the strain induced modulation. Although the effect is small due to the relatively broad cavity, the high-energy end of the modulation is consistently brighter than the low-energy side. Importantly, we do not observe any signs of cavity modulation by the SAW. When sending the collected emission through a monochromating grating, a small SAW-induced tuning suffices to periodically move the central wavelength in and out of the corresponding detection window.

We now describe resonance fluorescence measurements on this system. As in the previous chapter, a low-power non-resonant laser contribution is added to stabilize the charge environment

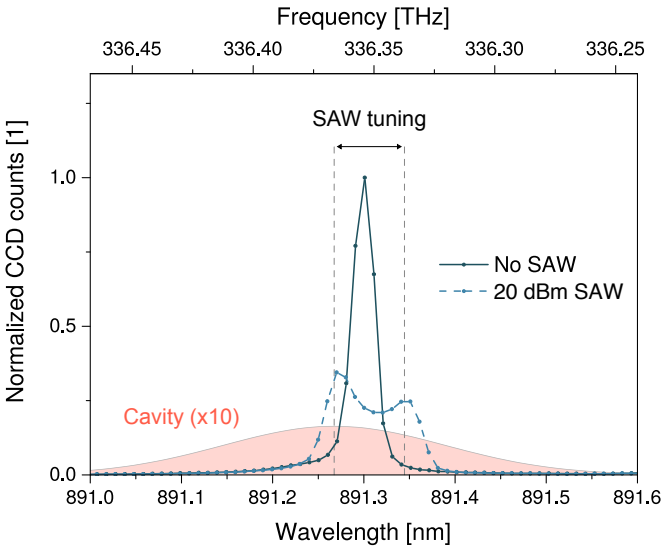

Fig. 3.8: Spectrum of a non-resonantly excited quantum dot in a pillar microcavity with and without the presence of a SAW at 26 K. The cavity spectrum inferred from a white-light measurement is highlighted.

and introduce the necessary charge in the dot. Since the transition energy is constantly changing due to the SAW while the cavity remains fixed, the resonance condition for optical excitation is only met at certain points during the SAW cycle. This phase is controlled by the detuning between the unperturbed transition and the laser as well as the SAW amplitude. For our experiments the resonant excitation is set to happen at one of the modulation extrema, coinciding with the spectral region filtered by the grating. We use the arrangement outlined in Fig.3.9 to achieve accurate tuning of the SAW modulation. An APD and a single-photon counting card are used to record arrival times of photons relative to the SAW. The rf input to the IDTs consists of Gaussian pulses (FWHM 250 ps) from a pulse generator, whose output is amplified (25 dB gain, 26 dBm saturation), and triggers the single-photon counting module. The collected light is sent through a grating to remove any non-resonant light, while the resonant laser contribution is suppressed by cross-polarisation filtering. Figure 3.10 schematically shows the principle and a series of recorded histograms for increasing SAW amplitude. When the tuning by the SAW is lower than the deliberate detuning of the transition no light reaches the detector, resulting in a flat curve. As the SAW amplitude increases, so does the overlap of the transition with the laser and grating window and a periodic signal starts to appear. Further increment of the tuning range results in the transition crossing this resonance point twice per period and a second peak becomes visible in the trace. We thus set the amplitude such that only one peak is clearly visible in the time-resolved measurement, which corresponds to an optimal input power of 15 dBm.

In order to prove single-photon emission, the arrangement from Fig.3.9 is modified to include a Hanbury-Brown and Twiss interferometer after the grating. Measurements of the second-order autocorrelation function $g^{(2)}(\tau)$ were carried out under resonant, continuous-wave (cw) optical excitation (16 nW laser power) with a small amount (4 nW) of non-resonant 660 nm

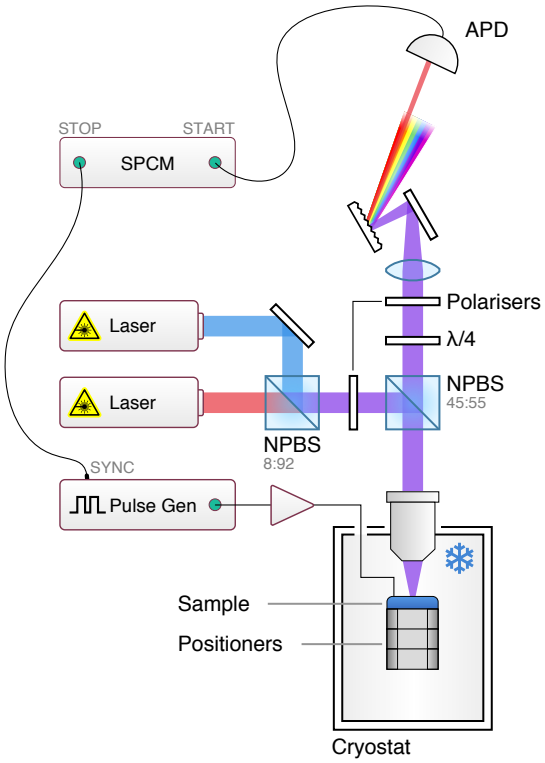

Fig. 3.9: Experimental arrangement for time-resolved measurement of the SAW tuning. The IDTs are driven by Gaussian pulses from a pulse generator, whose sync signal acts as the stop trigger on the photon-counting electronics. The start pulse is given by a photon detection event on the energy defined by the monchromating grating. The rf input for the IDTs goes through an amplifier (SHF 826H) before the cryostat. SPCM: single-photon counting module, APD: avalanche photodiode, NPBS: non-polarizing beam splitter.

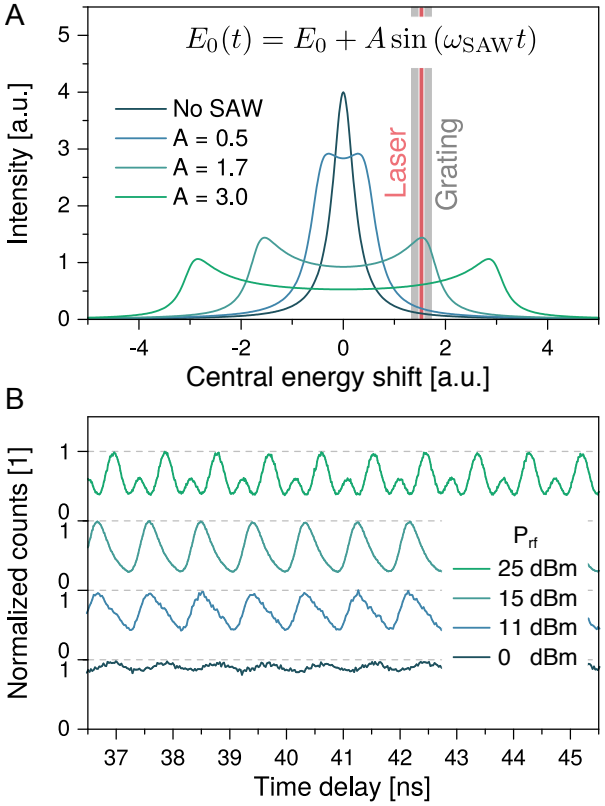

Fig. 3.10: Time-resolved measurement of the SAW tuning. **A.** Illustration of the time-averaged spectra for a sinusoidally tuned Lorentzian line as a function of the tuning parameter A, as defined in the inset. The position of the detuned excitation laser and the grating window is marked. **B.** Time-resolved measurement of the modulation for increasing applied voltage on the input transducer and thus increasing SAW modulation. The curves are offset for clarity. For low modulation amplitudes the transition is not shifted enough to compensate for the initial detuning. As the modulation increases the periodic driving with f_{SAW} becomes evident as photons start to be detected. With even stronger tuning the transition overlaps with the resonant laser and grating twice per period and a second peak becomes visible.

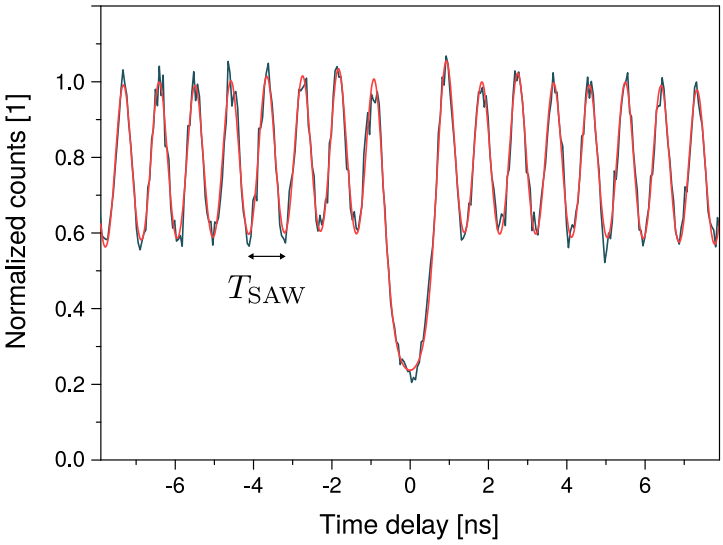

Fig. 3.11: Second-order autocorrelation measurement under cw resonant excitation. A continuous SAW is applied such that the blue extreme of the modulation overlaps with the laser and cavity. The pulsed curve reflects the SAW-modulation period and shows anti-bunching at zero delay. The red line is a cumulative Voigt peak fit with fixed width.

laser light. The SAW is also excited continuously, as heating is not an issue. The periodic filtering resulting from the effect of the SAW and the experimental setup gives rise to a pulsed signature in $g^{(2)}(\tau)$, as presented in Fig.3.11, where the spacing between pulses corresponds to the SAW period $T_{\mathrm{SAW}} = 0.92\,\mathrm{ns}$. The central peak is clearly suppressed, with $g^{(2)}(0) = 0.21$ measured in the raw data. It is evident that there is some overlap with the neighbouring peaks, so we can be confident that the actual multi-photon emission in a given pulse is lower. Indeed, a simple fit to the data as a series of overlapping Voigt functions with fixed width yields a curve in reasonable agreement with the measurement (red curve in Fig.3.11). An upper bound of $g^{(2)}(0) < 0.06$ can be extracted from the ratio of zero-delay peak area to average peak area at long time delays.

3.5 Resolved Sideband Regime

The simultaneous driving of the transition with a resonant laser and an acoustic field also enables strong phonon-assisted transitions[228]. By introducing a Fabry-Pérot etalon (free spectral range = 30 GHz, finesse $\mathcal{F} = 156$) between the monochromating grating and the detection APD, the corresponding sidebands can be resolved in our experiments. The high-resolution spectrometry arrangement is presented in Fig.3.12. Using this system we can measure spectral features with sub-natural linewidth. Each transition is broadened by the instrumental resolution δf_{FP}, resulting in a total linewidth equal to the sum of QD and etalon linewidths[231]

$$\delta f = \delta f_{\mathrm{QD}} + \delta f_{\mathrm{FP}}. \tag{3.3}$$

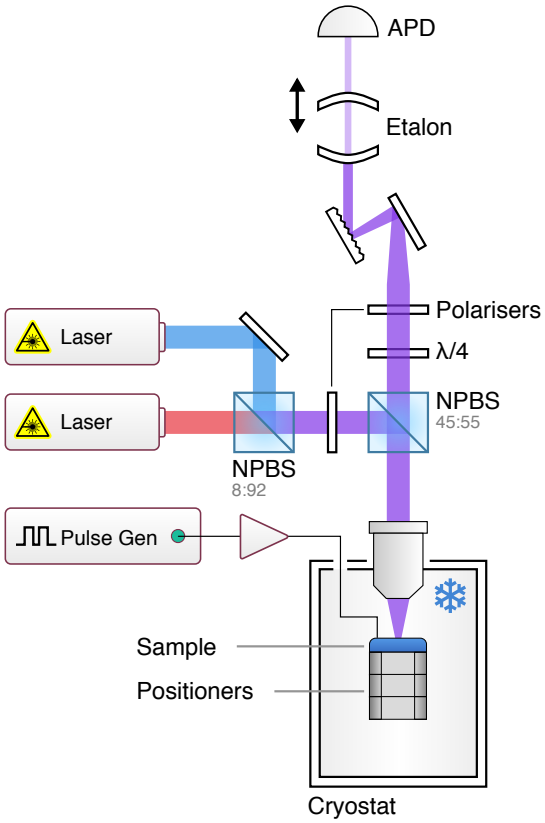

Fig. 3.12: Modified experimental arrangement for the high-resolution measurement of spectral lines. The length of the Fabry-Pérot etalon is controlled by a piezoelectric element. The spectral resolution of the system is $\delta f_{\mathrm{FP}} \approx 0.8\,\mu\mathrm{eV}$.

Fig.3.13A shows the spectrum resulting from scanning the etalon, while exciting the dot with the resonant (33.75 nW) and red (4 nW) lasers as well as a continuous SAW. In addition to the central carrier line, sidebands at integer multiples of the SAW frequency $f_{\mathrm{SAW}} = 1.08\,\mathrm{GHz}$ are clearly observed. We also note a strong asymmetry in the number of sidebands (> 5 red and 2 blue), which we attributed to the position of the laser relative to the transition energy. The reasoning is that as the central wavelength moves away from the laser, processes involving different numbers of phonons can contribute to the same sideband, as illustrated in the inset. We can reverse the asymmetry by detuning the laser from the blue side of the unperturbed transition to the red. Figures 3.13B and 3.13C show that the situation is indeed reversed, showing more blue sidebands for a red-detuned laser.

Neither the sideband positions nor their relative strengths are significantly affected by changes in the resonant laser power over an order of magnitude. The SAW power, on the other hand, determines the intensity ratio of carrier frequency to sidebands, with the higher SAW amplitude strengthening the sidebands. We note that we observe a high number of sidebands. Figure 3.14 shows a scan with up to 10 discernible sidebands on the low-energy side. Access to these sidebands is interesting for operations such as optical sideband cooling[228].

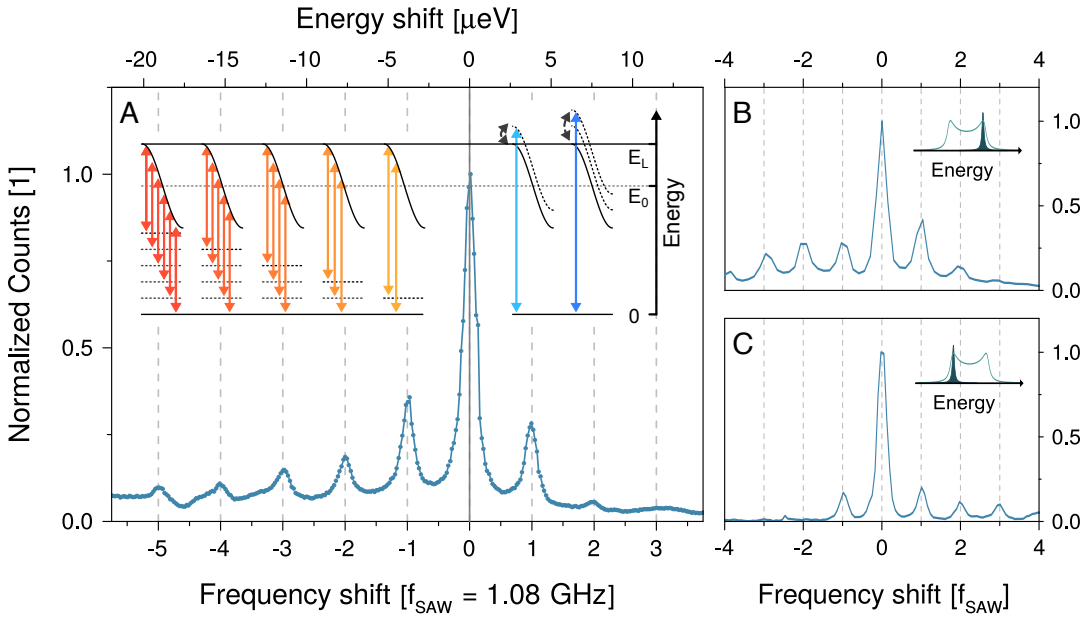

Fig. 3.13: Appearance of sidebands in the presence of a SAW with $P_{\mathrm{rf}} = 15\,\mathrm{dBm}$. **A.** High-resolution spectrum of the resonantly driven transition, showing clear sidebands due to multiple phonon-assisted transitions. The inset schematically shows the energy level diagram and some of the contributing transitions (phonon arrows on the red side are omitted for clarity). The modulation of the transition energy during half a SAW period is shown for each sideband. The energies E_0 and E_{L} mark the unperturbed transition and laser energy, respectively, and the distance between dashed lines represents the phonon energy $\hbar\omega_{\mathrm{SAW}}$. **B, C.** Spectra as in A for the same (B), and opposite (C) spectral alignment of the laser relative to the SAW induced tuning range, as illustrated in the respective insets.

In all measurements, the linewidths of the central peak and sidebands are very close to the instrumental resolution of 192.3 MHz (0.80 µeV), indicating that at these powers the device operates in the resonant Rayleigh scattering regime[16, 70]. For the measurement of Fig.3.13A, the extracted linewidth of the central peak is 245.3(37) MHz (1.01(2) µeV) and coincides with that of the sidebands within the error margin.

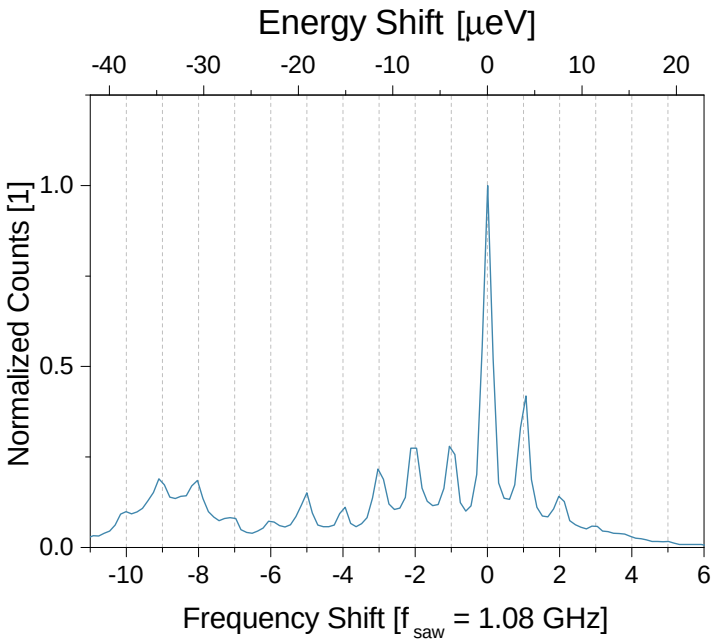

Fig. 3.14: High-resolution spectrum showing evidence of up to 10 red sidebands. The data is the same as pictured in Fig.3.13B.

3.6 Conclusion

In summary, we have developed a device integrating surface acoustic waves and arrays of cavity-enhanced quantum dots. Planar DBR cavities are partially etched to form pillar microcavities containing single QDs. A 165 µm wide SAW can be launched across the pillar field, modifying the emission energy of the QDs. We find that the SAW can uniformly act on large arrays of emitter-cavity systems, offering the possibility of parallel operation of single-photon sources. A single dot-pillar system is capable of coherently scattering cw resonant laser light into single-photons with GHz repetition rate, inherited from the SAW. This is confirmed by antibunching in the second-order autocorrelation. We show that the scattered light consists of a “comb" of sub-natural linewidth emission peaks, spaced at the SAW frequency. Beyond single-photon generation, the studied SAW-based platform opens up possibilities for acousto-optical systems with two coherent manipulation pathways[163, 232] and has the potential to serve as an on-chip quantum interface with spins in quantum dots[162].

In future experiments, it would be interesting to increase the SAW tuning range relative to the cavity linewidth. This would enable further studies on the dynamics of the Purcell factor modulation. To achieve this, the device can be modified by starting from a higher Q factor cavity with more DBR repeats or by reducing the IDT aperture and adding an acoustic reflector to increase the acoustic energy. It would also be worthwhile to study the efficiency of the photon generation per acoustic period. With a resonant π pulse and deterministic charging schemes, it could be possible to ensure a photon on each pulse, making the source essentially on-demand.

Chapter 4

Acoustic Modulation of a Quantum Dot in a WGM Microcavity

In this chapter we present the exploration of a hybrid approach to integrated quantum photonics combining GaAs photonic elements on $LiNbO_3$ carrier substrates with acoustic transducers. We transfer a membrane of GaAs containing InAs QDs by epitaxial lift-off (ELO) (Ch.2). The presented project was conceived as part of a collaboration with the group of Hubert Krenner at the University of Augsburg within the SAWtrain network. Their group has experience on the transfer of GaAs membranes onto $LiNbO_3$ by ELO and have shown that an acoustic wave generated on the $LiNbO_3$ substrate will couple into the membrane achieving a strong modulation of the dots found within[233]. As a joint project with Emeline Nysten, the network's Ph.D. student based in Augsburg, we expanded on this by further processing this membrane into optical microresonators. Numerical simulations and mask design were performed at Toshiba by the author while fabrication was jointly carried out at Augsburg University as part of a secondment. The optimization of the process required further samples whose fabrication started in Augsburg and finished in Cambridge. A reciprocal secondment of Emeline served for initial measurements at Toshiba. At the time of writing, experiments are ongoing in Augbsurg. The first part of this chapter outlines the results of the modeling and discusses the details of the fabricated devices. The second part presents the preliminary measurements performed on these devices.

4.1 Introduction

As quantum photonic applications mature there is an increasing interest in moving key components on chip, creating functional quantum photonic integrated circuits (QPICs). One of the challenges is to find a suitable material platform that allows the integration of single-photon emitters and detectors together with linear elements like phase shifters in a highly integrated fashion. Silicon on insulator (SOI) is undoubtedly the most advanced in terms of processing technology and has provided the base for remarkable devices (e.g. arbitrary two-qubit processing[234] and high-dimensional entangled states[235]), but the single-photon sources rely on non-linear parametric processes and are therefore inherently inefficient. Although efforts to integrate single-photon emitters onto waveguides have been successful, more often than not the complexity of the methods precludes large-scale fabrication[236, 237]. In light of these issues, III-V materials such as GaAs have been suggested as a platform for on-chip integration[238]. Among the attractive properties of GaAs are a high refractive index, allowing for high integration density of components, readily available integrated single-photon emitters with a strong spin-photon interface, integrated detectors[239], integrated laser sources[240], and electro-optical phase modulation with low applied voltages[238]. For QPIC in particular, high coupling factors β of QD emission[241, 242] and chiral QD emission in waveguides have also

been demonstrated[243]. The hybrid approach of combining a waveguiding material on a foreign substrate has recently gained traction in the research community and there is a wide variety of material combinations being explored[40, 174, 240, 244].

Here we are additionally interested in the incorporation of SAWs on this type of platform. SAWs can be useful both for next-generation optical components[163, 174, 245] as well as QPIC. In the context of the latter, SAWs can be used for phase modulation and routing by the elasto-optic effect[159] and on-chip optomechanics[220]. Their interaction with single emitters can also be exploited for the implementation of non-linear components and single-photon routing[246]. Furthermore, recent demonstrations of coherent SAW-spin coupling[232, 247, 248] have sparked interest in the possibility of scalable solid-state spin systems with phononic control[249]. SAWs can be used for the coherent control of multiple emitters in parallel or targeted to specific sites, helped by the fact that SAWs can be guided on acoustic waveguides[156, 163, 250].

In the following, we examine the feasibility of a hybrid platform incorporating GaAs photonic elements on $LiNbO_3$. As a substrate, $LiNbO_3$ provides high thermal stability and strong piezoelectricity[251]. Throughout this chapter the mentions of $LiNbO_3$ refer to 128° Y-cut $LiNbO_3$, which is used exclusively. We transfer a simple membrane of GaAs containing a layer of self-assembled InAs dots by ELO but we note that it is in principle possible to transfer more complicated layered and doped structures[252]. We design and fabricate optical ring resonators, showing that the fabrication is scalable and straightforward. We then perform low temperature spectroscopic measurements, demonstrating Purcell enhancement of individual dot emission and their acoustic tuning by a SAW.

4.2 Device Design

The chosen device to study in this preliminary feasibility test is a ring resonator, as schematically presented in Fig.4.1. The ring can sustain whispering-gallery-modes and enhance the emission from dots in the material. An auxiliary waveguide is used to couple light evanescently to the ring. Grating couplers are used in turn to inject and collect light from this waveguide. The couplers are chosen to lie perpendicular to the SAW propagation direction to avoid interference with possible acoustic effects on the ring.

The addition of a SAW opens the possibility to investigate the effects of the wave on the optical properties of the system. In contrast to Ch.3, we can expect the cavity to be modulated by the acoustic wave. The mechanical deformation should have a negligible effect on the resonance condition but the indirect effect of refractive index modulation has been shown to modify the resonances of such cavities[159, 174]. Naively, we can roughly expect two regimes of operation. Where the diameter of the ring is much greater than the acoustic wavelength the

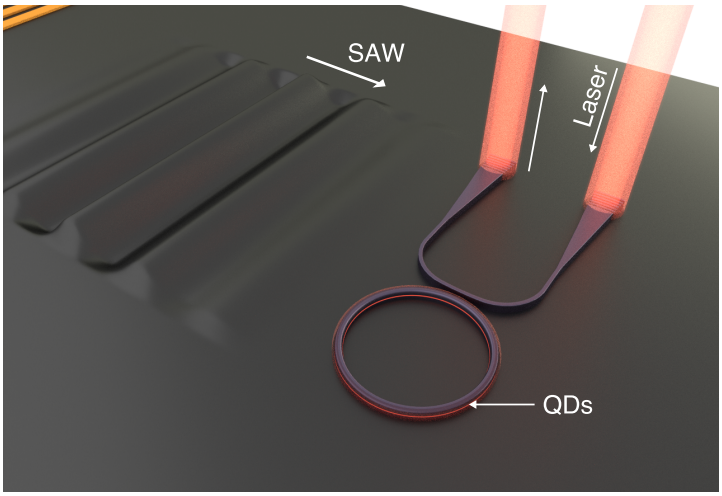

Fig. 4.1: Schematic of the proposed device. $LiNbO_3$ is shown in dark grey and GaAs in purple. Grating couplers are used for vertical optical access. GaAs Microrings and microdisks containing QDs are patterned in the path of a SAW on $LiNbO_3$.

refractive index modulation can average out, resulting in minimal modulation of the cavity and strong modulation of the dots. On the other hand, where the diameter is comparable to the wavelength we can expect to see the modulation of the cavity mode. These two situations are analogous to SAW modulation of QDs in pillar microcavities and photonic-crystal cavities, respectively. We aim to have both cases in one device by having rings of varying radius and an IDT with the ability to produce a wide range of frequencies.

One critical question is the reliability of the adhesion between GaAs and $LiNbO_3$. Previous experiments with membranes have not been patterned. In contrast, the contact area of a device such as the one in Fig.4.1 will be greatly reduced. Furthermore, a Pd adhesion layer is commonly used because it provides an extremely strong bond[253]. A metal layer in direct contact with the optical resonators would be disadvantageous for our purpose as it would introduce losses. The test devices studied here have proven that the Van-der-Waals bonding of GaAs structures to $LiNbO_3$ is rather robust. There was no damage or detachment of devices during conventional processing and the samples survive the local ultrasound needed for wire bonding as well as multiple thermal cycles between 5 and 300 K. This is true even for the finer structures found in the grating, with sides down to ~200 nm in length.

We note that without access to positioned dots the usage of this platform for quantum optics experiments has the obvious drawback of containing QDs all along the photonic elements. For resonant experiments, their contribution may be negligible with moderate dot densities.

We now describe the considerations and simulations that led to the final design shown in Fig.4.1 and subsequently discuss the arrangement of devices on the samples.

	GaAs	$LiNbO_3$	
n	3.472	2.2	
	Waveguide ($350 \times 350\,nm^2$)	Ring ($1500 \times 350\,nm^2$)	Ring ($350 \times 350\,nm^2$)
n_{eff} (TE)	3.0413	3.3630	3.0421
n_{eff} (TM)	3.0621	3.3860	3.0647

Table 4.1: Refractive indices used for the mode profile simulations and calculated effective indices.

4.2.1 Numerical Simulations

Ring resonators are widely used in the telecommunications industry and are commonplace in the laboratory. Their properties have been the subject of considerable investigation. Nevertheless, it is necessary to perform simulations of key components with the specifics of the platform chosen here. This is important in determining the sizes and geometry of the devices, and in particular, the critical dimensions of ring-waveguide coupling gap and grating coupler period. Unless explicitly mentioned, the simulations assume an optical wavelength of 940 nm. Figure 4.1 shows a schematic of the device for reference.

Mode Profiles

The first step in the simulations is to calculate the mode profiles in the ring and in the access waveguide to extract the effective refractive indices and to ensure single-mode operation of the waveguide. As mentioned in Ch.2, the system is modelled in Comsol. Iterating a simulation of the modes supported on a cross-section of the waveguide one can arrive at a set of dimensions supporting a single TE and a single TM mode. In this case the target dimension is $350 \times 350\,nm^2$. This fixes the thickness of the GaAs slab to be grown by MBE. The dots are grown in the middle of the GaAs layer. The ring can be any width above 350 nm, up to a full disk. The effective refractive indices for TE and TM modes for a 30 µm radius ring are summarized in Tab.4.1. These values are useful for further simulations that are computationally too expensive to be performed in 3D.

Ring–Waveguide Coupling

The evanescent coupling between waveguide and ring is extremely important, as this dimension is fixed by the fabrication and cannot be changed during experiments. If the system is either under or overcoupled, the light field does not build up inside the ring. The parameter to control to try to reach critical coupling is the gap or separation between both components. Simulations were performed in 2D due to the computational complexity of a complete 3D model. For the

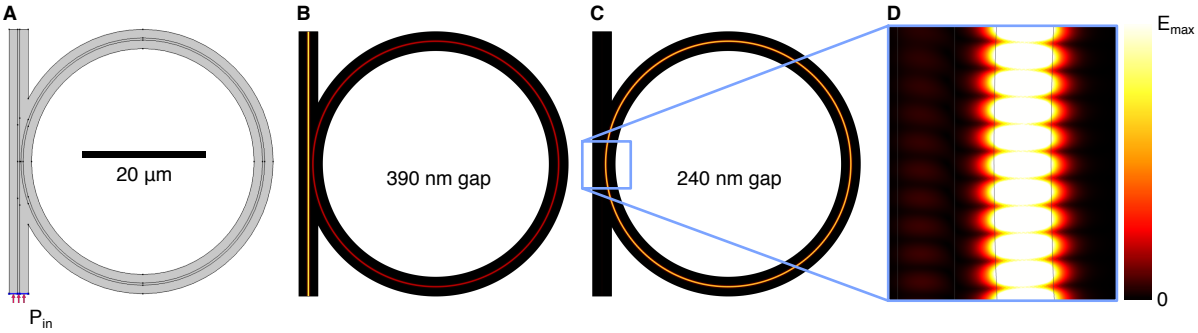

Fig. 4.2: Simulated electric field distributions for a ring coupled to a waveguide. **A.** Comsol geometry. **B,C.** Solutions for waveguide-ring gaps of 390 and 240 nm. **D.** Magnification of the coupling region.

waveguiding domains we use the effective index rather than the GaAs index as a way of taking the $LiNbO_3$ substrate, which is not directly modelled, into account.

We model the domain containing the waveguide and the ring in a top-view configuration, as presented in Fig.4.2A. The bottom port of the waveguide is used for excitation and the top port of the waveguide is absorbing. The rest of the figure shows the calculated field distribution for 350 nm wide rings of 20 µm radius for two gap values. For a gap of 390 nm there is some coupling into the ring, but most of the light is guided straight through the waveguide. In contrast, for a gap of 240 nm the system is critically coupled and the field builds up in the ring to the point that the light in the waveguide is barely visible with the linear colour scale. The stored energy diminishes when increasing or decreasing the gap, as discussed in Ch.1. Figure 4.3 shows the integral of the electric energy over the ring versus wavelength for various gaps. Each point in this graph is extracted from a simulation like those in Fig.4.2. These coarse scans show that this particular ring has a resonance at ~938.2 nm and the optimal coupling gap lies around 240 nm. This optimal value for the gap varies depending on the width and radius of the studied ring, but it is consistently between 210 nm and 300 nm. Since fabrication imperfections and deviations from the assumed refractive index can cause deviations in the experimentally optimal value, the best strategy is to fabricate multiple structures covering this gap range. We note that for some simulations the correct resonance might not be found in an automatic parameter sweep and in the interest of limiting computation time the resolution of the wavelength sweep is coarse. As a result, the stored energy in Fig.4.3 is not always smoothly varying as a function of the gap.

Waveguide Taper

A taper is included in the design in order to reduce the size mismatch between the waveguide mode and the free-space Gaussian mode of the optical setup. Here, it is important to check the dimensions to ensure the mode is expanded adiabatically and there is no conversion to the higher order modes supported in a wider waveguide. Ideally we want to reach a spot size of

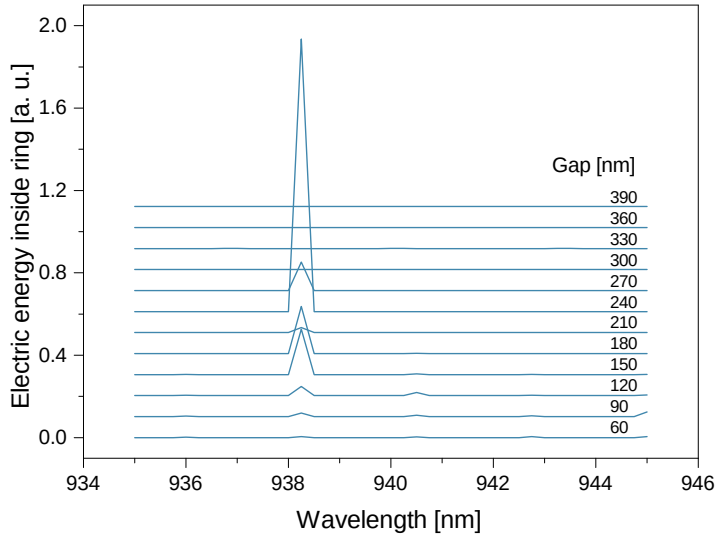

Fig. 4.3: Integrated electric energy over the ring versus the wavelength for multiple gap values, showing a clear resonance and the dependence of the coupling on the gap. The data shown is for a 350 nm ring of 20 µm radius.

about $3 \times 3\,\mu m^2$ while minimizing the device footprint. We complete 3D FEM simulations in Comsol to determine the optimal taper dimensions. Figure 4.4 shows the computation domains. We can exploit symmetry to solve only a half space, by setting the cut line through the middle of the waveguide to have perfect magnetic conductor conditions ($\boldsymbol{n} \times \boldsymbol{H} = 0$).

The meshing of the domains constitutes a particular challenge in 3D simulations and has an impact on the speed of the simulation as well as the accuracy of the results. For an electromagnetic simulation such as this one, we need to resolve each wavelength with at least three elements. Because the wavelength is shorter in GaAs, which has the higher refractive index of the materials used here, and because we expect the electromagnetic wave to be confined to the GaAs region, it is meshed more finely. We use auxiliary cut planes at the start and end of the taper to help with the meshing. Using these planes we can first mesh the end facets of the two separate waveguides with a rectangular grid. After this step we can use a swept mesh to cover the length of the waveguide and taper, which is subsequently triangulated. The air/vacuum and $LiNbO_3$ domains can then be easily meshed with a tetrahedral mesh. Not shown in Fig.4.4 are the perfectly matched layers (PMLs) (see Sec.2.8) which surround the structure to avoid reflections at the simulation domain boundaries. These are meshed with a swept mesh as well.

Having meshed the domains we proceed to solve for the field distribution. We insert a wave on the left waveguide port and absorb it on the right port. Figure 4.5 shows the top view of the solution for a 7 µm long taper going into 1.5 and 3.5 µm wide waveguides. From these images one can see that the taper in A efficiently expands the mode. In contrast, the taper in B expands too quickly and the mode is split into the guided modes of the wider waveguide. For a given target waveguide width we can extract the transmission S-parameter S_{21} between input and output ports, as presented in Fig.4.6 for a 3.0 µm wide waveguide. This measurement provides an absolute minimum length for the coupler to avoid losses. It does not however give detailed

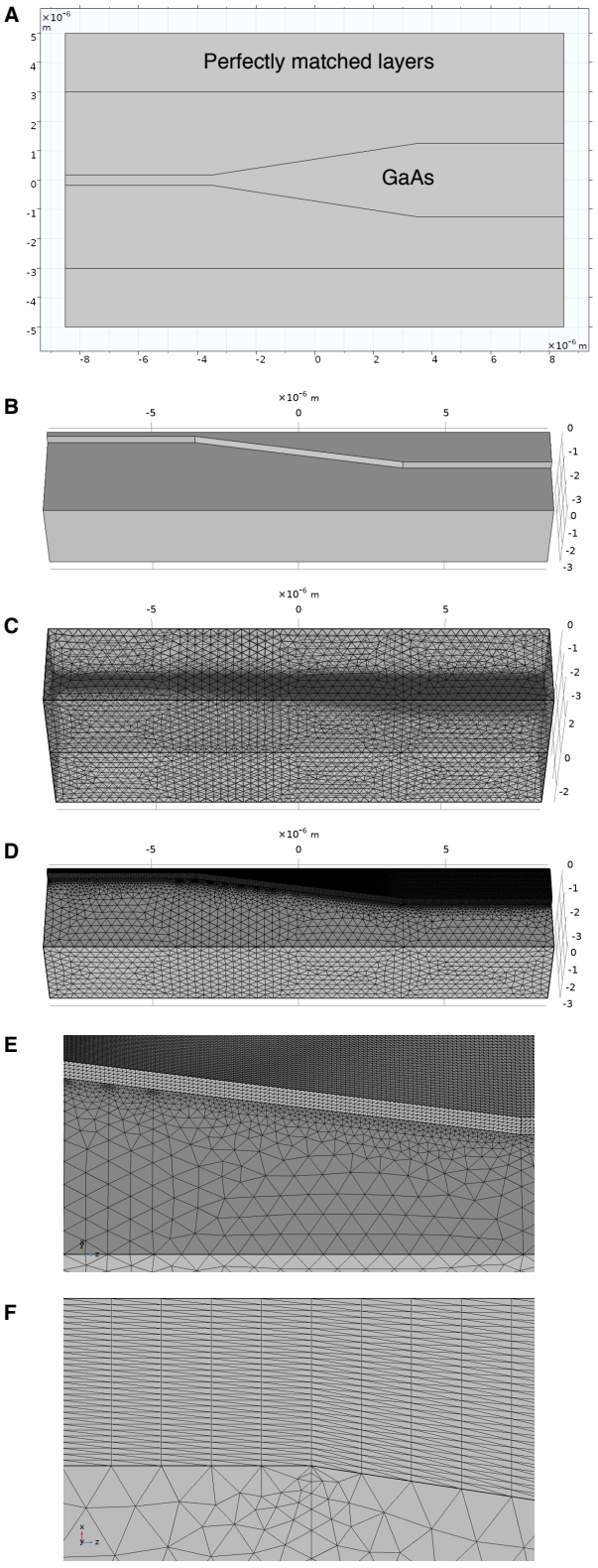

Fig. 4.4: Arrangement of simulation domains and meshing. **A.** Top view of a simple taper. A 350 nm wide waveguide is linearly expanded into second waveguiding region. The studied parameters are the width of the wider waveguide and the length of the taper region. **B.** Angled view of the 3D $LiNbO_3$ and GaAs domains. The cladding and PMLs are hidden. The back plane is the symmetry plane. **C.** Meshing of the three main domains. **D.** Meshing of the domains with the cladding hidden. **E.** Magnification of the mesh in the taper region. **F.** Further magnification of the taper meshing, focused on the start of the taper. The top region shows the waveguide sidewall, while the bottom shows the substrate.

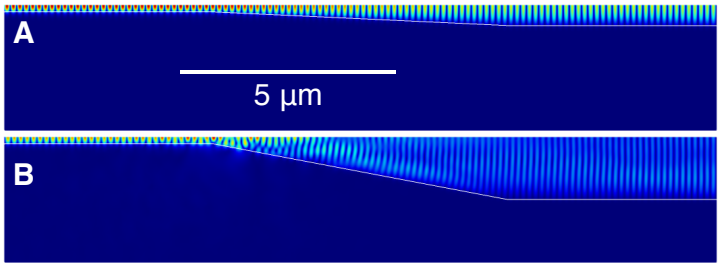

Fig. 4.5: Solutions for the electric field amplitude in two tapers. **A.** A 7 µm long taper from a 350 nm into a 1.5 µm wide waveguide. **B.** As in A but for a 3.5 µm waveguide.

information on the conservation of the mode. Combining the information from both types of simulation we conclude that we should design tapers with a 10 µm long expansion region ending in a 3.0 µm waveguide.

Grating Coupler

At the end of a taper, light is coupled perpendicularly in or out by a grating coupler[254]. These are fairly standard components that allow the study of individual devices anywhere on the chip. The main alternative is edge coupling, which involves direct coupling from a fibre at the edge of the chip. This naturally requires the waveguides to extend to the chip edge and the face to be polished for good contact. Generally grating couplers are therefore more flexible but achieve lower efficiencies. They are usually designed to work straight with optical fibres at a small angle from the surface normal. Here we need to optimize the grating design and dimensions to our material system and the coupling to a free-space Gaussian beam. We propose an apodized grating coupler, as presented in Fig.4.7, where the grating periodicity Λ is linearly varied along

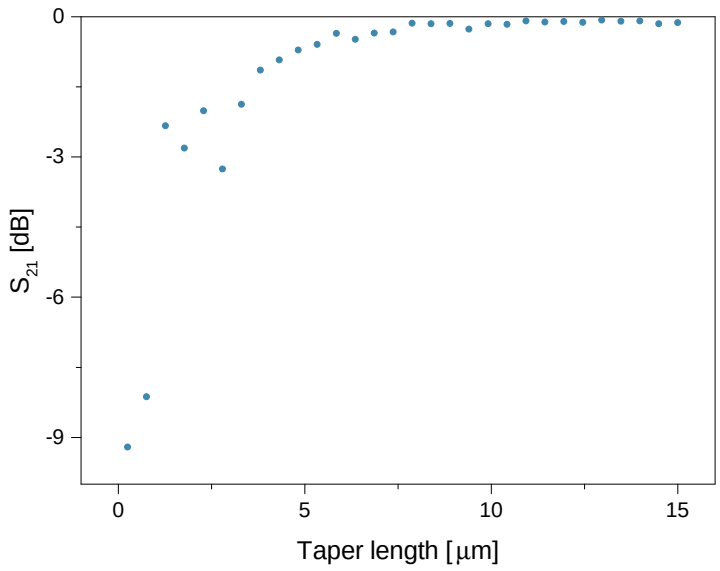

Fig. 4.6: Extracted S_{21} against taper length for a taper going into a 3.0 µm wide waveguide.

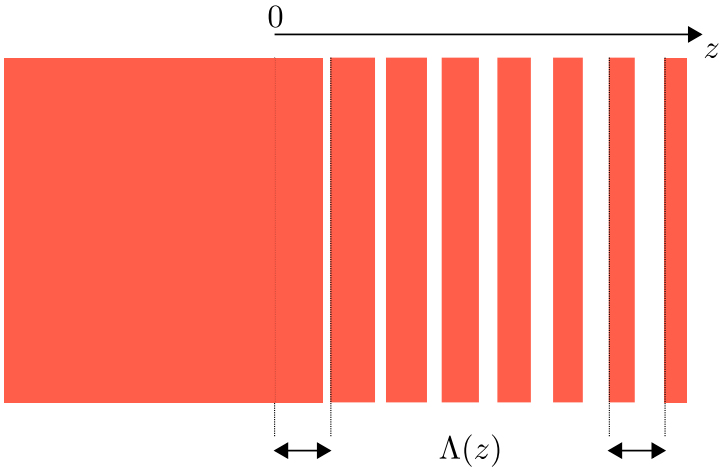

Fig. 4.7: Top-view schematic of an apodized grating coupler with period $\Lambda(z)$, where the shaded areas correspond to the high-refractive-index material. Light propagates along z.

the length of the structure according to

$$\Lambda(z) = \frac{\lambda_0 - \lambda_{\text{offset}}}{(F_0 - Rz)n_{\text{GaAs}} + (1 - F_0 + Rz)n_{\text{air}}}, \tag{4.1}$$

where the light is assumed to propagate along z and the start of the grating is at $z = 0$, F_0 is the initial fill factor and R the apodization rate. Figure 4.8A shows the side view of such a grating and the simulation domain we consider to evaluate it. The simulations for this component are again performed in 2D due to computational limitations. First, we examine the spectral response of the grating by investigating the scattering of a Gaussian beam. We arbitrarily choose 16 grating periods, $R = 0.0675\,\mu\text{m}^{-1}$ and $F_0 = 0.8$. Most of the scattering happens in the first elements so there is no need for a large number of periods, but we do want an area that can be easily found in the optical microscope. As before, PMLs are used around the structure. We solve for the scattered field from a perpendicularly incoming Gaussian beam, as shown in Fig.4.8B. The beam is polarised out of plane and has a beam waist of 2 µm, focused on the $LiNbO_3$ interface. Fig.4.8C shows the resulting scattered field amplitude for an efficiently

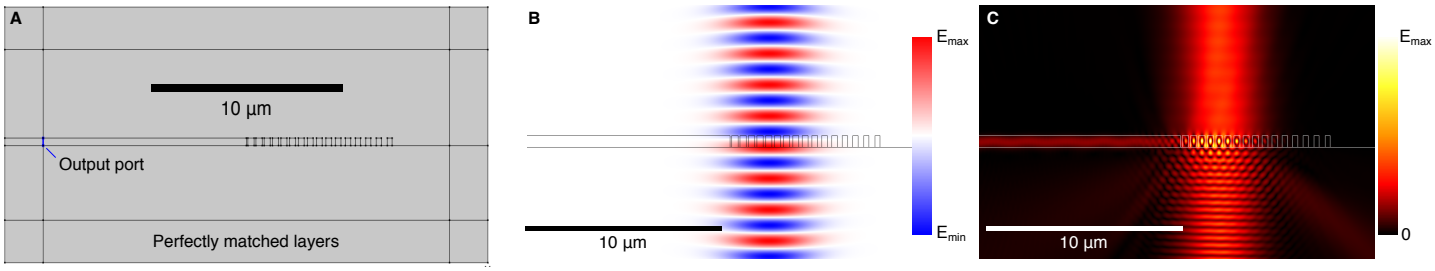

Fig. 4.8: Simulations for a grating coupler. **A.** Comsol geometry. The domain is surrounded by perfectly matched layers. **B.** Electric field distribution for the background Gaussian beam. **C.** Scattered field amplitude for the optimal wavelength, where the light is effectively coupled into the waveguide.

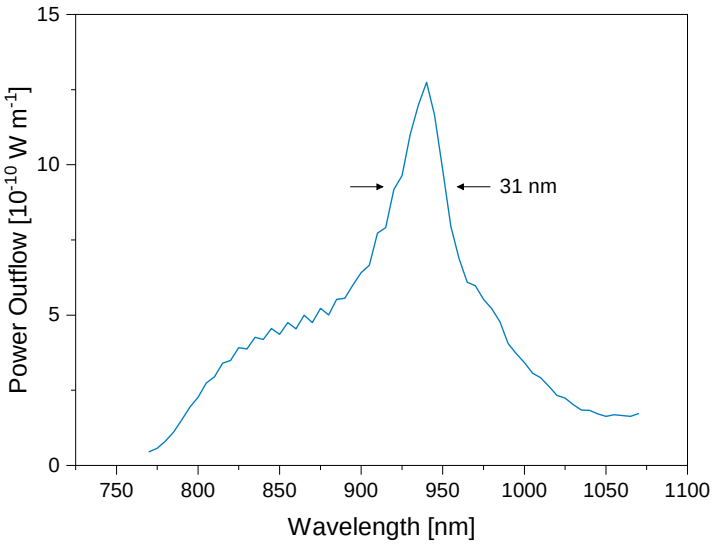

Fig. 4.9: Power coupled into the waveguide as a function of wavelength.

coupled wavelength. We sweep the wavelength of the beam while monitoring the power flow through the left port of the waveguide. This yields the dependence presented in Fig.4.9. We note that the position of the Gaussian beam impacts the absolute power through the waveguide but crucially not the spectral dependence.

We next repeat this procedure to study the effect of the apodization rate. Figure 4.10A shows the power outflow through the waveguide versus the wavelength and the apodization rate. The results show that a uniform grating has the best performance for a specific central wavelength. However, the improved efficiency comes at the expense of a reduced bandwidth. We choose to use an apodization rate of $0.05\,\mu m^{-1}$ in order to increase the probability of having devices with couplers working at the targeted wavelength of 940 nm, even in the case of strong deviation from the simulations. Compared to no apodization, this reduces the coupled power by a factor of 2.3 but increases the bandwidth from 7.8 to 29.9 nm. It is worth noting that the wavelength range studied is reduced in the interest of reducing computation time. As seen in Fig. 4.9, the output power drops further outside of this studied range.

We use the same type of simulation to confirm that the parameter λ_{offset} linearly shifts the centre of the coupling efficiency peak. This is an ad-hoc parameter that allows the tuning of the grating to work at the desired wavelength after other parameters have been set. Figure 4.10B shows the evolution of the spectral response for increasing λ_{offset}. The simulation shows that the actual response indeed varies linearly, although the scaling is not one to one. In addition to the linear shift, it can be seen that the peak power is not constant. However, since changing λ_{offset} affects the periodicity of the grating elements, and with that the position of the complete element relative to the incoming beam, quantitative comparisons should be avoided. In order for the peak efficiency to be comparable across simulations, the position of the beam would

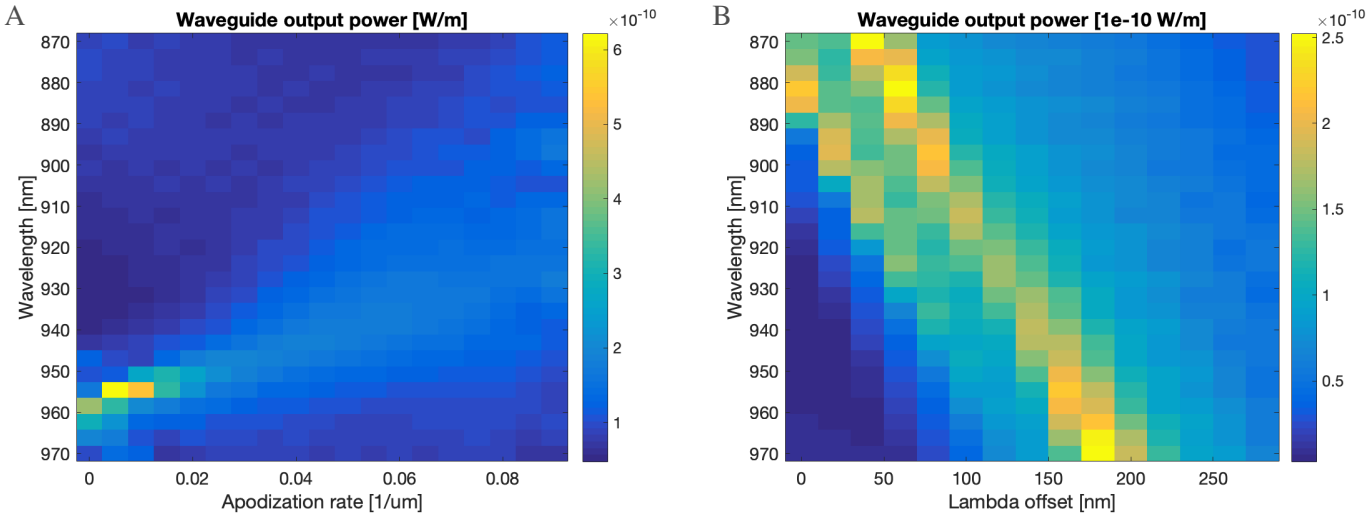

Fig. 4.10: A. Spectral waveguide output power against apodization rate. **B.** Spectral waveguide output power against the central wavelength offset.

have to be optimized for each simulation of the spectral response. This is not done here since absolute efficiency figures are not the goal of the simulations. Finally, at $\lambda_{\text{offset}} \approx 30\,\text{nm}$, the main peak shifts from being on the long wavelength side of the coupling region to the short wavelength side. There is no physical reason to expect this. It is therefore reasonable to believe this is an artefact from the simulation. One possibility is that it is a meshing effect, given that the geometry changes significantly in the studied range. Despite this, the required λ_{offset} can be estimated from such a coarse sweep, after which a subsequent simulation with a refined mesh can yield a more accurate result.

The last parameter to consider is the initial fill factor F_0, which determines the degree of refractive index contrast in the first grating period. It is not explicitly simulated, as it can be reasonably expected to yield better performance for higher initial fills that account for a smoother transition from the waveguiding into the diffracting region. The limiting factor for large F_0 is how small the first trench can be and is therefore determined by the fabrication tolerance. Following this logic and the simulations we arrive at an optimal set of parameters $F_0 = 0.8$, $R = 0.05\,\mu\text{m}^{-1}$ and $\lambda_{\text{offset}} = 140\,\text{nm}$. As a final thought we note that the efficiency of the grating can be greatly improved by etching only partially through the grating elements or at an angle to create a blazed grating[255, 256]. However, this adds unnecessary complexity that we prefer to avoid at the early stage of this project.

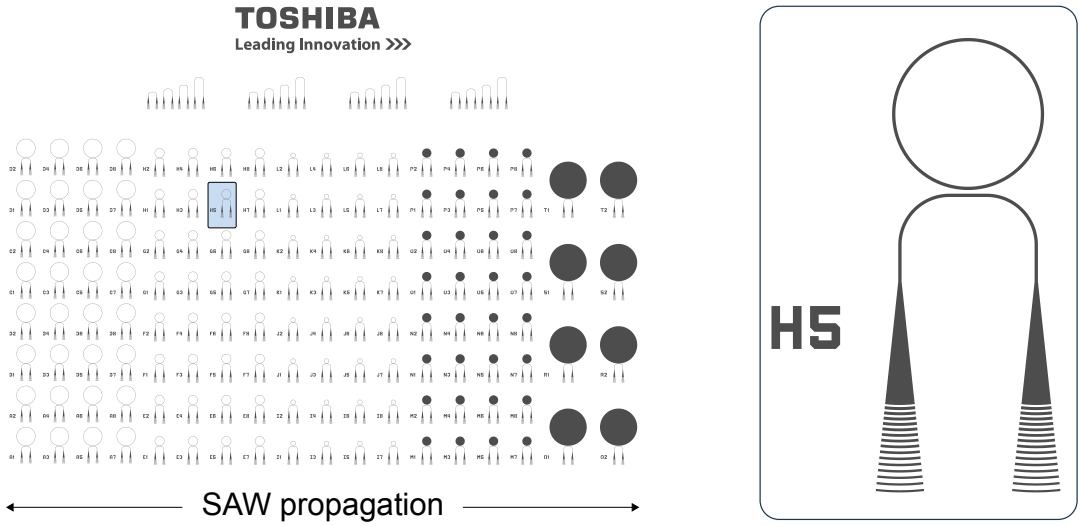

Fig. 4.11: Mask for a test chip containing multiple variations of the design. The IDTs are pre-patterned and their aperture covers the field of devices. The field is $800 \times 400\,\mu m^2$. Waveguides of different length without rings are included to test coupler efficiency and propagation losses. The inset shows a close-up of one structure with its label. The ring has a 6 µm radius.

4.2.2 Final Mask

Putting the results from the previous section together we arrive at the mask design presented in Fig.4.11. The devices are arranged in a grid with eight rows and sixteen columns. The primary parameters that are varied across the mask are the ring radius and the waveguide-ring gap. The former allows for the investigation of different regimes of the ratio of acoustic wavelength to ring circumference. The latter is necessary to increase the chances of having critically coupled structures, as there needs to be some room for fabrication tolerances and the fact that, especially for such a critical parameter, the simulated value can easily deviate from the actual optimal distance. We also note that the 2D coupler design is rotated around its origin to follow the profile of the taper to compress the footprint relative to a rectangular cross-section coupler at the end of a waveguide.

In order to ease the characterization, all couplers are identical. This allows for a single alignment step of the optics on the input and output. It is desirable to have the gratings at the ends of the waveguide as far apart as possible to minimize collection of scattered light from the input. However, the confocal microscope setup and the objective within it pose some limitations here if one wants to avoid large modifications of the system. The maximal separation for input and collection spots in our system is ~10 µm. The particular U-bend design was chosen with this in mind to have the two gratings within close proximity, such that both can be reached comfortably. It is worth noting that the presented arrangement is not ideal for resonance fluorescence measurements given that the couplers are strongly polarising. Therefore

the conventional polarisation filtering presented in earlier chapters is not applicable here. A 90° bend would be necessary, as has been employed on suspended beams[257, 258]. Such a bend was not included in our design to avoid tight curvature of the waveguide to fit the gratings within 10 µm of each other.

Not shown in Fig.4.11 are the IDTs and rectangular areas left unetched for reference and optical beam alignment. In a single chip there are four identical fields of devices placed in pairs within two separate acoustic delay lines, similar to the configuration presented in Ch.3. The unetched areas are located between the delay lines and are thus unaffected by SAWs. The chosen design for the IDTs in the samples studied is the chirped split-5-2 variant (Ref.[150] and Sec.1.4.1) with the fundamental band at 250 MHz. This allows for SAW generation over four broad (~100 MHz) harmonic bands, thus enabling the study of multiple SAW wavelengths on a single device.

In total, four samples were fabricated. This was not enough to optimize the e-beam lithography step, which presented some issues due to charging. This is a known problem in $LiNbO_3$ and an electrically conducting polymer was used to alleviate it. However, this was not enough and future processing should make use of thin metal films. The problem was compounded by a low accelerating voltage (20 kV) in the e-beam gun available. Tests recreating these structures with a higher voltage and on a silicon dioxide chip were successful in producing high-quality structures with high yield. We concentrate on a single device, that has a mixture of well-defined and less-well-defined structures. Figure 4.12 shows SEM images of this sample. Some structures are very close to the design while in others the gratings and waveguide-ring gap are not resolved. We define the terminology of hard-edge coupler for a coupler such as the one at the bottom of Fig.4.12B, where the grating essentially extends the taper to a hard edge. It is still possible to couple light into the structures by focusing on this edge.

4.3 Experimental Results

We present preliminary results from the sample described above. The sample contains 272 devices though the actual number available for experiments is more limited due to the described issue with the fabrication in this early stage. All measurements presented are taken at low temperature (10 K) unless stated otherwise.

4.3.1 Coupler Characterization

We first present the response of the optical elements disregarding the QDs. The experimental apparatus can be modified to separate the input and collection paths, such that they lie on the

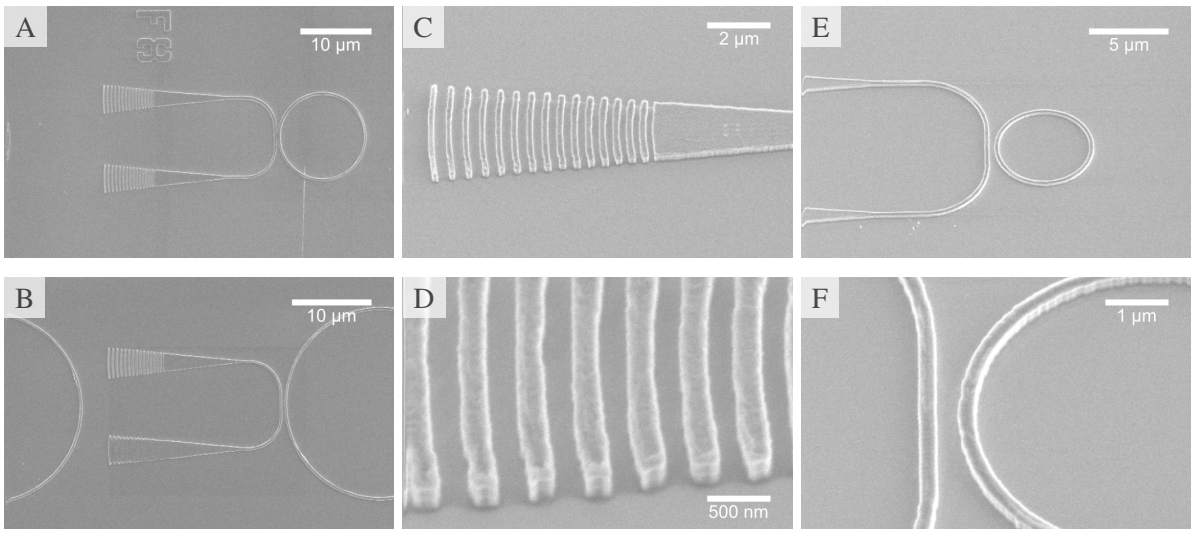

Fig. 4.12: SEM micrographs. **A.** Top view of a successful device. **B.** Top view of a device with one non-cleared coupling grating. **C, D.** Angled view of a grating coupler and close-up. **E, F.** Angled views of the coupling gap region.

corresponding coupling gratings of a device, as shown in Fig.4.13. With this system it is then possible to send the laser through the structure and collect the light from the output onto an APD.

We measure the bandwidth of the couplers using a superluminescent diode (SLD) on the input coupler, and looking at the spectrum from the output. To cancel information from the wavelength dependence of the SLD emission and of the CCD efficiency, the collected signal is normalized by the input signal. The spectra from the SLD and as collected from a representative structure are presented in Fig.4.14. The measured spectra exhibit strong oscillations from reflections at the waveguide ends, which are discussed below. Comparing the spectrum to the simulated profile shows some discrepancy with the simulation. There is a clear offset in central wavelength of 28(2) nm. The bandwidth is larger than expected from the simulations with a FWHM of 47 nm versus 31 nm. It is not unreasonable to attribute the discrepancy to the difference in dimensions between the simulations and the fabricated devices.

The interference fringes highlight a potential problem to consider in future devices, which is the reflection from the couplers back into the waveguide. A measurement on waveguides of different lengths with no rings and hard-edge couplers shows that the waveguide and its ends form a textbook Fabry-Pérot cavity, as presented in Fig.4.15. The fringe periodicity matches the predicted periodicity from considering the waveguide as a Fabry-Pérot cavity, proving the fringes do not stem from the optical arrangement. Furthermore, no similar feature is present when measuring other structures or with the spots aligned. It is worthwhile to minimize this effect. One option is to completely separate the input and output by placing them in separate

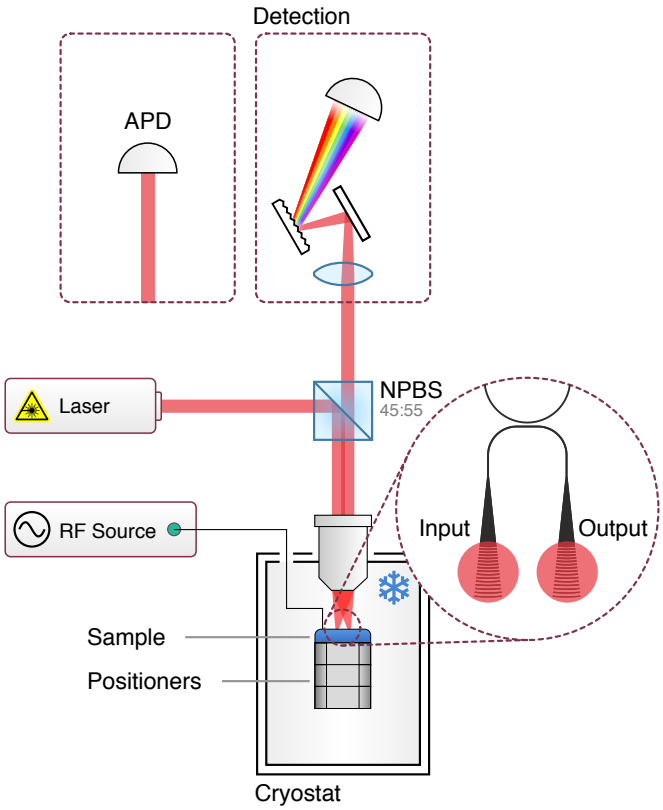

Fig. 4.13: Experimental arrangement for microscopic mesurements with spatially separated input and output focal spots. Optional polarisers are not shown. For most measurements the collected signal is sent either to a spectrometer or to an APD.

waveguides in an add-drop configuration[114]. Another option is to add a sub-grating within the coupler grating[259]. A third option is a modification of the fabrication to have a shallow grating, in which the GaAs is not completely etched through between grating elements.

To estimate the coupling efficiency we direct the collection spot onto an APD. We use a tunable diode laser and overlap excitation and collection spots on a flat GaAs surface. This gives a reference for the APD signal level going through the system I_{ref}. Next, we separate the two spots and navigate to a structure, again collecting the APD counts I_{dev} from the light passing through the system. Ignoring losses from waveguide propagation, from the taper and from coupling to rings, we can calculate a lower bound for the efficiency η of a single grating coupler following

$$I_{\mathrm{dev}} = \eta^2 I_{\mathrm{ref}}. \tag{4.2}$$

Averaging over five devices for each wavelength, we obtain the efficiency per coupler reported in table 4.2. The best efficiency is far from the record efficiencies close to 70 % reported for Si devices operating in the telecom-C band[260, 261] but is close to the more modest values reported at near-infrared wavelengths (22 %)[262] and sufficient for experiments with single dots. As a final note on these gratings, it is worth noting that they are highly polarising.

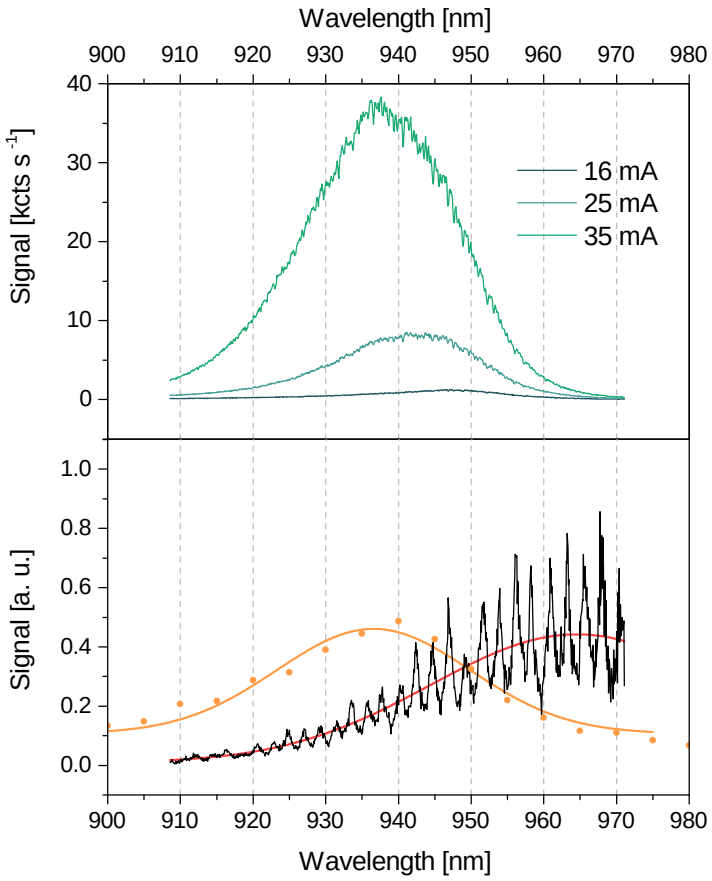

Fig. 4.14: Top. Spectra of the SLD output at different currents. The emission increases and blueshifts as the current is increased. **Bottom.** Collected signal through a single device normalized by the input spectrum. The red line is a Gaussian fit to the data. The orange data points show the simulated profile, as presented in Fig.4.9. The solid orange line is a Gaussian fit to these data points.

Finally, we note that the strong interference in the hard-edge couplers prevents us from accurately measuring the Q factor of the resonators in transmission using the SLD. There are not enough structures with both a gap between waveguide and ring and two good couplers. In order to estimate the Q factor we use direct excitation on rings with a gap, as described in the next section.

4.3.2 μPL Measurements

Figure 4.16 shows μPL spectra from large unetched regions, confirming the presence of QDs in the sample, reflected in the individual lines. Due to the limited number of devices with well-defined grating couplers and coupling gaps, we measure single QD lines with the input and collection spots aligned, exciting the dots directly from the top. This is less efficient but

Wavelength [nm]	920	940	950	960
η [%]	6.76	8.69	10.28	11.65

Table 4.2: Extracted efficiencies for a single grating coupler.

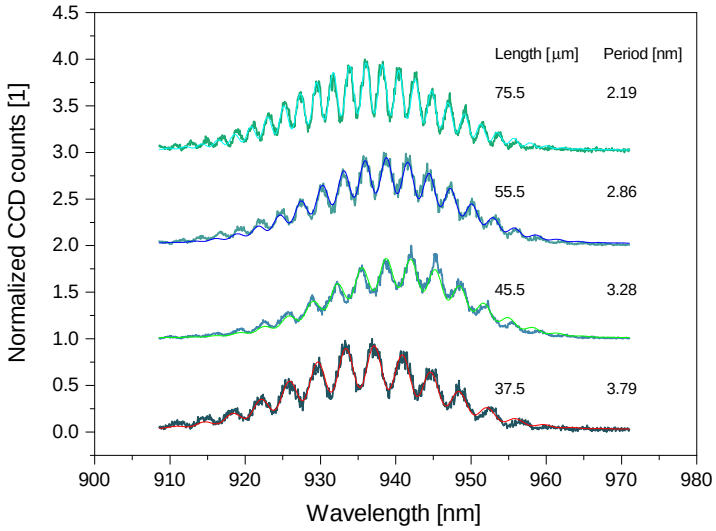

Fig. 4.15: Fabry-Pérot effect on waveguides without rings and with hard-edge couplers (no grating). The curves are shifted vertically for clarity.

sufficient for these preliminary measurements. Figure 4.17 shows the spectrum from a dot in a 12 µm radius ring, with a signal level significantly above what is observed in the planar measurements of Fig.4.16. The bottom panel shows fine spectra taken at different temperatures in order to tune the transition relative to the cavity. The difference in signal level is clear evidence for Purcell enhancement in this system. Several other dots with analogous spectra and temperature dependence were found in other devices on this sample.

While performing measurements on individual QDs it was established that the devices suffer from detrimental charging effects. In particular, after continuous prolonged illumination (> 12 h) with ~13 µW 850 nm laser light, the QD transition can disappear and only be observed

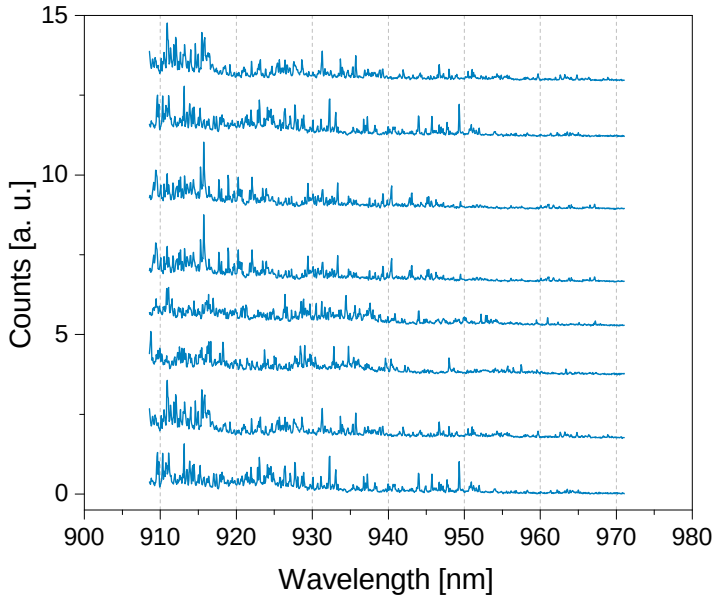

Fig. 4.16: µPL spectra from unetched areas of a device, showing the presence of QDs in the membrane. The curves are shifted vertically for clarity.

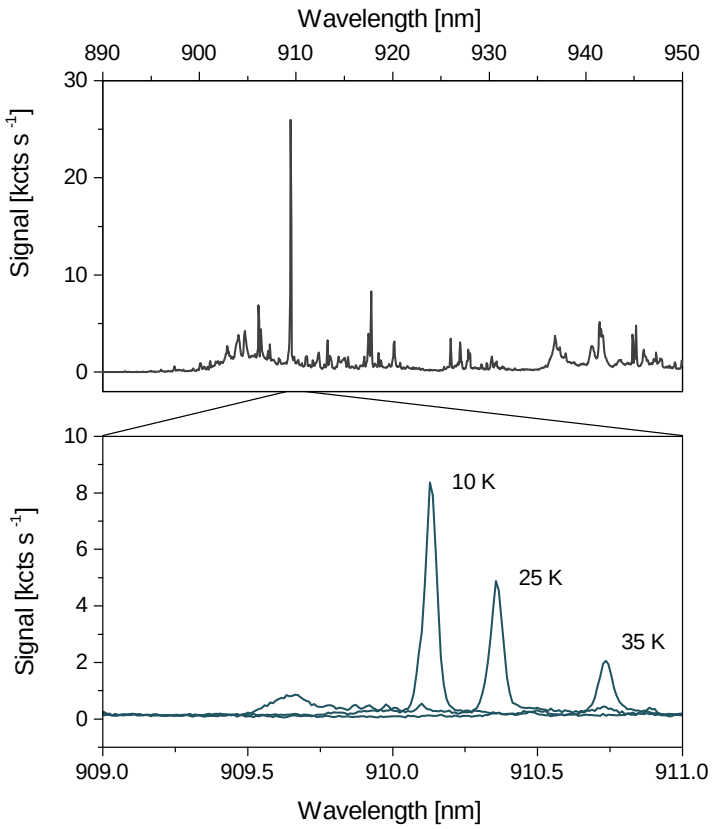

Fig. 4.17: Top. Spectrum taken on a ring resonator under non-resonant 850 nm laser irradiation. A QD line dominates the spectrum. **Bottom.** High-resolution spectra around the bright QD line taken at various temperatures.

again after thermal cycling of the device. Figure 4.18 shows a series of spectra taken one second apart. There are intermittent and oscillatory features across the spectrum while the main peaks are mostly constant across this timescale (~1 min). This behaviour is not observed in the same cryogenic system with other samples. Given that $LiNbO_3$ is an electrical insulator and charging was a source of problems in the e-beam lithography steps, it is tempting to conclude that this behaviour stems from charge fluctuations. If that is the case it could potentially be mitigated with a thin coating of indium tin oxide. Due to this issue we avoid prolonged uninterrupted measurements on a single dot.

Coming back to the Q factor, it can be extracted from spectra taken directly on rings with a gap to the waveguide. Figure 4.19 shows such a spectrum, where the dominant lines are resonator modes. Fitting these with Lorentzian curves yields Q factors around 30000. This is not unreasonable considering that Q factors of 1×10^5 have been reported in similar structures[263]. Furthermore, the minimal Q factor needed to reach the observed Purcell enhancement factor $F_P \sim 4$ in the rings with 12 µm radius is ~14000, using a mode volume of 13 μm^3.

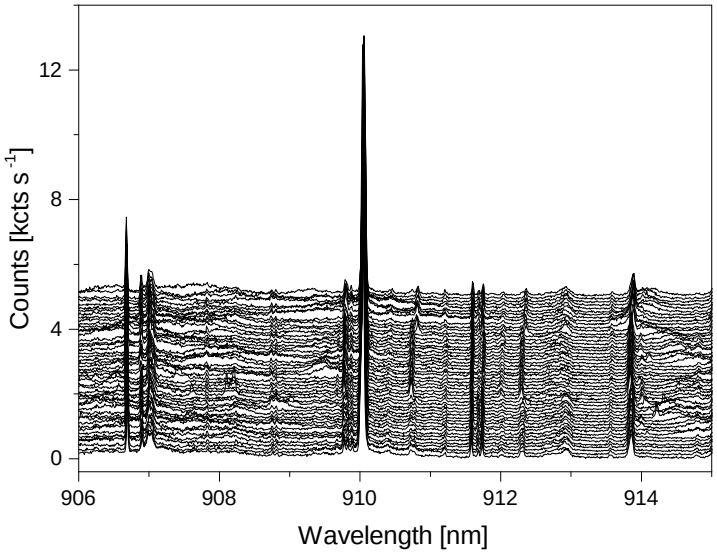

Fig. 4.18: Stability test consisting of a sequence of spectra under constant conditions. The sample is illuminated with a 13 µW non-resonant cw laser. The curves are shifted vertically for clarity.

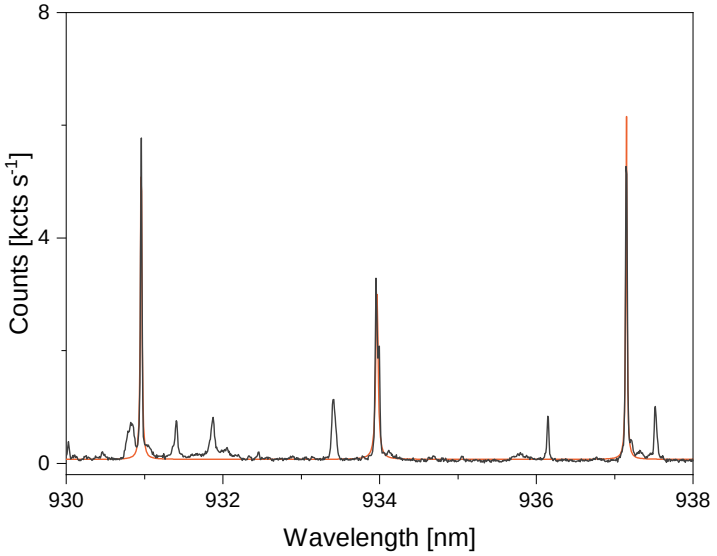

Fig. 4.19: Spectrum with overlapping spots on the edge of a 6 µm radius ring under 4 µW non-resonant illumination. The main peaks are fitted with Lorentzians.

4.3.3 SAW Modulation of Dot Lines

As mentioned above, the IDTs patterned on this device are of split-5-2 design with a chirp to extend the frequency range of SAW generation. The measured S-parameters are presented in Fig.4.20. The fundamental mode at 250 MHz is clearly visible in both reflection and transmission. The higher harmonics cannot be discerned in the reflection measurements, which is a common issue with these IDTs. The first two harmonics, however, can be identified in the transmission measurement, with a reduced efficiency. The generation of SAWs in the corresponding frequency ranges can be readily verified by the resulting modulation of QD transitions. In the following we refer to SAWs around 250 MHz, 500 MHz and 750 MHz as being in the 1st, 2nd or 3rd band, respectively.

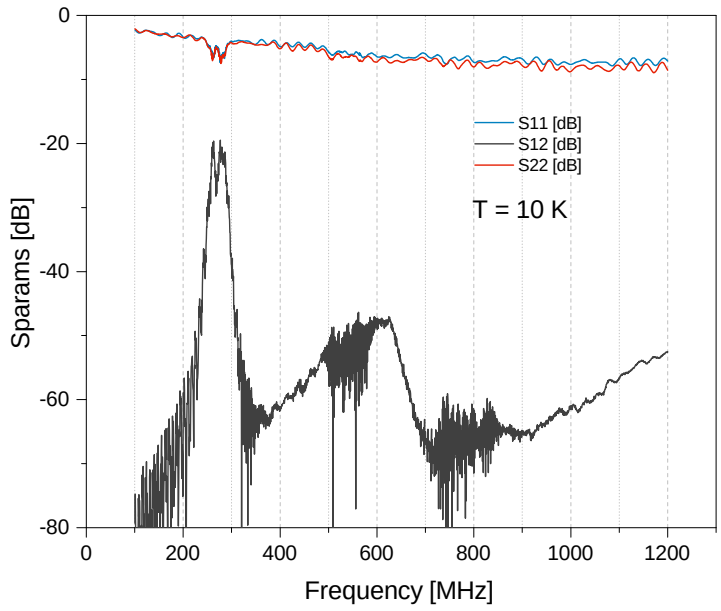

Fig. 4.20: S-parameters of the chirped split-5-2 acoustic delay line at low temperature.

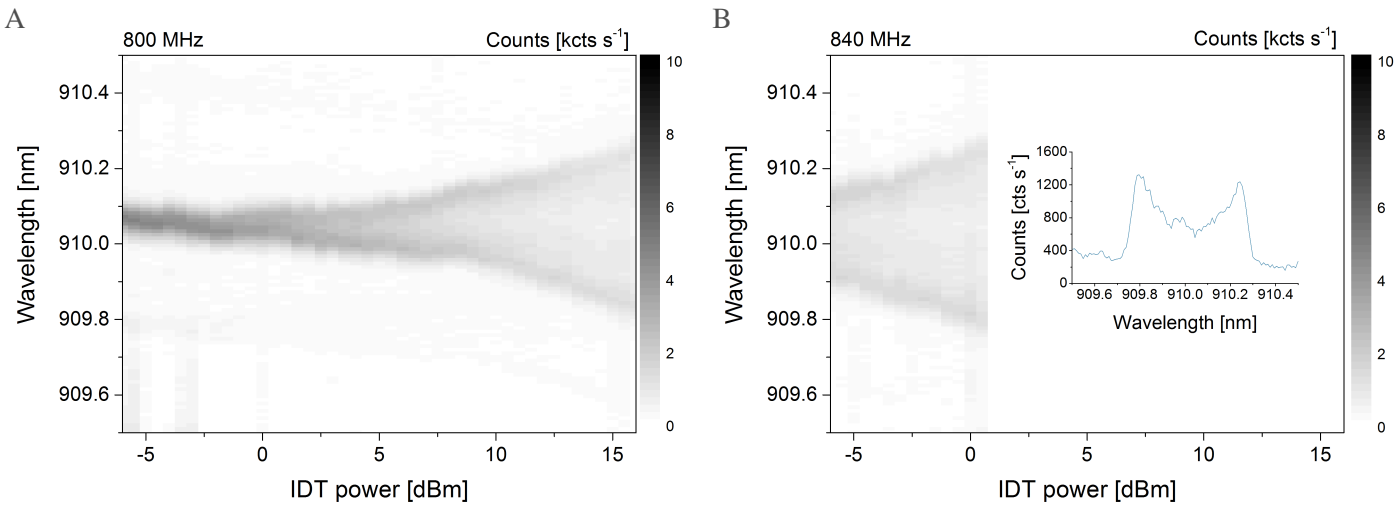

Fig. 4.21: SAW modulation of a cavity-enhanced QD line. Excitation with 13 µW 850 nm non-resonant laser. **A.** SAW splitting at 800 MHz. **B.** SAW splitting at 840 MHz. The inset shows the spectrum at 0.5 dBm applied power, where this scan was halted manually.

We take a closer look at the modulation of the QD line from the dot shown in Fig.4.17. Figure 4.21 shows the SAW-induced splitting as a function of applied rf power. As in the device presented in Ch.3, we observe a clear broadening in the time-averaged spectrum. Interestingly, there is a large discrepancy in the SAW-induced splitting at a given input power for 800 and 840 MHz. The natural explanation is that the IDT does not produce an acoustic wave of constant power at different frequencies, but rather shows evidence of a complex interference pattern that results in varied output powers for each frequency. However, we believe the difference in splitting between Figs. 4.21A and B is too great for this to be the only contribution. These

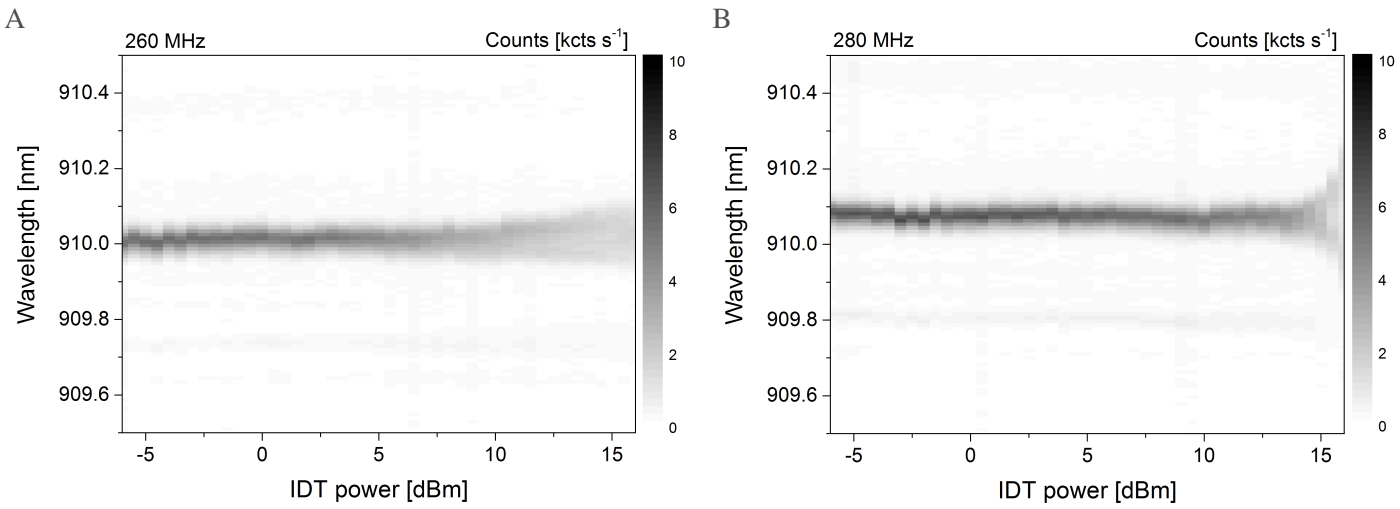

Fig. 4.22: SAW modulation of a cavity-enhanced QD line. Excitation with 13 µW 850 nm non-resonant laser. **A.** SAW splitting at 260 MHz. **B.** SAW splitting at 280 MHz.

transducers* were investigated in unpatterned GaAs with shallow dots in Ref.[152]. The optical transitions in a spectrum serve as a readout of the local strain and reveal the expected variations in frequency but these are within 50 %, especially in the third band. As we discuss below, there is another effect at play.

First, we consider the analogous measurements presented in Fig 4.22, which are taken for frequencies in the first band. In this case there is barely any splitting observable before reaching high powers. This difference in measurements between the first and third bands is compatible with the experiments reported by the Augsburg group in Ref.[233]. Their analysis shows that in thin membranes, the derivative of the hydrostatic pressure scales linearly with frequency for frequencies below ~1 GHz. We also note that the dependence on acoustic power is steeper for the higher of the two frequencies in the first band. This behaviour could be traced back to the IDT performance across the band.

We now take a look at sweeps over the frequency at a constant input power. Figure 4.23A shows the scan across the first frequency band for the same QD discussed so far and labelled QD 1. The orange lines delimit the rough region where SAW splitting of the QD line is observed, corresponding to the SAW generation window of the IDT, in agreement with the measured S-parameters. What is striking in this scan is the well-defined steep modulation around 276.9 MHz. As mentioned before, we do expect the actual acoustic power to vary in frequency, but not by the magnitude observed in this feature. In addition, the shape is indicative of a resonant process, which we believe comes from the SAW exciting a mechanical eigenmode

*The transducer design used is identical to the one discussed in the publication.

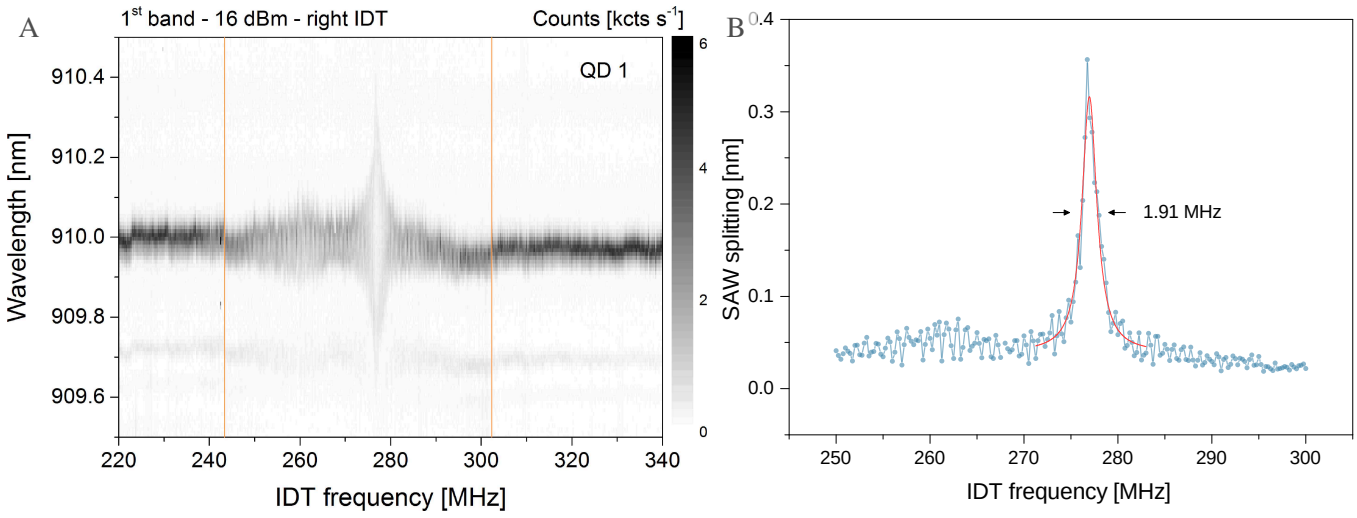

Fig. 4.23: **A.** Frequency scan over the first band on QD 1. The orange lines delimit the rough range of SAW generation by the IDT. **B.** SAW-splitting extracted from fits as in Ch.3 to the measurement in panel A. The data is fit with a Lorentzian with FWHM 1.91 MHz.

of the ring. Fitting the SAW-split spectra yields the frequency dependence of the splitting presented in Fig.4.23B. A Lorentzian fit to the splitting implies a mechanical Q factor of 145.

In Fig.4.24 we show measurements on a different dot in another ring resonator, labelled QD 2. Both rings have a radius of 12 µm. For QD 1, the *right* IDT is closer, because this QD is on a field towards the right of the device. The opposite is true for QD 2, which is in a field on the left. We note that there is no equivalent measurement on QD 1 for SAW excitation from the left IDT because of the aforementioned charging issues, which made it impossible to find the QD again in the same cooldown. In the measurements on QD 2 we do not observe the same resonant structure.

Figure 4.25 shows further measurements on QD 2 for the second and third frequency bands, using the closer IDT. In the former, we observe a roughly homogeneous broadening across the band. On the other hand, for the third band we see two very clear resonances at ~697.6 MHz and ~833.2 MHz, with little sign of splitting inbetween (note this measurement is taken at lower rf power). Fits to these features suggest mechanical modes with Q factors of 239 and 177, respectively. We note there is an additional shift at 850 MHz but this is not a split line and its origin is unknown.

From this data we can conclude that there is an enhanced strain interaction at resonant frequencies, and the resonance depends on the ring and on the position of the QD within the ring. Intuitively, two possible explanations are a Fabry-Pérot type resonance by reflection of the waves on the inner boundaries, and a mode propagating along the circumference of the ring. These situations are depicted in Fig.4.26. Considering the mechanical Fabry-Pérot situation

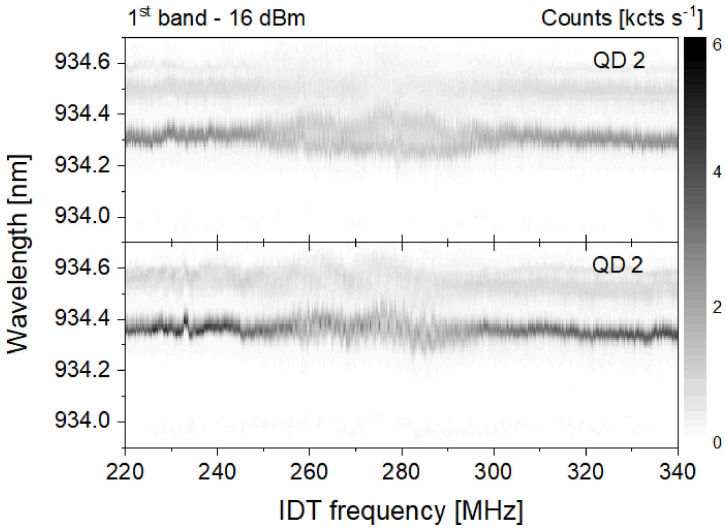

Fig. 4.24: Frequency scan over the first band on QD2. The top panel shows acoustic excitation from the left IDT, while the bottom panel shows excitation from the right IDT.

first, the resonance condition is satisfied when the distance travelled is

$$L = m\,\lambda_{\mathrm{SAW}} = 4R|\sin\alpha|, \tag{4.3}$$

with an integer m. The QDs studied are roughly located at 8 and 3 o'clock in their respective rings. From Eq. 4.3 we can extract the predicted resonant frequencies. Using the speed of sound on $LiNbO_3$ of $3990\,\mathrm{m\,s^{-1}}$ these do not match the experimental values. In order to reconcile the experimental data with the model, a speed of $3323\,\mathrm{m\,s^{-1}}$ would be necessary, which is too far off the speeds on GaAs or $LiNbO_3$. In addition, a SAW incident on a metallic strip is

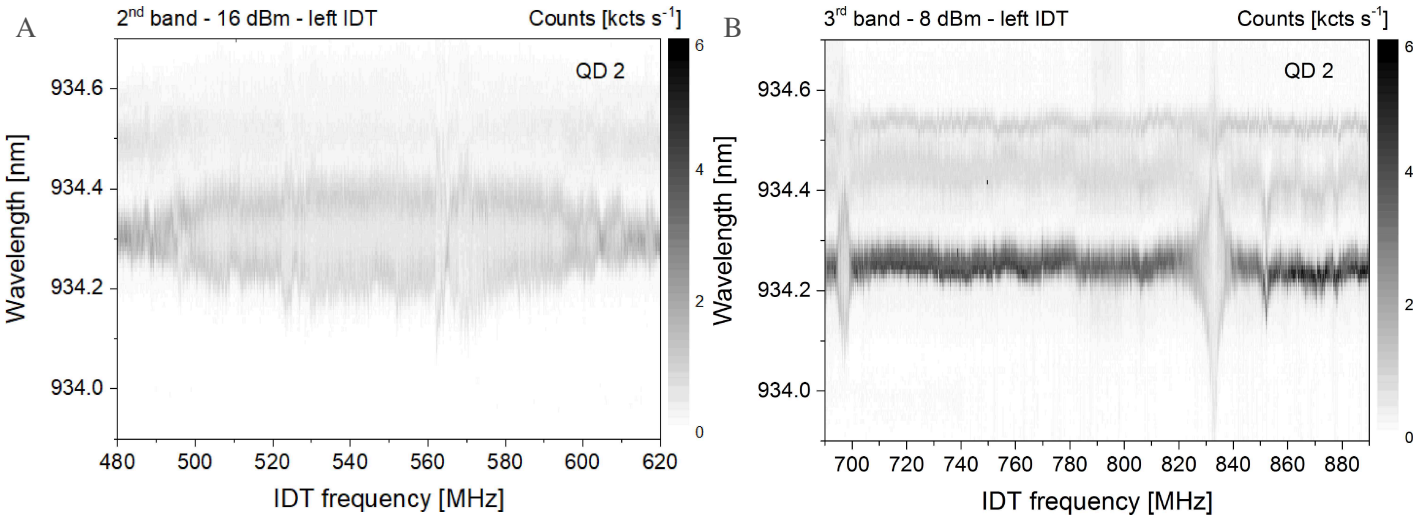

Fig. 4.25: **A.** Frequency scan over the second band on QD 2. **B.** Frequency scan over the third band on QD 2. Two resonant features are observed. The power for this measurement is lower than the others, at 8 dBm.

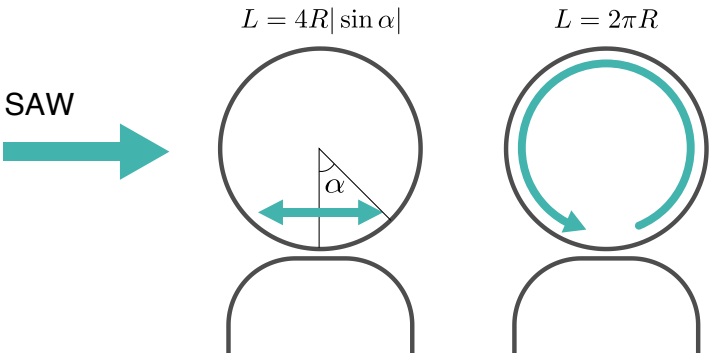

Fig. 4.26: Schematics for the simplest mechanical resonance models. The left ring shows the buildup of a standing wave inside the ring by reflection on the inner boundaries. The right ring shows a standing wave along the circumference of the ring.

reflected with a reflection coefficient of ~1 %[158]. Allowing for a comparable reflection on the thin GaAs ring would not lead to the high-quality mode observed. We therefore conclude that the behaviour measured cannot be explained by this type of resonance.

The alternative simple model of a mechanical mode propagating around the circumference of the ring requires the resonance condition

$$L = m\lambda_{\mathrm{SAW}} = 2\pi R. \tag{4.4}$$

In this case we would expect the wave to propagate with the speed of sound on GaAs of 2868 m s^{-1}. This model fits the data in Fig.4.23A and Fig.4.25B with $m = 7$, and $m = 18$ and $m = 21$, respectively. The speed shows little dispersion and is in the range $v = 2922 - 2992$ m s^{-1}. Notably, the resonances at $m = 19$ and $m = 20$ are not present in the data. It is possible that this is due to the positioning of the dot, as it can be close to a node of the standing wave for the missing modes. If this is the case, an equivalent measurement on another dot in a different position should show a different set of resonances. Considering the data in Fig.4.25A, it is also interesting that no resonance is measured across the transducer band. The SAW splitting is roughly constant throughout the ~100 MHz band. Given that the predicted free spectral range is

$$\Delta f = \frac{v}{2\pi R} \approx 38\,\mathrm{MHz}, \tag{4.5}$$

the observation of modes here would be expected. Again, the lack of clear modes in this range could be a consequence of the position of the dot.

Despite the partial agreement with the data, this simple model poses the problem of requiring waveguiding along the ring. The cross-section of the ring is 350×350 nm^2, compared to acoustic wavelengths of 4.6 - 14 µm. The ring could therefore not support a guided mode. Consequently, it is safe to say that there is a more intricate process taking place and more data is needed to pinpoint the origin of the resonances and selectively avoid or encourage them. These measurements are being continued at Augsburg University.

4.4 Conclusion

This chapter has introduced a novel hybrid platform for QPIC, combining epitaxial GaAs devices hosting single quantum emitters and a strong piezoelectric substrate, $LiNbO_3$. We have demonstrated that the fabrication is relatively simple and that the transferred membranes show remarkably strong adhesion despite the lack of adhesion promoter. This technique can be scaled to transfer complete wafers[264], making it indeed attractive for future applications.

Simple photonic devices were designed and fabricated, performing reasonably close to expectations. Characterisation of the structures shows a clear Purcell enhancement of single emitters with F_P~4. Quantum dot spectroscopy revealed instabilities in the emission, attributed to charging of the device. This issue needs to be investigated further to allow its mitigation. Furthermore, coherence measurements are required to confirm the conservation of the outstanding QD optical properties after processing.

The study of QD optical transitions with the addition of a SAW allowed the identification of strong acoustic resonances within the rings with Q factors in the 140 - 240 range. Although more detailed measurements are necessary, the preliminary data points towards the excitation of intrinsic mechanical modes which can be exploited to enhance the optomechanical interaction. Work on these devices continues with collaborators at the University of Augsburg at the time of writing.

Chapter 5

LEDs with Acoustical, Electrical and Optical Control

This chapter presents work to investigate the possibility of coherent control of single spins in self-assembled QDs via mechanical waves. We fabricate a charge-tunable diode that provides control over the charge state of a QD and interface it with an acoustic wave. We demonstrate optical spin pumping on a single hole and its frustration by the presence of a SAW.

5.1 Introduction

Spin-based qubits are one of the most promising candidates for a solid-state quantum information processing platform. Semiconductor quantum dots are particularly seen as a viable technology thanks to their high quantum efficiency and coherence properties, together with mature integration into photonic and electronic circuits. As mentioned in the previous chapters, SAWs have recently gained attention as a coherent control mechanism and on-chip interface between distinct physical qubits. Recent reports have demonstrated coherent manipulation of the spin in an NV centre in diamond by a SAW[232, 247]. This has been extended to spins in defect centres in silicon carbide[248] through the same spin-orbit-based mechanisms. A natural question is whether an analogous experiment can be performed with the InAs dots studied here and what the nature of the interaction between a SAW and a charge spin is. To date, single spins in self-assembled dots can be controlled by ultrafast pulses in Voigt geometry fields, as demonstrated in Refs.[265, 266], and there is one report of spin-flips with a magnetic antenna in a Faraday field[267]. If proven to coherently rotate a spin, an acoustic mechanism could be used to address single emitters individually and build complex, on-chip circuits[249]. Spin-flips based on spin-orbit interaction have been demonstrated for electrostatically defined dots through pulsed electric fields[268]. Phonons cannot directly flip a spin as they carry no angular momentum and such a process would thus violate angular momentum conservation. However, they can induce a spin-flip through indirect processes as a consequence of the spin-orbit interaction[269–271]. Both electron and hole spins can be expected to show spin-flips. In the case of holes, additional effects can be expected from heavy- and light-hole band mixing[272] (see Ch.1), which theory predicts becomes dominant for fields > 1 T[273].

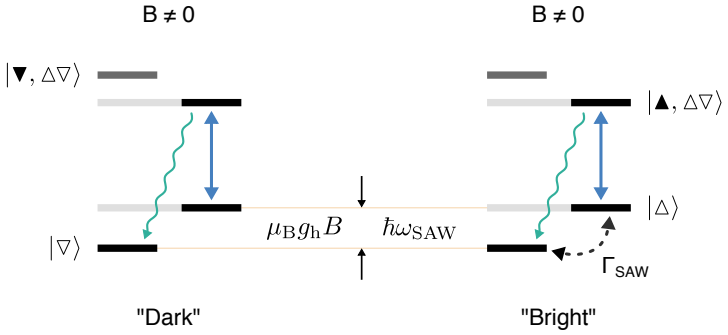

Fig. 5.1: Energy levels for a single hole in a QD in a magnetic field. A driving resonant laser field is represented by the blue arrow. Raman scattering is represented by the green arrow. Once the system is in $|\triangledown\rangle$ it remains there and the system goes dark. Ideally, a resonant SAW can complete the circuit.

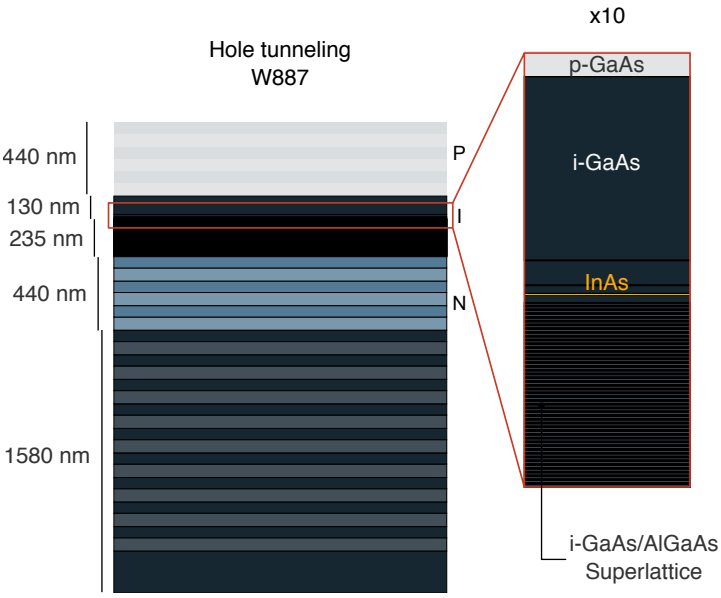

Fig. 5.2: Wafer structure of the samples for controlled hole tunnelling. The corresponding Cavendish wafer number is W887. The colours show the type of doping in the structure and the shading differentiates GaAs and AlGaAs layers. The inset shows a magnification of the QD region.

Here we study the feasibility of such an acoustic control mechanism, the idealized version of which is presented in Fig.5.1. With the transitions separated to a degree that they become individually addressable and spin-flips are suppressed, the state of the spin is initialised in $|\triangledown\rangle$ after continuous resonant illumination as shown. Ideally, a SAW phonon with energy matching the hole (electron) Zeeman splitting can coherently rotate the spin and thus close the excitation loop as shown in the right-hand side of the figure. We present a device with integrated electrical and acoustical control over individual QDs and preliminary experiments on it.

5.2 Device Design

Our devices consist of a weak planar cavity with doped mirrors to form a charge-tunable diode structure as described in Ch.1 (See Fig.1.10). Silicon and carbon are used to achieve the negative and positive doping, respectively. In both cases the doping concentration is $2\text{-}4 \times 10^{18}\,\mathrm{cm}^{-3}$. We perform measurements on devices from a wafer designed for controlled tunnelling of holes. Figure 5.2 shows the layer structure of the wafer. The GaAs/AlGaAs superlattice that serves as a blocking barrier is on the n-doped side. On the opposite side of the dot layer is the tunnelling barrier to the corresponding carrier reservoir, which is 20 nm thick.

The samples are etched into square mesas with 230 µm side length. Each sample has four individual mesas on a main mesa where the ohmic contact to the n-doped layers is made. Figure 5.3 shows the sample layout. IDTs are deposited on the intrinsic region below all doped layers. We note that, as detailed in Ch.2, initial tests were made with IDTs directly on the n-doped DBR. This has the advantage of reducing the losses at the mesa edges and avoiding the need for

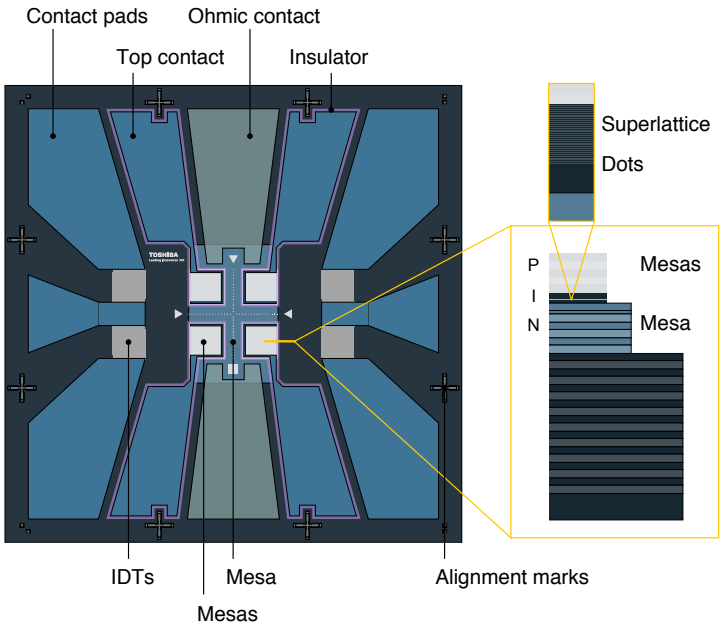

Fig. 5.3: Mask layout for charge-tunable LEDs. The inset shows the layers in growth direction along the highlighted cut-line for the case of controllable tunnelling of electrons. A single mesa (shown in white) is $230 \times 230\,\mu m^2$.

the main support mesa. The cost is increased damping of the SAW through screening of the electric potential component and crosstalk between the IDT and the diode. These tests found that the IDTs were completely shorted with resistivities $< 100\,\Omega$ between fingers. The addition of a reverse bias to deplete the doped layer[145] did not regain IDT functionality.

The fabricated samples use a variety of IDTs. From the literature, the charge spin is expected to be initialized at Faraday fields above 300 mT[62]. Assuming a g-factor of 0.5* this is equivalent to a SAW frequency of 2.1 GHz, which is readily attainable on GaAs. Two issues are considered at this point. First, IDTs have a very limited bandwidth in the MHz to tens of MHz range depending on the number of fingers. In this experiment it is desirable to have a wider range in order to scan the applied frequency in search of the resonance. Allowing for a 10 MHz bandwidth, the equivalent magnetic field range is less than 2 mT, which is on the order of the expected resonance width[267, 268]. Scanning the magnetic field instead is possible in principle but in practice the precision is not sufficient. To alleviate this issue most devices use chirped IDTs. Second, the higher frequencies confine the wave closer to the surface, which translates into higher reflection at the mesa edge(s). In addition, the doped layers will damp the wave by screening its electric component. It is therefore especially crucial to efficiently generate SAWs in these devices. Generally speaking, the number of fingers will determine the balance between efficiency and bandwith.

*Dots in our devices often exhibit unusually large in-plane hole g-factors. For dots with smaller g-factors the corresponding SAW frequency is reduced, making the fabrication requirements less stringent.

5.3 Deterministic Charge Control and Spin Initialisation

The starting point for these experiments is the demonstration of control over the charge state of the dot by the voltage applied across the p-i-n structure. This voltage shifts the QD energy levels across the Fermi energy, at which point a single charge carrier can tunnel into the dot. Single occupancy is guaranteed by Coulomb blockade[274]. Once in the dot, the trapped charge is not completely isolated but rather interacts with the reservoir. In particular, it is possible for the dot and back contact to exchange charge carriers of opposite spins. This process is known as co-tunnelling[51]. In the following sections we show the operation for holes. All data shown is taken at 8 K. Additional experiments with similar devices for controlled tunnelling of electrons were carried out but in those devices the spin initialisation was unsuccessful. This is discussed in more detail in appendix A.

5.3.1 Controllable Tunnelling of Holes

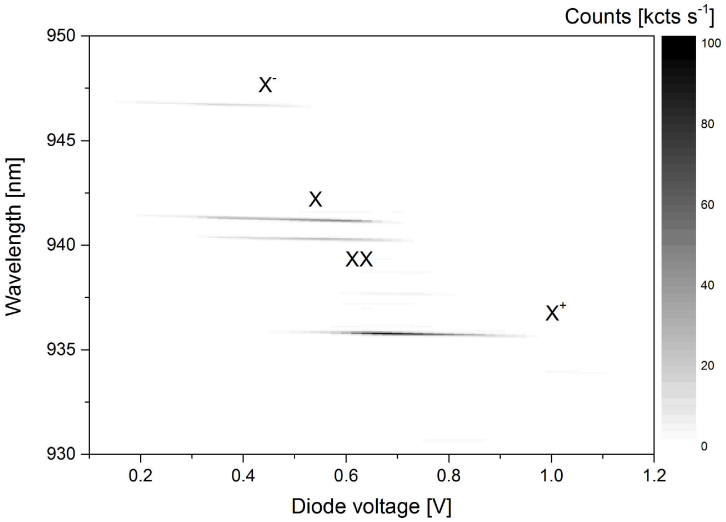

Fig. 5.4: Non-resonant PL charge map for a hole charge-tunable diode. The laser power is 3 µW.

Multiple devices for the controlled tunneling of holes were fabricated. Figure 5.4 shows the charge map of such a device. This is a µPL measurement of a single QD while the voltage across the diode is swept in forward bias. The non-resonant excitation laser has a wavelength of 850 nm. The map reveals transition lines spanning well-defined voltages, which we refer to as charge plateaus. This is the defining measurement of a charge-tunable device[72]. The plateaus are labelled according to their power dependence and FSS, as discussed in Ch.2. We note that due to Coulomb interaction, single electrons and holes charge at different voltages than excitons and charged excitons, resulting in the observed overlap of plateaus for different exciton complexes[71]. In the following, all measurements are performed on the X^+ line.

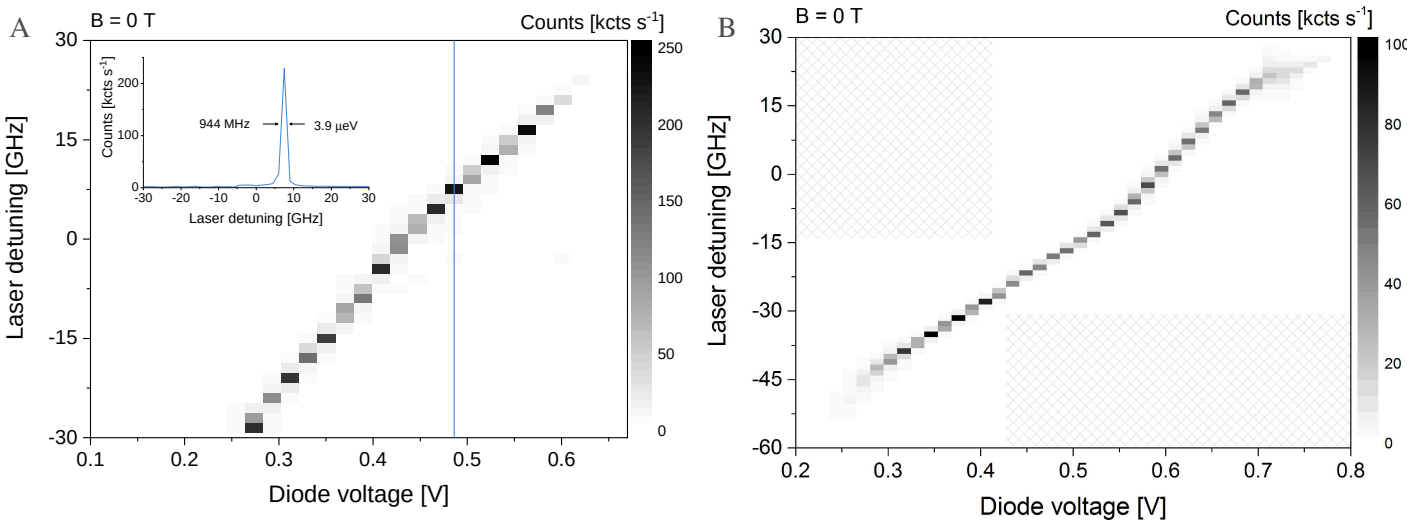

Fig. 5.5: Resonance fluorescence maps of the X^+ line for two dots in the same sample but different mesas. The inset of (**A**) shows the measurement at 0.486 V from which we extract a linewidth of 3.9 µeV. Shaded areas in (**B**) are not measured.

In contrast to the experiments shown in the previous chapters, the controlled tunnelling of carriers directly into the dots allows us to perform resonance fluorescence measurements without the addition of a weak non-resonant laser. Since the resonant laser is filtered by its polarisation, we can also omit a monochromating grating in the detection path. An RF* measurement of the X^+ plateau for two different dots is presented in Fig.5.5. The data clearly shows a plateau analogous to the non-resonant PL measurement. The emission energy shifts with the applied voltage due to the quantum-confined Stark effect. It is worth noting that there are small deviations from the underlying voltage dependence in the data. These are uncorrected artefacts from the laser, as the wavelength is scanned by a piezo stage with finite hysteresis, resulting in the possibility of small offsets between subsequent laser scans. The scan also shows another characteristic of charge-tunable diodes: at the centre of the plateau the behaviour is dominated by tunnelling of charges (first-order), whereas the edges are dominated by co-tunnelling (second-order) and appear blurred[62, 275, 276]. Figure 5.5(A) only shows the right-hand side of the plateau because it extends over a broad enough range for the Stark tuning to exceed the laser tuning range. We omit the left-hand side of the plateau in the following, as there is no fundamental reason to expect a different behaviour there. This is confirmed by the measurement presented in panel B, which is the same type of measurement on the same sample but on a dot in a different mesa. The laser is shifted coarsely to scan the plateau in two separate measurements. We note that the voltage values that define the plateau are different for the two

*Throughout this chapter there are references to resonance fluorescence (RF) and radio frequency (rf). The case of the acronyms is used to differentiate the two.

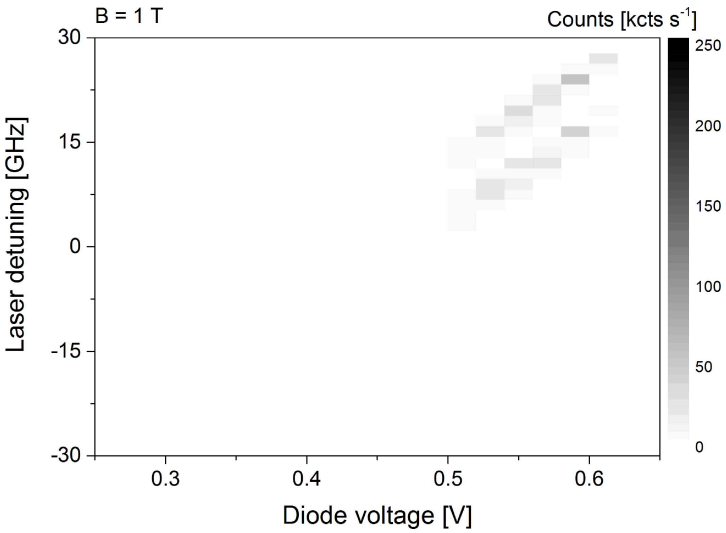

Fig. 5.6: Resonance fluorescence map of the X^+ line in a 1 T Voigt magnetic field. Only the plateau edges are visible for the two diagonal transitions, indicating spin pumping.

mesas due to differences in their contact resistances. Unless explicitly mentioned, all following measurements are performed on the dot presented in Fig.5.5A.

These measurements show that the devices work as intended in terms of charge control and we can address the desired transition. The next step is to demonstrate spin initialisation by optical pumping in a magnetic field, as reported in Ref.[62]. Resonantly driving one of the Zeeman-split transitions "shelves" the spin in the opposite Zeeman sublevel as the spontaneous spin-flip rate due to hyperfine interaction with the nuclear InAs nuclear spins is suppressed[62]. This is reflected in the vanishing RF signal from the central region of the plateau, while the edges remain unaffected.

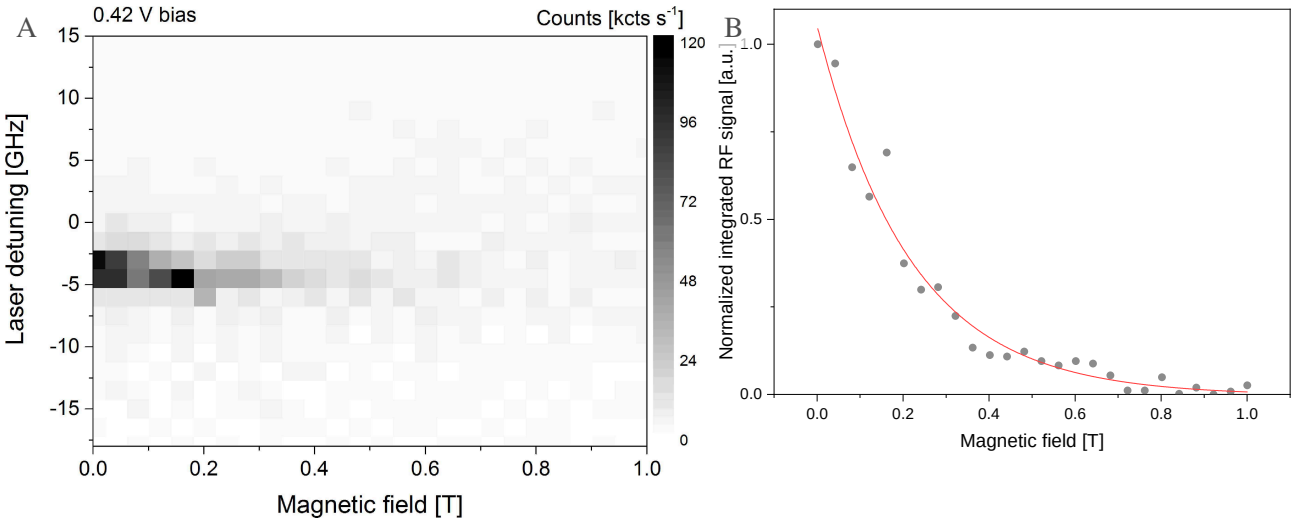

Fig. 5.7: **A.** Resonance fluorescence vs. magnetic field at 0.42 V bias. **B.** Integrated signal from (A) versus magnetic field. The data is fit with an exponential decay. The decay constant is 216 mT.

Figure 5.6 shows an RF scan over the dot in a 1 T Voigt field. Spin pumping is immediately evident as there is no measurable RF signal in the centre of the plateaus, while the right-hand side edge of each is clearly visible. The two curves observed correspond to the split vertical transitions over which the laser is scanned. In Fig.5.7 we show the measured RF signal at a fixed voltage in the centre of the plateau against the magnetic field. The signal is seen to decrease exponentially with increasing field magnitude, showing high-fidelity spin initialisation below 1 T. This provides the base conditions to investigate the response of the system to a SAW.

5.4 Effects of a Surface Acoustic Wave on a Hole Spin

We now investigate the effects of a SAW on the system. As in Ch.4, we use chirped split-5-2 IDTs in this sample. Their fundamental frequency lies at 825 MHz. Figure 5.8 shows RF scans in the centre of the plateau with varying acoustic powers. Contrary to the measurements shown thus far, we record the RF intensity as the transition is tuned through the laser by Stark tuning, rather than the other way around. The energy detuning is calibrated with the RF measurement of Fig.5.5A. Without a SAW we observe a sharp transition line corresponding to the X^+ decay. In the presence of a SAW the peak is split, as is familiar from previous chapters. At increased power, oscillations can be seen in the middle of the two-lobed split signal. Theoretically, such curves follow the intensity distribution

$$I(\omega) = \sum_{n=-\infty}^{\infty} \frac{J_n^2(\chi)}{\gamma^2 + (\omega - \omega_0 + n\omega_{\mathrm{SAW}})^2}, \tag{5.1}$$

where J_n is the Bessel function of the first kind, its argument χ is the dimensionless parameter quantifying the SAW splitting and γ is half the linewidth of the transition[228]. We find that this expression reproduces the observed lines. The acoustic frequency ω_{SAW} is used as a fitting parameter with values close to $2\pi \times 825\,\mathrm{MHz}$. Deviations are attributed to the uncertainty in the calibration of the energy scale. It is important to note that these measurements are taken without spectral filtering. Thus, at each point the APD records all the signal coming from the sample regardless of wavelength. They are therefore not comparable to the sideband measurements presented in Ch.3. The arrangement is equivalent to the laser sweeping across the SAW-modulated transition but all spectral information is reduced into an intensity value at each point.

As mentioned in the introduction, we ideally aim to match the Zeeman splitting to the SAW phonon energy. To that end, the first task is to determine the hole g-factor. Working in the Voigt geometry, it can be directly read out from a spectrum with all transitions resolved. With the detection polariser set at 45° we can detect all transitions simultaneously, as shown in Fig.5.9

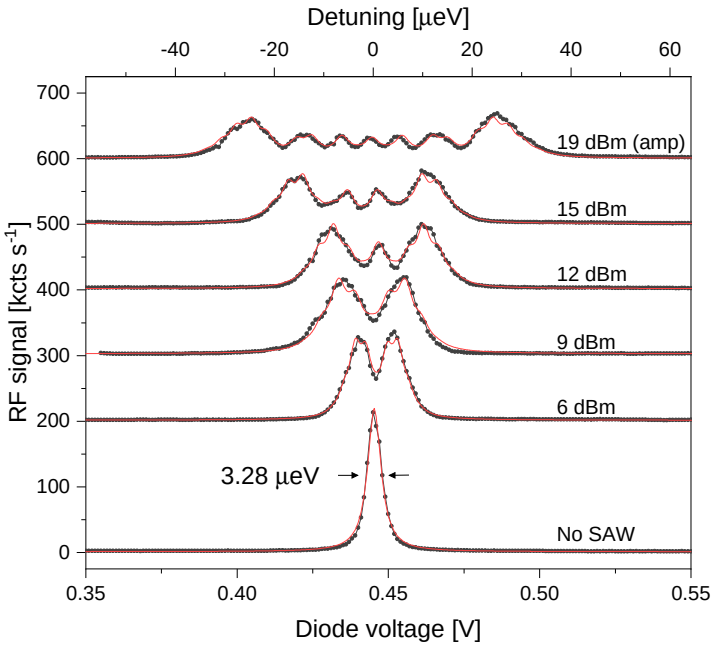

Fig. 5.8: Resonant fluorescence measurements for varying acoustic power at 825 MHz. The laser is kept constant at zero detuning while the transition is tuned by the bias on the diode. In the top curve the rf signal to the IDTs goes through an amplifier. Solid lines are fits to the data following Eq. (5.1) or a Lorentzian in the case without a SAW.

for a 6 T Voigt field. All transitions associated with the X^+ complex are clearly resolved, with corresponding wavelengths $\lambda_1 \ldots \lambda_4$ and energies $E_1 \ldots E_4$. From the splittings we can extract the magnitude of the electron and hole g-factors following $\mu_B|g_e^{\parallel}|B = E_1 - E_2 = E_3 - E_4$ and $\mu_B|g_h^{\parallel}|B = E_1 - E_3 = E_2 - E_4$, under the assumption that both have the same sign[277]. We note that we assign the central energies of the measured peaks to the corresponding transitions based on the polarisation measurement and previous experience on these samples. The assignment can be proven by means of a pump–repump scheme, or alternatively, a pump scheme with randomization. In the former, resonant laser fields are used to drive two of the four transitions, which, together with knowledge of the polarisations, allows the precise determination of the energy level scheme. This has been demonstrated for both electrons[278] and holes[279]. The latter technique involves simultaneous driving of the system with one weak non-resonant and one resonant laser. The non-resonant laser ensures the system is randomized by driving all transitions, while the resonant laser will only drive one of them at a time. Depending on which transition is being driven preferentially, some peaks will be dominant in the spectrum. This is demonstrated in the next chapter.

Following our assignment, we obtain $|g_e^{\parallel}| = 0.239$ and $|g_h^{\parallel}| = 0.571$. We note that observing $|g_h^{\parallel}| \gtrsim |g_e^{\parallel}|$ is not common, but has been reported previously[277, 279] and we have measured such behaviour in a number of dots. The extracted value for $|g_h^{\parallel}|$ is equivalent to a splitting of 2.4 GHz at 300 mT. The chirped split-5-2 IDTs found in this device should generate SAWs in the 825, 1650, 2475 and 3300 MHz bands. Unfortunately, we only see evidence of acoustic tuning in the first of these bands and experiments are thus limited to this frequency. Other

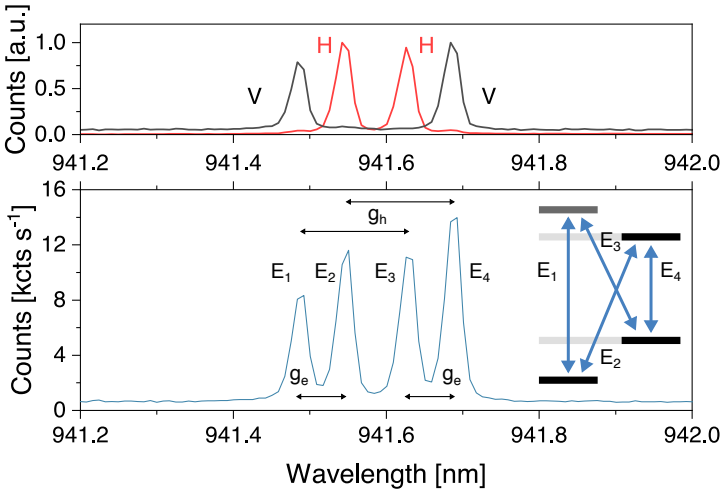

Fig. 5.9: Spectrum of the X^+ transitions in a 6 T Voigt field under 3 µW 850 nm laser irradiation. The bottom panel shows a spectrum with the polarisation adjusted so all transitions are visible, while the top panel resolves their polarisation. The inset presents the assignment of the energies to the transitions in the energy level diagram.

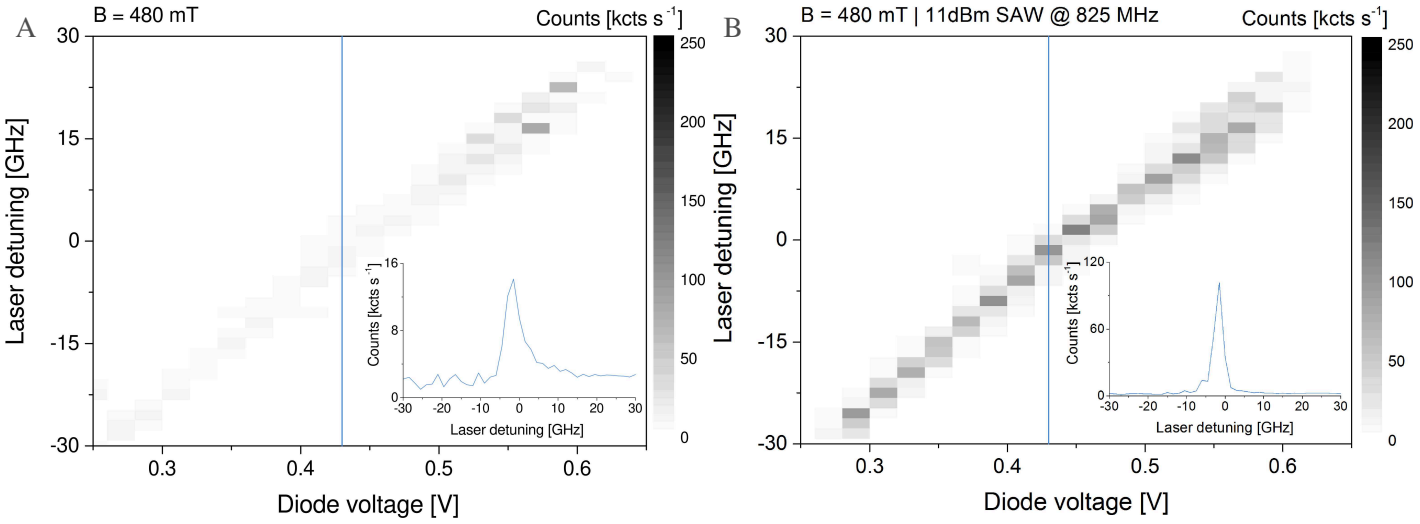

Fig. 5.10: Resonance fluorescence maps of the X^+ lines at a Voigt field of 480 mT. **A.** No SAW. The inset shows a cut line at 0.43 V bias. **B.** Addition of a SAW at 825 MHz and 11 dBm input power. The inset shows a cut line at 0.43 V bias.

charge-tunable devices show acoustic tuning at 2500 MHz with single finger IDTs designed for that frequency. We therefore attribute the lack of acoustic tuning in the higher bands to the lower SAW generation efficiency at those frequencies. The frequency of 825 MHz corresponds to a magnetic field of 100 mT, at which the RF signal is minimally suppressed in the centre of the plateau, making any type of optically detected spin resonance challenging. Barring a resonant experiment, we focus on the RF plateau at 480 mT. Figure 5.10 compares its measurement with and without a SAW. Following from the previous section, we observe clear but incomplete spin initialisation, as some degree of signal remains in the middle of the plateau. In the case of a SAW being present, the signal recovers to around half its original value.

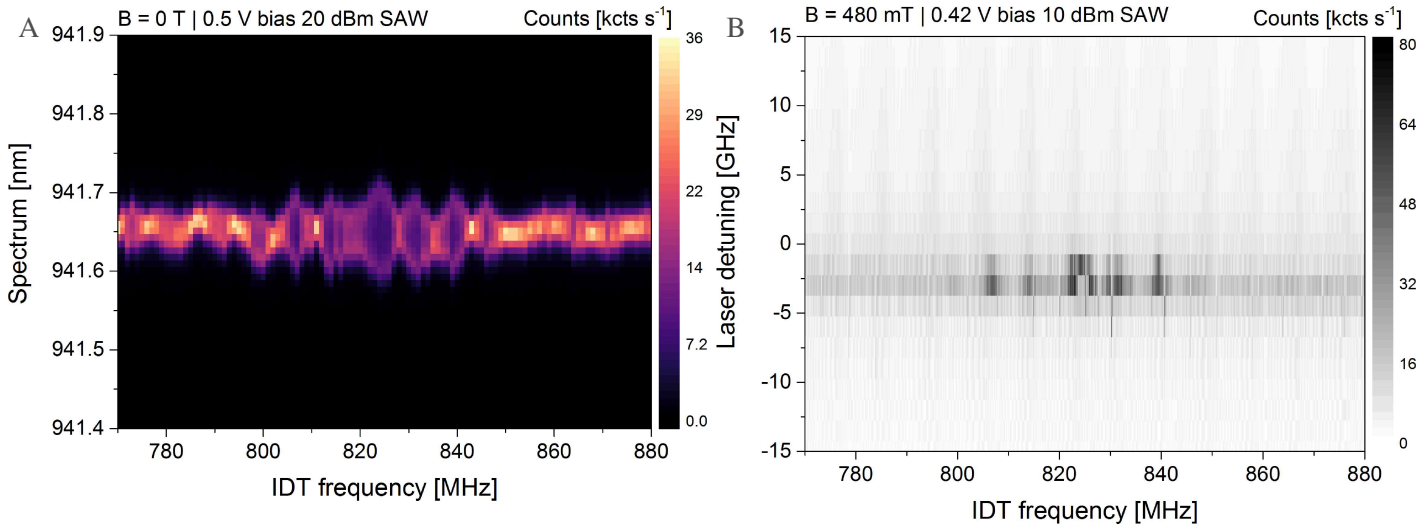

Fig. 5.11: **A.** PL spectrum vs. IDT frequency for an X^+ line at 0 T. **B.** RF measurements over the same transition vs. IDT frequency at a field of 480 mT.

We next investigate the frequency dependence of this RF signal recovery, as presented in Fig.5.11. The chirped IDT produces the complex interference patterns mentioned in the previous chapter. This is reflected in the oscillating SAW modulation amplitude within the SAW generation band in Fig.5.11A. This feature is faithfully replicated when the measurement is performed with resonant excitation, as presented in Fig.5.11B. Comparing the two measurements it is clear that the RF signal recovery matches the frequencies at which the SAW amplitude is maximal. This measurement proves that the signal recovery originates from the SAW. However, it is not a resonant process and the mechanisms at play need to be identified. One possible explanation is that the SAW locally heats the sample. We note that at the applied rf power there is no measurable increase in the temperature reading from a thermometer underneath the sample holder but this is not a reliable proxy for the direct surroundings of the dot. We can locally heat the sample by applying a high rf power on the IDT at a frequency where no SAW generation is expected. Our particular cabling is especially lossy around 2.0 GHz. We find that it is indeed possible to heat the sample to a degree where we recover roughly half of the original signal. However, the linewidth is broader in that case (2.96 GHz vs 2.23 GHz). In addition, we do not observe a shift in emission energy with the rf powers applied for SAW generation. From this we conclude that although an increased temperature is certainly expected to be detrimental and a potential contributing factor at high powers, it is not the main reason for the recovery here. A different possibility is that the SAW drags away charges from the QD and introduces new ones, whose spin is randomly orientated. SAWs are known to have such an effect in 2D electron gases and in QDs. To investigate this further we measure the RF plateau at 1 T for three different acoustic powers. These are presented in Fig.5.12. Panel A shows that

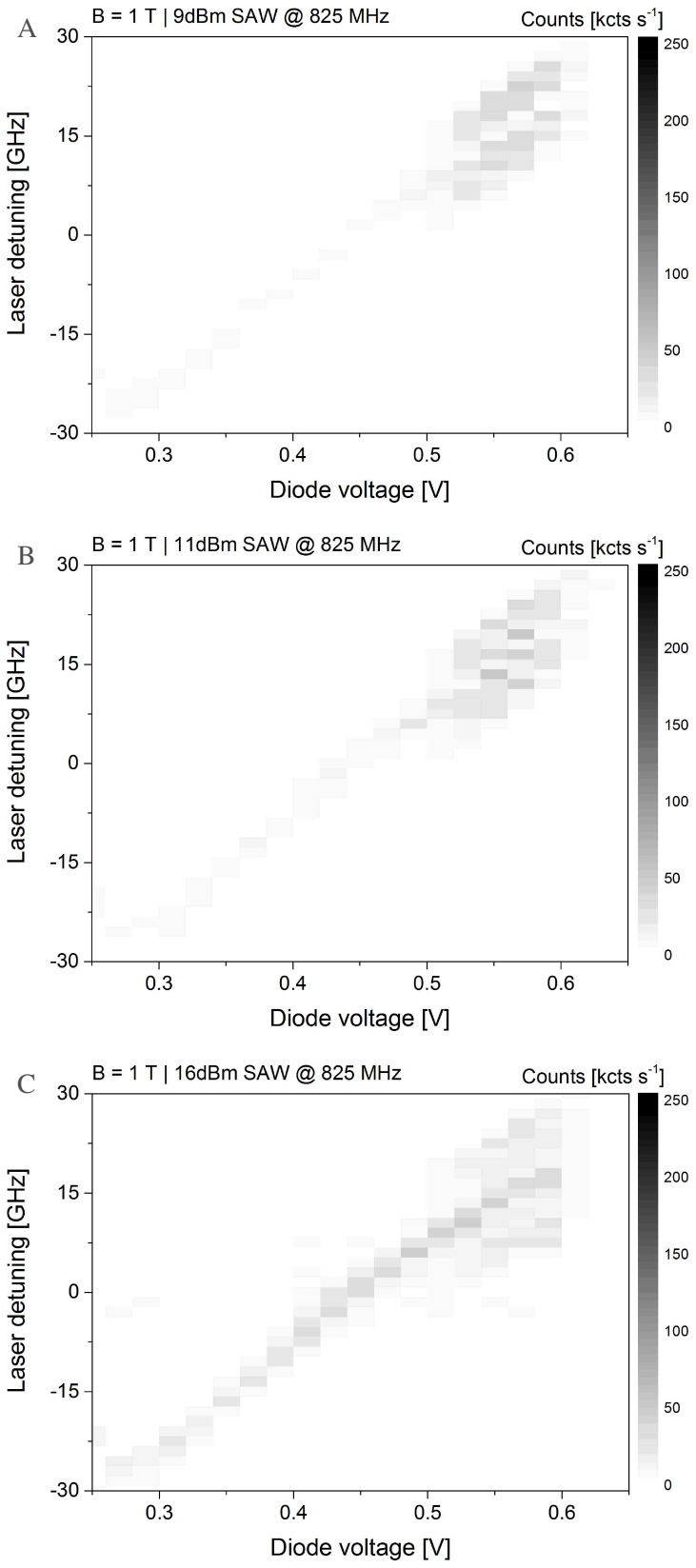

Fig. 5.12: Resonance fluorescence measurements of the X^+ plateau at 1 T Voigt field. A cw SAW at 825 MHz is added to the system. The laser power is 40 nW. **A.** 9 dBm SAW. **B.** 11 dBm SAW. **C.** 16 dBm SAW.

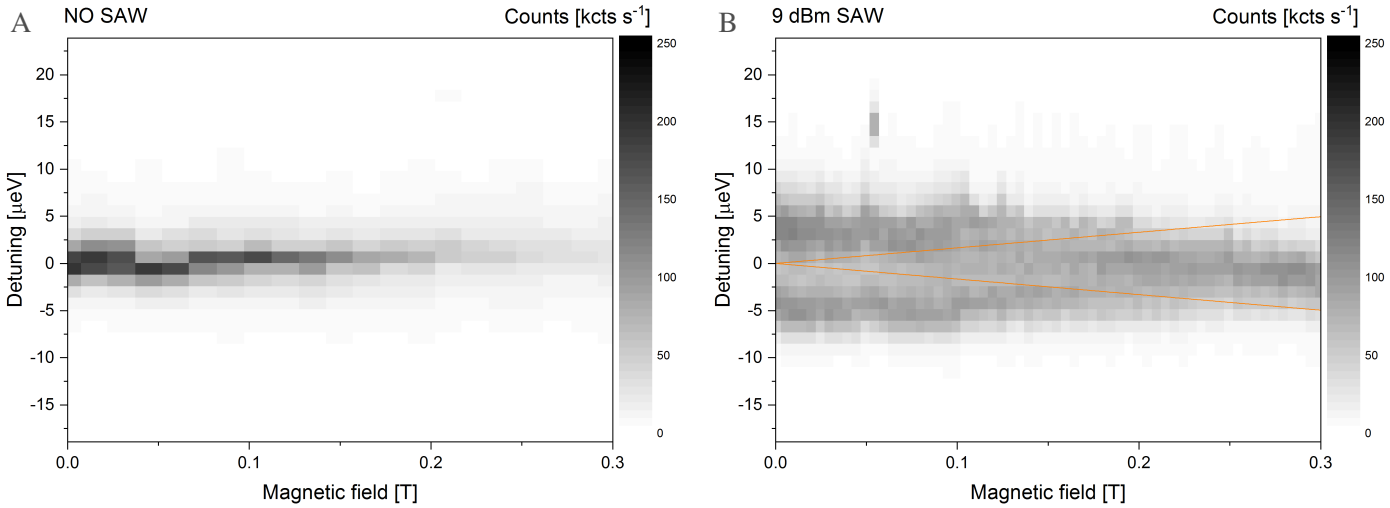

Fig. 5.13: Resonance fluorescence measurements with fixed laser energy vs. magnetic field. The transition is scanned over the laser by Stark tuning. **A.** No SAW. **B.** 9 dBm cw SAW excitation at 825 MHz. The orange lines mark the Zeeman splitting of the vertical transitions.

an acoustic power of 9 dBm does not significantly increase the RF signal in the centre of the plateau, contrary to the measurement at 480 mT. This would not be the case if the SAW were sweeping charges in and out of the dot. The other two scans show that a higher power increases the degree of signal recovery, which we discuss below.

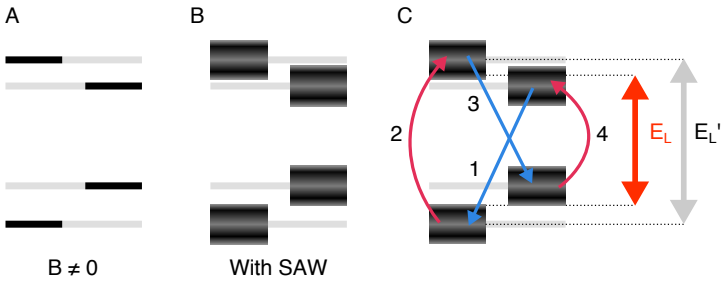

Fig. 5.14: **A.** Energy levels in a magnetic field. **B.** Energy levels effectively broadened under the presence of a SAW. **C.** The broadening leads to some overlap between Zeeman split levels depending on the SAW modulation amplitude. When the laser energy E_L matches the overlapped regions, the system can cycle through the energy levels. When the detuning is larger than the SAW modulation amplitude (E_L'), only one of the vertical transitions is driven and spin pumping takes place.

Focusing on a SAW with 9 dBm input power we perform RF measurements against the magnitude of the magnetic field as presented in Fig.5.13. Without a SAW we observe the exponential decay as measured before in Fig.5.7. With a SAW we can see the splitting at zero field as in Fig.5.8. This evolves into a single RF peak between the two transitions at 300 mT. At first glance this is counter-intuitive. We note that the SAW-induced energy shift affects Zeeman-split transitions equally and there is no dependence of the splitting on the magnetic

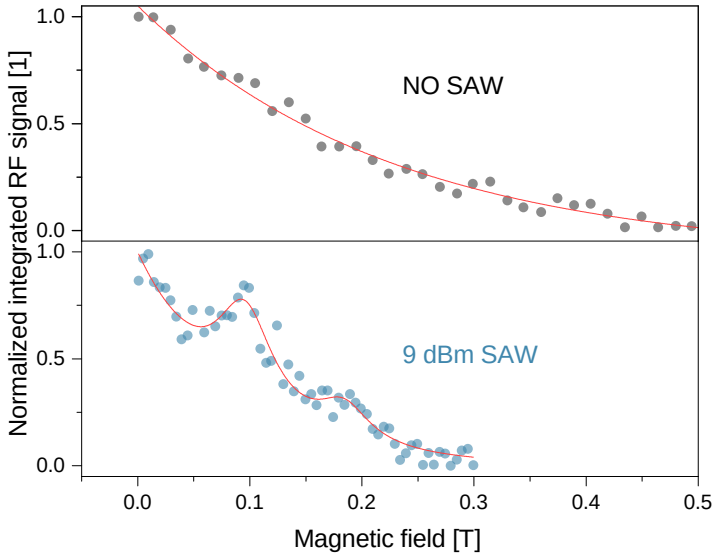

Fig. 5.15: Integrated RF signal vs. magnetic field, extracted from the measurements in Fig.5.13. The curve without a SAW is fitted with an exponential decay. The decay constant of 228 mT agrees with the previous measurement in Fig.5.7. The bottom curve is fitted with the sum of an exponential decay and two Lorentzians with FWHM of 61 and 56 mT.

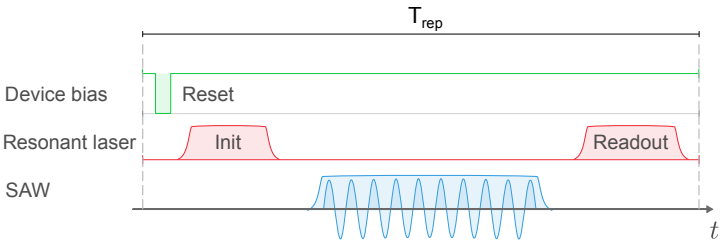

Fig. 5.16: Pulse sequence for pulsed measurements separating the acoustic and optical effects.

field. Therefore, one could expect the measurement to reveal two SAW-broadened spectra following the Zeeman-split transitions marked in orange. However, this neglects the fact that the measurement is performed resonantly with the conditions for fast optical spin pumping, leading to the exponential decrease in signal recorded in panel A. Figure 5.14 schematically presents the energy levels for the dot at non-zero magnetic field. With a SAW, the energy levels are effectively broadened, leaving an energy range where the Zeeman-split levels overlap. From Fig. 5.8 we can extract a SAW tuning amplitude χ of 11.73 µeV. At 300 mT and zero detuning, this SAW tuning leads to a dynamic overlap of both transitions with the laser. Therefore, the system can cycle in a figure-of-eight loop and no spin initialisation takes place, resulting in the strong signal observed. On the other hand, for detunings greater than $\chi/2$, the same SAW tuning can only bring one of the transitions into resonance with the laser and not the other one. In this case spin pumping takes place and no signal is recorded. This also fits with the measurements at 1 T presented in Fig.5.12: when the Zeeman splitting surpasses the SAW modulation amplitude no RF is recovered. A higher acoustic power increases the SAW tuning range and hence the overlap between Zeeman levels and the observed signal.

Figure 5.15 shows the integrated RF signal as a function of magnetic field*. Interestingly, there is a clear peak around 100 mT, where a resonance is expected and a second, weaker peak at twice that field. We fit the data with the sum of an exponential decay and two Lorentzians with 61 and 56 mT linewidths. This is much broader than what can be expected for a single spin-flip event but in the same order of magnitude as reported values for averaged measurements on electron spins[268]. These peaks could indeed be due to a resonant process but they can also stem from sideband transitions allowing the cycling through the energy level diagram in the mentioned figure of eight fashion. In order to discern the contributions involved it is necessary to temporally separate the optical and acoustic excitation. A measurement sequence as outlined in Fig.5.16 could give some insight into the dynamics of the process. If there is a resonant effect on the spin through mechanical action alone, Rabi oscillations should be present in the readout with changes in the SAW pulse duration. This measurement is feasible but requires fast pulsing of the SAW compared to the lifetime T_1 of the charge. Lifetimes of 20 ms have been demonstrated for electrons in charge-tunable diodes[14]. For holes, values around ~1 ms have been reported[74, 280]. Dephasing lifetimes between 20 and 100 ns have been reported[281, 282]. The length of the SAW pulses is limited by the time needed to build up the wave inside the IDT. The shortest SAW pulses are around 20 ns long. The temporal separation of acoustic and optical pulses is therefore in principle possible. A new device with acoustic transducers at higher frequencies is needed to investigate this.

5.5 Conclusion

We have presented devices with controllable tunnelling of holes, integrated with acoustic transducers for SAW generation. We demonstrate high fidelity spin initialisation by means of optical pumping in Voigt magnetic fields below 1 T. We then perform resonant excitation of the system and show that a SAW can frustrate spin initialisation, proven by the revival of the fluorescence signal. This recovery is observed at different fields to varying degree depending on the acoustic power, which is explained by the SAW modulation of the two vertical transitions of the system and does therefore not involve a spin-flip. Nevertheless, we record data indicating the possible existence of a resonant process in addition to this modulation. Further work is needed to determine if this is a consequence of sideband transitions or spin-flips. The investigated device is limited to a relatively low frequency of 825 MHz, which needs to be increased to determine if the SAW can indeed induce a coherent spin rotation in this system.

*The bright point at 50 mT and 15 µeV detuning is an artefact of the laser and is not included in the summed curve.

Chapter 6

Proposal for Generation of Multi-Photon Entangled States from a Quantum Dot

This chapter is devoted to the introduction of a proposal for the generation of multi-photon entangled states, which constitute an invaluable resource for the development of all-optical quantum information processing architectures and quantum technologies in general. The following expands on the results published in Ref.[18]. The work was jointly carried out with James P. Lee, a fellow Ph.D. student who did much of the prior work on resonance fluorescence from QDs in pillar microcavities[283]. The measurements presented here were performed as a team. The data analysis was also collectively carried out, albeit with a larger contribution by the author. In the first part of the chapter the proposal is introduced and discussed in the context of similar proposals. The second part presents our preliminary efforts towards its experimental implementation using quantum dots, in which we show proof-of-principle experimental validation of the key parts of the protocol. We note that the scheme is in principle applicable to any photon-emitting qubit system with coherent rotations.

6.1 Introduction

The motivation for this particular experiment is set out in the introduction to this thesis and Ch.1. In a single sentence, the drive behind it is the realisation of a practical source of multi-photon entangled states that can be used to create larger entangled states through HOM-based fusion[32]. Large states could be used to perform quantum computation. Consequently, multiple proposals for the generation of such a stream of photons have recently been put forward[46, 48, 284, 285]. Here we focus on sequential generation schemes, where photons build up the entangled state as they are emitted from an ancillary qubit[286]. Of particular interest is Lindner and Rudolph's scheme for the generation of a linear cluster state from a QD: the photonic cluster state machine gun[49]. Their scheme proposes the creation of polarisation-entangled states from resonant scattering off a singly charged QD. The idea works by synchronising the sequential pulsed excitation of the system with the precession of the associated spin in a magnetic field. A natural challenge is that the polarisation entanglement is incompatible with polarisation filtering for RF. Linder and Rudolph's scheme was recently demonstrated experimentally by Schwartz *et al.* using the dark exciton, thereby bypassing the RF problem[287]. This proves the validity of the scheme and is a strong motivation for the pursuit of this approach to LOQC. The disadvantage of the dark exciton approach is unresolved questions as to the nature of the information conservation in the phonon-assisted transitions needed.

Here we explore the impact of applying recent developments in coherent spin control and cavity-QED techniques to the challenge of building a source of photonic states useful for quantum computing applications. With this aim, we introduce a new scheme that encodes the photons in time-bins instead of polarisation. This scheme has the potential to be modified

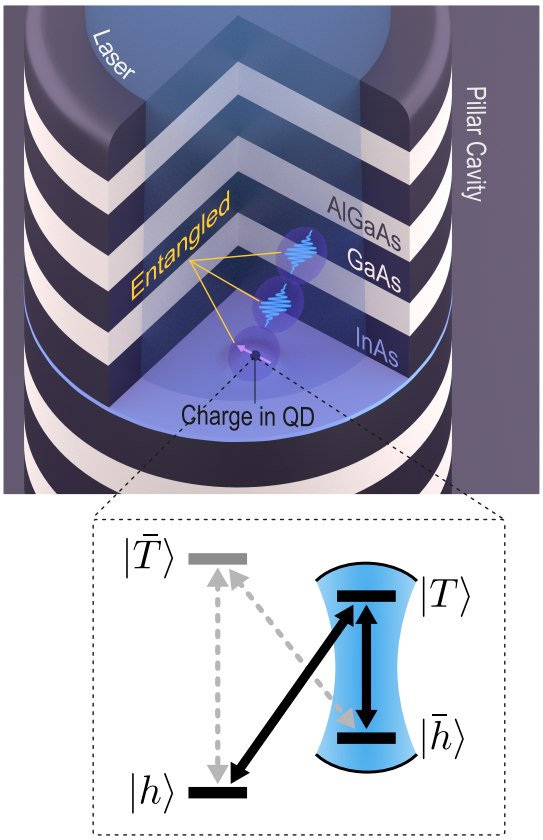

Fig. 6.1: Artist's impression of the proposed system, consisting of a QD embedded in a micropillar cavity. The QD is probabilistically charged with a single hole and placed in a Voigt magnetic field, resulting in the presented energy level diagram. The Zeeman-split hole (trion) states are denoted by $|h\rangle$ and $|\bar{h}\rangle$ ($|T\rangle$ and $|\bar{T}\rangle$). The $|T\rangle \rightarrow |\bar{h}\rangle$ transition is brought into resonance with the cavity. A chain of entangled photons is then generated by repeated excitation of the system as described in the main text.

to create a broad set of useful states, as characterized in Ref.[286], with linear cluster states being particularly attractive. For this work however, we focus on how we could generate a Greenberger-Horne-Zeilinger (GHZ) state as it is conceptually and experimentally simpler. The necessary modification to the protocol to turn the output into a linear cluster state is outlined in Sec.6.4.

We focus on a QD embedded in an optical microcavity in a Voigt magnetic field. A single charge carrier trapped in the dot has an associated spin that can be controlled by ultrashort optical pulses. Spins in QDs are especially attractive for the task at hand thanks to their coherent properties[282] and readily available entanglement with photons[288–290]. Photons are generated sequentially by resonant scattering from the quantum dot, while the charge's spin is used to determine the encoding of the photons into time-bins. In this way a multi-photon entangled state can be gradually built up. Figure 6.1 shows a representation of the idealised system*. With a simple optical pulse sequence we demonstrate a proof-of-principle experiment of our proposal by showing that the time-bin of a single-photon is dependent on the measured state of the trapped charge's spin.

*We use a shorthand notation for the states to represent the hole and trion by $|h\rangle$ and $|T\rangle$, respectively. In the notation of Ch.1, $|T\rangle = |\blacktriangle, \triangle\triangledown\rangle_x$.

6.2 Scheme

As discussed in Ch.1 and shown in Fig.6.1, a single hole and the corresponding trion in the QD exhibit a double Λ system, where the four distinct and individually addressable transitions enable fast spin manipulation. We assume the cavity selectively enhances one of the vertical transitions. For our scheme we exploit this enhancement to allow a cycling transition suitable for spin-state readout and entangled-photon generation. The proposal for generating time-bin encoded GHZ states, as illustrated in Fig.6.2, is as follows:

1. Prepare the trapped hole spin in the $\left(|h\rangle + \left|\bar{h}\right\rangle\right)/\sqrt{2}$ superposition state by performing spin initialisation and subsequently using an off-resonant pulse to perform a $\pi/2$ rotation of the spin.

2. Resonantly drive the cavity-enhanced transition with a π-pulse to generate a photon in the *first* time-bin conditional on the spin being in the $\left|\bar{h}\right\rangle$ state. The resulting state is $\left(|h\rangle\,|0_{\tau=1}\rangle + \left|\bar{h}\right\rangle|1_{\tau=1}\rangle\right)/\sqrt{2}$.

3. Flip the spin of the trapped charge to produce the state $\left(\left|\bar{h}\right\rangle|0_{\tau=1}\rangle - |h\rangle\,|1_{\tau=1}\rangle\right)/\sqrt{2}$.

4. Resonantly drive the cavity-enhanced transition with a π-pulse to generate a photon in the *second* time-bin conditional on the spin being in the $\left|\bar{h}\right\rangle$ state. The resulting state is $\left(\left|\bar{h}\right\rangle|0_{\tau=1}1_{\tau=2}\rangle - |h\rangle\,|1_{\tau=1}0_{\tau=2}\rangle\right)/\sqrt{2}$.

5. Another spin-flip yields $-\left(|h\rangle\,|0_{\tau=1}1_{\tau=2}\rangle + \left|\bar{h}\right\rangle|1_{\tau=1}0_{\tau=2}\rangle\right)/\sqrt{2}$.

6. Repeating steps 2-5 builds up the desired entangled state. After three repetitions the state of the system is $\left(\left|\bar{h}\right\rangle|0_{\tau=1}1_{\tau=2}0_{\tau=3}1_{\tau=4}0_{\tau=5}1_{\tau=6}\rangle - |h\rangle\,|1_{\tau=1}0_{\tau=2}1_{\tau=3}0_{\tau=4}1_{\tau=5}0_{\tau=6}\rangle\right)/\sqrt{2}$.

7. Finally, a spin readout can be done by applying a $\pi/2$ spin rotation and resonantly driving the cavity-enhanced transition. This effectively performs a measurement in the $|\pm\rangle = \frac{1}{\sqrt{2}}\left(|h\rangle \pm \left|\bar{h}\right\rangle\right)$ basis. Assuming we measure the spin to be in the $|-\rangle$ state, we are left with the photonic state $\left(|0_{\tau=1}1_{\tau=2}0_{\tau=3}1_{\tau=4}0_{\tau=5}1_{\tau=6}\rangle + |1_{\tau=1}0_{\tau=2}1_{\tau=3}0_{\tau=4}1_{\tau=5}0_{\tau=6}\rangle\right)/\sqrt{2}$. Rewriting this state using a photon in an odd-numbered time-bin to be a logical 1 and a photon in an even-numbered time-bin as a logical 0 we have the state $\left(|111\rangle + |000\rangle\right)/\sqrt{2}$, which is a 3-photon GHZ state.

The outlined scheme is conceptually similar to Lindner and Rudolph's in the sense that it relies on periodic resonant excitation of a charged QD for the generation of photons. However, it provides a series of improvements:

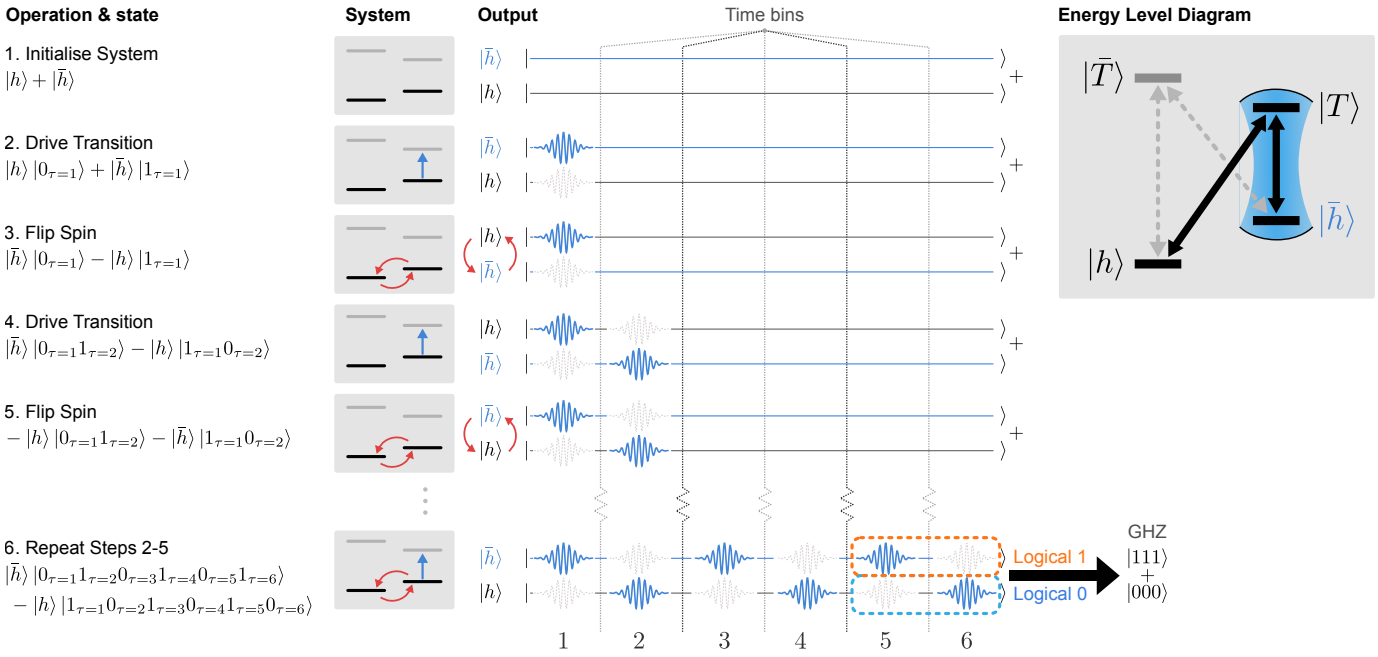

Fig. 6.2: Diagram of the proposed scheme for the sequential generation of time-bin-encoded multi-photon entangled states. The double-lambda energy level diagram corresponds to a single hole trapped in a QD in a Voigt magnetic field. The Zeeman-split hole (trion) states are denoted by $|h\rangle$ and $|\bar{h}\rangle$ ($|T\rangle$ and $|\bar{T}\rangle$). The vertical $|T\rangle \leftrightarrow |\bar{h}\rangle$ transition is selectively enhanced by an optical cavity and is used to resonantly scatter photons. Each photon (qubit) is spread across two time-bins.

Time-bin encoding Rather than having the state encoded in the photon polarisation, encoding it in time has two important benefits. First, it allows for polarisation filtering to reject the reflected laser light when performing resonance fluorescence measurements. This is naturally incompatible with polarisation encoding. Second, time-bin-encoded states are well suited for transmission through optical fibre and integrated waveguide technologies as they suffer less from decoherence than polarisation-encoding techniques[291, 292].

Voigt geometry field and spin rotations The orientation of the magnetic field determines the allowed transitions between the energy levels. At zero magnetic field or in Faraday fields only the vertical transitions are allowed. This configuration is required for the proposal in Ref.[49]. The authors suggest using a weak Voigt magnetic field to allow the spin to precess in order to perform the spin rotations needed to generate the cluster state. It is unclear to what extent this Voigt field would remove the Faraday-like selection rules, as in a Voigt field both vertical and diagonal transitions are allowed. This is complicated by the fact that, ideally, one would use a larger magnetic field, as this has been shown to improve the coherence time of the trapped spin[293, 294].

In addition, a key advantage of using Voigt magnetic fields is that it allows for high-fidelity coherent optical spin rotations, which has not been reproduced in Faraday fields. Of particular interest here are the experiments reported in Refs.[265, 266], where a several-picosecond circularly polarised laser pulse was used to induce a spin rotation via the AC Stark effect. We propose to use this technique to implement the required spin rotations while using cavity enhancement to negate the detrimental effect of the allowed diagonal transitions.

Cavity enhancement The selective cavity enhancement of a single transition has been used to demonstrate fast spin preparation, cavity-enhanced Raman scattering and the generation of time-bin-encoded single-photon states[295, 296]. In addition to increasing the expected number of repeated excitations of the vertical transition resulting in a higher probability of a successful spin readout, cavity enhancement has been shown to improve the coherence properties of the emitted light under resonant excitation[90, 94, 297]. Photons generated in this way are highly indistinguishable and so are suitable for HOM interference-based operations[16, 298]. We note that for a linear cluster state generated using Lindner and Rudolph's scheme, the coherence of the photons' wavepackets does not matter[299]. However, in order to be useful for quantum computing applications via HOM interference-based operations, the generated photons must have good coherence properties because 'degree of indistinguishability equals the degree of coherence'[300].

6.3 Control over a Hole Spin in a Quantum Dot

Here we present the initial experimental step required for the implementation of our scheme with the proposed QD-based system. The sample consists of a single layer of self-assembled InAs QDs, grown in the center of an AlAs/GaAs microcavity. The cavity is asymmetric with 25 DBR pairs on the bottom and 17 pairs on the top to enhance the collection efficiency by directing the emission away from the substrate. It is etched into ~2 μm diameter pillars. The sample was fabricated in 2008 by Dr. David Ellis from a wafer grown by Dr. Ian Farrer*. We focus on the positive trion transition within a single QD. The latter is confirmed with a standard second-order autocorrelation measurement (Inset of Fig.6.3).

The experimental arrangement used throughout is presented in Fig.6.3. Three lasers are used to control the state of the system. A continuous-wave (cw) laser (blue) is used for resonant excitation. Its output is modulated by an electro-optic modulator and combined on a beam splitter with a pulsed non-resonant laser (green – 850 nm). Spin rotations are performed by

*Cavendish wafer number W162.

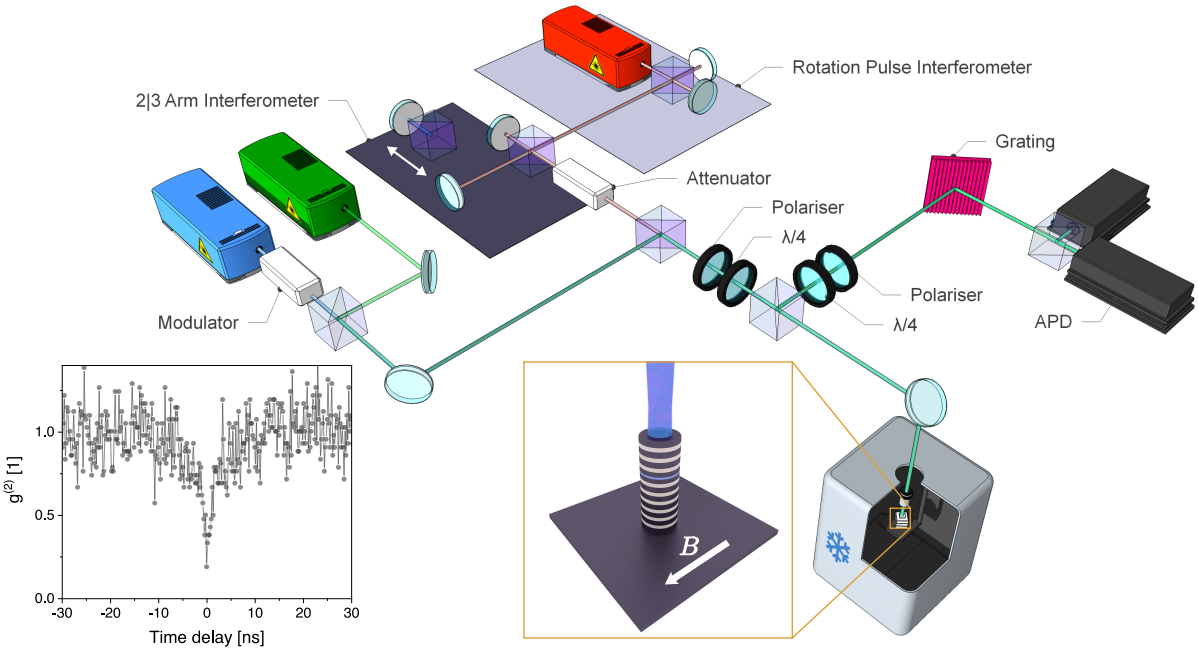

Fig. 6.3: Illustration of the experimental arrangement. See main text for details. The insets show a $g^{(2)}$ measurement under 1 µW non-resonant illumination and a schematic of the micropillar relative to the magnetic field.

pulses from a red-detuned mode-locked Ti:sapphire laser (red). The pulses are sent through an interferometer in order to create two closely spaced pulses required for the rotations, as will be discussed later. These double pulses are directed to a second interferometer that can have either two or three arms, depending on the pulse sequence required. This in turn is combined on a beam splitter with the output of the resonant and non-resonant lasers and focused on the cooled QD-micropillar system via a dark-field microscope. The output light is polarisation filtered by the dark-field microscope to remove the resonant laser light and a grating is used to spectrally filter the light from the other two lasers. The filtered output light is directed into a pair of APDs with timing electronics to time-tag each detection event.

For all data presented here we use the positive trion transition. The X^+ line is identified in the spectrum based on experience with the dots grown in the Cavendish Laboratory chamber W. We observe consistent spectral features across wafers, with the X^- and X^+ always present on the same side of the neutral transitions. These charged transitions corresponding to an excess electron or an excess hole are differentiated with certainty by growing charge-tunable diodes, as presented in the previous chapter. We note that the difficulty in assigning a spectral feature to a particular transition in a pillar is that transitions outside the cavity mode are suppressed and therefore hard to detect. This particular dot has been used for previous experiments, where the X and XX emission could be observed, allowing the identification of the transition as the

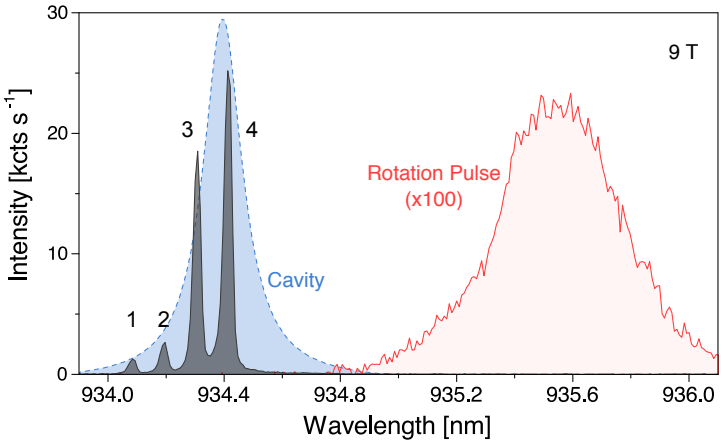

Fig. 6.4: Spectrum of the positive trion transitions in a 9 T Voigt geometry magnetic field. The cavity lineshape inferred from a white-light reflectivity measurement is shown in blue. The spectrum of the detuned rotation pulses before entering the fibre is shown in red.

positively charged trion. Figure 6.4 shows the spectrum at 5 K under non-resonant excitation in a 9 T Voigt geometry magnetic field. The spectrum indicates that the cavity-enhanced transition is Purcell-enhanced by a factor of ~5 and fitting a Lorentzian peak to the cavity mode allows us to determine that the cavity has a Q factor of ~7500. A typical spectrum from the Ti:sapphire

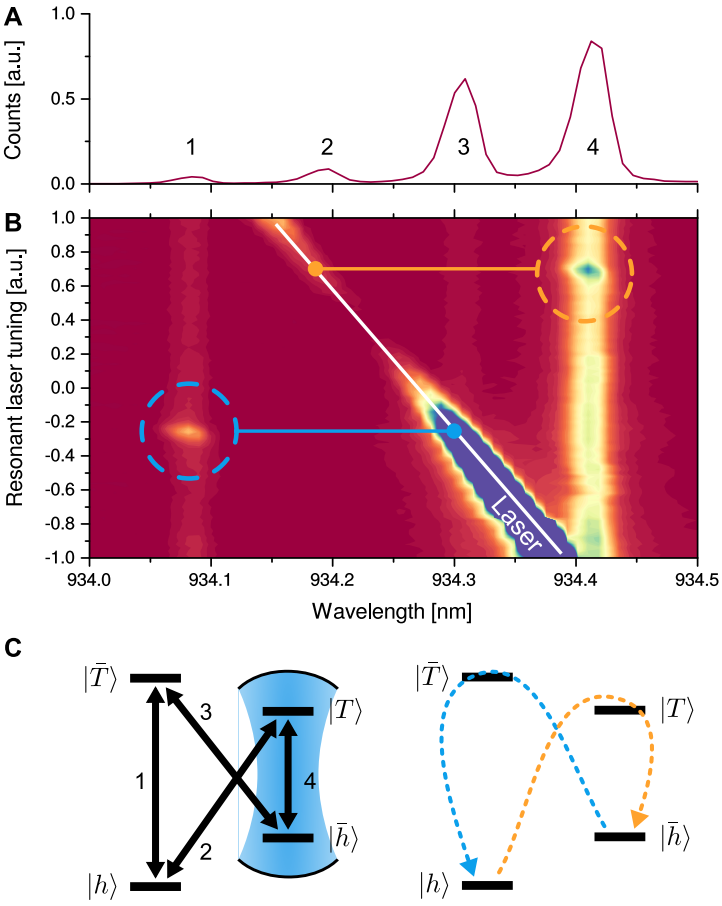

Fig. 6.5: Identification of spectral lines. **A.** Spectrum under non-resonant optical excitation. **B.** Spectra obtained under optical excitation with a non-resonant laser and a resonant laser scanned over the diagonal transitions (marked white line). The signal from the laser is not constant within the scan due to the fact that it is rejected by polarization filtering and this is optimized for a limited wavelength range. **C.** Deduced energy level diagrams.

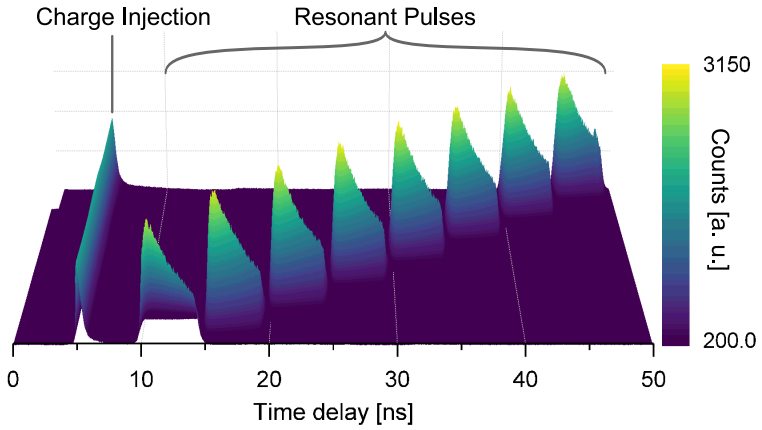

Fig. 6.6: Test of hole lifetime within the dot. A hole is inserted by a short 850 nm pulse and it is subsequently probed by a resonant pulse. A series of pulse sequences where the pulse separation is increased by 5 ns at a time shows no drop in probe pulse intensity, suggesting that the hole remains trapped within the dot for timescales >50 ns.

laser is also shown. As discussed later the laser pulses reach the cryostat through optical fibre and the actual incoming spectrum deviates from the one presented.

The spectrum at high magnetic fields gives information on the electron and hole g-factors but not on their sign[301]. In order to determine which spectral peak corresponds to each transition with absolute confidence, we excite the system using non-resonant light and simultaneously scan the narrow linewidth resonant laser across the central two transitions. Figure 6.5 shows the measured spectra, where intensity changes in the vertical transitions can be seen when the resonant laser crosses a diagonal transition. From this information we can assign each transition in the spectrum to the corresponding transition in the energy diagram. From the spectrum it is noticeable that transition #3 is also Purcell-enhanced. Fortunately, this transition links the $|\bar{h}\rangle$ state with the $|\bar{T}\rangle$ state, which is unpopulated during the photon generation scheme. If the situation was reversed and transition #2 was enhanced, the QD would not be suitable for the implementation of the scheme, as the readout and photon generation rely on resonant scattering on $|\bar{h}\rangle$ without modification of the state. As in the previous chapter, we use the assignment of the transitions to the peaks in the spectrum to extract the magnitude of the in-plane hole and electron g-factors. This particular dot also shows $|g_{\mathrm{h}}^{\parallel}| > |g_{\mathrm{e}}^{\parallel}|$, with $|g_{\mathrm{h}}^{\parallel}| = 0.605$ and $|g_{\mathrm{e}}^{\parallel}| = 0.294$.

The non-resonant laser is used throughout to probabilistically introduce a hole into the QD and to stabilize the charge environment[16, 116, 302]. We probe the lifetime of the hole in the QD by injecting a hole with a non-resonant pulse and subsequently probing it with a resonant pulse on the cavity-enhanced transition after a variable amount of time. The results are shown in Fig.6.6 and indicate that the hole remains trapped in the dot for times greater than 50 ns, since no decrease in readout signal intensity is observed. This is enough for the demonstration performed here. Deterministic charging schemes[303–305] could be used in future. As mentioned in the previous chapters, the spin storage time in such devices is shown to be at least 20 ms[14].

6.3.1 Spin Initialization

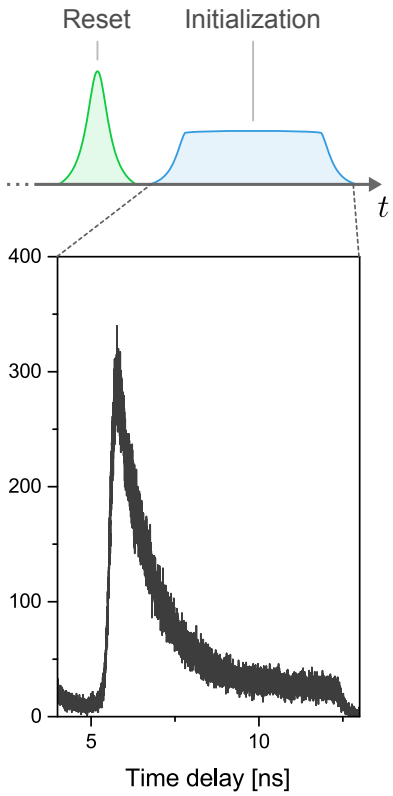

Fig. 6.7: Pulse sequence used for the injection of a charge carrier and its spin initialisation. The measurement shows the exponential decay of the recorded signal as the spin is shelved in the $|h\rangle$ state.

The probe pulses in Fig.6.6 show a marked exponential decay for the duration of the pulse (4.5 ns). This is a clear sign of spin initialisation and the first requirement for control over the spin state of the hole. After probabilistic injection of a charge, spin initialisation is observed upon driving transition #4 owing to the allowed decay path from $|T\rangle$ to $|h\rangle$ (transition #2), which means the population is eventually shelved in $|h\rangle$ after some excitation and relaxation cycles. Figure 6.7 shows the time-resolved trace of an initialisation pulse with a steep decay, indicating that the $|h\rangle$ state can be prepared with high fidelity. From this data we can estimate the initialisation fidelity F_{ini} of this operation. The maximum signal is observed immediately after spin injection and can therefore be assumed to be equally distributed between the two spin states, or equivalent to 0.5. In that case $F_{\text{ini}} = 1 - 0.5\text{min/max} = 95.63\%$. However, we note that the maximum signal is actually closer to 0.9, as will be clarified later. This modification yields $F_{\text{ini}} = 92.14\%$. We take the uncertainty between these two values, which is larger than that from a fit to the data, as the error. These values will also have some contribution from the background, which is not removed. Therefore, we conclude we achieve initialisation in line with the reported state of the art[62]. We note that cavity-enhanced spin preparation in a similar experimental setup has been demonstrated by driving a non-enhanced transition in order to increase the speed of spin-preparation[296]. We choose not to initialise this spin to avoid additional experimental complexity at the cost of longer spin-preparation times.

6.3.2 Spin Rotations and Ramsey Interference

Having a reliable way to initialise the spin, the next operation needed for the implementation of the photon generation scheme is spin rotations. In order to coherently rotate the spin we use the Ti:sapphire laser to produce ~6 ps long pulses, which allow for spin manipulation via the AC Stark effect[265, 266]. To demonstrate this, we prepare the system in $|h\rangle$, apply a rotation

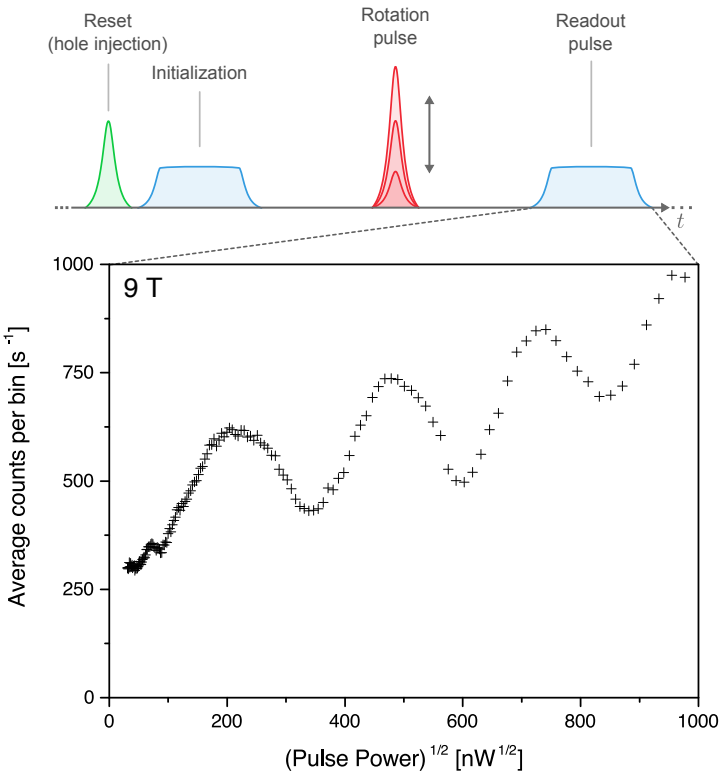

Fig. 6.8: Pulse sequence used to measure Rabi oscillations and the corresponding measured RF intensity as a function of the square root of the rotation-pulse power. The signal is averaged over twenty 50 ps time-bins

pulse, and then apply a second resonant pulse to serve as a readout pulse. We will only see emission if the $|\bar{h}\rangle$ state has a non-zero probability of being occupied. Fig.6.8 shows the result of varying the rotation pulse power. Rabi oscillations can be seen in the intensity of the readout pulse. As well as observing the expected oscillations, we record a substantial increase in signal as the rotation pulse power is increased. We attribute this to two factors. First, the spectral detuning of the rotation laser is not sufficient to completely suppress off-resonant excitation of the system. Second, a long fibre propagation length ($\sim$ 10 m between laser and sample) allows for non-linear effects such as chirping and broadening through stimulated Raman scattering in the fibre. The spectral and temporal profile of the pulses is thus altered by the time they arrive at the sample[306, 307]. Both of these issues are exacerbated by the high laser power used, which is an unavoidable consequence of using a laser in the stopband of the cavity. These effects inevitably reduce the fidelity of the spin rotation. We believe they can be alleviated using a free-space setup and spectral filtering of the rotation laser in future experiments.

In order to demonstrate complete control of the spin state, we perform Ramsey interference with the hole spin. An interesting detail here is that, unlike in prior work, a single rotation pulse is not sufficient to flip the spin state. Due to the 9 T magnetic field, the hole spin precession time is $\sim$ 13 ps – comparable to the length of the Fourier-transform-limited rotation pulse (the hole splitting is 75.26 GHz). As a result, a single pulse does not perform a rotation about the y (or an equivalent) axis (see Fig.6.9A), but about an axis with some z-component – high fidelity

spin-flips are therefore not possible. This situation is depicted in Fig.6.9B. To counter this problem, we lower the magnetic field to 6T to increase the spin-precession time (the Larmor frequency drops to 49.58 GHz). This on its own is not enough to enable high fidelity π rotations. We therefore additionally use a two-pulse sequence to flip the spin, as reported for trapped ions in Ref.[308]. This two-pulse sequence allows us to perform a complete π rotation as illustrated in Fig.6.9C. Since high magnetic fields are required to separate the transitions enough to allow for selective cavity enhancement, the precession time for the trapped spin will be short. Consequently this two-pulse rotation scheme is likely to be useful for all realisations of our scheme.

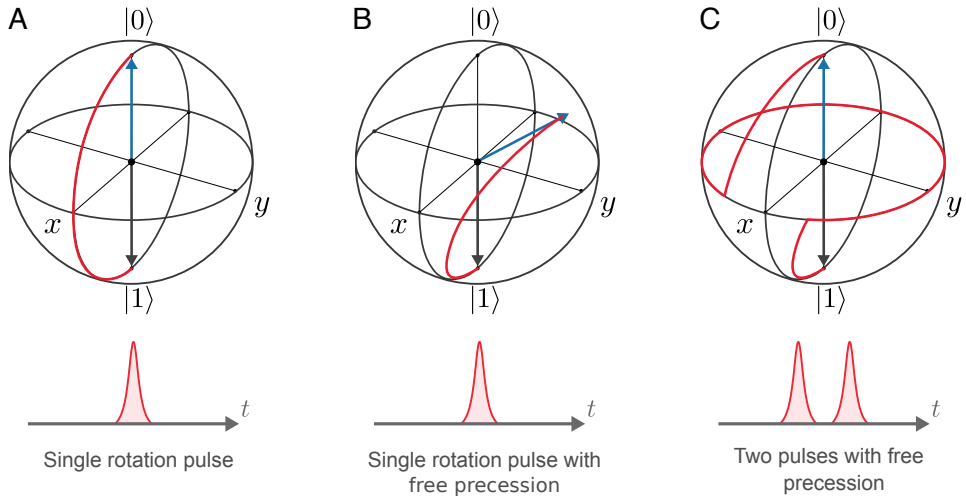

Fig. 6.9: Rotation pulses on the Bloch sphere. **A.** Ideal π rotation about y with a rotation pulse. **B.** The trayectory of the Bloch vector is affected by the precession during the rotation pulse when the Larmor precession frequency is comparable to the length of the pulse. As a consequence, the vector cannot reach the opposite pole. **C.** Workaround for fast-precession issue by having two accurately timed pulses. The first rotation brings the Bloch vector to the equator, where it precesses around z. A second rotation can then complete the transfer onto the pole $|0\rangle$.

To implement this two-pulse scheme we start by performing a Ramsey interference measurement with the interferometer in front of the laser, as presented in Fig.6.10. The position of the movable interferometer arm determines the separation between consecutive pulses and with that the free precession time. We note that the two-pulses are too close in time to be individually resolved in our measurement. In fact, we can identify the position of zero delay where the two-pulses interfere. We therefore fix this interferometer to operate close to this time delay.

Having established the time delay between the double pulses, we measure Ramsey interference using the two-pulse rotation scheme. Figure 6.11 shows the intensity of the RF signal from the readout pulse as a function of the separation between the rotation pulses for $\pi/2$

and π rotation pulses, comparing the single-pulse and double-pulse cases. For two-pulse $\pi/2$ rotations, we observe Ramsey fringes with a visibility of 42%. In the case of π pulses, we do not observe Ramsey fringes (Fig.6.11), indicating that we are reliably flipping the spin state as expected. This is in strong contrast with the case of using only single rotation pulses, where the spin can't be flipped to the same degree. We conclude that it is therefore necessary for us to use this two-pulse rotation technique to perform the time-bin entanglement scheme. The Ramsey fringe visibility is low relative to prior work[265]. We attribute this to both the slow drift in laser power and intensity over the duration of a measurement and the aforementioned issues of non-linear effects in the fibre. From this data we can estimate the $\pi/2$ rotation fidelity in a similar manner as for the initialisation fidelity. Here we take $F = \max(\min + \max)^{-1} = 71.22\%$ to be the fidelity of the measurement. This in turn is equivalent to

$$F = \frac{1 + p_s}{2} \tag{6.1}$$

with the probability of sucess p_s, which determines the fidelity over the 50 % baseline. The probability of success follows from the probabilities of success of each individual step as

$$p_s = p_{s\,\mathrm{ini}}(p_{s\,\pi/2})^2 = (2F_{\mathrm{ini}} - 1)\,(2F_{\pi/2} - 1)^2 \approx (2F_{\pi/2} - 1)^2. \tag{6.2}$$

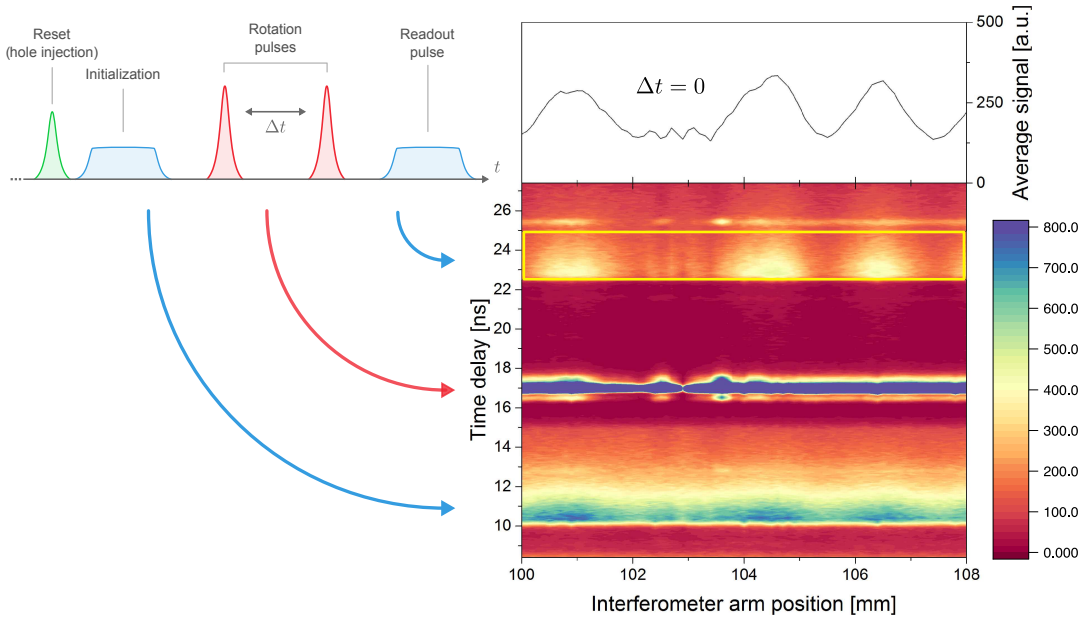

Fig. 6.10: Ramsey interference pulse sequence and measurement with the interferometer in front of the laser ("rotation pulse interferometer" in Fig.6.3). The area highlighted in yellow corresponds to the readout pulse and the average RF intensity is recorded in the top panel. The interference of the laser pulses around 103 mm marks their zero relative delay.

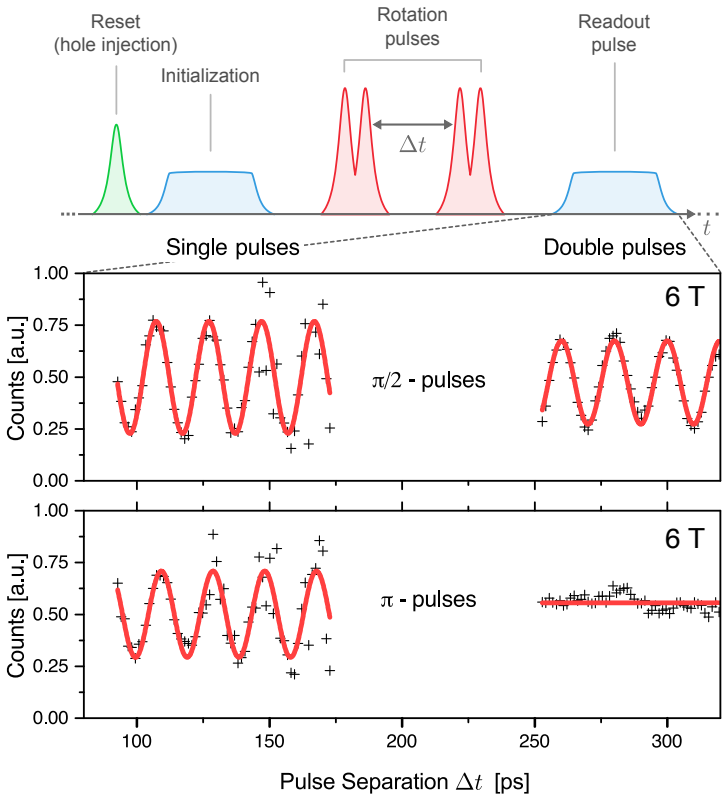

Fig. 6.11: Measurement sequence for Ramsey interference using double rotation pulses. The data shows the recorded interference for both single and double rotation pulses with the powers corresponding to $\pi/2$ and π rotations. Note that the data has not been artificially shifted but the measurements are taken at different time delays.

From this we infer $F_{\pi/2} = (1 + \sqrt{2F-1})/2 = 82.58\%$ for an individual rotation. The fidelity for a π rotation has a very similar value, as shown in the next section.

Figure 6.12A shows the time traces for initialisation and readout pulses at the maximum and minimum signal of the double pulse $\pi/2$ Ramsey interference measurement. Panel B of the figure shows the equivalent time trace for a double-pulse π rotation (not Ramsey interference). As mentioned above, one could expect the charge to be in a random state upon injection, such that the peak of RF signal in the initialisation trace is around 50 % of its maximal value. This maximal intensity should then be observed after having initialised the system in $|h\rangle$ and performing a spin-flip to $|\bar{h}\rangle$. However, this is not what we observe. After the π pulse rotation the state is of roughly equal brightness, suggesting that the bright spin state is preferentially populated.

Finally, we use a Ramsey interference measurement to extract the T_2^* time of the hole spin, as shown in Fig.6.13. From an exponential decay fit we find that $T_2^* = 2.11 \pm 0.11$ ns, in close agreement with the work in Ref.[309] but an order of magnitude lower than other reported values[281, 310]. This value is in line with measurements on other dots in the same sample[311]. The reported longer coherence times for hole spins are encouraging for the extension of the scheme. Although this is long enough for this experimental demonstration,

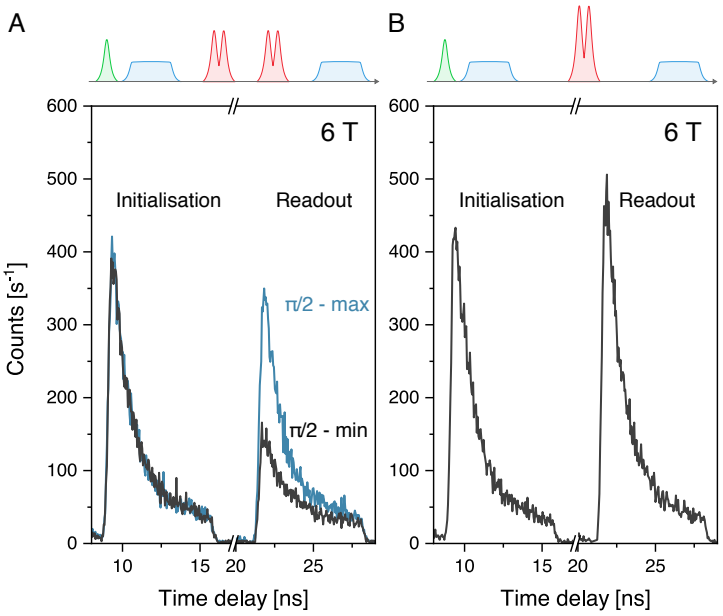

Fig. 6.12: **A.** Time-resolved measurement of the initialisation and readout pulses for the maximum and minimum readout signal in a Ramsey interference measurement with $\pi/2$ pulses. **B.** Time-resolved measurement of the initialisation and readout pulses for a π rotation.

there are techniques available to extend the coherence time via dynamical decoupling and nuclear-field manipulation[312, 313].

6.4 Proof-of-Principle Demonstration

Having demonstrated control operations over the spin we move on to implementing the first step of the proposed scheme by showing that the time-bin of the first photon is dependent on the measured state of the spin. The pulse sequence for generating a time-bin encoded photon is shown in Fig.6.14A. Just as before, the spin is injected and prepared in the $|h\rangle$ state. A double-pulse sequence is used to perform a $\pi/2$ spin rotation which prepares the spin in a superposition state. Then a sequence of a photon-generation pulse, followed by a double-pulse π rotation, and a second photon-generation pulse is used to generate a photon in the early or late time-bin, conditional on the spin state. The result of this process should be to generate a spin – time-bin entangled state. Finally, we projectively measure the spin state. To measure the $|\bar{h}\rangle$ state, we use a long resonant pulse to drive the $|\bar{h}\rangle \rightarrow |T\rangle$ transition – measuring a photon here projects the hole into $|\bar{h}\rangle$ (sequence A). To measure the $|h\rangle$ state, we apply a double-pulse π rotation sequence to flip the populations of $|h\rangle$ and $|\bar{h}\rangle$ and then measure $|\bar{h}\rangle$ (sequence B). Time-tagging each measured photon allows us to investigate the correlations between different events.

Figure 6.14B shows the degree of correlation of the prepared two-qubit states. This is the classical counterpart to the state fidelity and hence omits the phase relationship between spin and photons. For sequence A, where we measure the system in the $|\bar{h}\rangle$ state, there is a 77 %

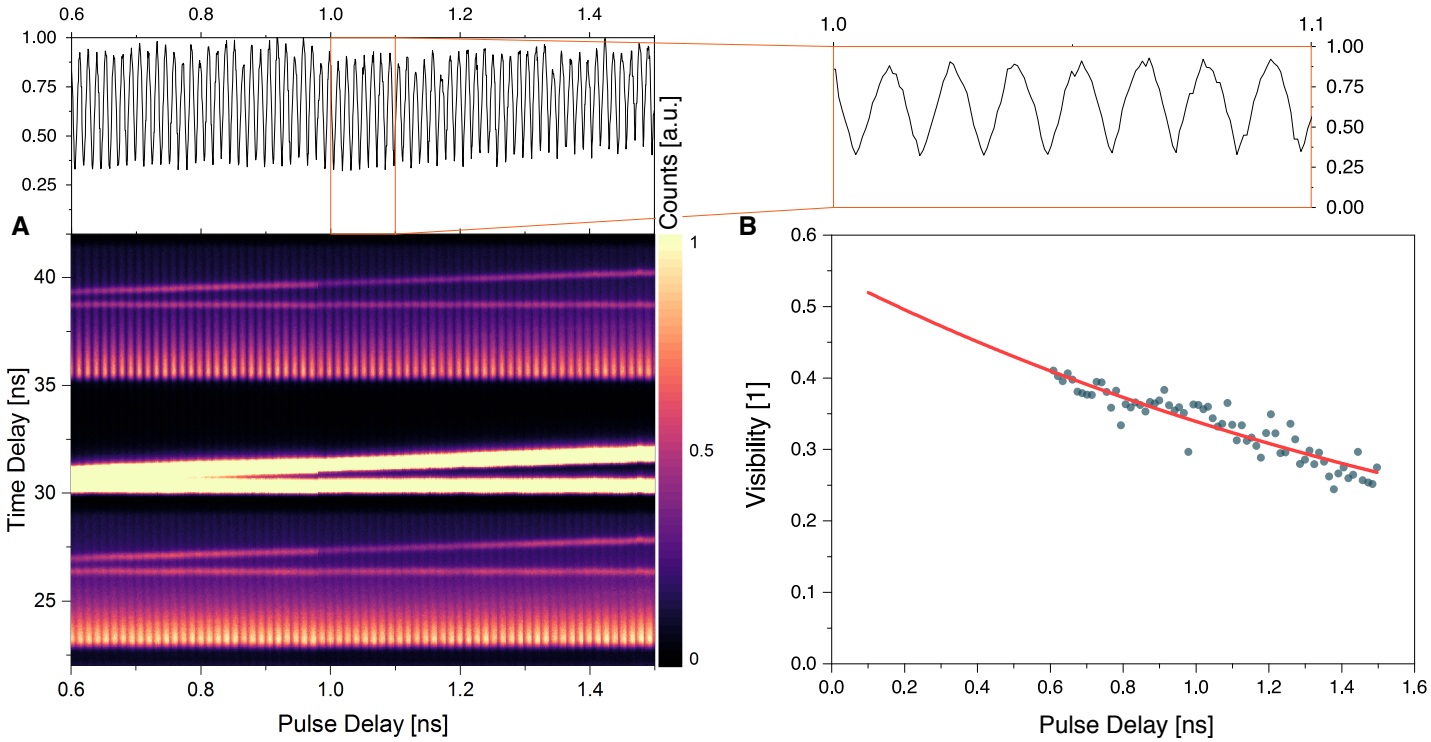

Fig. 6.13: **A.** Raw measurement of Ramsey interference. The bottom panel shows the complete measurement. The bright pulses in the middle are the rotation pulses, whose temporal distance increases. Reflections in the system are noticeable at the power used. The signal between 21 and 28 ns comes from the initialisation pulses, while that after the rotations is the readout. The top panel shows a cut line through the readout pulses. The inset shows a magnification of a 0.1 ns region. **B.** Extracted visibility versus pulse separation. An exponential decay curve is fitted to the data, giving a measurement of the coherence time $T_2^* = 2.11 \pm 0.11$ ns.

probability that the photon is in the second time-bin. In contrast, for sequence B, this probability drops and detecting the photon in the first time-bin becomes the more likely outcome (68 %) as expected. We therefore conclude that the photon time-bin is dependent on the measured state of the trapped hole spin.

From this measurement we can estimate F_π by comparing the two-pulse sequences. We can take the probability of success for sequence A to be $p_s^A = (2F_{\text{ini}} - 1)(2F_{\pi/2} - 1)(2F_\pi - 1)$. Then $p_s^B = p_s^A(2F_\pi - 1)$. Taking the ratio of these and using $F^{A|B} = (1 + p_s^{A|B})/2$ we can solve for $F_\pi = 83.35\%$.

Our results are consistent with the expected behaviour, albeit with reduced fidelity. The main hurdle to overcome in order to extend the produced state to two or more photons is the fidelity of the spin rotations. The decrease in output degree of correlation observed between sequences A and B in Fig.6.14 can be attributed to the additional π pulse employed in the latter. From our data we estimate fidelities of $F_{\text{ini}} = 92.14 \pm 3.49\%$ and $F_\pi \approx F_{\pi/2} = 82.58 \pm 2.73\%$

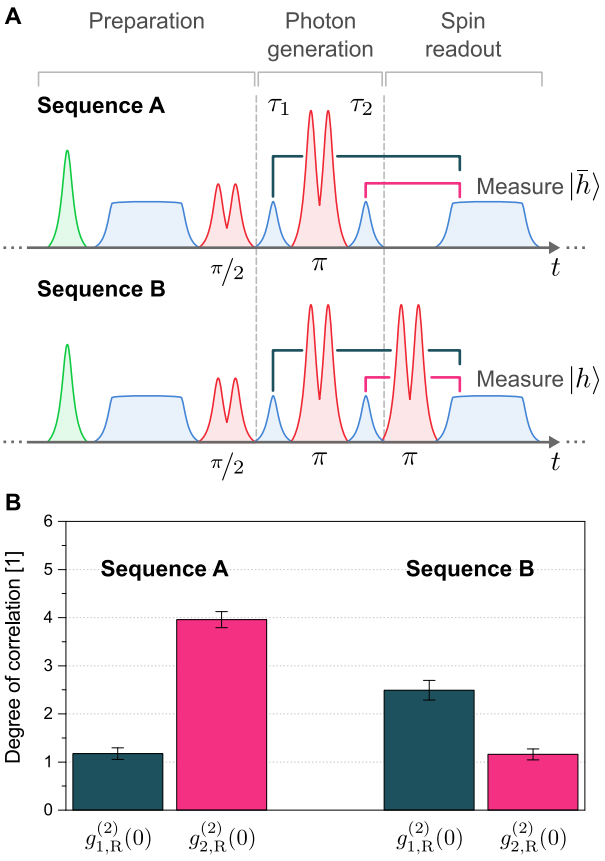

Fig. 6.14: Correlations between hole spin state and photon time-bin. **A.** Pulse sequence used to generate the entangled state. In sequence A the readout stage is simply a pulse resonant with the enhanced transition – the measurement of a photon projects the hole spin on the $|\bar{h}\rangle$ state. In sequence B the combination of a spin-flip and the resonant pulse results in the measurement of a photon projecting the spin into the $|h\rangle$ state. The coloured lines between the photon generation and the readout pulses indicate the time ranges used to calculate the degrees of correlation. A single pulse sequence repetition is 25 ns long. The nominal pulse durations are: non-resonant: 800 ps; resonant (initialisation/readout): 7 ns; resonant (photon generation): 250 ps; rotation: 6 ps. **B.** Measurements of the degree of correlation between the photon-generation pulses and the readout pulse for each sequence.

for spin initialisation and rotation, respectively. The quality of these rotations, which is critical to the success of the scheme, is therefore below the state of the art and constitutes the limiting factor here. Assuming the measured degree of correlation to be equivalent to the fidelity and extrapolating to the fidelity for the 3-photon GHZ state yields $F_{\mathrm{GHZ}} \approx 16\%$*. Given that spin initialisation fidelities of 99.8% and rotation fidelities in excess of 90% have been reported in QDs[62, 265, 309], we expect the generation of longer entangled states to be attainable with current techniques. For the scheme shown here, the fidelity of a 3 qubit GHZ state goes with the seventh power of the rotation fidelity, so any small improvement of this operation has a dramatic effect on the fidelity of the output state. With $F_{\pi/2} = 99\%$ we can expect $F_{\mathrm{GHZ}} \approx 90\%$.

We note that the number of spin rotations needed can be reduced by altering the pulse sequence for a GHZ state but not for a cluster state. The focus here lies on the 3-photon GHZ state but as mentioned in the introduction, the protocol can be modified to generate linear cluster states. As suggested in Ref.[49], an additional $\pi/2$ spin rotation about the y axis between subsequent photons will accomplish this. With spin rotations being a central part of

*The fidelity for a 3-photon GHZ state (or cluster state) can be estimated from these fidelities and corresponding success probabilities as $F_{\mathrm{GHZ}} = p_s + (1 - p_s)/8$, where seven rotation operations are needed (two $\pi/2$ and 5 π rotations or two $3\pi/2$ and 5 π rotations).

the scheme, this step can be directly incorporated. Note that a photon here is distributed among two time-bins, so the $\pi/2$ pulse is only needed every two photon-generation pulses. In step #4 of Fig.6.2, the state would evolve from

$$\left|\bar{h}\right\rangle |0_{\tau=1}1_{\tau=2}\rangle - |h\rangle |1_{\tau=1}0_{\tau=2}\rangle \tag{6.3}$$

to

$$\left(\left|\bar{h}\right\rangle - |h\rangle\right) |0_{\tau=1}1_{\tau=2}\rangle - \left(|h\rangle + \left|\bar{h}\right\rangle\right) |1_{\tau=1}0_{\tau=2}\rangle \,. \tag{6.4}$$

Following the operations outlined in the introduction of the scheme, including an additional $\pi/2$ pulse between time-bins 4 and 5, it can be seen that the extracted photonic state in the logical basis will be $|111\rangle + |101\rangle - |011\rangle + |001\rangle - |110\rangle + |100\rangle + |010\rangle + |000\rangle$, which is a linear 3-photon cluster state.

We now comment on other considerations for future improvements. First, with the particular sample used here the hole spin is probabilistically injected into the QD. Therefore, photons are not generated in repetitions of the pulse sequence in which a hole is not present. In order to make the scheme deterministic, it would be necessary to have a trapped spin present with unit probability. This can be done via deterministic charging methods[72, 303–305].

Second, in this implementation we use the electro-optic modulation of a cw resonant laser to generate short excitation pulses (250 ps). These pulses are long relative to the Purcell-enhanced decay time meaning that multiple excitations are possible within the length of the pulse[314]. This can result in the actual output state differing from the ideal output state. Future implementations should avoid this problem by using shorter pulses to perform deterministic excitation, although as the pulse length is reduced the system can leave the RSS regime and questions open up as to what determines the phase difference between successive time-bins. Nevertheless, we believe that the theoretical investigation of the classes of states that could be produced by varying the number of photons generated in each excitation pulse (whether accidental or intentional) would be an interesting avenue for further work.

Third, the decay rate of the cavity-enhanced transition used is increased by a factor of ~ 5. The system is thus ~ 5 times more likely to decay vertically, as required, than decaying diagonally. This is sufficient for a proof-of-principle demonstration, but to generate much longer states deterministically, the diagonal transition should be further suppressed relative to the vertical transition. Their ratio can be improved with a higher Purcell factor.

Lastly, the spin investigated here has a relatively short coherence time. Although it is long enough for the demonstration, it could become a limiting factor for long pulse sequences. Our scheme involves a π pulse half way through, which should increase the effective coherence time via the spin-echo effect. Future work could make use of available techniques such as dynamical

decoupling, nuclear-field manipulation and reduced nuclear spin noise to extend the coherence time[88, 312, 315].

6.5 Conclusion

We have presented a novel scheme for generating entangled, time-bin encoded multi-photon states based on cavity-enhanced resonance fluorescence from a hole spin in a quantum dot. We experimentally demonstrate complete coherent control over the trapped hole via multi-pulse sequences and show that the time-bin of the generated photons is dependent on the state of the spin. The correlations presented do not include phase information, which is the next step for the extension of the scheme. We stress that recent works on resonance fluorescence of QDs in micropillar cavities have shown photons generated in this manner to be highly indistinguishable. The generated light can thus be expected to be suitable for HOM based fusion operations. The results presented here constitute a key step on the way to producing multi-photon entangled states following the proposed scheme. We foresee no fundamental barrier on the extension of these experiments onto full linear photonic cluster states with current technology, implementing the improvements discussed above. Indeed, after the publication of this work, we became aware of a preprint detailing the implementation of a similar scheme using nitrogen-vacancy centres in diamond[316].

Chapter 7

Conclusions & Outlook

7.1 Conclusion & Future Work

We have presented work on an array of devices with potential for mid to long-term applications in quantum information processing. All devices rely on self-assembled semiconductor quantum dots for the generation of quantum light states. The first and last experimental chapters detailed the generation of two particularly useful states: chains of single-photons and multi-photon entangled states. The second and third experimental chapters have extended the idea of novel devices exploiting acoustic control over quantum dots. We now summarize each chapter's conclusions and provide avenues for further work.

7.1.1 Chapter 3 – SAW-Driven Single-Photon Generation

Here we developed a device integrating pillar microcavities and large-area surface acoustic waves. A passing acoustic wave periodically shifts the energy of the quantum dot transitions while leaving the cavity mode unperturbed. This gives rise to a temporal dependence of the detuning between cavity and emitter and therefore a dynamic Purcell effect. Under these conditions we perform resonance fluorescence and demonstrate that a continuous laser field is scattered into a pulsed single-photon stream inheriting the acoustic frequency of 1 GHz as the repetition rate. Furthermore, we perform high-resolution spectroscopy on the scattered light, revealing up to ten acoustic sidebands, which can be controlled by the original detuning between emitter and cavity as well as the acoustic wave amplitude.

The experiments presented did not completely tune the emitter from Purcell enhancement to suppression, but rather between different degrees of enhancement. In future work it would be interesting to increase the acoustic tuning range and decrease the cavity linewidth to explore this regime. Additionally, the maximal theoretical repetition rate of such a source is limited by the radiative lifetime of the transition, which is usually about 1 ns, corresponding to 1 GHz. A higher Purcell effect can increase this limit and the acoustic frequency can be increased in turn. Finally, it would be worth investigating the efficiency of the source and determine if the frequency can be set such that the time on resonance corresponds to a π pulse.

7.1.2 Chapter 4 – Hybrid SAW Devices

This chapter also looked at the tuning of quantum dot transitions by a surface acoustic wave, but it explored a novel platform for integration of the sources with the emission in-plane. We designed optical ring resonators with grating couplers and fabricated these on a GaAs membrane transferred on $LiNbO_3$ by epitaxial lift-off. The technique is scalable and straightforward, exhibiting remarkable adhesion properties without a promoting layer. We showed that the

resonators lead to a modest Purcell enhancement F_P~4 of the quantum dot transitions. In addition, the acoustic waves couple to well-defined mechanical resonances of the rings, exhibiting strong modulation of the transitions at specific frequencies. We extracted mechanical Q factors in the 140–240 range for this modes. Overall, the work shows that GaAs photonic structures on $LiNbO_3$ are a viable candidate for quantum photonic integrated circuits.

Additional work is needed to fully investigate the nature of the mechanical modes and exploit them or suppress them as needed. In addition, the coherence of the emission needs to be investigated to ensure that it is not degraded relative to that from dots in unprocessed GaAs. There are also open questions regarding charging issues seen on the devices. This can presumably be mitigated adding conducting or doped layers. Once these are understood, the platform can be expanded to demonstrate low-footprint photonic circuits and test the integration of active guiding elements and single-photon detectors.

7.1.3 Chapter 5 – SAW Integrated LEDs

We studied devices with control over the charge state of single quantum dots and acoustic waves. We presented devices with controlled tunnelling of electrons and holes and studied the optical spin initialisation in magnetic fields by resonant excitation of a single electron and a single hole. In the former case, high-fidelity spin initialisation was not achieved across dots and samples, indicating a strong remnant spin-flip mechanism that is not suppressed by the Zeeman splitting. On the other hand, single holes were readily initialised in weak magnetic fields < 1 T. Under resonance fluorescence we demonstrated the frustration of this spin initialisation by a SAW at 825 MHz. The main mechanism is related to the acoustic modulation of the transitions and does not directly affect the spin. However, we recorded evidence of a potential resonant process happening in parallel.

In order to conclusively determine if there is a resonant process involving acoustic interaction with the single spin, time-resolved measurements of pulsed acoustic and optical sequences are needed. This is the next step for these experiments and requires the fabrication of a new sample with higher acoustic frequencies. Beyond the study of the effect on the spin, these devices could be used to study the possibility of exploiting the acoustic strain to minimize the fine structure splitting. This is a requirement for high-fidelity entangled-photon pair generation by the biexcition-exciton radiative cascade. If the splitting is minimized at a particular phase in the acoustic period, an excitation laser can be locked to that phase to produce photon pairs entangled in polarisation with high repetition rates.

7.1.4 Chapter 6 – Multi-Photon Entangled State Generation

We introduced a scheme for the generation of multi-photon entangled states, which constitute a key resource for measurement-based quantum computation. The scheme focuses on the sequential generation of single photons by resonant scattering from a cavity-enhanced quantum dot. The dot is populated with a single charge carrier, whose energy levels are separated by the Zeeman energy in a Voigt magnetic field. The spin state of this charge determines the presence or lack of a resonantly scattered photon in a given time-bin, acting as a switch on the system. It can be coherently manipulated by optical pumping and optically induced rotations, allowing for the implementation of a pulse sequence generating long chains of entangled photons in the time-bin basis. We demonstrated the first step in the implementation of this scheme by showing that the time-bin of a single-photon is indeed dependent on the measured state of the trapped spin.

We found that our spin rotations lack fidelity compared to the state of the art and limited our capability to extend the scheme to higher numbers of photons. We attribute these issues to non-linear effects in the optical fibre and are confident that the use of a free-space arrangement for the high-power spin-rotation laser pulses would solve them. Future work should therefore prioritise this and aim to extend the scheme to three-photon states. The next step would be the demonstration of entanglement between the individual photons by interferometry. Lastly, the verification of Hong-Ou-Mandel based fusion of two independent three-photon chains would pose the most significant advance for all-photonic quantum computation.

Bibliography

[1]S. W. Hell and J. Wichmann, "Breaking the diffraction resolution limit by stimulated emission: stimulated-emission-depletion fluorescence microscopy", Optics Letters **19**, 780–782 (1994).

[2]N. Gisin and R. Thew, "Quantum communication", Nature Photonics **1**, 165–171 (2007).

[3]H. J. Kimble, "The quantum internet", Nature **453**, 1023–1030 (2008).

[4]N. Sangouard, C. Simon, H. De Riedmatten, and N. Gisin, "Quantum repeaters based on atomic ensembles and linear optics", Reviews of Modern Physics **83**, 33 (2011).

[5]C. H. Bennett and G. Brassard, "Quantum cryptography: Public key distribution and coin tossing", in International Conference on Computer System and Signal Processing, IEEE, 1984 (1984), pp. 175–179.

[6]T. D. Ladd, F. Jelezko, R. Laflamme, Y. Nakamura, C. Monroe, and J. L. O'Brien, "Quantum computers", Nature **464**, 45–53 (2010).

[7]R. P. Feynman, "Simulating physics with computers", International journal of theoretical physics **21**, 467–488 (1982).

[8]P. Shor, "Polynomial-Time Algorithms for Prime Factorization and Discrete Logarithms on a Quantum Computer", SIAM Review **41**, 303–332 (1999).

[9]L. K. Grover, "Quantum Mechanics Helps in Searching for a Needle in a Haystack", Physical Review Letters **79**, 325–328 (1997).

[10]P. Grangier, G. Reymond, and N. Schlosser, "Implementations of quantum computing using cavity quantum electrodynamics schemes", Fortschritte der Physik **48**, 859–874 (2000).

[11]E. Knill, R. Laflamme, and G. J. Milburn, "A scheme for efficient quantum computation with linear optics", Nature **409**, 46–52 (2001).

[12]R. Hanson and D. D. Awschalom, "Coherent manipulation of single spins in semiconductors", Nature **453**, 1043–1049 (2008).

[13]P. Maletinsky and A. Imamoglu, "Quantum Dot Nuclear Spin Polarization", in *Single Semiconductor Quantum Dots*, edited by P. Michler (Springer Berlin Heidelberg, Berlin, Heidelberg, 2009), pp. 145–184.

[14]M. Kroutvar, Y. Ducommun, D. Heiss, M. Bichler, D. Schuh, G. Abstreiter, and J. J. Finley, "Optically programmable electron spin memory using semiconductor quantum dots", Nature **432**, 81–84 (2004).

[15]I. Aharonovich, D. Englund, and M. Toth, "Solid-state single-photon emitters", Nature Photonics **10**, 631–641 (2016).

[16]A. J. Bennett, J. P. Lee, D. J. P. Ellis, T. Meany, E. Murray, F. F. Floether, J. P. Griffths, I. Farrer, D. A. Ritchie, and A. J. Shields, "Cavity-enhanced coherent light scattering from a quantum dot", Science Advances **2**, e1501256 (2016).

[17]B. Villa, A. J. Bennett, D. J. P. Ellis, J. P. Lee, J. Skiba-Szymanska, T. A. Mitchell, J. P. Griffiths, I. Farrer, D. A. Ritchie, C. J. B. Ford, and A. J. Shields, "Surface acoustic wave modulation of a coherently driven quantum dot in a pillar microcavity", Applied Physics Letters **111**, 011103 (2017).

[18]J. P. Lee, B. Villa, A. J. Bennett, R. M. Stevenson, D. J. P. Ellis, I. Farrer, D. A. Ritchie, and A. J. Shields, "A quantum dot as a source of time-bin entangled multi-photon states", Quantum Science and Technology **4**, 025011 (2019).

[19]M. Nielsen and I. Chuang, *Quantum computation and quantum information* (Cambridge University Press, 2000).

[20]D. Leibfried, B. DeMarco, V. Meyer, D. Lucas, M. Barrett, J. Britton, W. M. Itano, B. Jelenković, C. Langer, T. Rosenband, et al., "Experimental demonstration of a robust, high-fidelity geometric two ion-qubit phase gate", Nature **422**, 412–415 (2003).

[21]L. DiCarlo, J. M. Chow, J. M. Gambetta, L. S. Bishop, B. R. Johnson, D. I. Schuster, J. Majer, A. Blais, L. Frunzio, S. M. Girvin, and R. J. Schoelkopf, "Demonstration of two-qubit algorithms with a superconducting quantum processor", Nature **460**, 240–244 (2009).

[22]M. Veldhorst, C. Yang, J. Hwang, W. Huang, J. Dehollain, J. Muhonen, S. Simmons, A. Laucht, F. Hudson, K. M. Itoh, et al., "A two-qubit logic gate in silicon", Nature **526**, 410 (2015).

[23]M. Pooley, D. Ellis, R. Patel, A. Bennett, K. Chan, I. Farrer, D. Ritchie, and A. Shields, "Controlled-not gate operating with single photons", Applied Physics Letters **100**, 211103 (2012).

[24]S. Pirandola, J. Eisert, C. Weedbrook, A. Furusawa, and S. L. Braunstein, "Advances in quantum teleportation", Nature Photonics **9**, 641–652 (2015).

[25]L.-M. Duan, M. D. Lukin, J. I. Cirac, and P. Zoller, "Long-distance quantum communication with atomic ensembles and linear optics", Nature **414**, 413–418 (2001).

[26]C. Hong and L. Mandel, "Experimental realization of a localized one-photon state", Physical Review Letters **56**, 58 (1986).

[27]P. G. Kwiat, K. Mattle, H. Weinfurter, A. Zeilinger, A. V. Sergienko, and Y. Shih, "New High-Intensity Source of Polarization-Entangled Photon Pairs", Physical Review Letters **75**, 4337–4341 (1995).

[28]R. M. Stevenson, R. J. Young, P. Atkinson, K. Cooper, D. A. Ritchie, and A. J. Shields, "A semiconductor source of triggered entangled photon pairs", Nature **439**, 179–182 (2006).

[29]B. Hacker, S. Welte, G. Rempe, and S. Ritter, "A photon–photon quantum gate based on a single atom in an optical resonator", Nature **536**, 193–196 (2016).

[30]M. Khazali, K. Heshami, and C. Simon, "Photon-photon gate via the interaction between two collective rydberg excitations", Phys. Rev. A **91**, 030301 (2015).

[31]P. van Loock, "Optical hybrid approaches to quantum information", Laser & Photonics Reviews **5**, 167–200 (2011).

[32]D. E. Browne and T. Rudolph, "Resource-Efficient Linear Optical Quantum Computation", Physical Review Letters **95**, 010501 (2005).

[33]M. A. Nielsen, "Cluster-state quantum computation", Reports on Mathematical Physics **57**, 147–161 (2006).

[34]M. A. Nielsen, "Optical Quantum Computation Using Cluster States", Physical Review Letters **93**, 040503 (2004).

[35]N. Yoran and B. Reznik, "Deterministic Linear Optics Quantum Computation with Single Photon Qubits", Physical Review Letters **91**, 037903 (2003).

[36]R. Raussendorf and H. J. Briegel, "A One-Way Quantum Computer", Physical Review Letters **86**, 5188–5191 (2001).

[37]P. Kok, W. J. Munro, K. Nemoto, T. C. Ralph, J. P. Dowling, and G. J. Milburn, "Linear optical quantum computing with photonic qubits", Reviews of Modern Physics **79**, 135–174 (2007).

[38]P. Walther, K. J. Resch, T. Rudolph, E. Schenck, H. Weinfurter, V. Vedral, M. Aspelmeyer, and A. Zeilinger, "Experimental one-way quantum computing", Nature **434**, 169–176 (2005).

[39]J. Wang, S. Paesani, R. Santagati, S. Knauer, A. A. Gentile, N. Wiebe, M. Petruzzella, J. L. O'Brien, J. G. Rarity, A. Laing, et al., "Experimental quantum hamiltonian learning", Nature Physics **13**, 551 (2017).

[40]E. Murray, D. J. P. Ellis, T. Meany, F. F. Floether, J. P. Lee, J. P. Griffiths, G. a. C. Jones, I. Farrer, D. A. Ritchie, A. J. Bennett, and A. J. Shields, "Quantum photonics hybrid integration platform", Applied Physics Letters **107**, 171108 (2015).

[41]D. Ellis, A. Bennett, C. Dangel, J. Lee, J. Griffiths, T. Mitchell, T.-K. Paraiso, P. Spencer, D. Ritchie, and A. Shields, "Independent indistinguishable quantum light sources on a reconfigurable photonic integrated circuit", Applied Physics Letters **112**, 211104 (2018).

[42]S. Ferrari, C. Schuck, and W. Pernice, "Waveguide-integrated superconducting nanowire single-photon detectors", Nanophotonics **7**, 1725–1758 (2018).

[43]F. Marsili, V. B. Verma, J. A. Stern, S. Harrington, A. E. Lita, T. Gerrits, I. Vayshenker, B. Baek, M. D. Shaw, R. P. Mirin, et al., "Detecting single infrared photons with 93% system efficiency", Nature Photonics **7**, 210 (2013).

[44]I. E. Zadeh, J. W. Los, R. Gourgues, G. Bulgarini, S. M. Dobrovolskiy, V. Zwiller, and S. N. Dorenbos, "A single-photon detector with high efficiency and sub-10ps time resolution", arXiv preprint arXiv:1801.06574 (2018).

[45]T. Rudolph, "Why I am optimistic about the silicon-photonic route to quantum computing", APL Photonics **2**, 030901 (2017).

[46]D. A. Herrera-Martıé, A. G. Fowler, D. Jennings, and T. Rudolph, "Photonic implementation for the topological cluster-state quantum computer", Phys. Rev. A **82**, 032332 (2010).

[47]S. E. Economou, N. Lindner, and T. Rudolph, "Optically generated 2-dimensional photonic cluster state from coupled quantum dots", Physical Review Letters **105**, 093601 (2010).

[48]A. Clark, B. Bell, J. Fulconis, M. M. Halder, J. G. Rarity, M. S. Tame, and M. S. Kim, "Cluster state generation using fibre sources", in Frontiers in optics (Optical Society of America, 2010), FMF5.

[49]N. H. Lindner and T. Rudolph, "Proposal for Pulsed On-Demand Sources of Photonic Cluster State Strings", Physical Review Letters **103**, 113602 (2009).

[50]A. J. Shields, "Semiconductor quantum light sources", Nature photonics **1**, 215–223 (2007).

[51]P. Michler, *Single semiconductor quantum dots* (Springer Berlin Heidelberg, 2009).

[52]P. Michler, *Single quantum dots: fundamentals, applications and new concepts* (Springer, 2003).

[53]O. Gywat, H. Krenner, and J. Berezovsky, *Spins in optically active quantum dots: concepts and methods* (John Wiley & Sons, 2010).

[54]B. Urbaszek, X. Marie, T. Amand, O. Krebs, P. Voisin, P. Maletinsky, A. Högele, and A. Imamoglu, "Nuclear spin physics in quantum dots: An optical investigation", Reviews of Modern Physics **85**, 79–133 (2013).

[55]Y. Cao, A. J. Bennett, I. Farrer, D. A. Ritchie, and A. J. Shields, "Polarization-correlated photons from a positively charged quantum dot", Physical Review B **92**, 081302 (2015).

[56]P. A. Maksym and T. Chakraborty, "Quantum dots in a magnetic field: Role of electron-electron interactions", Physical Review Letters **65**, 108–111 (1990).

[57]R. J. Warburton, "Single spins in self-assembled quantum dots", Nature Materials **12**, 483 (2013).

[58]M. Bayer, G. Ortner, O. Stern, A. Kuther, A. A. Gorbunov, A. Forchel, P. Hawrylak, S. Fafard, K. Hinzer, T. L. Reinecke, S. N. Walck, J. P. Reithmaier, F. Klopf, and F. Schäfer, "Fine structure of neutral and charged excitons in self-assembled In(Ga)As/(Al)GaAs quantum dots", Physical Review B **65**, 195315 (2002).

[59]M. Bayer, O. Stern, A. Kuther, and A. Forchel, "Spectroscopic study of dark excitons in $In_xGa_{1-x}As$ self-assembled quantum dots by a magnetic-field-induced symmetry breaking", Physical Review B **61**, 7273–7276 (2000).

[60]A. Ashmore, J. Finley, R. Oulton, P. Fry, A. Lemaître, D. Mowbray, M. Skolnick, M. Hopkinson, P. Buckle, and P. Maksym, "Optical properties of single charge tuneable InGaAs quantum dots", Physica E: Low-dimensional Systems and Nanostructures **13**, 127–130 (2002).

[61]P. Lodahl, "Quantum-dot based photonic quantum networks", Quantum Science and Technology **3**, 013001 (2017).

[62]M. Atatüre, J. Dreiser, A. Badolato, A. Högele, K. Karrai, and A. Imamoglu, "Quantum-Dot Spin-State Preparation with Near-Unity Fidelity", Science **312**, 551–553 (2006).

[63]C. Emary, X. Xu, D. G. Steel, S. Saikin, and L. J. Sham, "Fast Initialization of the Spin State of an Electron in a Quantum Dot in the Voigt Configuration", Physical Review Letters **98**, 047401 (2007).

[64]R. Heitz, M. Veit, N. N. Ledentsov, A. Hoffmann, D. Bimberg, V. M. Ustinov, P. S. Kop'ev, and Z. I. Alferov, "Energy relaxation by multiphonon processes in InAs/GaAs quantum dots", Physical Review B **56**, 10435–10445 (1997).

[65]S. Buckley, K. Rivoire, and J. Vučković, "Engineered quantum dot single-photon sources", Reports on Progress in Physics **75**, 126503 (2012).

[66]A. J. Bennett, J. P. Lee, D. J. P. Ellis, I. Farrer, D. A. Ritchie, and A. J. Shields, "A semiconductor photon-sorter", Nature Nanotechnology **11**, 857–860 (2016).

[67]A. Muller, E. B. Flagg, P. Bianucci, X. Y. Wang, D. G. Deppe, W. Ma, J. Zhang, G. J. Salamo, M. Xiao, and C. K. Shih, "Resonance Fluorescence from a Coherently Driven Semiconductor Quantum Dot in a Cavity", Physical Review Letters **99** (2007).

[68]B. R. Mollow, "Power spectrum of light scattered by two-level systems", Physical Review **188** (1969).

[69]A. Nick Vamivakas, Y. Zhao, C.-Y. Lu, and M. Atatüre, "Spin-resolved quantum-dot resonance fluorescence", Nature Physics **5**, 198–202 (2009).

[70]R. Loudon, *The quantum theory of light* (OUP Oxford, 2000).

[71]R. J. Warburton, B. T. Miller, C. S. Dürr, C. Bödefeld, K. Karrai, J. P. Kotthaus, G. Medeiros-Ribeiro, P. M. Petroff, and S. Huant, "Coulomb interactions in small charge-tunable quantum dots: A simple model", Physical Review B **58**, 16221–16231 (1998).

[72]R. J. Warburton, C. Schäflein, D. Haft, F. Bickel, A. Lorke, K. Karrai, J. M. Garcia, W. Schoenfeld, and P. M. Petroff, "Optical emission from a charge-tunable quantum ring", Nature **405**, 926–929 (2000).

[73]S. Seidl, M. Kroner, P. A. Dalgarno, A. Högele, J. M. Smith, M. Ediger, B. D. Gerardot, J. M. Garcia, P. M. Petroff, K. Karrai, and R. J. Warburton, "Absorption and photoluminescence spectroscopy on a single self-assembled charge-tunable quantum dot", Physical Review B **72**, 195339 (2005).

[74]B. D. Gerardot, D. Brunner, P. A. Dalgarno, P. Öhberg, S. Seidl, M. Kroner, K. Karrai, N. G. Stoltz, P. M. Petroff, and R. J. Warburton, "Optical pumping of a single hole spin in a quantum dot", Nature **451**, 441–444 (2008).

[75]Z. Yuan, B. E. Kardynal, R. M. Stevenson, A. J. Shields, C. J. Lobo, K. Cooper, N. S. Beattie, D. A. Ritchie, and M. Pepper, "Electrically Driven Single-Photon Source", Science **295**, 102–105 (2002).

[76]A. J. Bennett, D. C. Unitt, P. See, A. J. Shields, P. Atkinson, K. Cooper, and D. A. Ritchie, "Microcavity single-photon-emitting diode", Applied Physics Letters **86**, 181102 (2005).

[77]A. J. Bennett, R. B. Patel, J. Skiba-Szymanska, C. A. Nicoll, I. Farrer, D. A. Ritchie, and A. J. Shields, "Giant Stark effect in the emission of single semiconductor quantum dots", Applied Physics Letters **97**, 031104 (2010).

[78]C. Gerry and P. Knight, *Introductory quantum optics* (Cambridge University Press, 2004).

[79]M. O. Scully and A. A. Svidzinsky, "The Super of Superradiance", Science **325**, 1510–1511 (2009).

[80]R. H. Brown and R. Q. Twiss, "Correlation between photons in two coherent beams of light", Nature **177**, 27–29 (1956).

[81]M. Scully and M. Zubairy, *Quantum optics* (Cambridge University Press, 1997).

[82]M. Fox, *Quantum optics: an introduction* (OUP Oxford, 2006).

[83]F. Jahnke, *Quantum optics with semiconductor nanostructures* (Elsevier Science, 2012).

[84]J. Houel, A. V. Kuhlmann, L. Greuter, F. Xue, M. Poggio, B. D. Gerardot, P. A. Dalgarno, A. Badolato, P. M. Petroff, A. Ludwig, D. Reuter, A. D. Wieck, and R. J. Warburton, "Probing Single-Charge Fluctuations at a GaAs / AlAs Interface Using Laser Spectroscopy on a Nearby InGaAs Quantum Dot", Physical Review Letters **108**, 107401 (2012).

[85]A. V. Kuhlmann, J. Houel, A. Ludwig, L. Greuter, D. Reuter, A. D. Wieck, M. Poggio, and R. J. Warburton, "Charge noise and spin noise in a semiconductor quantum device", Nature Physics **9**, 570–575 (2013).

[86]A. V. Kuhlmann, J. H. Prechtel, J. Houel, A. Ludwig, D. Reuter, A. D. Wieck, and R. J. Warburton, "Transform-limited single photons from a single quantum dot", Nature Communications **6**, 8204 (2015).

[87]L. Lanco and P. Senellart, "A highly efficient single photon-single quantum dot interface", in *Engineering the Atom-Photon Interaction* (Springer, 2015), pp. 39–71.

[88]R. N. E. Malein, T. S. Santana, J. M. Zajac, A. C. Dada, E. M. Gauger, P. M. Petroff, J. Y. Lim, J. D. Song, and B. D. Gerardot, "Screening Nuclear Field Fluctuations in Quantum Dots for Indistinguishable Photon Generation", Physical Review Letters **116**, 257401 (2016).

[89]C. Santori, D. Fattal, J. Vučković, G. S. Solomon, and Y. Yamamoto, "Indistinguishable photons from a single-photon device", Nature **419**, 594–597 (2002).

[90]X. Ding, Y. He, Z.-C. Duan, N. Gregersen, M.-C. Chen, S. Unsleber, S. Maier, C. Schneider, M. Kamp, S. Höfling, C.-Y. Lu, and J.-W. Pan, "On-Demand Single Photons with High Extraction Efficiency and Near-Unity Indistinguishability from a Resonantly Driven Quantum Dot in a Micropillar", Physical Review Letters **116**, 020401 (2016).

[91]J. C. Loredo, N. A. Zakaria, N. Somaschi, C. Anton, L. de Santis, V. Giesz, T. Grange, M. A. Broome, O. Gazzano, G. Coppola, I. Sagnes, A. Lemaitre, A. Auffeves, P. Senellart, M. P. Almeida, and A. G. White, "Scalable performance in solid-state single-photon sources", Optica **3**, 433 (2016).

[92]R. M. Stevenson, C. L. Salter, J. Nilsson, A. J. Bennett, M. B. Ward, I. Farrer, D. A. Ritchie, and A. J. Shields, "Indistinguishable Entangled Photons Generated by a Light-Emitting Diode", Physical Review Letters **108** (2012).

[93]S. Ates, S. M. Ulrich, S. Reitzenstein, A. Löffler, A. Forchel, and P. Michler, "Post-Selected Indistinguishable Photons from the Resonance Fluorescence of a Single Quantum Dot in a Microcavity", Physical Review Letters **103** (2009).

[94]Y.-M. He, Y. He, Y.-J. Wei, D. Wu, M. Atatüre, C. Schneider, S. Höfling, M. Kamp, C.-Y. Lu, and J.-W. Pan, "On-demand semiconductor single-photon source with near-unity indistinguishability", Nature Nanotechnology **8**, 213–217 (2013).

[95]P. Michler, A. Imamoglu, M. D. Mason, P. J. Carson, G. F. Strouse, and S. K. Buratto, "Quantum correlation among photons from a single quantum dot at room temperature", Nature **406**, 968–970 (2000).

[96]Y. Yamamoto, F. Tassone, and H. Cao, *Semiconductor cavity quantum electrodynamics* (Springer, Berlin; New York, 2000).

[97]K. Koyama, M. Yoshita, M. Baba, T. Suemoto, and H. Akiyama, "High collection efficiency in fluorescence microscopy with a solid immersion lens", Applied Physics Letters **75**, 1667–1669 (1999).

[98]J. Claudon, J. Bleuse, N. S. Malik, M. Bazin, P. Jaffrennou, N. Gregersen, C. Sauvan, P. Lalanne, and J.-M. Gérard, "A highly efficient single-photon source based on a quantum dot in a photonic nanowire", Nature Photonics **4**, 174–177 (2010).

[99]E. M. Purcell, "Spontaneous emission probabilities at radio frequencies", Physical Review **69**, 681 (1946).

[100]A. Kavokin, J. Baumberg, G. Malpuech, and F. Laussy, *Microcavities* (OUP Oxford, 2011).

[101] A. Kiraz, P. Michler, C. Becher, B. Gayral, A. Imamoğlu, L. Zhang, E. Hu, W. V. Schoenfeld, and P. M. Petroff, "Cavity-quantum electrodynamics using a single InAs quantum dot in a microdisk structure", Applied Physics Letters **78**, 3932 (2001).

[102] T. D. Happ, I. I. Tartakovskii, V. D. Kulakovskii, J.-P. Reithmaier, M. Kamp, and A. Forchel, "Enhanced light emission of In x Ga 1 - x As quantum dots in a two-dimensional photonic-crystal defect microcavity", Physical Review B **66**, 041303(R) (2002).

[103] T. Yoshie, A. Scherer, J. Hendrickson, G. Khitrova, H. M. Gibbs, G. Rupper, C. Ell, O. B. Shchekin, and D. G. Deppe, "Vacuum Rabi splitting with a single quantum dot in a photonic crystal nanocavity", Nature **432**, 200–203 (2004).

[104] J. P. Reithmaier, G. Sęk, A. Löffler, C. Hofmann, S. Kuhn, S. Reitzenstein, L. V. Keldysh, V. D. Kulakovskii, T. L. Reinecke, and A. Forchel, "Strong coupling in a single quantum dot–semiconductor microcavity system", Nature **432**, 197–200 (2004).

[105] E. Peter, P. Senellart, D. Martrou, A. Lemaître, J. Hours, J. M. Gérard, and J. Bloch, "Exciton-Photon Strong-Coupling Regime for a Single Quantum Dot Embedded in a Microcavity", Physical Review Letters **95**, 067401 (2005).

[106] K. J. Vahala, "Optical microcavities", Nature **424**, 839–846 (2003).

[107] L. C. Andreani, G. Panzarini, and J.-M. Gérard, "Strong-coupling regime for quantum boxes in pillar microcavities: Theory", Physical Review B **60**, 13276–13279 (1999).

[108] A. Ulhaq, S. Ates, S. Weiler, S. M. Ulrich, S. Reitzenstein, A. Löffler, S. Höfling, L. Worschech, A. Forchel, and P. Michler, "Linewidth broadening and emission saturation of a resonantly excited quantum dot monitored via an off-resonant cavity mode", Physical Review B **82**, 045307 (2010).

[109] J. M. Gérard, B. Sermage, B. Gayral, B. Legrand, E. Costard, and V. Thierry-Mieg, "Enhanced spontaneous emission by quantum boxes in a monolithic optical microcavity", Physical review letters **81**, 1110 (1998).

[110] G. S. Solomon, M. Pelton, and Y. Yamamoto, "Single-mode Spontaneous Emission from a Single Quantum Dot in a Three-Dimensional Microcavity", Physical Review Letters **86**, 3903–3906 (2001).

[111] M. Pelton, C. Santori, J. Vučković, B. Zhang, G. S. Solomon, J. Plant, and Y. Yamamoto, "Efficient Source of Single Photons: A Single Quantum Dot in a Micropost Microcavity", Physical Review Letters **89** (2002).

[112] N. Somaschi, V. Giesz, L. De Santis, J. C. Loredo, M. P. Almeida, G. Hornecker, S. L. Portalupi, T. Grange, C. Antón, J. Demory, C. Gómez, I. Sagnes, N. D. Lanzillotti-Kimura, A. Lemaítre, A. Auffeves, A. G. White, L. Lanco, and P. Senellart, "Near-optimal single-photon sources in the solid state", Nature Photonics **10**, 340–345 (2016).

[113] L. De Santis, C. Antón, B. Reznychenko, N. Somaschi, G. Coppola, J. Senellart, C. Gómez, A. Lemaître, I. Sagnes, A. G. White, L. Lanco, A. Auffèves, and P. Senellart, "A solid-state single-photon filter", Nature Nanotechnology **12**, 663–667 (2017).

[114] K. Vahala, *Optical microcavities* (World Scientific, 2004).

[115] A. J. Bennett, P. Atkinson, P. See, M. B. Ward, R. M. Stevenson, Z. L. Yuan, D. C. Unitt, D. J. P. Ellis, K. Cooper, D. A. Ritchie, and A. J. Shields, "Single-photon-emitting diodes: a review", physica status solidi (b) **243**, 3730–3740 (2006).

[116]O. Gazzano, S. Michaelis de Vasconcellos, C. Arnold, A. Nowak, E. Galopin, I. Sagnes, L. Lanco, A. Lemaître, and P. Senellart, "Bright solid-state sources of indistinguishable single photons", Nature Communications **4**, 1425 (2013).

[117]A. Yariv and P. Yeh, *Photonics: optical electronics in modern communications* (Oxford University Press, 2007).

[118]J. P. Reithmaier, M. Röhner, H. Zull, F. Schäfer, A. Forchel, P. A. Knipp, and T. L. Reinecke, "Size Dependence of Confined Optical Modes in Photonic Quantum Dots", Physical Review Letters **78**, 378–381 (1997).

[119]J. M. Gérard, D. Barrier, J. Y. Marzin, R. Kuszelewicz, L. Manin, E. Costard, V. Thierry-Mieg, and T. Rivera, "Quantum boxes as active probes for photonic microstructures: The pillar microcavity case", Applied Physics Letters **69**, 449–451 (1996).

[120]W. Barnes, G. Björk, J. Gérard, P. Jonsson, J. Wasey, P. Worthing, and V. Zwiller, "Solid-state single photon sources: light collection strategies", The European Physical Journal D - Atomic, Molecular and Optical Physics **18**, 197–210 (2002).

[121]D. C. Unitt, A. J. Bennett, P. Atkinson, D. A. Ritchie, and A. J. Shields, "Polarization control of quantum dot single-photon sources via a dipole-dependent Purcell effect", Physical Review B **72**, 033318 (2005).

[122]J. W. S. Rayleigh, *The theory of sound* (Macillan & co., 1878).

[123]I. S. Grudinin, V. S. Ilchenko, and L. Maleki, "Ultrahigh optical Q factors of crystalline resonators in the linear regime", Physical Review A **74**, 063806 (2006).

[124]A. E. Shitikov, I. A. Bilenko, N. M. Kondratiev, V. E. Lobanov, A. Markosyan, and M. L. Gorodetsky, "Billion Q-factor in silicon WGM resonators", Optica **5**, 1525 (2018).

[125]V. Sandoghdar, F. Treussart, J. Hare, V. Lefevre-Seguin, J.-M. Raimond, and S. Haroche, "Very low threshold whispering-gallery-mode microsphere laser", Physical Review A **54**, R1777 (1996).

[126]D. J. Moss, R. Morandotti, A. L. Gaeta, and M. Lipson, "New CMOS-compatible platforms based on silicon nitride and Hydex for nonlinear optics", Nature Photonics **7**, 597–607 (2013).

[127]B. J. M. Hausmann, I. Bulu, V. Venkataraman, P. Deotare, and M. Lončar, "Diamond nonlinear photonics", Nature Photonics **8**, 369–374 (2014).

[128]L. Razzari, D. Duchesne, M. Ferrera, R. Morandotti, S. Chu, B. E. Little, and D. J. Moss, "CMOS-compatible integrated optical hyper-parametric oscillator", Nature Photonics **4**, 41–45 (2010).

[129]A. C. Turner, M. A. Foster, A. L. Gaeta, and M. Lipson, "Ultra-low power parametric frequency conversion in a silicon microring resonator", Optics Express **16**, 4881–4887 (2008).

[130]S. M. Spillane, T. J. Kippenberg, K. J. Vahala, K. W. Goh, E. Wilcut, and H. J. Kimble, "Ultrahigh- Q toroidal microresonators for cavity quantum electrodynamics", Physical Review A **71** (2005).

[131]D. W. Vernooy, A. Furusawa, N. P. Georgiades, V. S. Ilchenko, and H. J. Kimble, "Cavity QED with high-Q whispering gallery modes", Physical Review A **57**, R2293 (1998).

[132]B. Bhushan, ed., *Encyclopedia of Nanotechnology* (Springer Netherlands, Dordrecht, 2012).

[133]P. Rath, M. Hirtz, G. Lewes-Malandrakis, D. Brink, C. Nebel, and W. H. P. Pernice, "Diamond Nanophotonic Circuits Functionalized by Dip-pen Nanolithography", Advanced Optical Materials **3**, 328–335 (2015).

[134]Q. Li, M. Davanço, and K. Srinivasan, "Efficient and low-noise single-photon-level frequency conversion interfaces using silicon nanophotonics", Nature Photonics **10**, 406–414 (2016).

[135]S. M. Hendrickson, C. N. Weiler, R. M. Camacho, P. T. Rakich, A. I. Young, M. J. Shaw, T. B. Pittman, J. D. Franson, and B. C. Jacobs, "All-optical-switching demonstration using two-photon absorption and the Zeno effect", Physical Review A **87**, 023808 (2013).

[136]B. Gayral, J.-M. Gérard, B. Sermage, A. Lemaître, and C. Dupuis, "Time-resolved probing of the Purcell effect for InAs quantum boxes in GaAs microdisks", Applied Physics Letters **78**, 2828–2830 (2001).

[137]A. N. Oraevsky, "Whispering-gallery waves", Quantum Electronics **32**, 377–400 (2002).

[138]S. Spillane, T. Kippenberg, O. Painter, and K. Vahala, "Ideality in a Fiber-Taper-Coupled Microresonator System for Application to Cavity Quantum Electrodynamics", Physical Review Letters **91** (2003).

[139]G. C. Righini, Y. Dumeige, P. Féron, M. Ferrari, G. Nunzi Conti, D. Ristic, and S. Soria, "Whispering gallery mode microresonators: fundamentals and applications", Rivista del Nuovo Cimento **34**, 435–488 (2011).

[140]J. E. Heebner, R. Grover, and T. A. Ibrahim, *Optical microresonators theory, fabrication, and applications* (Springer, London, 2008).

[141]J. Devkota, P. Ohodnicki, and D. Greve, "Saw sensors for chemical vapors and gases", Sensors **17**, 801 (2017).

[142]T. Joos and P. Fortina, *Microarrays in clinical diagnostics* (Humana Press, 2005).

[143]D. Morgan, *Surface acoustic wave filters: with applications to electronic communications and signal processing* (Elsevier Science, 2010).

[144]S. Datta, *Surface acoustic wave devices* (Prentice Hall, 1986).

[145]C. Campbell, *Surface acoustic wave devices and their signal processing applications* (Elsevier Science, 2012).

[146]M. M. d. Lima and P. V. Santos, "Modulation of photonic structures by surface acoustic waves", Reports on Progress in Physics **68**, 1639–1701 (2005).

[147]C. Thomsen, H. T. Grahn, H. J. Maris, and J. Tauc, "Surface generation and detection of phonons by picosecond light pulses", Physical Review B **34**, 4129 (1986).

[148]D. Veysset, A. A. Maznev, I. A. Veres, T. Pezeril, S. E. Kooi, A. M. Lomonosov, and K. A. Nelson, "Acoustical breakdown of materials by focusing of laser-generated Rayleigh surface waves", Applied Physics Letters **111**, 031901 (2017).

[149]C. Flannery, E. Chilla, S. Semenov, and H.-J. Frohlich, "Elastic properties of GaAs obtained by inversion of laser-generated surface acoustic wave measurements", in , Vol. 1 (1999), pp. 501–504.

[150]F. J. R. Schülein, E. Zallo, P. Atkinson, O. G. Schmidt, R. Trotta, A. Rastelli, A. Wixforth, and H. J. Krenner, "Fourier synthesis of radiofrequency nanomechanical pulses with different shapes", Nature Nanotechnology **10**, 512–516 (2015).

[151]R. H. Tancrell and M. G. Holland, "Acoustic surface wave filters", Proceedings of the IEEE **59**, 393–409 (1971).

[152]M. Weiß, A. L. Hörner, E. Zallo, P. Atkinson, A. Rastelli, O. G. Schmidt, A. Wixforth, and H. J. Krenner, "Multiharmonic frequency-chirped transducers for surface-acoustic-wave optomechanics", arXiv:1708.00261 [cond-mat, physics:physics], arXiv: 1708.00261 (2017).

[153]K. Yamanouchi, C. H. Lee, K. Yamamoto, T. Meguro, and H. Odagawa, "GHz-range low-loss wide band filter using new floating electrode type unidirectional transducers", in Ultrasonics Symposium, 1992. Proceedings., IEEE 1992 (1992), pp. 139–142.

[154]G. Bu, D. Ciplys, M. Shur, L. J. Schowalter, S. Schujman, and R. Gaska, "Electromechanical coupling coefficient for surface acoustic waves in single-crystal bulk aluminum nitride", Applied Physics Letters **84**, 4611 (2004).

[155]T. W. Grudkowski, G. K. Montress, M. Gilden, and J. F. Black, "Integrated circuit compatible surface acoustic wave devices on gallium arsenide", IEEE Transactions on Microwave Theory and Techniques **29**, 1348–1356 (1981).

[156]Y. Takagaki, E. Wiebicke, P. V. Santos, R. Hey, and K. H. Ploog, "Propagation of surface acoustic waves in a GaAs/AlAs/GaAs heterostructure and micro-beams", Semiconductor science and technology **17**, 1008 (2002).

[157]R. Hadfield and G. Johansson, *Superconducting devices in quantum optics* (Springer International Publishing, 2016).

[158]K. Hashimoto, *Surface acoustic wave devices in telecommunications: modelling and simulation* (Springer Berlin Heidelberg, 2013).

[159]A. C. Poveda, D. D. Bühler, A. C. Sáez, P. V. Santos, and M. M. d. Lima Jr, "Optical waveguide devices modulated by surface acoustic waves", arXiv:1811.03051 [physics], arXiv: 1811.03051 (2018).

[160]E. H. El Boudouti, B. Djafari-Rouhani, and A. Akjouj, "Resonant guided elastic waves in an adsorbed bilayer: Theoretical analysis of the density of states", Physical Review B **55**, 4442–4448 (1997).

[161]C. Wiele, F. Haake, C. Rocke, and A. Wixforth, "Photon trains and lasing: The periodically pumped quantum dot", Physical Review A **58**, R2680 (1998).

[162]M. J. A. Schuetz, E. M. Kessler, G. Giedke, L. M. K. Vandersypen, M. D. Lukin, and J. I. Cirac, "Universal Quantum Transducers Based on Surface Acoustic Waves", Physical Review X **5**, 031031 (2015).

[163]K. C. Balram, M. I. Davanço, J. D. Song, and K. Srinivasan, "Coherent coupling between radiofrequency, optical and acoustic waves in piezo-optomechanical circuits", Nature Photonics **10**, 346–352 (2016).

[164]A. H. Safavi-Naeini, D. Van Thourhout, R. Baets, and R. Van Laer, "Controlling phonons and photons at the wavelength scale: integrated photonics meets integrated phononics", Optica **6**, 213 (2019).

[165]S. Hermelin, S. Takada, M. Yamamoto, S. Tarucha, A. D. Wieck, L. Saminadayar, C. Bäuerle, and T. Meunier, "Electrons surfing on a sound wave as a platform for quantum optics with flying electrons", Nature **477**, 435–438 (2011).

[166]M. Kataoka, R. J. Schneble, A. L. Thorn, C. H. W. Barnes, C. J. B. Ford, D. Anderson, G. A. C. Jones, I. Farrer, D. A. Ritchie, and M. Pepper, "Single-Electron Population and Depopulation of an Isolated Quantum Dot Using a Surface-Acoustic-Wave Pulse", Physical Review Letters **98**, 046801 (2007).

[167]R. P. G. McNeil, M. Kataoka, C. J. B. Ford, C. H. W. Barnes, D. Anderson, G. A. C. Jones, I. Farrer, and D. A. Ritchie, "On-demand single-electron transfer between distant quantum dots", Nature **477**, 439–442 (2011).

[168]C. H. W. Barnes, J. M. Shilton, and A. M. Robinson, "Quantum computation using electrons trapped by surface acoustic waves", Physical Review B **62**, 8410–8419 (2000).

[169]I.-C. Hoi, A. F. Kockum, L. Tornberg, A. Pourkabirian, G. Johansson, P. Delsing, and C. M. Wilson, "Probing the quantum vacuum with an artificial atom in front of a mirror", Nature Physics **11**, 1045–1049 (2015).

[170]M. V. Gustafsson, P. V. Santos, G. Johansson, and P. Delsing, "Local probing of propagating acoustic waves in a gigahertz echo chamber", Nature Physics **8**, 338–343 (2012).

[171]M. V. Gustafsson, T. Aref, A. F. Kockum, M. K. Ekstrom, G. Johansson, and P. Delsing, "Propagating phonons coupled to an artificial atom", Science **346**, 207–211 (2014).

[172]P. Arrangoiz-Arriola and A. H. Safavi-Naeini, "Prospects for quantum acoustics with phononic crystal devices", (2016).

[173]Y. Chu, P. Kharel, W. H. Renninger, L. D. Burkhart, L. Frunzio, P. T. Rakich, and R. J. Schoelkopf, "Quantum acoustics with superconducting qubits", Science **358**, 199–202 (2017).

[174]S. A. Tadesse and M. Li, "Sub-optical wavelength acoustic wave modulation of integrated photonic resonators at microwave frequencies", Nature Communications **5**, 5402 (2014).

[175]S. A. Tadesse, H. Li, Q. Liu, and M. Li, "Acousto-optic modulation of a photonic crystal nanocavity with Lamb waves in microwave K band", Applied Physics Letters **107**, 201113 (2015).

[176]M. Aspelmeyer, T. J. Kippenberg, and F. Marquardt, "Cavity optomechanics", Reviews of Modern Physics **86**, 1391–1452 (2014).

[177]M. Metcalfe, "Applications of cavity optomechanics", Applied Physics Reviews **1**, 031105 (2014).

[178]T. Sogawa, P. V. Santos, S. K. Zhang, S. Eshlaghi, A. D. Wieck, and K. H. Ploog, "Transport and Lifetime Enhancement of Photoexcited Spins in GaAs by Surface Acoustic Waves", Physical Review Letters **87**, 276601 (2001).

[179]J. A. H. Stotz, R. Hey, P. V. Santos, and K. H. Ploog, "Coherent spin transport through dynamic quantum dots", Nature Materials **4**, 585–588 (2005).

[180]O. D. D. Couto, S. Lazić, F. Iikawa, J. A. H. Stotz, U. Jahn, R. Hey, and P. V. Santos, "Photon anti-bunching in acoustically pumped quantum dots", Nature Photonics **3**, 645–648 (2009).

[181]M. Ohring, *Materials science of thin films* (Elsevier Science, 2001).

[182]H. Scheel, P. Capper, and P. Rudolph, *Crystal growth technology: semiconductors and dielectrics* (John Wiley & Sons, 2010).

[183]T.-K. Hsiao, "A Single-photon Source Based on a Lateral n-i-p Junction Driven by a Surface Acoustic Wave", PhD thesis (University of Cambridge, 2018).

[184]I. N. Stranski and L. Krastanow, "Zur theorie der orientierten ausscheidung von ionenkristallen aufeinander", Abhandlungen der Mathematisch-Naturwissenschaftlichen Klasse IIb. Akademie der Wissenschaften Wien **146**, 797–810 (1938).

[185]A. Pimpinelli and J. Villain, *Physics of crystal growth* (Cambridge University Press, 1998).

[186]D. Andrews, *Photonics, nanophotonic structures and materials* (Wiley, 2015).

[187]D. Leonard, K. Pond, and P. Petroff, "Critical layer thickness for self-assembled inas islands on gaas", Physical Review B **50**, 11687 (1994).

[188]E. Pelucchi, S. Watanabe, K. Leifer, Q. Zhu, B. Dwir, P. De Los Rios, and E. Kapon, "Mechanisms of Quantum Dot Energy Engineering by Metalorganic Vapor Phase Epitaxy on Patterned Nonplanar Substrates", Nano Letters **7**, 1282–1285 (2007).

[189]C. Schneider, T. Heindel, A. Huggenberger, P. Weinmann, C. Kistner, M. Kamp, S. Reitzenstein, S. Höfling, and A. Forchel, "Single photon emission from a site-controlled quantum dot-micropillar cavity system", Applied Physics Letters **94**, 111111 (2009).

[190]F. Albert, S. Stobbe, C. Schneider, T. Heindel, S. Reitzenstein, S. Höfling, P. Lodahl, L. Worschech, and A. Forchel, "Quantum efficiency and oscillator strength of site-controlled InAs quantum dots", Applied Physics Letters **96**, 151102 (2010).

[191]M. Strauß, A. Kaganskiy, R. Voigt, P. Schnauber, J.-H. Schulze, S. Rodt, A. Strittmatter, and S. Reitzenstein, "Resonance fluorescence of a site-controlled quantum dot realized by the buried-stressor growth technique", Applied Physics Letters **110**, 111101 (2017).

[192]F. Laermer and A. Schilp, "Method of anisotropically etching silicon", 5501893 ((Stuttgart, DE), (Schwäbisch Gmünd, DE)) (Mar. 1996).

[193]N. G. Stoltz, M. Rakher, S. Strauf, A. Badolato, D. D. Lofgreen, P. M. Petroff, L. A. Coldren, and D. Bouwmeester, "High-quality factor optical microcavities using oxide apertured micropillars", Applied Physics Letters **87**, 031105 (2005).

[194]A. V. Kuhlmann, J. Houel, D. Brunner, A. Ludwig, D. Reuter, A. D. Wieck, and R. J. Warburton, "A dark-field microscope for background-free detection of resonance fluorescence from single semiconductor quantum dots operating in a set-and-forget mode", Review of Scientific Instruments **84**, 073905 (2013).

[195]Becker & Hickl GmbH, "Time-correlated single photon counting modules", SPC module manual (2002).

[196]P. Kapusta, M. Wahl, and R. Erdmann, *Advanced photon counting: applications, methods, instrumentation* (Springer International Publishing, 2015).

[197]K.-J. Bathe, "Finite element method", Wiley encyclopedia of computer science and engineering (2008).

[198]K. H. Huebner, D. L. Dewhirst, D. E. Smith, and T. G. Byrom, *The finite element method for engineers* (John Wiley & Sons, 2008).

[199]J.-P. Berenger, "A perfectly matched layer for the absorption of electromagnetic waves", Journal of computational physics **114**, 185–200 (1994).

[200]N. Gisin, G. Ribordy, W. Tittel, and H. Zbinden, "Quantum cryptography", Reviews of modern physics **74**, 145 (2002).

[201]E. Waks, K. Inoue, C. Santori, D. Fattal, J. Vuckovic, G. S. Solomon, and Y. Yamamoto, "Secure communication: Quantum cryptography with a photon turnstile", Nature **420**, 762–762 (2002).

[202]H. J. Kimble, M. Dagenais, and L. Mandel, "Photon antibunching in resonance fluorescence", Physical Review Letters **39**, 691 (1977).

[203]A. Kuhn, M. Hennrich, and G. Rempe, "Deterministic Single-Photon Source for Distributed Quantum Networking", Physical Review Letters **89**, 067901 (2002).

[204]F. Diedrich and H. Walther, "Nonclassical radiation of a single stored ion", Physical review letters **58**, 203 (1987).

[205]T. Basché, W. E. Moerner, M. Orrit, and H. Talon, "Photon antibunching in the fluorescence of a single dye molecule trapped in a solid", Physical review letters **69**, 1516 (1992).

[206]C. Kurtsiefer, S. Mayer, P. Zarda, and H. Weinfurter, "Stable solid-state source of single photons", Physical review letters **85**, 290 (2000).

[207]R. Brouri, A. Beveratos, J.-P. Poizat, and P. Grangier, "Photon antibunching in the fluorescence of individual color centers in diamond", Optics letters **25**, 1294–1296 (2000).

[208]P. Michler, A. Kiraz, C. Becher, W. V. Schoenfeld, P. M. Petroff, L. Zhang, E. Hu, and A. Imamoglu, "A Quantum Dot Single-Photon Turnstile Device", Science **290**, 2282–2285 (2000).

[209]C. Santori, M. Pelton, G. Solomon, Y. Dale, and Y. Yamamoto, "Triggered single photons from a quantum dot", Physical Review Letters **86**, 1502 (2001).

[210]E. Moreau, I. Robert, J. M. Gérard, I. Abram, L. Manin, and V. Thierry-Mieg, "Single-mode solid-state single photon source based on isolated quantum dots in pillar microcavities", Applied Physics Letters **79**, 2865 (2001).

[211]J. L. O'Brien, A. Furusawa, and J. Vučković, "Photonic quantum technologies", Nature Photonics **3**, 687–695 (2009).

[212]P. Lodahl, S. Mahmoodian, and S. Stobbe, "Interfacing single photons and single quantum dots with photonic nanostructures", Reviews of Modern Physics **87**, 347–400 (2015).

[213]D. Englund, D. Fattal, E. Waks, G. Solomon, B. Zhang, T. Nakaoka, Y. Arakawa, Y. Yamamoto, and J. Vučković, "Controlling the Spontaneous Emission Rate of Single Quantum Dots in a Two-Dimensional Photonic Crystal", Physical Review Letters **95**, 013904 (2005).

[214]O. Couto, S. Lazić, F. Iikawa, J. Stotz, U. Jahn, R. Hey, and P. Santos, "Evidence for photon anti-bunching in acoustically pumped dots", Physica E: Low-dimensional Systems and Nanostructures **42**, 2497–2500 (2010).

[215]C. L. Foden, V. I. Talyanskii, G. J. Milburn, M. L. Leadbeater, and M. Pepper, "High-frequency acousto-electric single-photon source", Physical Review A **62**, 011803 (2000).

[216]S. Völk, F. J. R. Schülein, F. Knall, D. Reuter, A. D. Wieck, T. A. Truong, H. Kim, P. M. Petroff, A. Wixforth, and H. J. Krenner, "Enhanced Sequential Carrier Capture into Individual Quantum Dots and Quantum Posts Controlled by Surface Acoustic Waves", Nano Letters **10**, 3399–3407 (2010).

[217]T.-K. Hsiao, A. Rubino, Y. Chung, S.-K. Son, H. Hou, J. Pedrós, A. Nasir, G. Éthier-Majcher, M. J. Stanley, R. T. Phillips, T. A. Mitchell, J. P. Griffiths, I. Farrer, D. A. Ritchie, and C. J. B. Ford, "Single-photon Emission from an Acoustically-driven Lateral Light-emitting Diode", arXiv:1901.03464 [cond-mat, physics:physics, physics:quant-ph], arXiv: 1901.03464 (2019).

[218]S. Kapfinger, T. Reichert, S. Lichtmannecker, K. Müller, J. J. Finley, A. Wixforth, M. Kaniber, and H. J. Krenner, "Dynamic acousto-optic control of a strongly coupled photonic molecule", Nature Communications **6**, 8540 (2015).

[219]D. A. Fuhrmann, S. M. Thon, H. Kim, D. Bouwmeester, P. M. Petroff, A. Wixforth, and H. J. Krenner, "Dynamic modulation of photonic crystal nanocavities using gigahertz acoustic phonons", Nature Photonics **5**, 605–609 (2011).

[220]H. Li, S. A. Tadesse, Q. Liu, and M. Li, "Nanophotonic cavity optomechanics with propagating acoustic waves at frequencies up to 12 GHz", Optica **2**, 826 (2015).

[221]A. Schlehahn, A. Thoma, P. Munnelly, M. Kamp, S. Höfling, T. Heindel, C. Schneider, and S. Reitzenstein, "An electrically driven cavity-enhanced source of indistinguishable photons with 61% overall efficiency", APL Photonics **1**, 011301 (2016).

[222]A. Schlehahn, R. Schmidt, C. Hopfmann, J.-H. Schulze, A. Strittmatter, T. Heindel, L. Gantz, E. R. Schmidgall, D. Gershoni, and S. Reitzenstein, "Generating single photons at gigahertz modulation-speed using electrically controlled quantum dot microlenses", Applied Physics Letters **108**, 021104 (2016).

[223]D. J. P. Ellis, A. J. Bennett, S. J. Dewhurst, C. A. Nicoll, D. A. Ritchie, and A. J. Shields, "Cavity-enhanced radiative emission rate in a single-photon-emitting diode operating at 0.5 GHz", New Journal of Physics **10**, 043035 (2008).

[224]M. Reischle, C. Kessler, W.-M. Schulz, M. Eichfelder, R. Roßbach, M. Jetter, and P. Michler, "Triggered single-photon emission from electrically excited quantum dots in the red spectral range", Applied Physics Letters **97**, 143513 (2010).

[225]A. J. Bennett, D. C. Unitt, P. See, A. J. Shields, P. Atkinson, K. Cooper, and D. A. Ritchie, "Electrical control of the uncertainty in the time of single photon emission events", Physical Review B **72**, 033316 (2005).

[226]A. Schlehahn, M. Gaafar, M. Vaupel, M. Gschrey, P. Schnauber, J.-H. Schulze, S. Rodt, A. Strittmatter, W. Stolz, A. Rahimi-Iman, T. Heindel, M. Koch, and S. Reitzenstein, "Single-photon emission at a rate of 143 MHz from a deterministic quantum-dot microlens triggered by a mode-locked vertical-external-cavity surface-emitting laser", Applied Physics Letters **107**, 041105 (2015).

[227]J. R. Gell, M. B. Ward, R. J. Young, R. M. Stevenson, P. Atkinson, D. Anderson, G. A. C. Jones, D. A. Ritchie, and A. J. Shields, "Modulation of single quantum dot energy levels by a surface-acoustic-wave", Applied Physics Letters **93**, 081115 (2008).

[228]M. Metcalfe, S. M. Carr, A. Muller, G. S. Solomon, and J. Lawall, "Resolved Sideband Emission of InAs / GaAs Quantum Dots Strained by Surface Acoustic Waves", Physical Review Letters **105**, 037401 (2010).

[229]M. Weiß, S. Kapfinger, T. Reichert, J. J. Finley, A. Wixforth, M. Kaniber, and H. J. Krenner, "Surface acoustic wave regulated single photon emission from a coupled quantum dot–nanocavity system", Applied Physics Letters **109**, 033105 (2016).

[230]H. Hou and C. Hall, "Low-dimensional electron transport and surface acoustic waves in GaAs and ZnO heterostructures", PhD thesis (University of Cambridge, 2018).

[231]M. Metcalfe, A. Muller, G. S. Solomon, and J. Lawall, "Active feedback of a Fabry-Perot cavity to the emission of a single InAs/GaAs quantum dot", JOSA B **26**, 2308–2314 (2009).

[232]D. A. Golter, T. Oo, M. Amezcua, K. A. Stewart, and H. Wang, "Optomechanical Quantum Control of a Nitrogen-Vacancy Center in Diamond", Physical Review Letters **116**, 143602 (2016).

[233]E. D. S. Nysten, Y. H. Huo, H. Yu, G. F. Song, A. Rastelli, and H. J. Krenner, "Multi-harmonic quantum dot optomechanics in fused LiNbO3–(Al)GaAs hybrids", Journal of Physics D: Applied Physics **50**, 43LT01 (2017).

[234]X. Qiang, X. Zhou, J. Wang, C. M. Wilkes, T. Loke, S. O'Gara, L. Kling, G. D. Marshall, R. Santagati, T. C. Ralph, J. B. Wang, J. L. O'Brien, M. G. Thompson, and J. C. F. Matthews, "Large-scale silicon quantum photonics implementing arbitrary two-qubit processing", Nature Photonics (2018).

[235]M. Kues, C. Reimer, P. Roztocki, L. R. Cortés, S. Sciara, B. Wetzel, Y. Zhang, A. Cino, S. T. Chu, B. E. Little, D. J. Moss, L. Caspani, J. Azaña, and R. Morandotti, "On-chip generation of high-dimensional entangled quantum states and their coherent control", Nature **546**, 622–626 (2017).

[236]S. Aghaeimeibodi, B. Desiatov, J.-H. Kim, C.-M. Lee, M. A. Buyukkaya, A. Karasahin, C. J. K. Richardson, R. P. Leavitt, M. Lončar, and E. Waks, "Integration of quantum dots with lithium niobate photonics", Applied Physics Letters **113**, 221102 (2018).

[237]I. E. Zadeh, A. W. Elshaari, K. D. Jöns, A. Fognini, D. Dalacu, P. J. Poole, M. E. Reimer, and V. Zwiller, "Deterministic integration of single photon sources in silicon based photonic circuits", Nano Letters **16**, 2289–2294 (2016).

[238]C. P. Dietrich, A. Fiore, M. G. Thompson, M. Kamp, and S. Höfling, "GaAs integrated quantum photonics: Towards compact and multi-functional quantum photonic integrated circuits", Laser & Photonics Reviews **10**, 870–894 (2016).

[239]J. P. Sprengers, A. Gaggero, D. Sahin, S. Jahanmirinejad, G. Frucci, F. Mattioli, R. Leoni, J. Beetz, M. Lermer, M. Kamp, S. Höfling, R. Sanjines, and A. Fiore, "Waveguide superconducting single-photon detectors for integrated quantum photonic circuits", Applied Physics Letters **99**, 181110 (2011).

[240]S. Bogdanov, M. Y. Shalaginov, A. Boltasseva, and V. M. Shalaev, "Material platforms for integrated quantum photonics", Optical Materials Express **7**, 111–132 (2017).

[241]U. Rengstl, M. Schwartz, T. Herzog, F. Hargart, M. Paul, S. L. Portalupi, M. Jetter, and P. Michler, "On-chip beamsplitter operation on single photons from quasi-resonantly excited quantum dots embedded in GaAs rib waveguides", Applied Physics Letters **107**, 021101 (2015).

[242]A. Laucht, S. Pütz, T. Günthner, N. Hauke, R. Saive, S. Frédérick, M. Bichler, M.-C. Amann, A. W. Holleitner, M. Kaniber, and J. J. Finley, "A Waveguide-Coupled On-Chip Single-Photon Source", Physical Review X **2**, 011014 (2012).

[243]R. J. Coles, D. M. Price, J. E. Dixon, B. Royall, E. Clarke, P. Kok, M. S. Skolnick, A. M. Fox, and M. N. Makhonin, "Chirality of nanophotonic waveguide with embedded quantum emitter for unidirectional spin transfer", Nature Communications **7**, 11183 (2016).

[244]M. Davanco, J. Liu, L. Sapienza, C.-Z. Zhang, J. V. D. M. Cardoso, V. Verma, R. Mirin, S. W. Nam, L. Liu, and K. Srinivasan, "Heterogeneous integration for on-chip quantum photonic circuits with single quantum dot devices", Nature Communications **8**, 889 (2017).

[245]D. B. Sohn, S. Kim, and G. Bahl, "Time-reversal symmetry breaking with acoustic pumping of nanophotonic circuits", Nature Photonics **12**, 91 (2018).

[246]G. Calajo, M. J. A. Schuetz, H. Pichler, M. D. Lukin, P. Schneeweiss, J. Volz, and P. Rabl, "Quantum acousto-optic control of light-matter interactions in nanophotonic networks", arXiv:1901.02899 [cond-mat, physics:physics, physics:quant-ph], arXiv: 1901.02899 (2019).

[247]D. A. Golter, T. Oo, M. Amezcua, I. Lekavicius, K. A. Stewart, and H. Wang, "Coupling a Surface Acoustic Wave to an Electron Spin in Diamond via a Dark State", Physical Review X **6**, 041060 (2016).

[248]S. J. Whiteley, G. Wolfowicz, C. P. Anderson, A. Bourassa, H. Ma, M. Ye, G. Koolstra, K. J. Satzinger, M. V. Holt, F. J. Heremans, A. N. Cleland, D. I. Schuster, G. Galli, and D. D. Awschalom, "Spin–phonon interactions in silicon carbide addressed by Gaussian acoustics", Nature Physics **15**, 490–495 (2019).

[249]M. C. Kuzyk and H. Wang, "Scaling Phononic Quantum Networks of Solid-State Spins with Closed Mechanical Subsystems", Physical Review X **8**, 041027 (2018).

[250]S. Benchabane, A. Khelif, J.-Y. Rauch, L. Robert, and V. Laude, "Evidence for complete surface wave band gap in a piezoelectric phononic crystal", Physical Review E **73**, 065601(R) (2006).

[251]L. Arizmendi, "Photonic applications of lithium niobate crystals", physica status solidi (a) **201**, 253–283 (2004).

[252]J. Pustiowski, K. Müller, M. Bichler, G. Koblmüller, J. J. Finley, A. Wixforth, and H. J. Krenner, "Independent dynamic acousto-mechanical and electrostatic control of individual quantum dots in a LiNbO3-GaAs hybrid", Applied Physics Letters **106**, 013107 (2015).

[253]E. Yablonovitch, T. Sands, D. M. Hwang, I. Schnitzer, T. J. Gmitter, S. K. Shastry, D. S. Hill, and J. C. C. Fan, "Van der Waals bonding of GaAs on Pd leads to a permanent, solid-phase-topotaxial, metallurgical bond", Applied Physics Letters **59**, 3159–3161 (1991).

[254]D. Taillaert, W. Bogaerts, P. Bienstman, T. F. Krauss, P. Van Daele, I. Moerman, S. Verstuyft, K. De Mesel, and R. Baets, "An out-of-plane grating coupler for efficient butt-coupling between compact planar waveguides and single-mode fibers", Quantum Electronics, IEEE Journal of **38**, 949–955 (2002).

[255]X. Zhou, I. Kulkova, T. Lund-Hansen, S. L. Hansen, P. Lodahl, and L. Midolo, "High-efficiency shallow-etched grating on GaAs membranes for quantum photonic applications", Applied Physics Letters **113**, 251103 (2018).

[256]L. Su, R. Trivedi, N. V. Sapra, A. Y. Piggott, D. Vercruysse, and J. Vučković, "Fully-automated optimization of grating couplers", Optics Express **26**, 4023–4034 (2018).

[257]D. Hallett, A. P. Foster, D. L. Hurst, B. Royall, P. Kok, E. Clarke, I. E. Itskevich, A. M. Fox, M. S. Skolnick, and L. R. Wilson, "Electrical control of nonlinear quantum optics in a nano-photonic waveguide", Optica **5**, 644–650 (2018).

[258]A. Javadi, I. Söllner, M. Arcari, S. L. Hansen, L. Midolo, S. Mahmoodian, G. Kiršanskė, T. Pregnolato, E. H. Lee, J. D. Song, S. Stobbe, and P. Lodahl, "Single-photon non-linear optics with a quantum dot in a waveguide", Nature Communications **6**, 8655 (2015).

[259]Y. Wang, X. Wang, J. Flueckiger, H. Yun, W. Shi, R. Bojko, N. A. F. Jaeger, and L. Chrostowski, "Focusing sub-wavelength grating couplers with low back reflections for rapid prototyping of silicon photonic circuits", Optics Express **22**, 20652 (2014).

[260]Y. Ding, H. Ou, and C. Peucheret, "Ultrahigh-efficiency apodized grating coupler using fully etched photonic crystals", Optics Letters **38**, 2732 (2013).

[261]D. Vermeulen, S. Selvaraja, P. Verheyen, G. Lepage, W. Bogaerts, P. Absil, D. Van Thourhout, and G. Roelkens, "High-efficiency fiber-to-chip grating couplers realized using an advanced CMOS-compatible silicon-on-insulator platform", Optics express **18**, 18278–18283 (2010).

[262] A. Z. Subramanian, S. Selvaraja, P. Verheyen, A. Dhakal, K. Komorowska, and R. Baets, "Near-Infrared Grating Couplers for Silicon Nitride Photonic Wires", IEEE Photonics Technology Letters **24**, 1700–1703 (2012).

[263] L. Ding, C. Baker, P. Senellart, A. Lemaitre, S. Ducci, G. Leo, and I. Favero, "High Frequency GaAs Nano-Optomechanical Disk Resonator", Physical Review Letters **105**, 263903 (2010).

[264] C.-W. Cheng, K.-T. Shiu, N. Li, S.-J. Han, L. Shi, and D. K. Sadana, "Epitaxial lift-off process for gallium arsenide substrate reuse and flexible electronics", Nature Communications **4**, 1577 (2013).

[265] D. Press, T. D. Ladd, B. Zhang, and Y. Yamamoto, "Complete quantum control of a single quantum dot spin using ultrafast optical pulses", Nature **456**, 218–221 (2008).

[266] A. Greilich, S. E. Economou, S. Spatzek, D. R. Yakovlev, D. Reuter, A. D. Wieck, T. L. Reinecke, and M. Bayer, "Ultrafast optical rotations of electron spins in quantum dots", Nature Physics **5**, 262–266 (2009).

[267] M. Kroner, K. M. Weiss, B. Biedermann, S. Seidl, S. Manus, A. W. Holleitner, A. Badolato, P. M. Petroff, B. D. Gerardot, R. J. Warburton, and K. Karrai, "Optical Detection of Single-Electron Spin Resonance in a Quantum Dot", Physical Review Letters **100** (2008).

[268] K. C. Nowack, F. H. L. Koppens, Y. V. Nazarov, and L. M. K. Vandersypen, "Coherent Control of a Single Electron Spin with Electric Fields", Science **318**, 1430–1433 (2007).

[269] L. M. Woods, T. L. Reinecke, and Y. Lyanda-Geller, "Spin relaxation in quantum dots", Physical Review B **66**, 161318 (2002).

[270] A. V. Khaetskii and Y. V. Nazarov, "Spin relaxation in semiconductor quantum dots", Physical Review B **61**, 12639 (2000).

[271] A. V. Khaetskii and Y. V. Nazarov, "Spin-flip transitions between Zeeman sublevels in semiconductor quantum dots", Physical Review B **64** (2001).

[272] J. Fischer, W. A. Coish, D. V. Bulaev, and D. Loss, "Spin decoherence of a heavy hole coupled to nuclear spins in a quantum dot", Physical Review B **78**, 155329 (2008).

[273] D. V. Bulaev and D. Loss, "Spin Relaxation and Decoherence of Holes in Quantum Dots", Physical Review Letters **95**, 076805 (2005).

[274] J. J. Finley, A. D. Ashmore, A. Lemaître, D. J. Mowbray, M. S. Skolnick, I. E. Itskevich, P. A. Maksym, M. Hopkinson, and T. F. Krauss, "Charged and neutral exciton complexes in individual self-assembled In (Ga) As quantum dots", Physical Review B **63** (2001).

[275] X. Xu, Y. Wu, B. Sun, Q. Huang, J. Cheng, D. G. Steel, A. S. Bracker, D. Gammon, C. Emary, and L. J. Sham, "Fast Spin State Initialization in a Singly Charged InAs-GaAs Quantum Dot by Optical Cooling", Physical Review Letters **99** (2007).

[276] J. Dreiser, M. Atatüre, C. Galland, T. Müller, A. Badolato, and A. Imamoglu, "Optical investigations of quantum dot spin dynamics as a function of external electric and magnetic fields", Physical Review B **77** (2008).

[277] A. J. Bennett, M. A. Pooley, Y. Cao, N. Sköld, I. Farrer, D. A. Ritchie, and A. J. Shields, "Voltage tunability of single-spin states in a quantum dot", Nature Communications **4**, 1522 (2013).

[278] A. Imamoḡlu, E. Knill, L. Tian, and P. Zoller, "Optical Pumping of Quantum-Dot Nuclear Spins", Physical Review Letters **91** (2003).

[279]K. G. Lagoudakis, K. A. Fischer, T. Sarmiento, K. Mueller, and J. Vučković, "Hole-spin pumping and repumping in a p -type δ-doped InAs quantum dot", Physical Review B **90** (2014).

[280]D. Heiss, S. Schaeck, H. Huebl, M. Bichler, G. Abstreiter, J. J. Finley, D. V. Bulaev, and D. Loss, "Observation of extremely slow hole spin relaxation in self-assembled quantum dots", Physical Review B **76**, 241306 (2007).

[281]A. Greilich, S. G. Carter, D. Kim, A. S. Bracker, and D. Gammon, "Optical control of one and two hole spins in interacting quantum dots", Nature Photonics **5**, 702–708 (2011).

[282]D. Brunner, B. D. Gerardot, P. A. Dalgarno, G. Wüst, K. Karrai, N. G. Stoltz, P. M. Petroff, and R. J. Warburton, "A coherent single-hole spin in a semiconductor", science **325**, 70–72 (2009).

[283]J. P. Lee, "Photon Sources for Linear Optical Quantum Computing", PhD thesis (University of Cambridge, 2018).

[284]S. E. Economou, N. Lindner, and T. Rudolph, "Optically Generated 2-Dimensional Photonic Cluster State from Coupled Quantum Dots", Physical Review Letters **105**, 093601 (2010).

[285]A. Russo, E. Barnes, and S. E. Economou, "Photonic graph state generation from quantum dots and color centers for quantum communications", Physical Review B **98**, 085303 (2018).

[286]C. Schön, E. Solano, F. Verstraete, J. I. Cirac, and M. M. Wolf, "Sequential Generation of Entangled Multiqubit States", Physical Review Letters **95**, 110503 (2005).

[287]I. Schwartz, D. Cogan, E. R. Schmidgall, Y. Don, L. Gantz, O. Kenneth, N. H. Lindner, and D. Gershoni, "Deterministic generation of a cluster state of entangled photons", Science **354** (2016).

[288]J. R. Schaibley, A. P. Burgers, G. A. McCracken, L.-M. Duan, P. R. Berman, D. G. Steel, A. S. Bracker, D. Gammon, and L. J. Sham, "Demonstration of Quantum Entanglement between a Single Electron Spin Confined to an InAs Quantum Dot and a Photon", Physical Review Letters **110** (2013).

[289]W. B. Gao, P. Fallahi, E. Togan, J. Miguel-Sanchez, and A. Imamoglu, "Observation of entanglement between a quantum dot spin and a single photon", Nature **491**, 426–430 (2012).

[290]K. De Greve, L. Yu, P. L. McMahon, J. S. Pelc, C. M. Natarajan, N. Y. Kim, E. Abe, S. Maier, C. Schneider, M. Kamp, S. Höfling, R. H. Hadfield, A. Forchel, M. M. Fejer, and Y. Yamamoto, "Quantum-dot spin–photon entanglement via frequency downconversion to telecom wavelength", Nature **491**, 421–425 (2012).

[291]J. Brendel, N. Gisin, W. Tittel, and H. Zbinden, "Pulsed energy-time entangled twin-photon source for quantum communication", Physical Review Letters **82**, 2594 (1999).

[292]I. Marcikic, H. De Riedmatten, W. Tittel, H. Zbinden, M. Legré, and N. Gisin, "Distribution of time-bin entangled qubits over 50 km of optical fiber", Physical Review Letters **93**, 180502 (2004).

[293]R. Stockill, C. Le Gall, C. Matthiesen, L. Huthmacher, E. Clarke, M. Hugues, and M. Atatüre, "Quantum dot spin coherence governed by a strained nuclear environment", Nature Communications **7**, 12745 (2016).

[294]A. Bechtold, D. Rauch, F. Li, T. Simmet, P.-L. Ardelt, A. Regler, K. Müller, N. A. Sinitsyn, and J. J. Finley, "Three-stage decoherence dynamics of an electron spin qubit in an optically active quantum dot", Nature Physics **11**, 1005–1008 (2015).

[295]T. M. Sweeney, S. G. Carter, A. S. Bracker, M. Kim, C. S. Kim, L. Yang, P. M. Vora, P. G. Brereton, E. R. Cleveland, and D. Gammon, "Cavity-stimulated Raman emission from a single quantum dot spin", Nature Photonics **8**, 442–447 (2014).

[296]J. P. Lee, A. J. Bennett, R. M. Stevenson, D. J. P. Ellis, I. Farrer, D. A. Ritchie, and A. J. Shields, "Multi-dimensional photonic states from a quantum dot", Quantum Science and Technology **3**, 024008 (2018).

[297]T. Grange, N. Somaschi, C. Ant?n, L. De Santis, G. Coppola, V. Giesz, A. Lema?tre, I. Sagnes, A. Auff?ves, and P. Senellart, "Reducing Phonon-Induced Decoherence in Solid-State Single-Photon Sources with Cavity Quantum Electrodynamics", Physical Review Letters **118** (2017).

[298]V. Giesz, S. L. Portalupi, T. Grange, C. Antón, L. De Santis, J. Demory, N. Somaschi, I. Sagnes, A. Lemaître, L. Lanco, A. Auffèves, and P. Senellart, "Cavity-enhanced two-photon interference using remote quantum dot sources", Physical Review B **92**, 161302(R) (2015).

[299]I. Schwartz, E. R. Schmidgall, L. Gantz, D. Cogan, E. Bordo, Y. Don, M. Zielinski, and D. Gershoni, "Deterministic Writing and Control of the Dark Exciton Spin Using Single Short Optical Pulses", Physical Review X **5**, 011009 (2015).

[300]L. Mandel, "Coherence and indistinguishability", Opt. Lett. **16**, 1882–1883 (1991).

[301]R. M. Stevenson, R. J. Young, P. See, D. G. Gevaux, K. Cooper, P. Atkinson, I. Farrer, D. A. Ritchie, and A. J. Shields, "Magnetic-field-induced reduction of the exciton polarization splitting in InAs quantum dots", Physical Review B **73**, 033306 (2006).

[302]K. G. Lagoudakis, K. A. Fischer, T. Sarmiento, P. L. McMahon, M. Radulaski, J. L. Zhang, Y. Kelaita, C. Dory, K. Müller, and J. Vučković, "Observation of Mollow Triplets with Tunable Interactions in Double Lambda Systems of Individual Hole Spins", Physical Review Letters **118** (2017).

[303]K. G. Lagoudakis, K. Fischer, T. Sarmiento, A. Majumdar, A. Rundquist, J. Lu, M. Bajcsy, and J. Vučković, "Deterministically charged quantum dots in photonic crystal nanoresonators for efficient spin–photon interfaces", New Journal of Physics **15**, 113056 (2013).

[304]M. Ediger, P. Dalgarno, J. Smith, B. Gerardot, R. Warburton, K. Karrai, and P. Petroff, "Controlled generation of neutral, negatively-charged and positively-charged excitons in the same single quantum dot", Applied Physics Letters **86**, 211909 (2005).

[305]B. Ellis, T. Sarmiento, M. Mayer, B. Zhang, J. Harris, E. Haller, and J. Vuckovic, "Electrically pumped photonic crystal nanocavity light sources using a laterally doped pin junction", Applied Physics Letters **96**, 181103 (2010).

[306]S. Coen, A. H. L. Chau, R. Leonhardt, J. D. Harvey, J. C. Knight, W. J. Wadsworth, and P. S. J. Russell, "Supercontinuum generation by stimulated raman scattering and parametric four-wave mixing in photonic crystal fibers", JOSA B **19**, 753–764 (2002).

[307]T. Kaldewey, S. Lüker, A. V. Kuhlmann, S. R. Valentin, J.-M. Chauveau, A. Ludwig, A. D. Wieck, D. E. Reiter, T. Kuhn, and R. J. Warburton, "Demonstrating the decoupling regime of the electron-phonon interaction in a quantum dot using chirped optical excitation", Physical Review B **95**, 241306 (2017).

[308]J. Mizrahi, B. Neyenhuis, K. Johnson, W. Campbell, C. Senko, D. Hayes, and C. Monroe, "Quantum control of qubits and atomic motion using ultrafast laser pulses", Applied Physics B **114**, 45–61 (2014).

[309]K. De Greve, P. L. McMahon, D. Press, T. D. Ladd, D. Bisping, C. Schneider, M. Kamp, L. Worschech, S. Höfling, A. Forchel, and Y. Yamamoto, "Ultrafast coherent control and suppressed nuclear feedback of a single quantum dot hole qubit", Nature Physics **7**, 872–878 (2011).

[310]Z. Sun, A. Delteil, S. Faelt, and A. Imamoğlu, "Measurement of spin coherence using Raman scattering", Physical Review B **93**, 241302 (2016).

[311]J. P. Lee, L. M. Wells, B. Villa, S. Kalliakos, R. M. Stevenson, D. J. P. Ellis, I. Farrer, D. A. Ritchie, A. J. Bennett, and A. J. Shields, "Controllable photonic time-bin qubits from a quantum dot", Phys. Rev. X **8**, 021078 (2018).

[312]D. Press, K. De Greve, P. L. McMahon, T. D. Ladd, B. Friess, C. Schneider, M. Kamp, S. Höfling, A. Forchel, and Y. Yamamoto, "Ultrafast optical spin echo in a single quantum dot", Nature Photonics **4**, 367–370 (2010).

[313]R. N. Malein, T. S. Santana, J. M. Zajac, A. C. Dada, E. Gauger, P. M. Petroff, J. Y. Lim, J. D. Song, and B. D. Gerardot, "Screening nuclear field fluctuations in quantum dots for indistinguishable photon generation", Physical review letters **116**, 257401 (2016).

[314]K. A. Fischer, L. Hanschke, J. Wierzbowski, T. Simmet, C. Dory, J. J. Finley, J. Vučković, and K. Müller, "Signatures of two-photon pulses from a quantum two-level system", Nature Physics (2017).

[315]G. Éthier-Majcher, D. Gangloff, R. Stockill, E. Clarke, M. Hugues, C. Le Gall, and M. Atatüre, "Improving a solid-state qubit through an engineered mesoscopic environment", Physical review letters **119**, 130503 (2017).

[316]R. Vasconcelos, S. Reisenbauer, C. Salter, G. Wachter, D. Wirtitsch, J. Schmiedmayer, P. Walther, and M. Trupke, "Scalable spin-photon entanglement by time-to-polarization conversion", arXiv:1812.10338 [quant-ph], arXiv: 1812.10338 (2018).

[317]M. S. Skolnick, D. G. Hayes, P. E. Simmonds, A. W. Higgs, G. W. Smith, H. J. Hutchinson, C. R. Whitehouse, L. Eaves, M. Henini, O. H. Hughes, M. L. Leadbeater, and D. P. Halliday, "Electronic processes in double-barrier resonant-tunneling structures studied by photoluminescence spectroscopy in zero and finite magnetic fields", Physical Review B **41**, 10754–10766 (1990).

[318]R. J. Warburton, C. S. Dürr, K. Karrai, J. P. Kotthaus, G. Medeiros-Ribeiro, and P. M. Petroff, "Charged Excitons in Self-Assembled Semiconductor Quantum Dots", Physical Review Letters **79**, 5282–5285 (1997).

[319]D. Pinotsi, P. Fallahi, J. Miguel-Sanchez, and A. Imamoglu, "Resonant Spectroscopy on Charge Tunable Quantum Dots in Photonic Crystal Structures", IEEE Journal of Quantum Electronics **47**, 1371–1374 (2011).

Appendix A

Deterministic Charge Control and Spin Initialisation of a Single Electron

In addition to the experiments on single holes reported in Ch.5, multiple devices with controlled tunnelling of electrons were investigated for spin storage and initialisation. The wafer structure used for these samples is similar, as shown in Fig. A.1. In the case of electron-tunnelling diodes, the superlattice is located between the dots and the p-doped top layers. The width of the tunneling barrier to the n-doped layers is 30 nm, compared to 20 nm for holes.

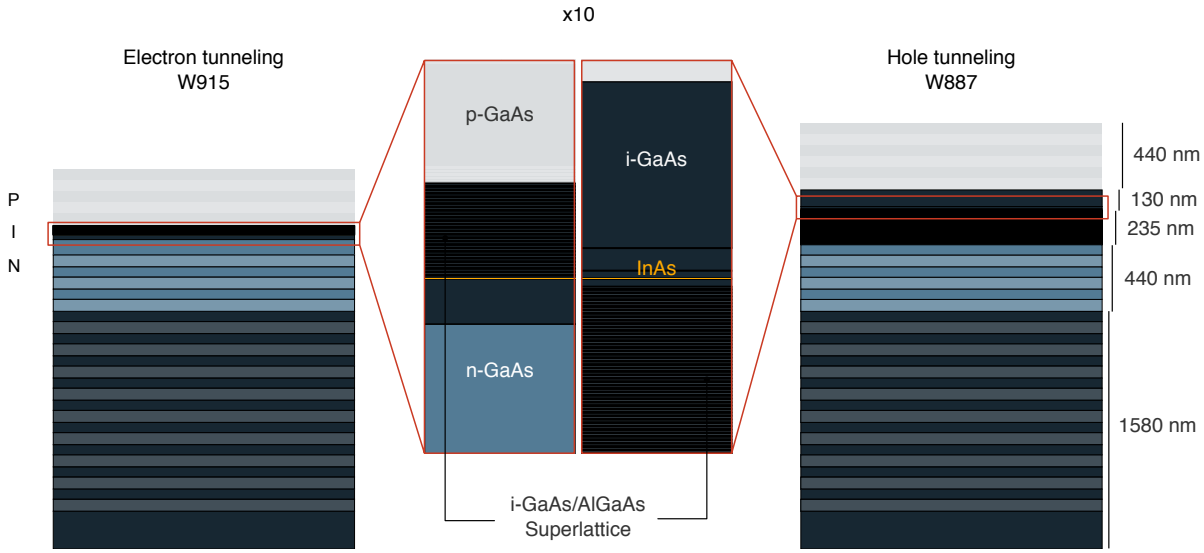

Fig. A.1: Wafer structure of the samples for electron and hole tunnelling. The corresponding Cavendish wafer numbers are W915 and W887. The colours show the type of doping in the structure and the shading differentiates GaAs and AlGaAs layers. The centre shows a magnification of the QD region. The main difference between the wafers is the location of the superlattice.

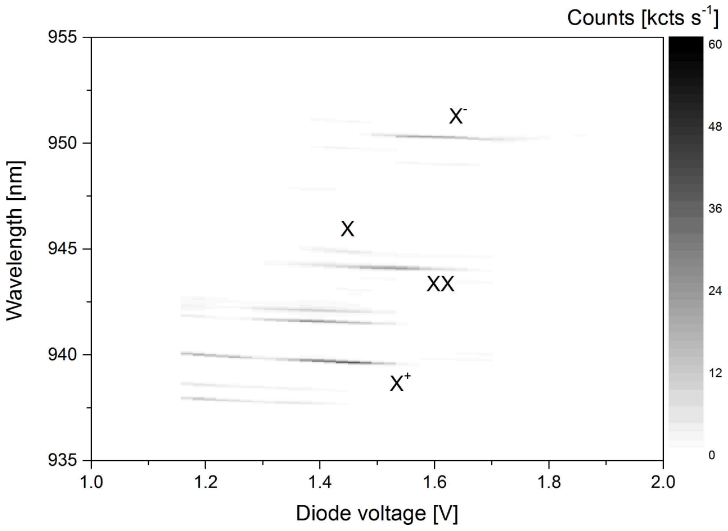

Fig. A.2: Non-resonant PL charge map for an electron charge-tunable diode. The dot is illuminated with 40 µW of an 850 nm laser.

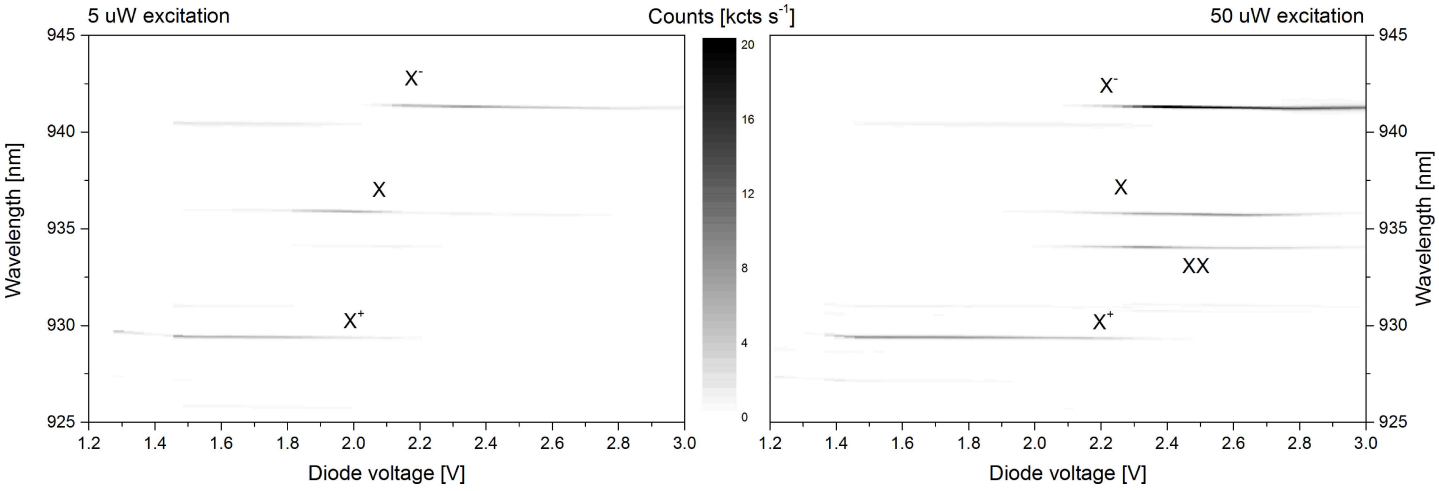

Fig. A.3: Non-resonant PL charge maps for two excitation powers. Higher power reveals the XX line and causes a shift of the plateaus due to charging.

Figure A.2 shows the µPL charge map of an electron-tunnelling device. As expected, the population of charges with applied bias is reversed compared to the hole tunnelling devices and we can controllably populate the dot with a single electron. The energy spacings between exciton complexes are comparable with the dots presented in Ch. 5. It is worth noting that the width and position of the plateaus is affected by the excitation laser power. Figure A.3 shows a comparison of maps taken at 5 and 50 µW illumination on another device. The higher power measurement exhibits extended plateaus and increased overlap in the emission from different complexes. It also highlights the position of the XX exciton complex. The distortion of the map at higher power is a consequence of charge accumulation at the blocking barrier[317, 318]. It is important to consider this effect when performing resonance fluorescence measurements, as

the absence of a non-resonant laser results in the plateau not necessarily extending as it might be expected from μPL measurements.

For the dots presented in Figs. A.2 and A.3, the equivalent RF measurement over the X^- line is shown in Fig.A.4. The measurement reveals the expected narrow resonance line with blurred edges at the plateau edge. Next, we look at the optical initialisation of the electron spin, in complete analogy to Ch.5 and Ch.6. Figure A.5 shows RF measurements on the two dots from Fig.A.4 for Faraday fields of 1 and 5 T, respectively. In Fig.A.5A two transitions can be clearly identified, corresponding to the vertical transitions of the system. They show a reduced signal compared to the $B = 0$ T measurement but it merely follows from the splitting into individually resolvable transitions. Contrary to the expectation, the spin is not initialised at this field, as the RF signal does not vanish in the central region of the plateau. This observation is consistent across dots and samples. Ref.[319] reports similar results, attributing the lack of spin pumping to current flow through the device or background doping. The current flowing through our devices at the voltages allowing for single electron tunnelling are < 0.1 nA and 16 μA for the dots presented in Fig.A.5 A and B, respectively. From the negligible current in the former device we do not expect this to be the reason for the lack of spin pumping. In Fig.A.5B the field is stronger and only one transition is visible, since the splitting exceeds the tuning range of the laser. This transition does exhibit some degree of extinction of the signal in the central region, marking the onset of spin initialisation, but is far from high-fidelity operation. The same behaviour is observed for Voigt magnetic fields. This evidence points to an insufficient suppression of the spin-flip rate which made it impossible to pursue experiments on single-electron spins. We note that the hole and electron tunnelling devices were processed in the same fashion, suggesting that the lack of spin initialisation in the latter is not related to the fabrication but intrinsic to the wafer. The hole-tunnelling device from Ch.5 also shows negligible current < 0.1 nA at the relevant voltage for measurement of the charged transition. Therefore, background doping is left as the likely cause of the lack of spin initialisation.

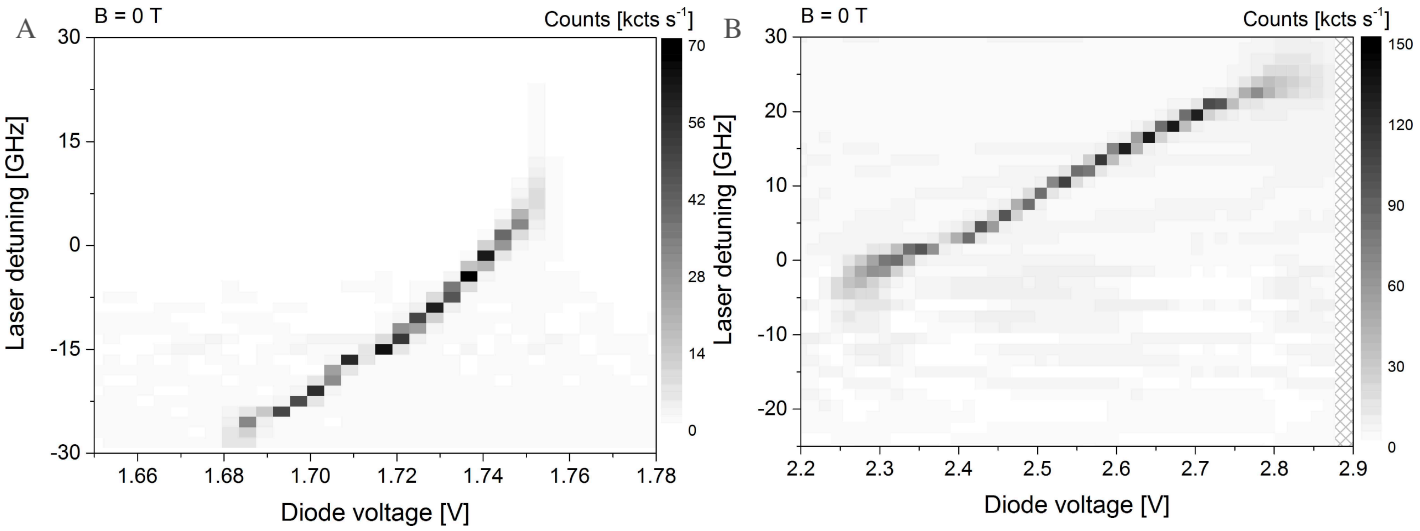

Fig. A.4: Resonance fluorescence maps of the X^- line for the dots presented in (**A**) Fig.A.2 and (**B**) Fig.A.3. The laser power is 40 nW in both cases.

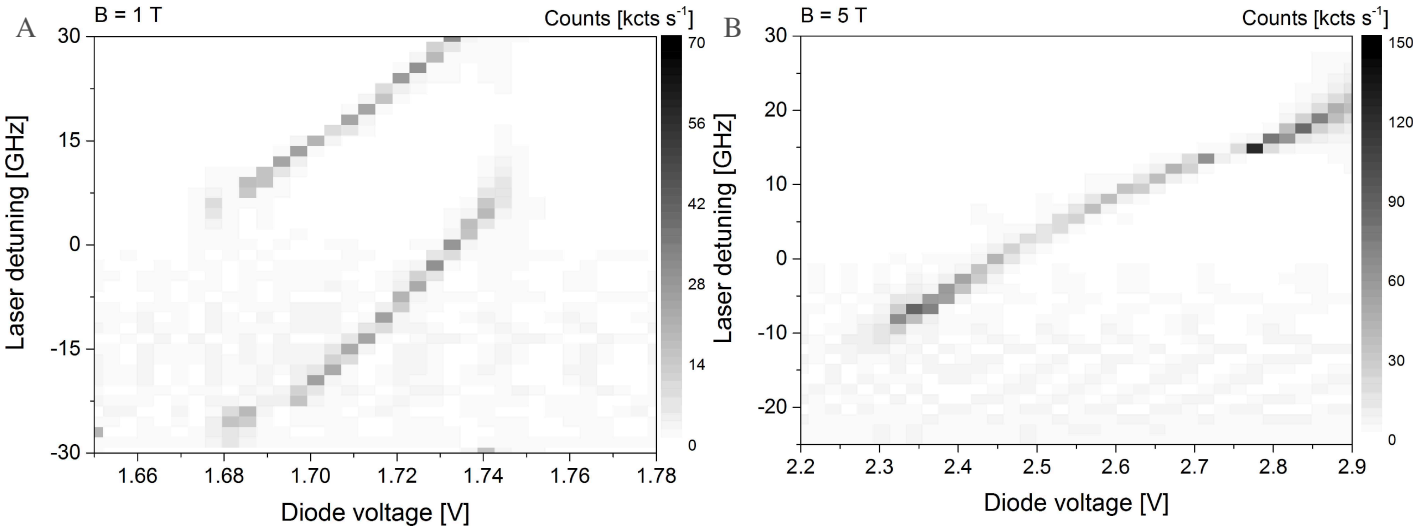

Fig. A.5: Resonance fluorescence maps of the X^- line for the dots presented in (**A**) Fig.A.2 and (**B**) Fig.A.3 at Faraday fields of (**A**) 1 T and (**B**) 5 T. The laser power is 40 nW in both cases.